Max-Planck-Institut für Physik
(Werner-Heisenberg-Institut)

Study of the VHE γ-ray emission from the Active Galactic Nucleus 1ES1959+650

Dissertation an der Fakultät für Physik
der Technischen Universität München
vorgelegt von

Nadia Tonello

Max-Planck-Institut für Physik
(Werner-Heisenberg-Institut)

Study of the VHE γ-ray emission from the Active Galactic Nucleus 1ES1959+650

Nadia Tonello

Vollständiger Abdruck der von der Fakultät für Physik der Technischen Universität München zur Erlangung des akademischen Grades eines

Doktors der Naturwissenschaften (Dr.rer.nat.)

genehmigten Dissertation.

Vorsitzender: Univ.-Prof. Dr. A. J. Buras

Prüfer der Dissertation:

1. Hon.-Prof. Dr. S. Bethke
2. Univ.-Prof. Dr. L. Oberauer

Die Dissertation wurde am 21.12.2005 bei der Technischen Universität München eingereicht und durch die Fakultät für Physik am 16.02.2006 angenommen.

Johannes Hevelius: Draco, from Uranographia (1690). The superimposed brown circle indicates the approximate position in the sky of the AGN 1ES1959+650.

A Valentino e Edda, i miei genitori
e in memoria di Gemma e Giulia.

Summary

Gamma(γ)-ray astronomy is one of the youngest branches of astro-particle physics. It started with V. Hess experiments and the discovery of cosmic rays, later with the scientific exploration of space and with the study of the phenomena that are the origin of the most energetic particles traveling in the Universe.

During the last decades, γ-ray astronomy by ground-based instruments to detect very high energy photons (E>30 GeV) has evolved considerably. After the pioneering work of the Whipple collaboration which detected the first γ-ray source, the Crab Nebula, the HEGRA collaboration contributed to discoveries in γ-ray astronomy, with its stand alone prototype CT1 and its array of 5 Cherenkov telescopes, called CT-System. Scientific goals of the collaboration included the study of the known TeV sources and the search for possible candidates. The first generation of telescopes was able to observe only γ-rays between a few hundreds of GeV and several TeV, while satellites gave us a view of the universe in γ-rays up to about 10 GeV. The lack of observations in the 10-300 GeV range was on one hand due to the small collection efficiency of satellite experiments and on the other hand to the high energy threshold ($>$ 300 GeV) of the first generation ground-based telescopes. In order to close this energy gap left by observations, the MAGIC collaboration designed and built a Cherenkov telescope adopting many novel technologies to reach the lowest energy threshold among the new generation IACTs (Imaging Atmospheric Cherenkov Telescopes). The physics program of Cherenkov telescopes covers several galactic and extragalactic types of sources, such as Supernova Remnants (SNR), pulsars, microquasars and Active Galactic Nuclei (AGNs).

In my thesis I report about a study of the AGN 1ES1959+650 based on data taken with the HEGRA CT1 and the new MAGIC telescope.

The physics interest in the AGN 1ES1959+650 concerns firstly the comparison of its spectral features to the ones of other known AGNs, the study of the most accepted γ-ray emission models and the correlations between activities of the source at different wavelengths.

The stand alone Cherenkov telescope CT1 of the HEGRA collaboration observed this AGN during several hundreds hours, starting from the year 2000. The first known period of high activity of the AGN 1ES1959+650 occurred in spring 2002. The CT1 telescope recorded it and the analysis results are presented here. The most remarkable outcome from the CT1 data analysis is the detection of an episode of high γ-ray emission, without coinciding high activity in X-rays. This was

classified as an orphan flare, occurring two nights before the orphan flare reported by the VERITAS collaboration. The CT1 spectrum obtained during the low state of the source is the first confirmation of the HEGRA System published low state spectrum. At the end of 2002 the CT1 telescope stopped taking data. At the same time, the MAGIC collaboration was completing the construction of its new telescope at the same site, the Roque de los Muchachos astronomical observatory on the Canary Island of La Palma (Spain). During the year 2003 I participated in the construction and installation of the huge tessellated reflector of the MAGIC telescope. Part of my thesis is dedicated to the description of MAGIC reflector, its technical features, and the studies that have been done before and during the installation on the main frame of the telescope. The reflector of the MAGIC telescope is unique among Cherenkov telescopes for its huge surface (236 m^2) and its low weight (17 t). New technologies have been used in its project. The material adopted for the construction of the mirror elements is the Aluminum alloy AlMgSi1. The mirror elements surface was machined with a diamond tool, such to obtain high reflectivity. The mirror elements are mounted onto a stiff and lightweight carbon fiber frame. The elements are equipped with a special control system of the so-called Active Mirror Control (AMC) to counteract the small deformations of the support frame and an internal heating to guarantee the best performances.

The low weight of the used materials allowed building such a large mirror area. The adopted technological choices have opened new horizons in γ-ray astronomy, as the possibility to detect lower energy γ-rays with respect to the past and to study some of the fastest, most enigmatic phenomena happening in the γ-ray universe, the Gamma-Ray Bursts (GRBs). The acquired experience is now source of new ideas for the development of the mirrors for the MAGIC project phase II: an improved clone of the MAGIC telescope is being built near the original one, such to form a stereoscopic system.

The first period of operation of MAGIC took place in 2004 during the commissioning phase. During the first cycle of observations the operation conditions of the telescope were not yet finalized. Both the hardware and the software were frequently corrected in order to reach the optimal integration of the subsystems. During that period the main targets of observation were the Crab Nebula, the TeV standard candle, and some of the well known TeV γ-ray sources, such as the AGN Mkn421, that had a period of strong emissions in TeV energies. Several hours of observation have been spent for the study of 1ES1959+650. I analyzed these data and compared them with the Crab Nebula observations during the same period and under similar observational conditions. By cross calibrating against a well-known source, I could avoid many telescope performance studies, which were difficult (even sometimes impossible) to obtain in the early operation of MAGIC. From the MAGIC measurements of 1ES1959+650 in September-October 2004, some of the first physics results were obtained with this new generation instrument. The high sensitivity around 100-200 GeV energy allowed us for the first time the monitoring of 1ES1959+650, which is a faint TeV source outside flaring periods, with only few hours of observation. The high sensitivity and the low threshold of MAGIC open

new perspectives for the study of AGNs in quiescent state. This possibility is extremely valuable because of the hypothesis that 1ES1959+650 might be a hadronic accelerator. In such a case a weak but steady γ-ray flux is expected. MAGIC and CT1 measurements presented in this work considerably increase the knowledge of the AGN 1ES1959+650 during the periods of high TeV γ-ray activity, as well as during the low state, in an energy range between 150 GeV and 20 TeV.

Zusammenfassung

Die Hochenergie-Gammastrahlenastronomie ist eine der jüngsten Bereiche der Astroteilchenphysik. Sie begann mit den Experimenten von V. Hess und der Entdeckung der kosmischen Strahlung, gefolgt von der wissenschaftlichen Erforschung des Weltraums und der Erforschung des Ursprungs der höchstenergetischen Teilchen im Universum.

In den letzten Jahrzehnten hat sich die Technik der Gammastrahlenastronomie mit erdgebundenen Experimenten für die Beobachtung von hochenergetischen Photonen (E>30 GeV) wesentlich verbessert. Nach den Pionierarbeiten der Whipple Kollaboration, die die erste Gammastrahlenquelle, den Krebsnebel, entdeckte, hat die HEGRA Kollaboration mit dem unabhängigen Prototypen CT1 und mit einem System von fünf Cherenkovteleskopen, dem CT-System, zur weiteren Entdeckungen in der Gamma-Astronomie beigetragen. Die wissenschaftlichen Ziele der HEGRA Kollaboration beinhalteten sowohl die Untersuchung von bereits bekannten TeV Quellen als auch die Suche nach neuen Kandidaten. Die erste Teleskopgeneration erlaubte lediglich die Beobachtung von Gammastrahlen im Energiebereich zwischen einigen hundert GeV bis einigen TeV, während Satellitenexperimente ein Bild des Universums im Energiebereich bis zu 10 GeV lieferten. Die Beobachtungslücke zwischen 10-300 GeV beruhte einerseits auf der geringen Sammelfläche der Satellitenexperimente und andererseits auf der hohen Energieschwelle der ersten Generation der erdgebundenen Teleskope. Um diese Beobachtungslücke zu schließen, entwickelte und baute die MAGIC Kollaboration ein Cherenkovteleskop, das mit Hilfe vieler neuartiger Technologien die niedrigste Energieschwelle unter den heute existierenden IACTs (Imaging Air Cherenkov Telescopes) erreichte.

Das Physikprogramm der erdgebundenen Gamma-Astronomie beinhaltet die Untersuchung einer Reihe von galaktischen - und extragalaktischen - Quellentypen wie Supernova-Überreste (SNR), Pulsare, Mikroquasare und Aktive Galaktische Kerne (AGN). Meine Doktorarbeit beschftigt sich mit einer Studie des Aktiven Galaktischen Kerns 1ES1959+650 und basiert auf den mit den Teleskopen HEGRA CT1 und MAGIC-I gewonnenen Daten.

Das physikalische Interesse an AGN 1ES1959+650 gilt hauptsächlich dem Vergleich der spektralen Eigenschaften mit denen bereits bekannter AGNs, sowie Tests von Modellen zur Gammastrahlenerzeugung und der Korrelation der Quellenaktivität bei verschiedenen Wellenlängen. Das von der HEGRA Kollaboration betriebene CT1 Teleskop beobachtete diesen AGN für mehrere hundert Stunden, be-

ginnend im Jahr 2000. Die erste bekannte aktive Periode von AGN 1ES1959+650 fand im Frühjahr 2002 statt. Während dieser Periode beobachtete CT1 diese Quelle, und die Ergebnisse der Analyse werden hier vorgestellt. Die wichtigste Erkenntnis aus der Datenanalyse des CT1 Teleskops ist die Entdeckung einer hochenergetischen Gamma-Emissionsphase ohne gleichzeitige Aktivität im Röntgenwellenlängenbereich. Diese Phase wird als *Orphan Flare* bezeichnet. Der mit CT1 beobachtete *Orphan Flare* wurde zwei Tage vor einem von der Veritas Kollaboration beobachteten, noch intensiveren *Orphan Flare* beobachtet.

Ende 2002 wurde die Datennahme mit dem CT1 Teleskop beendet. Zu diesem Zeitpunkt war die MAGIC Kollaboration am gleichen Ort, dem Observatorio del Roque De Los Muchachos auf der Kanarischen Insel La Palma, gerade dabei, den Bau des MAGIC Teleskops abzuschließen.

Ein Teil meiner Doktorarbeit beschäftigt sich mit der Beschreibung des segmentierten Spiegelreflektors des MAGIC Teleskops, an dessen Konstruktion und Montage ich 2003 teilnahm. Es werden die technische Eigenschaften des Spiegels vorgestellt, sowie Studien, die vor und während der Montage der Teleskopstruktur durchgeführt wurden. Der Reflektor des MAGIC Teleskops ist wegen seiner Größe (236 m^2) und seines geringen Gewichtes (17 t) einzigartig unter den existierenden IACTs. Mehrere neue Technologien wurden in diesem Projekt angewendet. Die Spiegelsegmente bestehen aus einer Aluminiumlegierung, AlMgSi1. Die hohe Reflektivität der Spiegeloberfläche wurde durch das Ausdrehen mit einer Diamantspitze erreicht. Die Spiegel sind auf einer sehr leichten und stabilen Kohlefaser-Rohr-Konstruktion befestigt. Um die geringen Spiegelträgerdeformationen auszugleichen, sind die Spiegel mit einer sogenannten Aktiven Spiegelsteuerung ausgestattet. Eine interne Spiegelheizung garantiert Schutz gegen Taubeschlag und Vereisung.

Die angewandten innovativen Technologien eröffnen neue Horizonte in der Gammastrahlenastronomie, wie z.B. die Möglichkeit, niedrigere Gammastrahlenenergien nachzuweisen als früher, und damit die kürzesten, rätselhaftesten Phänome im Gammastrahlenuniversum, sogenannten Gammastrahlen Blitze (GRB), zu untersuchen. Die gesammelten Erfahrungen sind jetzt die Grundlage für neue Ideen bei der Entwicklung der Spiegel für Phase II des MAGIC Experiments: dem Bau eines verbesserten Klons des MAGIC Teleskops in der Nähe des bestehenden, um so ein Stereosystem zu bilden. Die erste Beobachtungsperiode mit MAGIC fand 2004 während der Inbetriebnahme statt. Während dieser Phase waren die Teleskopeigenschaften noch nicht stabil. Sowohl die Software als auch die Hardware mussten ständig angepasst werden, um die optimale Integration der Teilsysteme zu ermöglichen. Während dieser Periode wurden als Hauptquellen der Krebsnebel, die Standardkerze im TeV Energiebereich, sowie auch einige der anderen, bereits bekannten TeV Gamma-Quellen, wie etwa AGN Mkn421, beobachtet, der in diesem Zeitraum starke Emissionen im TeV Energiebereich aufwies. Mehrere Stunden wurden für die Beobachtung der Quelle 1ES1959+650 verwendet. Diese Daten habe ich analysiert und mit denen vom Krebsnebel in der gleichen Periode und unter ähnlichen Bedingungen gewonnenen Daten verglichen. Durch die Gegenkalibrierung

mit einer bekannten Quelle konnte ich viele Teststudien am MAGIC Teleskop umgehen, die die Beobachtung in dieser frühen Phase schwer (wenn nicht gar unmöglich) gemacht hätten. Mit der Messung von 1ES1959+650 im September-Oktober 2004 konnten einige der ersten physikalischen Ergebnisse der neuen Teleskopgeneration mit MAGIC gewonnen werden. Die hohe Sensitivität im Energiebereich zwischen 100-200 GeV erlaubte uns zum ersten Mal die kontinuierliche Beobachtung von 1ES1959+650 im sogenannten Low State (Ruhezustand), bei dem nur eine sehr schwache, aber kontinuierliche Gamma-Abstrahlung auftreten sollte. Die hohe Empfindlichkeit, zusammen mit der niedrigen Energieschwelle, eröffnen für MAGIC neue Perspektiven für die Untersuchung von AGNs im Ruhezustand. Dies ist von enorm hohem Nutzen hinsichtlich der Hypothese, dass 1ES1959+650 ein Hadronenbeschleuniger sein könnte. In diesem Falle würde ein schwacher, aber ständiger Gammastrahlenfluss erwartet.

Die in dieser Arbeit vorgestellten Messungen von MAGIC und CT1 im Energiebereich von 150 GeV bis 20 TeV, erweitern in erheblichem Maße das Wissen über den AGN 1ES1959+650 sowohl während der Phasen hoher TeV-Aktivität als auch im Ruhezustand.

Sommario

L'astronomia dei raggi gamma è una delle più giovani discipline dell'astrofisica. Ha visto il suo inizio con gli esperimenti di Victor Hess e la scoperta dei raggi cosmici, con l'esplorazione scientifica dello spazio e lo studio di fenomeni che sono all'origine delle particelle più energetiche che viaggiano nell'Universo.

Durante gli ultimi decenni, l'astronomia gamma e gli strumenti che da terra rilevano fotoni di altissima energia (E> 30 GeV) si sono notevolmente evoluti. Dopo il pionieristico lavoro della collaborazione Whipple e la scoperta della prima sorgente di raggi gamma, la nebulosa del Granchio, nel 1989, la collaborazione HEGRA contribuì alle successive scoperte nella astronomia dei raggi gamma con il telescopio Cherenkov prototipo chiamato CT1 e il sistema di 5 telescopi Cherenkov operanti in stereo, chiamato CT-System. Gli obiettivi scientifici della collaborazione comprendevano lo studio di sorgenti conosciute di raggi gamma e la ricerca di nuove possibili sorgenti.

I telescopi Cherenkov di prima generazione erano in grado di osservare solo raggi gamma di energia superiore a parecchie centinaia di GeV, fino a qualche decina di TeV, mentre da strumenti installati su satellite era possibile ottenere una visione dell'Universo in raggi gamma al di sotto di una decina di GeV. La mancanza di osservazioni possibili tra 10 e 300 GeV era dovuta da una parte alla limitata area efficace degli esperimenti da satellite e d'altra parte all'alta soglia di energia degli strumenti operanti da terra. Allo scopo di coprire il vuoto lasciato dalle osservazioni in questo intervallo di energia la collaborazione MAGIC progettò la costruzione di un telescopio Cherenkov di nuova concezione, adottando molte innovazioni tecnologiche in modo da raggiungere la minor soglia di energia possibile tra i telescopi Cherenkov di nuova generazione.

Il programma scientifico dei telescopi Cherenkov comprende l'osservazione e lo studio di diversi tipi di sorgenti galattiche ed extra-galattiche, come resti di supernova (SNR), pulsars, micro-quasars e nuclei galattici attivi (AGN).

L'interesse scientifico per lo studio dell'AGN 1ES1959+650 riguarda in primo luogo il confronto del suo spettro con le caratteristiche dello spettro di altri AGN, lo studio di modelli di emissione di raggi gamma e la correlazione tra l'attività della sorgente a diverse lunghezze d'onda.

La mia tesi riguarda lo studio dell'AGN 1ES1959+650 attraverso l'analisi dei dati ottenuti sia con il telescopio HEGRA CT1 che con il nuovo telescopio MAGIC.

Il telescopio CT1 osservò la sorgente durante qualche centinaio di ore, a partire

dall'anno 2000. Il primo periodo conosciuto in cui si sia osservata una notevole attività in raggi gamma da 1ES1959+650 è la primavera del 2002. Le osservazioni di CT1 in quel periodo sono state analizzate e in questa tesi presento i risultati ottenuti.

Il risultato più interessante emerso dall'analisi dei dati di CT1 è l'osservazione di un episodio di forte emissione di raggi gamma non accompagnato da un'alta attività in raggi X. Questo episodio, classificato come *flare orfano*, anticipa di circa 2 notti un episodio analogo osservato dalla collaborazione VERITAS con il telescopio Whipple. Lo spettro di 1ES1959+650 ottenuto dall'analisi dei dati di CT1 durante periodi di stato di bassa emissione della sorgente rappresenta la prima conferma dello spettro pubblicato dalla collaborazione HEGRA e ottenuto da osservazioni effettuate con il CT-System durante il corso di 3 anni.

Alla fine del 2002 il telescopio CT1 smise di prendere dati. Allo stesso tempo il telescopio MAGIC era in costruzione nello stesso osservatorio astronomico, nell'isola de La Palma (Isole Canarie, Spagna).

Nell'anno 2003 ho partecipato alla costruzione e installazione del mosaico di specchi che costituisce la superficie riflettente del telescopio MAGIC. Parte della mia tesi è dedicata alla descrizione del riflettore, delle sue caratteristiche tecniche e dei test che sono stati effettuati su alcuni suoi elementi prima e durante l'installazione nel telescopio.

Il riflettore del telescopio MAGIC è unico tra i telescopi Cherenkov, con la sua enorme superficie pari a 236 m^2 e il suo peso ridotto (17 t). Nel progettarla sono state impiegate nuove soluzioni tecnologiche. I materiali adottati per la costruzione degli specchi di cui è composto il riflettore sono leghe di alluminio. La superficie è stata lavorata utilizzando uno strumento di diamante che ne conferisce un'alta riflettività. Gli elementi che compongono la superficie riflettente sono montati su una struttura in fibra di carbonio, rigida e leggera al tempo stesso. Sono dotati di sistemi di controllo per garantirne le massime prestazioni, come il controllo attivo dell'orientazione (AMC) e un sistema di riscaldamento interno. Il ridotto peso complessivo degli specchi ha reso possibile la costruzione di una superficie riflettente così grande.

Le scelte tecnologiche adottate nella costruzione di MAGIC hanno aperto nuovi orizzonti nella astronomia dei raggi gamma, come la possibilità di osservare raggi gamma di energia più bassa rispetto al passato e lo studio dei fenomeni più enigmatici e rapidi nell'Universo dei raggi gamma: i *Gamma Ray Bursts* (GRB). L'esperienza acquisita con gli specchi di MAGIC è ora fonte di nuove idee per lo sviluppo degli specchi per la seconda fase del progetto: un secondo telescopio con caratteristiche simili a quelle di MAGIC è attualmente in costruzione vicino al primo e insieme andranno a formare un sistema stereoscopico.

L'anno 2004 rappresenta il primo periodo di operazioni del telescopio MAGIC. Durante il primo ciclo di osservazioni la configurazione del telescopio si stava evolvendo al fine di raggiungere l'ottima integrazione dei sottosistemi che lo compongono. In quel periodo i principali oggetti astronomici osservati furono la nebulosa del granchio (Crab Nebula), considerata la candela standard per le osservazioni

in raggi gamma, e alcune tra le sorgenti di raggi gamma meglio conosciute, quale l'AGN Mkn421 in un periodo di forte attività. Alcune ore di osservazione sono state spese per lo studio di 1ES1959+650 in quello stesso periodo. I dati ottenuti sono stati analizzati e comparati con dati presi osservando la nebulosa del granchio in simili condizioni di osservazione. La calibrazione incrociata con una sorgente nota ha permesso di evitare studi di prestazione del telescopio, difficili (quando non impossibili) da effettuarsi vista la rapida evoluzione delle condizioni del telescopio in quel primo periodo di attività.

Le misure di 1ES1959+650 del Settembre-Ottobre 2004 hanno portato ai primi risultati scientifici ottenuti con il nuovo telescopio MAGIC. L'alta sensitività del rivelatore a energie pari a qualche centinaio di GeV ha permesso per la prima volta di osservare in dettaglio 1ES1959+650, sorgente debole di raggi gamma (al di fuori di brevi periodi di intensa emissione e alta viariabilità), dopo sole poche ore di osservazione. Questa possibilità apre nuove prospettive nello studio di AGN in periodi di bassa emissione e la valutazione dell'ipotesi sempre più probabile che la produzione di raggi gamma da parte di 1ES1959+650 sia dovuta ad accelerazione di particelle adroniche.

Le misure effettuate con MAGIC e CT1 e presentate in questa tesi contribuiscono in modo notevole all'aumento della conoscenza dell'AGN 1ES1959+650 sia durante periodi di forti che di basse emissioni e coprono l'intervallo di energia tra 150 GeV e 20 TeV.

Contents

List of Figures

List of Tables

List of acronyms and abbreviations

AC	Alternating Current
ACT	Air Cherenkov Telescope
AMANDA	Antarctic Muon and Neutrino Detector Array
ANTARES	Astronomy with a Neutrino Telescope and Abyss environmental RESearch
AGASA	Akeno Giant Air Shower Array
AGN	Active Galactic Nucleus
AMC	Active Mirror Control
asl	above sea level
BATSE	Burst and Transient Source Experiment
BH	Black Hole
CAT	Cherenkov Array at Themis
CCD	Charged Coupled Device
CMB	Cosmic Microwave Background
c.o.g.	center of gravity
CR	Cosmic Rays
DC	Direct Current
EAS	Extended Air Showers
EBL	Extragalactic Background Light
EGRET	Energetic Gamma-Ray Experiment Telescope
EM	Electro-Magnetic
FADC	Flash Analog-Digital-Converter
FOV	Field Of View
FR	Fanaroff-Riley
FSRQ	Flat Spectrum Radio Quasar
FWHM	Full Width at Half Maximum
GBM	GLAST Burst Monitor
GLAST	Gamma Ray Large Area Space Telescope
GRB	Gamma-Ray Burst
GZK	Greisen-Zatsepin-Kuzmin
HE	High Energy
HEGRA	High Energy Gamma Ray Astronomy
HETE	High Energy Transient Explorer
HV	high voltage
IACT	Imaging Atmospheric Cherenkov Telescope
IC	Inverse Compton
IR	Infra-Red
ISM	InterStellar Medium
LAT	Large Area Telescope
LED	Light Emitting Diode
LONS	Light Of the Night Sky
MAGIC	Major Atmospheric Gamma-ray Imaging Cherenkov
MARS	MAGIC Analysis and Reconstruction Software

MC	Monte Carlo (simulation)
MHD	Magneto-Hydro-Dynamic
MJD	Modified Julian Day
NESTOR	Neutrino Extended Submarine Telescope with Oceanographic Research
NRAO	U.S. National Radio Astronomy Observatory
NSB	Night Sky Background
PMT	Photo-Multiplier Tube
PSF	Point Spread Function
QE	Quantum Efficiency
QSO	Quasi-Stellar Object
RMS	root-mean-square
SED	Spectral Energy Distribution
SMBH	Super-Massive Black Hole
SNR	Super-Nova Remnant
SSC	Synchrotron Self Compton
VERITAS	Very Energetic Radiation Imaging Telescope Array System
VHE	Very High Energy
VLBA	Very Long Baseline Array
VLBI	Very Long Baseline Interferometry
UHE	Ultra High Energy
UTC	Coordinated Universal Time
UV	Ultra Violet
Z.A.	zenith angle

Useful conversion units and definitions

This section is a small collection of information and conversions of units that are commonly used in Astrophysics, inherited by Astronomy. They are also used in this work. Readers not familiar with astronomical units might find it helpful.

Electronvolt It is the energy an electron acquires in vacuum from rest through a potential difference of 1 volt.

1 eV = $1.6022 \cdot 10^{-12}$ erg = $1.6022 \cdot 10^{-19}$ joule (1 cal = 4,1840 joule)

Multiples are commonly used to express the energy in astroparticle physics:

1	10^3	10^6	10^9	10^{12}	10^{15}	10^{18}
eV	keV	MeV	GeV	TeV	PeV	EeV

LE	**HE**	**VHE**	**UHE**
$<$ 30 MeV	30 MeV - 30 GeV	30 GeV - 100 TeV	$>$ 100TeV

The classification of high (HE), very high (VHE) and ultrahigh (UHE) energy particle is commonly used, even if the definition is not standard and linked in part to the threshold of instruments. In this work we will use the definitions given in the table above.

MJD The Modified Julian Day (MJD) is defined as MJD = JD - 2400000.5 , where JD is the Julian Day.

Start of the JD count is from 0 at 12 noon 1 JAN -4712 (4713 BC). MJD is used when a continuous numbering of days is more convenient than the use of the civil calendar. Fractions of the day can be added to indicate the exact time of the day. The counting starts at midnight.

Example: January 1st 2005, 0:00 UTC = 53371.0 MJD = 2453371.5 JD

The site
`http://heasarc.gsfc.nasa.gov/cgi-bin/Tools/DateConv/dateconv.pl`
provides a useful tool for date conversions.

Sun units Mass of sun $M_\odot = 1.989 \times 10^{30}$ kg
Luminosity of sun $L_\odot = 3.90 \times 10^{26}$ W
Radius of sun $R_\odot = 6.96 \times 10^8$ m

Light year 1 light year = 9.4607×10^{15} m

AU The astronomical unit is the mean distance between the Earth and the Sun. It is commonly used to measure distances within the solar system.

1 astronomical unit (AU) = $1.49597870 \times 10^{11}$ m

Parsecs (pc) It is the distance at which an object would have a parallax of one arc second. Multiples are commonly used in astrophysics.

1 Mpc = 10^3 kpc = 10^6 pc
1 pc = 3.26 ly = 206,265 AU = 3.0857×10^{16} m

Jansky The Jansky (named after Karl Jansky, 1905-1950, who first discovered the existence of radio waves from space) is defined as:
1Jansky (Jy) = 10^{-26} W m^{-2} Hz^{-1}.
The energy flux received from astronomical objects is generally very small and at radio wavelengths, the 'radio brightness' is measured per unit frequency. Radio emissions from the sun during intense solar activity can be as high as 108 - 109 Jy, although most celestial sources are less than a few Jy.

Ra, Dec, equatorial coordinates Coordinates in the equatorial system, obtained projecting Earth's equator and poles to the celestial sphere by imagining straight half lines from the Earth's center. In this way it is possible to define the celestial equator as well as the north and the south celestial pole. Great circles through the celestial poles are always perpendicular to the celestial equator and are called hour circles. The coordinate corresponding to the latitude is called Declination (Dec) and it is the angle between the position of an object and the celestial equator measured along the hour circle.

The zero point of the longitudinal coordinate, called Right Ascension (RA), is the intersection point of the equatorial plane with Earth's orbital plane, the ecliptic, more precisely the so-called vernal equinox or "First Point of Aries". During the year, as Earth moves around the Sun, the Sun appears to move through this point each year around March 21 when spring begins on the Northern hemisphere. As a longitudinal coordinate, RA can take values between 0 and 360 deg. However, this coordinate is more often given in time units hours (h), minutes (m), and seconds (s), where 24 hours correspond to 360 degrees (so that RA takes values between 0 and 24 h).

Hour angle The hour angle of a source is defined as the angle measured westward along the celestial equator from the local meridian to the hour circle that passes through the source (see also the previous item).

Introduction

The birth of the modern science and its disciplines took place, in most of the cases, following the same, simple pattern: a practical problem had to be solved and the creativity and curiosity of brilliant people did the job, without forgetting the role that circumstance and luck have in these things. The road that led people to the study of cosmic rays is not an exception to this rule.

When Victor Hess (and his colleagues) organized to perform experiments in a flying balloon[1], he was trying to solve a problem: he wanted to understand the reason why his instrument to measure atmospheric electricity was discharging. He thought it was due to earth radioactivity, so he tried to reach the upper part of the atmosphere, which should have been a shield between the earth and his instruments, to prove his hypothesis. The result was the discovery that the radiation that caused the problem he was trying to solve, was entering the atmosphere *from above*. He was credited with the Nobel prize for Physics in 1936 "for his discovery of cosmic radiation".

γ-ray astronomy started with V. Hess' experiments, is one of the youngest branches of astrophysics together with the scientific exploration of space and the study of the phenomena that are origin of the most energetic particles traveling in the universe.

Pioneers of γ-ray astrophysics from earth were Galbraith and Jelley [1]. They first succeeded in observing Cherenkov light produced by atmospheric showers to study cosmic rays. They preformed the first measurements with simple instruments in 1955.

During the last decades, γ-ray astronomy and the related ground-based instruments to detect very high energy photons have evolved considerably.

The activity of the first generation of Imaging Atmospheric Cherenkov Telescopes (IACTs) began with the Whipple collaboration, that commissioned the first of this type of telescope in the Arizona desert. The discovery of the first TeV sources, such as the Crab Nebula in 1989 [2], pushed other collaborations to follow and elaborate the idea of telescopes for the detection of Cherenkov light produced by atmospheric showers. The HEGRA collaboration contributed to discoveries in γ-ray astronomy, with its standalone prototype CT1 and with its array of 5 Cher-

[1] On August 7, 1912, the Austrian physicist Victor Hess took three electroscopes up to 16,000 feet (4,877 meters) in an open balloon basket.

enkov telescopes, called CT-System. Scientific goals of the collaboration included the study of the known TeV sources and the search for possible new candidates. The first generation of telescopes were able to observe only γ-rays between a few hundreds of GeV and several TeV, while satellites gave us a view of the universe in γ-rays up to some GeV.

The energy range between 30 GeV and 300 GeV constitutes a fascinating field of exploration for γ-ray astronomers, due to the apparent discrepancy between the well populated sky-map of sources below 10 GeV and the few sources discovered by the previous generation IACTs above 300 GeV. The energy range below 10 GeV was covered by observations with satellite instruments, such as those in the EGRET experiment. More than half of the sources they detected are still unidentified (figure 1).

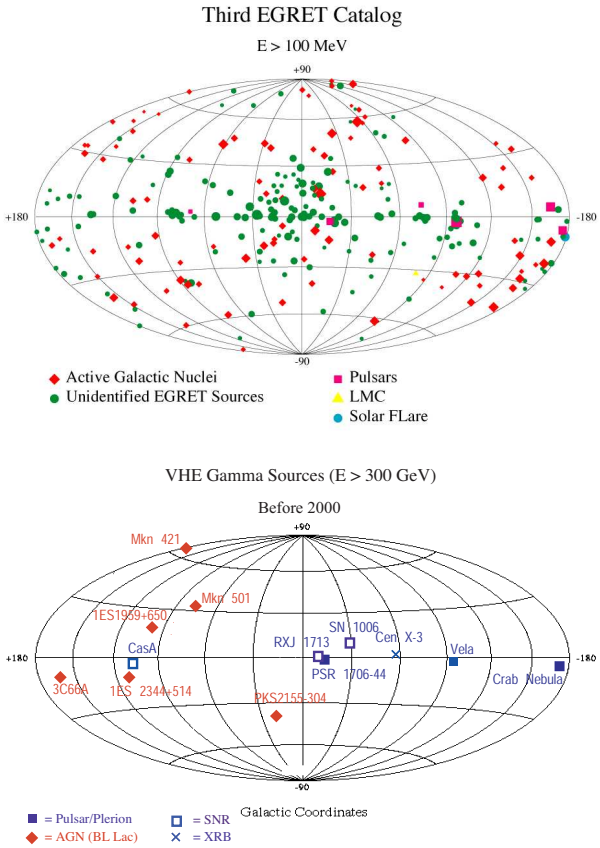

Figure 1: *Above: the EGRET map of the sky in γ-rays below 300 MeV, in galactic coordinates. The sources are listed in the third EGRET catalog [3]. Below: the sources detected as VHE γ-ray emitters until year 2000 and reported in [4] are marked. The study of the energy gap that divides the two maps would explain the big difference in number of sources detected.*

The lack of observations in the 10-300 GeV gap is, on one hand, due to the small collection efficiency of satellite experiments and, on the other hand, to the high energy threshold (> 300 GeV) of the first generation, ground-based telescopes. In order to close this gap the MAGIC collaboration built a Cherenkov telescope adopting many novel technologies to reach the lowest energy threshold among the new generation IACTs. With a 17 m diameter, high reflectivity mirror dish and a high quantum efficiency camera, MAGIC is designed for an energy threshold as low as 30 GeV close to the zenith.

MAGIC observations in this energy gap should allow us to study the mechanisms which cut off the spectra of several EGRET sources. Due to a higher flux sensitivity and a better angular resolution compared to EGRET, it may also help in their identification.

High energy γ- rays traveling cosmological distances interact with extragalactic background light (EBL), limiting the observation of distant sources. The so-called γ-ray horizon becomes more distant as the energy of the photons we are able to detect decreases. Low energy threshold IACTs will be able to observe a larger number of sources and more distant objects. This permits us to study the effect of the EBL, its density and origin. IACTs observations at low energy may contribute to measurements of fundamental physics such as searches of cold dark matter and quantum gravity effects.

My thesis, with the objective of studying the AGN 1ES1959+650 both with the HEGRA CT1 and the new MAGIC telescope, has the following structure.

- In **chapter 1** I give an overview of the still unresolved questions about cosmic rays and a short description of the astronomical objects, which are targets of γ-ray astronomy.

  The physics program of Cherenkov telescopes covers several galactic and extragalactic types of sources such as Supernova Remnants (SNR), pulsars, micro-quasars and Active Galactic Nuclei (AGNs). An unique feature of MAGIC is the possibility to observe γ-ray bursts (GRBs) only 30 seconds after an alert provided by satellite detectors.

- **Chapter 2** is dedicated to the AGN 1ES1959+650 and to its interesting features.

  The stand alone Cherenkov telescope of the HEGRA collaboration observed this AGN for several years and the MAGIC collaboration included 1ES1959+650 in its targets of opportunity list. In this thesis I present a new and more detailed analysis of the data taken with CT1 in 2002 and with MAGIC in 2004.

- In **chapter 3** I describe the main technical features of the IACTs HEGRA CT1 and MAGIC.

  At the end of 2002 the CT1 telescope was switched off. At the same time, the MAGIC collaboration was completing the construction of its telescope.

- During the year 2003, I participated to the construction and mounting of the huge tessellated reflector of the MAGIC telescope. **Chapter 4** is dedicated to the description of MAGIC reflector, its technical features, the studies that were done before and during the installation in the main fame of the telescope. Special emphasis is put on my own technical contribution to the work, which was completed in summer 2004.

- In **chapter 5** the extended atmospheric showers are described, together with the technique used to detect them from earth with IACTs. The techniques of analysing data taken with the Cherenkov telescopes HEGRA CT1 and MAGIC are described in **chapter 6**.

- In **chapters 7 and 8** I present the results of my analysis of CT1 and MAGIC data.

  The first known period of high activity of the AGN 1ES1959 +650 occurred in spring 2002. It was recorded by the CT1 telescope and it will be documented here. The year 2004 saw the first period of operation of MAGIC (commissioning phase). The configuration of the telescope changed during this phase, until optimal integration of subsystems activity was reached. During this period, the main targets for observation were the Crab Nebula, the TeV standard candle, and the well-known TeV γ-ray sources, such as Mkn 421, that had a period of strong emissions in TeV energies. Several hours of observation of the source 1ES1959+650 were taken in the test phase. I analyzed these data and compared them with the Crab Nebula observations of the same period and under similar observational conditions. By cross calibrating against a well-known source, I could avoid many telescope performance studies which were impossible to obtain in the early operation of MAGIC.

- The discussion of the results of my analysis is the subject of **chapter 9**. The physics interest in the AGN 1ES1959+650 concerns the comparison of the spectral features of 1ES1959+650 to the ones of other known AGNs and to the most accepted emission models, and the correlations between activity at different wavelengths.

Chapter 1

Physics of cosmic rays

1.1 Introduction to the physics of cosmic rays

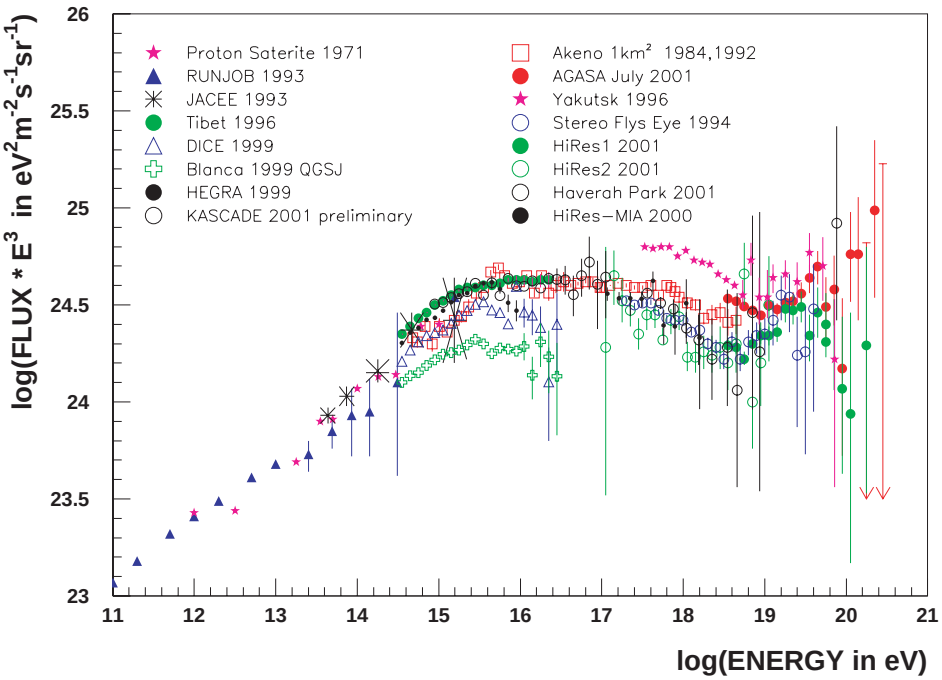

Figure 1.1: *Cosmic ray spectrum. The flux is multiplied by the energy to the third power to enhance the change in the spectral index.*

The earth's atmosphere is constantly bombarded by high energy particles coming from outer space, the so-called cosmic rays.

They have been known since 1912, after the balloon experiments of V. Hess. They are mainly electrically charged particles, such as protons (∼90%), alpha particles and ionized nuclei of heavier elements (∼9%) and only ∼0.1% are photons.

The flux of particles arriving at the earth is energy dependent and it drops from 10^4 $m^{-2}s^{-1}$ at some GeV to 10^{-2} $km^{-2}yr^{-1}$ at $\sim 10^{20}$ eV.

The origin of cosmic radiation is still an enigma, though the knowledge of the phenomenon has grown considerably in the last decades, but many models of their production procedure are still waiting for a decisive solution from the experimental data. For a recent review about the astrophysical origin of ultrahigh energy cosmic rays (UHECR) the reader is referred to [5].

The energy of cosmic rays covers more than 10 orders of magnitude and it extends up to 10^{20} eV, with a typical power law differential spectrum. The differential cosmic ray flux multiplied by E^3 is shown in Fig. 1.1. The CR spectral index α varies from 2.7 to 3.0 in the region around $10^{15.5}$ eV, forming the feature called *knee*. Measurements of particles below this part of the CR spectrum ($E< 10^{16}$ eV) are carried out with satellite-borne instruments outside the atmosphere. The presence of the galactic magnetic field makes the identification of the site of production and acceleration of charged cosmic rays of energy below few 10^{19} eV difficult. It is believed that the origin of cosmic rays up to 10^{15-17} eV is galactic, mostly accelerated by shock waves of supernovae remnants (SNR), binary star systems, pulsars and neutron stars. CR below 10^{15} eV (protons) - 10^{17} eV (iron) are confined inside our galaxy for 10^6 to 10^7 years, resulting in a high directional isotropy in this energy range.

At higher energies, around the knee region and above, the flux of particles is too low to be directly detected with satellite-borne instruments. The measurements are conducted with ground based arrays spread out sometimes over many km^2. Those instruments detect extensive atmospheric showers triggered by CR. There exist two main types of such detectors: the fluorescence detectors and the air shower arrays. The fluorescence detectors are sensitive to the 300-400 nm light produced by charged particles in the atmosphere. Those detectors allow us to study the longitudinal development of the showers. The air shower arrays are sensitive to the particles of the shower tail. In this case, the detectors are normally scintillators, which can identify the arrival direction and density of charged particles.

At ultra high energies, the spectrum steepens further to α= -3.3 at $\sim 10^{17.5}$ eV. It hardens again to α= -2.7 in the region called *ankle* ($\sim 10^{19}$ eV). Particles above $\sim 10^{17}$ eV are believed to be mostly of extragalactic origin, since the galactic magnetic field would not be able to trap them in our galaxy. At around $5 \cdot 10^{19}$ eV, the magnetic field cannot deflect them considerably.

The presence of the uniform cosmic 2.7 K background imposes a theoretical limit to the flux of UHECR: above 10^{20} eV, the particles interact with the photons of the cosmic microwave background (CMB), losing energy through the process:

$$p + \gamma_{2.7K} \rightarrow N^* \rightarrow p + \pi^0 \, , \, n + \pi^+ \tag{1.1}$$

Heavier nuclei can lose energy by a similar process. This phenomenon is known as Greisen-Zatsepin-Kuzmin (GZK) cutoff [6, 7]. The described process limits the

region of origin for CR above 10^{20} eV to less than 30 Mpc^3. Inside this volume, no possible accelerator has been found.

The presence of experimental data beyond the expected cut-off is one of the most hotly discussed questions in this field. The Akeno Giant Air Shower Array (AGASA) experiment [8, 9], an array of 111 scintillators covering $\sim$100 km^2 in Japan, detected 57 events above $4 \cdot 10^{19}$ eV. Among them, 11 events had an estimated energy above the GZK cutoff energy [10]. This result is in contradiction to the only two events above 10^{20} eV reported by the HiRes collaboration [11, 12]: using their two high resolution fluorescence detectors in monocular mode[1], they concluded that the flux of the most energetic particles confirms the presence of the GZK cutoff. However, the small number of events found by AGASA is such that the two measurements can be considered not significantly contradictory, assuming that the big systematic uncertainties in the events' energy estimation are, in both cases, concurring in opposite directions to the observed differences of the spectrum.

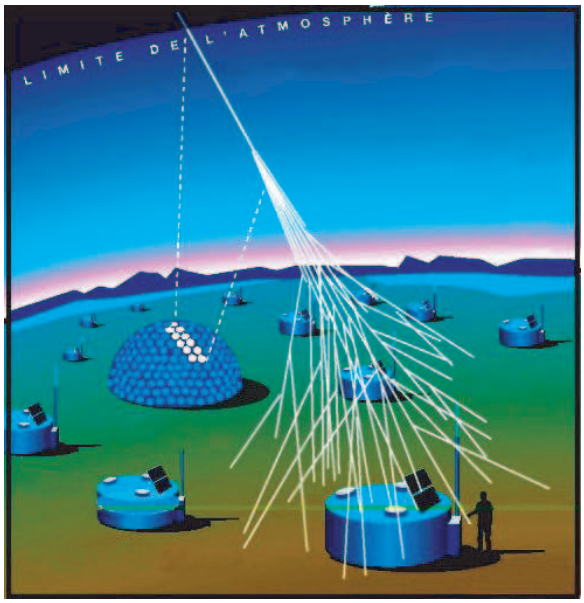

Figure 1.2: *Artist's view of the Pierre Auger Observatory. It consists on a hybrid system of fluorescence detectors and an array of Cherenkov water tanks.*

The new experiments for the detection of CR are supposed to contribute strongly to solving this issue, with both increased statistics and better energy reconstruction.

The hybrid array of detectors in construction in Argentina by the Pierre Auger collaboration [13] (figure 1.2) is the biggest experiment that is currently taking data at the very end of the UHECR spectrum. When completed, the Pierre Auger Observatory will consist of 1600 particle detectors covering a surface of 3000 km^2 and fluorescence detectors at the boundaries. A second array is foreseen in the northern hemisphere, thus allowing the entire sky to be monitored.

Another debated question in the field is the possible directional correlations between UHECRs and possible accelerators, like Supernova remnants (SNR) and OB associations, or powerful compact objects, like Active Galactic Nuclei (AGN), highly red-shifted quasars [14] and EGRET sources. Un-

[1]The energy threshold of HiRes monocular detector is 10^{17} eV and the acceptance is 1000 km^2 sr at $\sim 10^{20}$ eV.

fortunately, the lack of statistics is such that a claim of correlation is hardly possible.

Neutral particles are the best tool to study the origin of cosmic rays, because the magnetic fields have no effects on them and their trajectory gives information on the source position. Possible neutral particles are neutrons, neutrinos and photons. Because of their limited lifetime, neutrons are only suitable to study close cosmic objects if the neutron energy is sufficiently high ($\sim$10 kpc for E(n) $\sim 10^{18}$ eV). In the following, I will briefly elaborate on neutrinos and photons.

1.1.1 Neutrinos and neutrino telescopes

Neutrinos are neutral particles, introduced theoretically by Pauli in 1930 , to explain the spectrum of Beta-decay. For many years it was impossible to detect them. Now they are considered important messengers of information coming from the early Universe and of cosmic objects that produce them. In the universe, most low energy neutrinos are products of fusion of hydrogen into helium, like in the sun, or in supernova explosions. The study of the solar ν emissions introduced the concept of oscillation of neutrino flavors.

A supernova explosion is one of the possible ways a star ends its life and starts a new phase of activity. When the mass of the star is big enough and the pressure from fusion becomes too low to compensate for the gravitational pressure, its collapse forms a neutron star, with extremely high mass density. The pressure wave propagates from the neutron star, giving rise to a shock wave. Electrons and positrons are emitted and their interaction with protons and neutrons produces neutrinos.

Energetic neutrinos are produced by pion decay on hadronic interactions. They are a precious tool to understand acceleration mechanisms occurring inside astrophysical objects, like AGNs or SNRs, since they are particles with a strong penetration power.

Neutrino experiments have among their scientific goals the identification of point-like sources in the universe.

Neutrinos are detected indirectly. Neutrino telescopes consist of a huge amount of matter, usually water or ice and an array of strings with photomultiplier tubes (PMTs), located deep in the medium, to be shielded from CR particles (see figure 1.3, B and C). The medium acts both as target for neutrino interactions and as calorimeter for charged particles (leptons), which produce Cherenkov light, detected by strings of PMTs.

The principle of the detection mechanism is illustrated in figure 1.3, A. Cosmic neutrinos that are coming from below interact with heavy nuclei in the earth below the detector or inside the detector, and subsequently produce charged leptons. Hadronic CR, interacting with the nuclei of the upper atmosphere, produce the so-called atmospheric neutrinos. The reconstruction of the high energy neutrino direction is direct: it is basically the same direction as the detected lepton.

The experiment AMANDA [15] and its successor IceCube [16] detect leptons through the Cherenkov light produced in the ice of the South Pole. IceCube is the

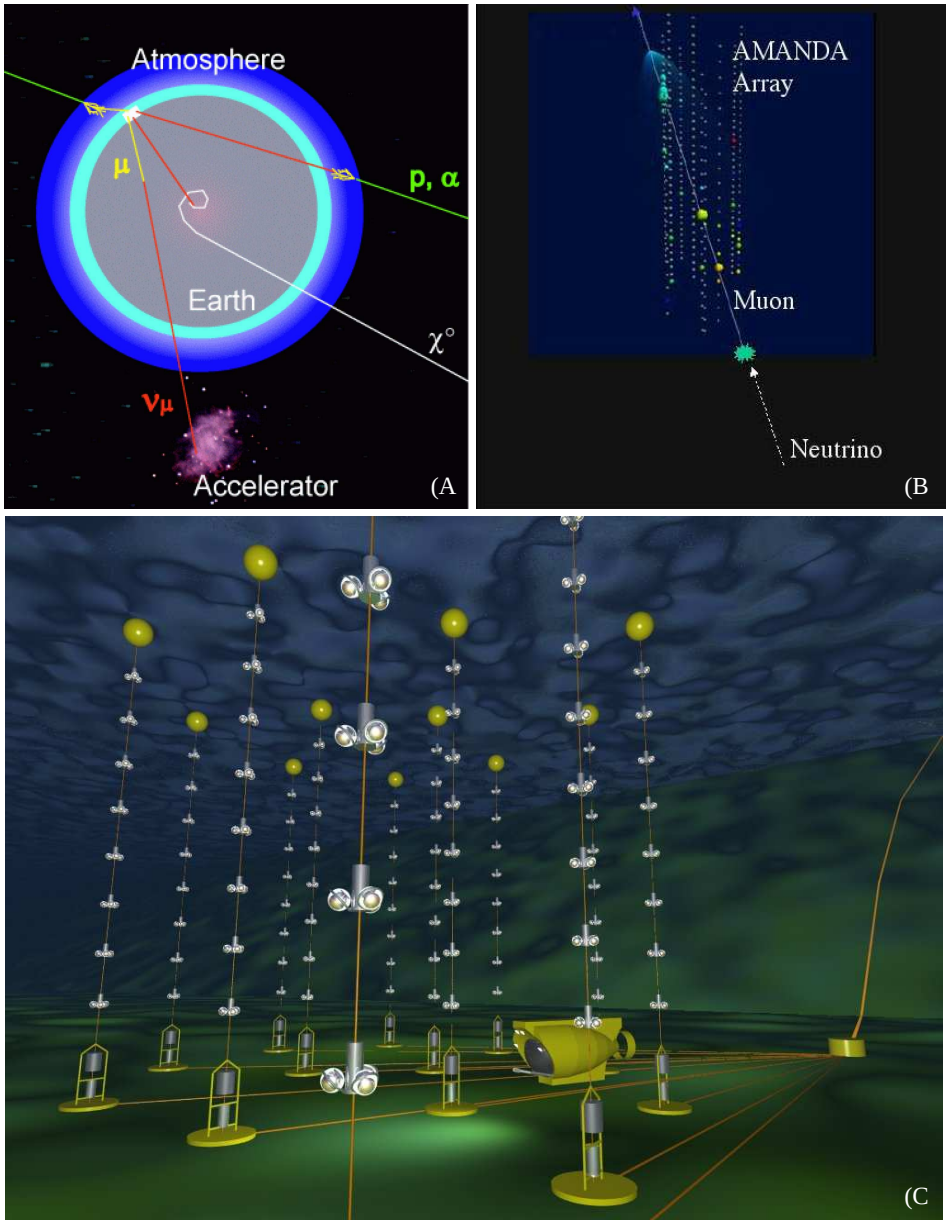

Figure 1.3: *A. The scheme illustrates the detection principle of neutrino telescopes. They use the detection of upward-moving muons as a signature of muon neutrino interactions in the matter below and inside the detector. Upward-moving muons are basically free of cosmic rays. B. The Cherenkov light produced by a muon seen by the photo-multiplier tubes of the AMANDA detector allows for the reconstruction of the direction of the incoming neutrino. C. Artist's view of the ANTARES detector. (c) F.Montanet, CNRS/IN2P3 for the ANTARES collaboration.*

most promising instrument in this field. It will consist of 1 km^3 of ice, scanned by 80 1km-long strings with 60 PMTs each. At the surface above IceCube, there will be an air shower array called IceTop, useful for calibration and background rejection. It will observe muons from 10^{11} eV to 10^{18} eV. Lake Baikal in Russia is the site of a neutrino telescope experiment [17]. European projects like ANTARES [18] (fig. 1.3, C) and NESTOR [19] are taking advantage of the water of the Mediterranean sea for the same purpose.

1.1.2 γ-rays production mechanisms

The best suited neutral 'messenger' particle is the high energy photon.

Photons traveling the universe with energies larger than a few hundreds keV are called γ-rays. Like neutrinos, their trajectories are not affected by magnetic fields, so they

- point to the origin of their generation
- carry energy information about their generation process
- carry, as massless particles, time information.

The production of VHE γ-rays is associated to phenomena that take place in the astronomical objects, resulting in the observed γ-ray flux. The most important processes responsible for producing high energy photons are shown in figure 1.4 and briefly explained in the following [2].

Electron-positron annihilation Figure 1.4, a. Wherever $e^+ - e^-$ coexist locally, they rapidly annihilate, giving 2 photons:

$$e^+ \, e^- \rightarrow \gamma \, \gamma \tag{1.2}$$

The process results in a spectral line at 511 keV $= m_e c^2$, if the system e^+e^- is basically at rest. Thermalized positrons interacting with cold electrons can give 3 γ. Their spectrum appears as a continuum in the MeV range, as described in [21], repeating the spectrum of the parent positrons, but steeper.

π^0 decay Figure 1.4, b. The interaction of high energy protons with matter or radiation of the interstellar medium (ISM) produces hadronic particles. $\pi^{\pm}$ and π^0 are produced with the same probability, thus one third of the π-mesons produced are neutral. The lifetime of π^0 is very short ($\gamma_\pi \cdot 10^{-16}$ s) and its decay produces two γ-rays.

$$pp \rightarrow pp \, \pi^+ \, \pi^- \, \pi^0 \qquad\qquad \pi^0 \rightarrow \gamma \, \gamma \tag{1.3}$$

[2] For a review of the production mechanisms, the reader is referred to [20].

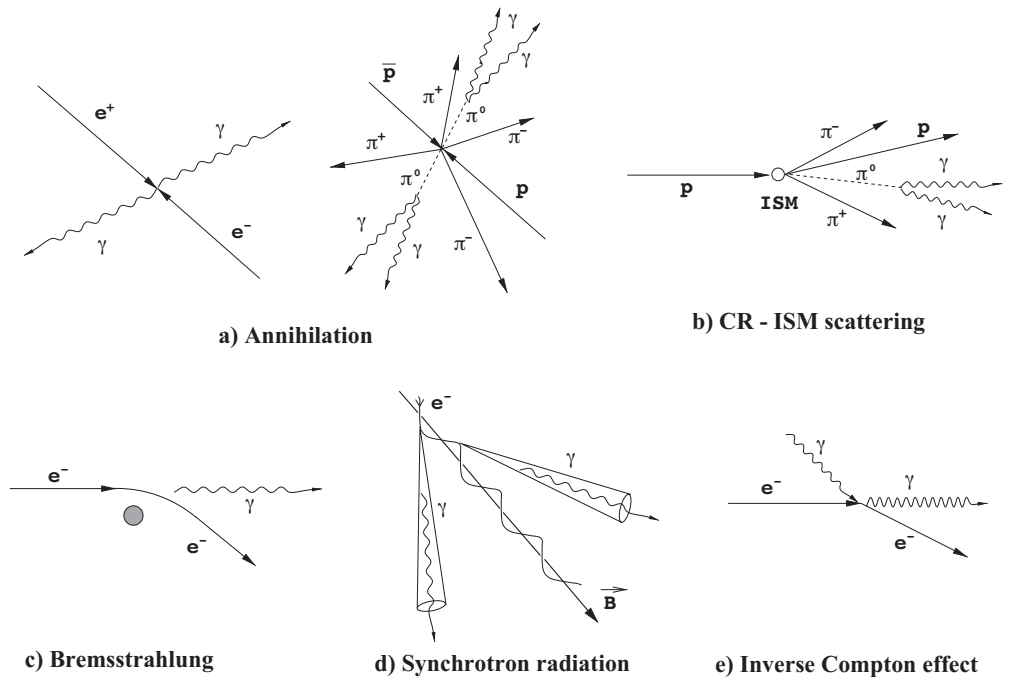

Figure 1.4: *Schematic illustration of the main mechanisms of γ-ray production. The Interstellar Medium (ISM), or CR particles can be protons or heavy ions.*

The minimum kinetic energy of a proton to produce a π^0 is

$$E_{th} = 2m_\pi c^2(1 + m_\pi)/4m_p \simeq 280 \text{ MeV} \tag{1.4}$$

where m_π is the mass of a π^0 and corresponds to 134.97 MeV.

The energy of the photons emitted by a π^0 at rest is $E_\gamma = \frac{1}{2} m_\pi c^2 \simeq 67.5$ MeV. If the π^0 is moving with velocity $v = \beta\, c$, the energy of the photons in the laboratory frame, is:

$$E_\gamma = \frac{1}{2} m_{\pi^0} c^2 \frac{1 + \beta \cos\theta_\gamma}{\sqrt{1 - \beta^2}} \tag{1.5}$$

with θ_γ the angle between the direction of the photon with respect to the pion.

Charged pions have significantly larger lifetime ($\simeq 2.6 \cdot 10^{-8}$ s). Their decay gives ν_e and ν_μ.

$$\pi^+ \to \mu^+ \bar{\nu_\mu} \qquad \mu^+ \to e^+ \bar{\nu_e}\, \nu_\mu \tag{1.6}$$

$$\pi^- \to \mu^- \nu_\mu \qquad \mu^- \to e^- \nu_e\, \bar{\nu_\mu} \tag{1.7}$$

Their spectrum would be similar to the γ-ray spectrum from π_0 decay. However, at high energies $\pi^{\pm}$ interactions before decay can occur, resulting in a smaller ν flux with respect to γ-rays. The ν and γ-ray associated spectra are the strongest indications of the hadronic component of an AGN jet.

Particles through electromagnetic fields Charged particles, usually electrons or protons, are accelerated in the electric field produced by a nucleus or ion. The trajectory of the particle is deviated and radiation is emitted. The effect is called **Bremsstrahlung** (Figure 1.4, c). The spectrum of this radiation has a power law shape, with the same spectral index as the charged particle spectrum. It is one of the most important phenomena, with the pair production, of the production of Cherenkov photons in the atmosphere.

High energy relativistic electrons produce **synchrotron radiation** when in presence of magnetic fields (Figure 1.4, d). The energy of the emitted photons has a peak, whose position is proportional to the transverse component of the magnetic field $B_{\perp}$ and to the Lorentz factor γ_e of the electron:

$$E_{max} = 5 \cdot 10^{-9} \cdot B_{\perp} \gamma^2 \tag{1.8}$$

Strong magnetic fields are present in AGN jets. Electrons and protons accelerated inside the jet emit synchrotron radiation, whose spectrum shows a broad hump. In TeV blazars, the peak occurs normally at keV energies (X-rays).

Inverse Compton (IC) scattering Figure 1.4, e. When relativistic electrons scatter on low energy photons, they transfer part of their energy, resulting in high energy γ-rays. When $\epsilon \ll 1$ ($\epsilon = \frac{E_\gamma}{m_e c^2}$)

$$\frac{dE}{dt} = \frac{4}{3} \sigma_T \, c \, U_{rad} \left(\frac{v^2}{c^2} \right) \gamma^2 \tag{1.9}$$

where

$$\sigma_T = \tfrac{8}{3} \cdot \pi r_0^2$$

is the Thomson cross-section, U_{rad} is the energy density of the radiation field and $\gamma = (\sqrt{1-\beta^2})^{-1}$). The spectrum of the scattered radiation has a maximum at

$$E_{max} \sim 4\gamma^2 E_0 \tag{1.10}$$

corresponding to head-on collision. This relation shows that for high Lorentz factors ($\gamma \sim 10^2 - 10^3$), the energy a photon can gain is $\sim 10^4 - 10^6$.

In the case of ultra-relativistic electrons ($\gamma \gg 1$), the Klein-Nishina regime starts playing a role and the corresponding cross section σ_{KN} must be used:

$$\sigma_{KN} = \pi r_e^2 \frac{m_e c^2}{\epsilon}(ln2\epsilon + 0.5) \tag{1.11}$$

This process is particularly important in the production of high energy γ-rays in AGNs jets: the inverse Compton scattering of synchrotron photons by relativistic electrons are able to produce the VHE photons observed in the TeV blazars. The emission model that associates the inverse Compton scattering with synchrotron radiation is called Synchrotron-Self Compton (SSC, see section 1.3.1).

High energy protons can also interact with soft photons, but the energy loss rate is suppressed by a factor $(m_e/m_p)^4 \approx 10^{-13}$ and significantly lower than pair production losses (when above threshold).

γ-rays, like CR, are absorbed by the earth's atmosphere. Satellites for direct measurements or ground-based detectors for indirect measurements of higher energy particles are the instruments to study the described phenomena, as shown in figure 1.5.

1.1.3 Absorption processes of VHE photons

When traveling cosmological distances to us, VHE photons can be absorbed via pair production by the extragalactic background light (EBL). The phenomenon involved is the inverse process of e^+e^- annihilation:

$$\gamma\gamma \rightarrow e^+ e^- \tag{1.12}$$

$$\frac{E_{\gamma 1} E_{\gamma 2}}{(m_e c^2)^2}(1 - \cos\theta) \geq 2 \tag{1.13}$$

where $E_{\gamma 1,2}$ are the energies of the interacting photons and θ the angle of collision, measured in the laboratory frame.

The study of the γ-ray flux that reaches the earth is correlated both with the intrinsic properties of the celestial accelerators and with the density of the cosmic background radiation. At TeV energies, the two aspects are both subject of study.

A compilation of EBL measurements of various experiments is shown in figure 1.6, together with predictions of some models. The spectral energy distribution (SED) of the background photons is measured with large uncertainty: the infrared (IR) radiation from our galaxy represents a foreground radiation, difficult to suppress. Most of the measurements are upper or lower limits, but it is commonly

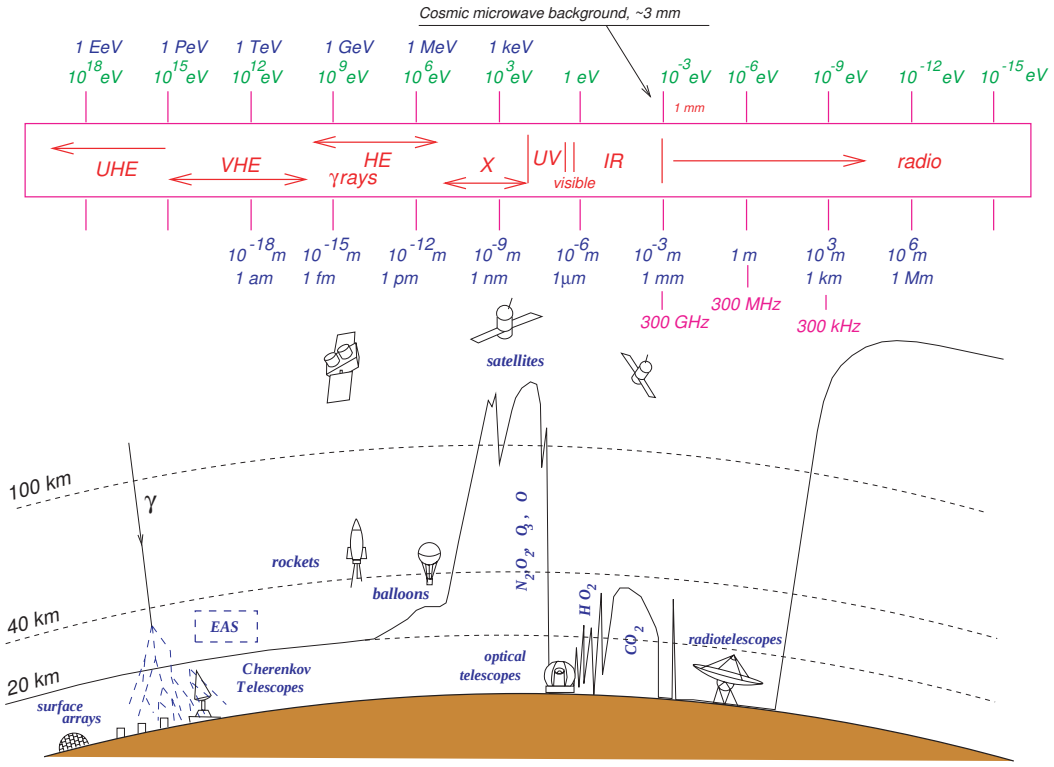

Figure 1.5: *Atmospheric windows for the observation of the Universe [20]. The continuous line indicates the height at which a detector can receive half of the total incoming radiation for every wavelength.*

accepted that the EBL SED shows two pronounced peaks. The first peak at $\sim$ 1 μm, known as the stellar component, is associated with light emitted by stars and red-shifted through the history of the Universe. The second peak at $\sim$ 100 μm comes from the re-processing of the starlight by dust and for this reason called dust component. Any attempt to model the shape of the EBL spectrum and its evolution must be based on strong assumptions on cosmological parameters, distribution of matter in the Universe, star formation rate, etc.

The part of the EBL spectrum corresponding to high wavelengths is poorly defined, because of significant uncertainty on the mechanisms of light reprocessing and re-radiation by dust. The best method of evaluating its density is the measurement of TeV photon flux produced by the same class of objects spread over a wide range of distances from us. The method implies that the characteristics of the emissions are strong enough to reach us and well known, so as to be able to estimate the expected flux. Active galactic nuclei are well suited for EBL studies.

The attenuation of VHE γ-rays by isotropic background photons is determined by the dust EBL component, corresponding to IR wavelengths (1-1000 μm, limits dependent on the selected model and cosmological parameters). Its main effect

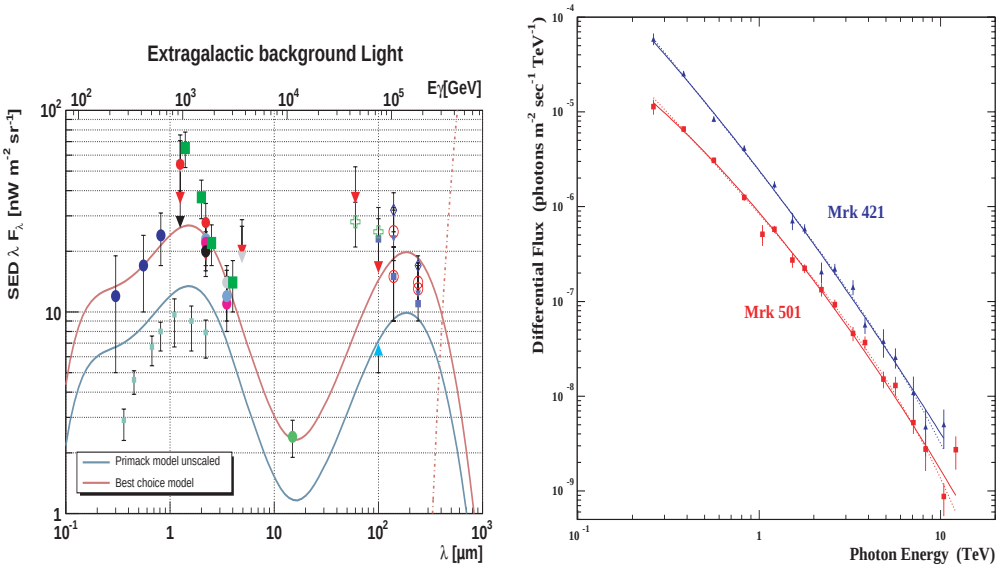

Figure 1.6: *Left: Collection of data and limits of the extra-galactic background light, taken from [22, 23], measured by various experiments (see references therein). Downward arrows indicate upper limits. The upper scale axis indicates the energy of the absorbed photons. Right: the spectra of Mkn421 and Mkn501 reported in [24]. The solid lines are the result of the fit of the experimental dots assuming a curved spectrum, while the dotted lines assume a fitted function with an exponential cutoff at 7.0 TeV and 4.9 TeV respectively for Mkn421 and Mkn501.*

on the observations is an exponential reduction in the flux of VHE γ-rays from extragalactic sources, such as a cut-off in the spectrum of blazars.

The optical depth $\tau(E,z)$ of γ-rays of energy E and produced at a distance z is defined as the path length before the photons are attenuated by a factor e^{-1}. The probability that a photon will reach us $\exp(-\tau(E,z))$ can be expressed with the formula (see [25, 26]):

$$\begin{aligned}\tau(E,z) &= \frac{1}{n_0 h_0}\int_0^z \sqrt{1+z}dz \int_{\frac{m_e^2}{E(1+z)^2}}^{\infty} d\epsilon \frac{dn(\epsilon)}{d\epsilon} F\left(\frac{m_e^2}{E(1+z)^2}\right) \\ \frac{1}{n_0 h_0} &= \frac{3}{8}\sigma_T \frac{c}{H_0}\end{aligned} \tag{1.14}$$

where $H_0 = 100 h_0$ km s^{-1} Mpc^{-1} is the Hubble constant, $0.5 < h_0 < 0.85$ is the normalized Hubble expansion rate, $n_0 = 4.33 \cdot 10^{-4}$ cm^{-3} is the characteristic density, $dn\epsilon/d\epsilon$ is the spectral EBL density measured *today*, m_e is the electron mass.

Assuming a spectral density for the EBL SED $d\epsilon/dE \propto (\epsilon/eV)^{-\beta}$, we can compute the energy dependent attenuation for the spectrum of a blazar at a distance

z, with differential energy spectrum following a power law of index δ and flux J:

$$\begin{aligned}
\frac{dN}{dE} &= JE^{-\delta}\exp(-\tau(E,z)) \\
\frac{dN}{dE} &= JE_c^{-\delta}\exp(-\delta ln\left(\frac{E}{E_c}\right)\left(\frac{E}{E_c}^{\beta-1}\right) \\
E_c &= \left(\frac{n_0\, h_0}{\alpha g(\beta) z}\right)^{\left(\frac{1}{\beta-1}\right)} \text{ TeV}
\end{aligned} \tag{1.15}$$

valid for $z \ll 1$. A sharp cutoff must exist in the spectrum if β is large enough to make the power-law term dominating the logarithmic term. According to some model estimates [27], it seems to be the case ($\beta \sim 2 - 2.5$).

In [26] we can find an analysis of the γ-ray spectral features of Mkn421 [28] and Mkn501 [29] (both with $z \sim 0.03$), related to the EBL absorption effects. The observational result of Whipple, shown in figure 1.6 right, is that there is no clear evidence for a sharp cutoff [3] in the spectra of the two blazars mentioned. An overall attenuation of the γ-ray flux, with a slight change in spectral curvature is masked by the unknown intrinsic spectrum of the source. The attenuation coefficient changes to produce such an effect when the SED is proportional to the energy of IR photons with logaritmic accuracy in the region 1-10 μm. This region affects observations between 250 GeV and 10 TeV. Observations outside this region, would show the (no longer invisible) effect of a rapidly falling EBL SED. If we consider the region 100-300 GeV, the absorption effect would produce a jump in the spectral index and curvature in the spectrum of blazars at $z \sim 0.03$. The other possibility is that the attenuation effect is, in general, very low, with a linear increase of the optical depth with distance. In such a case, the presence of EBL would produce a small curvature in the SED of blazars below 1 TeV of the order of:

$$\frac{1}{2}\frac{d^2\tau}{d\,\ln(E)^2} \sim 0.1 \tag{1.16}$$

The absorption of γ-rays makes highly red-shifted blazars invisible to ground-based γ-ray telescopes with an energy threshold near 1 TeV. The cutoff energy for blazars is shown in figure 1.7 as a function of the source red-shift, as computed in [31]. New generation Cherenkov telescopes have lower energy thresholds than the previous ones. We expect to have a larger portion of universe accessible to IACTs, thus an increasing number of blazars detected. The expected cutoff energy in blazars SED at increasing red-shift is inversely proportional to the optical depth for pair production, as shown in the right plot of figure 1.7. It is clear that new low-threshold IACTs will be able to increase our knowledge of the EBL density, with the detection of celestial objects at increasing distance to us.

[3] Above 5 TeV there is a considerable steepening of the spectra of Mkn421 and Mkn501 which can be explained by an exponential cutoff at $\sim$ 4-6 TeV [30].

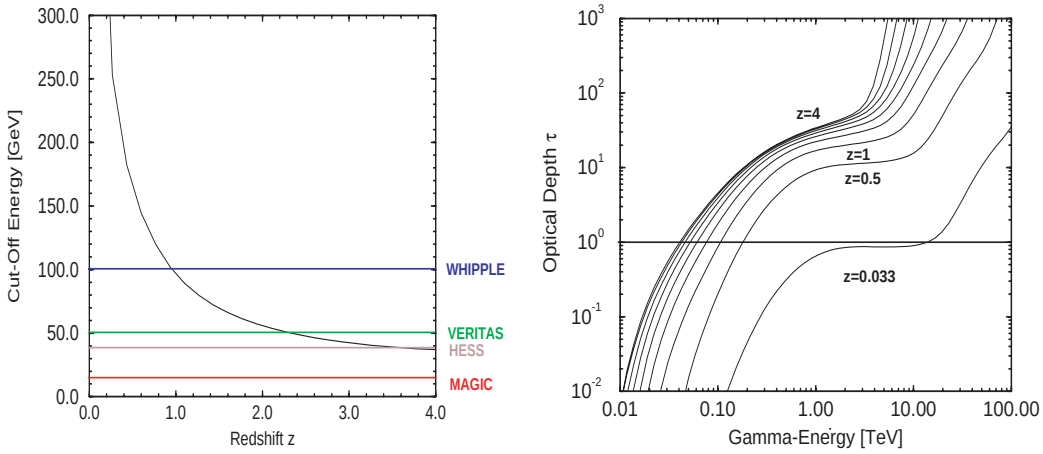

Figure 1.7: *Left: Cutoff energy as a function of red-shift for an optical depth of 1, compared with the lower energy threshold of some Cherenkov telescopes. Right: Optical depth for pair creation as a function of energy for sources at different red-shifts. Both pictures are taken from [31].*

An additional problem in detecting high red-shift AGNs might be caused by the intrinsic AGN accelerator when its power is not efficient enough at high energies or if the intrinsic absorption is enhanced by high photon density so as to cause a cutoff at lower energies.

The study of 1ES1959+650 spectral features is of great interest from this point of view. Its distance is comparable with that of the previously mentioned blazars Mkn421 and Mkn501, with a red-shift of $z = 0.047$. Similarities and differences in the spectrum will lead us to a better understanding of the standard (if any) phenomena occurring in blazars' jets and of the effects that EBL has on the information sent as γ-rays.

1.1.4 γ-ray sources

Some of the possible celestial sources of γ-rays are active galactic nuclei, microquasars, supernova remnants and γ-ray bursts. They will be briefly described in the following sections.

Active Galactic Nuclei (AGN)

These are galaxies with a super-heavy emitting core, commonly interpreted as a black hole (BH).

They include a variety of objects whose emissions have different spectral features, such as quasars, Seyfert galaxies, FR galaxies, radio galaxies. The difference between the observable properties of these objects depends on the orientation they

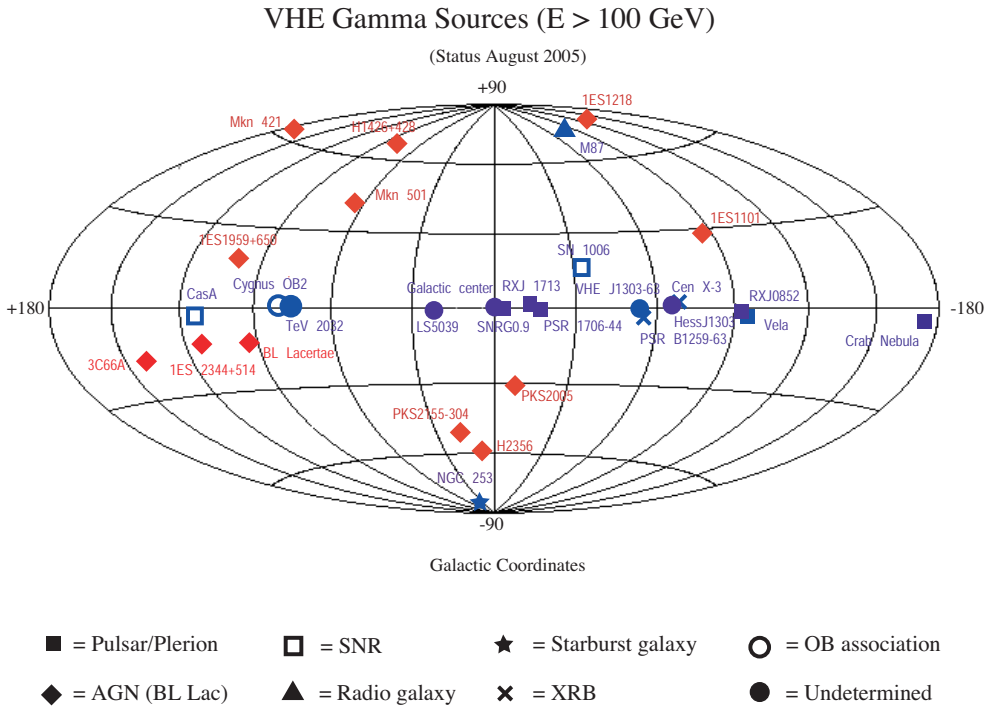

Figure 1.8: *Map of the VHE γ-ray sources as reported in August 2005 [32]. About 15 sources near the galactic center are not plotted here. The new low threshold and high sensitivity Cherenkov telescopes contribute strongly to the increase in the number of detected sources, with respect to the map showed in figure 1. This map will soon be out dated thanks to the γ-ray sources recently discovered by the H.E.S.S. collaboration.*

have with respect to the point of view [33]. VHE γ-ray emissions are characterized by high variability.

It is believed that VHE radiation is produced by energetic electrons (inverse Compton process) or by protons and soft photons inside the jet. The class of galaxies with the jet pointing towards the earth are called BL Lacs or blazars. VHE γ-rays come from this class of objects and the emissions are beamed.

Figure 1.14 above shows schematically the structure of a typical AGN, according to the unified model used to describe those objects [33]. My thesis work is related to the study of the AGN called 1ES1959+650. Further explanations on the unified model and spectral features of AGNs will be given in section 1.3.

Microquasars and binary systems

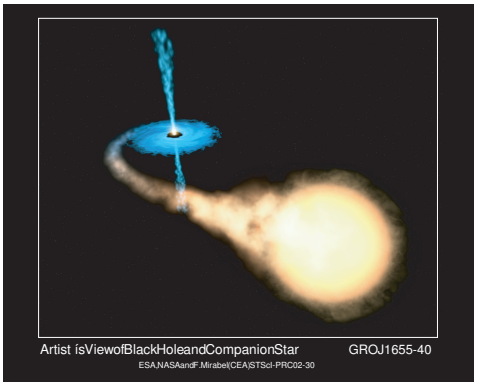

Figure 1.9: *Artist's view of a binary system. A companion star, in foreground, provides matter for the compact object, painted in the background. The material attracted by the black hole creates an accretion disc, when coming close to the Schwarzschild radius. Such material is partly absorbed by the BH and partly ejected forming a jet-like structure.*

Very massive stars can accrete matter from stars in orbit around them. Their connection forms the so-called binary system, that can have different characteristics and evolutions depending on the involved objects. X-ray binary systems are composed of a compact object, such as a neutron star or a black hole and a companion star (blue giant or white dwarf, very massive stars but less compact).

Microquasars are a selected class of X-ray binaries. An artist's view of such system is shown in figure 1.9. It is composed of a BH that produces relativistic jets (seen in radio, optical and often X-rays up to GeV and γ-rays wavelengths), and a companion responsible for mass accretion. Their name comes from the observed morphological and physical similarities with quasars. The mass of a microquasar is about seven orders of magnitude lower than that of quasars. They are interesting because the processes taking place in AGNs can be studied in a shorter time in microquasars, considered from many aspects as their scaled-down version. Some known microquasars are considered counterparts of unidentified EGRET sources. From the theoretical point of view, they might emit photons up to 10^2 GeV, but no emission has been detected from the previous generation of Cherenkov telescopes. They are good candidates for higher sensitivity and lower threshold instruments of the new generation [4].

[4] Recently, the H.E.S.S. collaboration reported on the detection of the VHE γ-ray emission from

A special binary system in our galaxy is PSR B 1259-63, in which a radio pulsar is orbiting a main sequence star, with very high eccentricity. The H.E.S.S. collaboration has recently reported on the γ-ray detection of PSR B 1259-63 at periastron, in March 2004 [35]. Previous observations carried out by CANGAROO II in December 2000 and March 2001 permitted acquisition of only upper limits to the flux [36]. The emissions of VHE γ-rays have been interpreted as the interaction of the pulsar with the inclined disc of the Be companion star. A possible interpretation can be found in [37]. After the pulsar leaves the disc, high energy electrons remain in the pulsar-wind bubble. These electrons emit synchrotron radiation in the radio frequencies. The hard X-ray emission up to 200 keV strongly implies that it originates from synchrotron radiation of non-thermal electrons. Electrons in the pulsar wind may be accelerated in a shock wave generated in the region where the relativistic pulsar wind interacts with dense mass flow from the Be star. [8, 9] have interpreted the measured hard X-ray spectrum on the basis of accelerated particles in the pulsar-side shock, with a Lorentz factor of $10^6 - 10^7$. These relativistic electrons in the radiative environment of the binary system may produce high energy gamma rays.

Supernova remnants

When a star finishes burning its *fuel* and its mass is high enough, one of the possible evolutions of the system is related to the non-equilibrium between internal pressure and gravitational potential, that makes it collapse. The result is a huge explosion, the external shells are ejected forming the nebula, and the core becomes a compact object, a neutron star or a black hole, depending on the mass. In case of a neutron star, this system is called supernova remnant (SNR). Some SNR are known to be steady emitters of VHE γ-rays coming from the nebula, while the central part emits pulsed radiation. The most famous and best studied SNR is known as Crab Nebula (or M1) that, for its properties, is considered the GeV-TeV standard candle for γ-ray astronomy.

Part of this work is also related to the analysis of data from the Crab Nebula to calibrate MAGIC and to understand its performance above 50 GeV. Properties of the Crab are described in session 1.2.

Gamma-ray bursts

GRBs are the most energetic and violent short term phenomena in the universe. GRBs occur at cosmological distances. During their short *life* (from tens of milliseconds to few hundred seconds) the γ-ray emissions can be stronger than any other known γ-ray source, with a large variety of temporal profiles and emission spectra. They have been studied in the past using mostly data collected by the satellite instrument BATSE (Burst and Transient Source Experiment) [38] and EGRET [39] (small statistics).

---

the X-ray binary LS 5039, a candidate microquasar (July 2005) [34].

The most accepted interpretation of the phenomena of GRBs is known as the *fireball model* [40]: a relativistic expanding plasma of unknown origin dissipates its kinetic energy. From the short duration and the fast rise of γ-ray flux, the sources must be compact. Due to their cosmological distance, they must be extremely luminous, releasing about 10^{52} erg of γ-rays in less than 1 s. GeV photons can, in principle, be produced via synchrotron and inverse Compton processes by accelerated electrons in internal shocks.

Currently, the satellite experiments HETE-2 [41](energy range 1 keV to 500 keV) and Swift [42](energy range 15 keV to 150 keV) are providing new data. Some bursts have observed spectra over 100 MeV. Waiting for GLAST (Gamma-ray Large Area Space Telescope) [43, 44] to cover the observations of GRBs from 10 MeV to more than 100 GeV using the instrument called LAT (the 5 keV - 25 MeV interval will be also covered by the GBM instrument), low threshold ground-based Cherenkov telescopes like MAGIC are the instruments best suited to study the higher energy band of the GRB picture that existing satellites are taking. Observation from earth with IACTs can be achieved only by alerts from satellites which can provide, after few seconds, quite precise information of the coordinates of the burst.

For new generation IACTs the biggest problems to confront in order to observe γ-rays from objects at cosmological distances are the IR absorption of GeV photons and the short time duration of the phenomenon. The attenuation by background photons plays a critical role, since the cut-off in the energy spectrum is expected between 30 and 100 GeV for GRBs at z= 1 or more (see figure 1.7).

To be able to observe GRBs with Cherenkov telescopes, they need a very short reaction time. The field of view of IACS is typical of 3°-5°. Without a precise indication of the burst position, there is no chance to see the explosion inside the field of view (FOV). Hundreds of seconds after the burst, the γ-ray emission from most GRBs is very likely completely gone, although in one case EGRET observed a GeV afterglow 70 minutes after the burst. Fast telescope repositioning is essential for this purpose. MAGIC is the only existing Cherenkov telescope designed for GRBs observations: it is the lowest energy threshold ground-based γ-ray telescope, with a very light-weight structure and fast slewing drive system ($\leq$ 25 seconds to any point on the sky).

1.2 The Crab Nebula: the TeV standard candle

The Crab Nebula is the most firmly established TeV steady γ-emitter in the northern sky. It can be seen in the constellation of Taurus (see figure 1.10), at a distance of about 1930 pc [45], with an apparent brightness corresponding to an absolute magnitude of -3.2. The overall luminosity in all the energies is estimated to be 10^5 $L_\odot$, corresponding to 5×10^{38} erg/s. The name comes from the drawing shown in figure 1.10 by William Parsons, the Third Earl of Rosse. He observed the nebula with his 36-inch reflector telescope at Birr Castle.

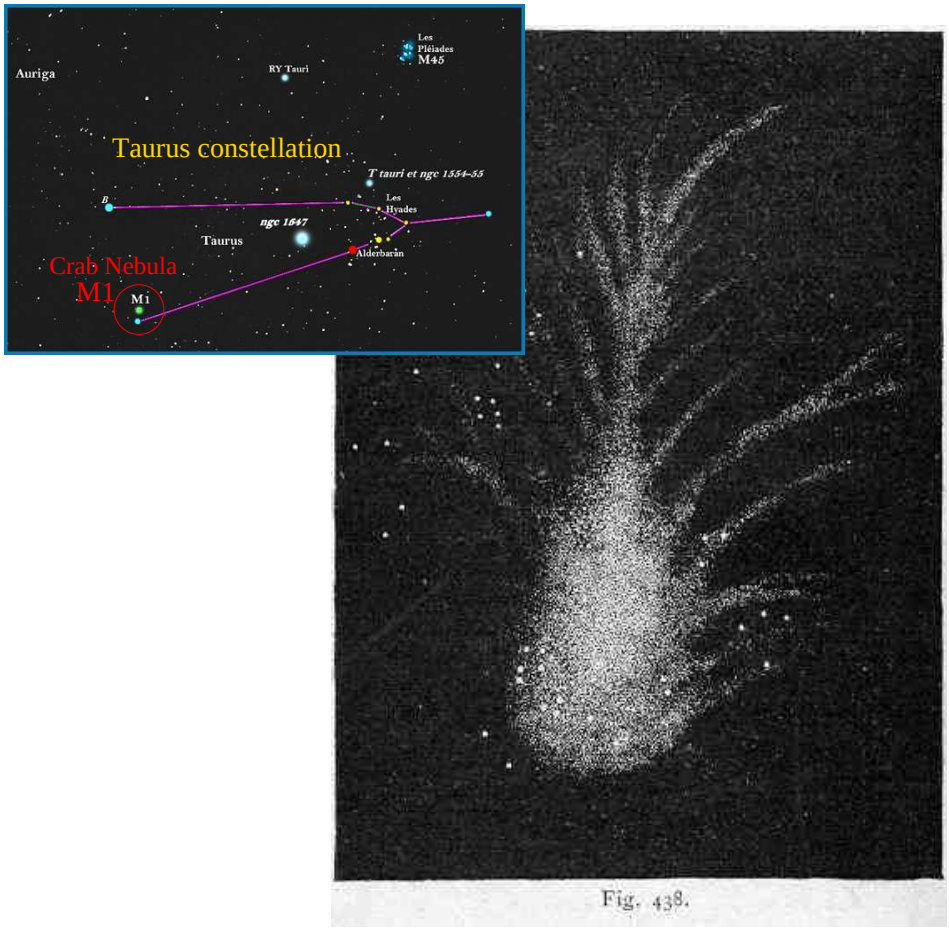

Figure 1.10: *Above-left: the map of the Taurus constellation, where the Crab Nebula, also known as Messier object M1, is located. Below: Drawing by Lord Rosse, which led to the name Crab Nebula. It was created in 1844 using the 36-inch reflector at Birr Castle.*

A supernova explosion in 1054 A.D. originated the structure we observe today. The Crab Nebula is one of the few historically observed and documented supernova explosions in our galaxy. Chinese astronomers and maybe also American Indian artists documented a bright star appearing in the sky and slowly becoming faint[5]. Figure 1.11 left is a combined picture of optical and X-ray emissions, taken by the Chandra satellite.

The Crab, also known as M1, consists of a (nearly) central compact object, the pulsar, surrounded by a nebula. A schematic view can be seen in figure 1.11 right. Crab is one of the best studied astronomical objects. It can be studied at all the accessible wavelengths, but questions regarding the progenitor star and its evolution

[5]From the Chinese documents, it appeared on July 4, 1054 A.D and it stayed visible in daylight for 23 days and in the night sky to the naked eye for 653 days.

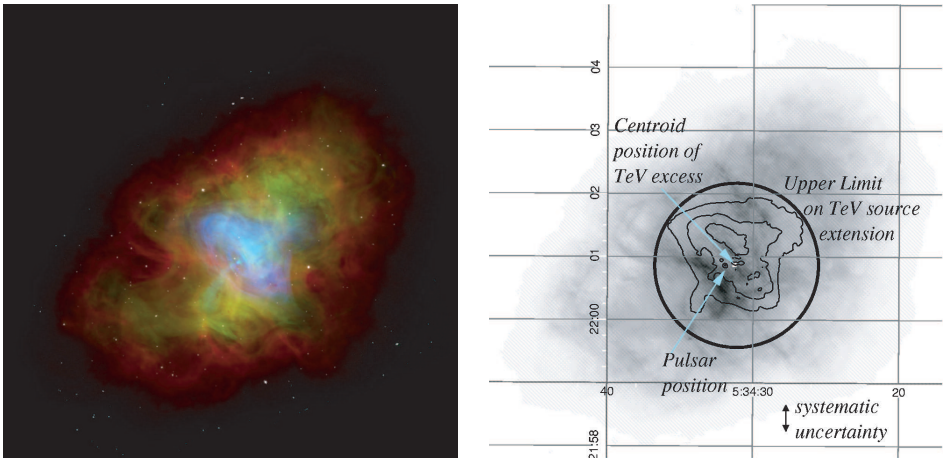

Figure 1.11: *Left: Composite image of the center of the Crab Nebula where red represents radio emission, green represents visible emission, and blue represents X-ray emission. The dot at the very center is the hot pulsar spinning 33 times per second. Right: the radio map is represented in gray scale and the X-ray contours are superimposed. The HEGRA upper limit on the TeV source extension is represented by the thick circle and it corresponds to 1.5 arcmin diameter. The arrows indicate the centroid position of the TeV emissions region and the position of the pulsar. Taken from [46].*

still remain unanswered. The observations of this object played an important role in the early history of radio and X-ray astronomy. It is the brightest X-ray object in our galaxy.

A recent review of the characteristics of the emissions of Crab can be found in [46] and references therein. The origin of high energy emissions are commonly interpreted as non-thermal processes: synchrotron radiation and inverse Compton scattering. The different regions where non-thermal radiation is produced are shown in figure 1.13.

Characteristics of the emissions from the pulsar

Pulsars are rapidly rotating magnetized neutron stars, produced in supernova explosions. The Crab pulsar is a source of pulsed radiation with a period of 33 ms. Since their discovery, pulsars have been observed in a wide range of wavelengths.

The EGRET detector measured pulsed emission from several high energy pulsars up to energies of about 10 GeV. No pulsed emissions above this threshold has been observed yet, because of the small collection area of EGRET (equivalent to two A4 pages). The energy band between 20-100 GeV is at present unexplored.

The Crab pulsed spectrum is shown in figure 1.12. At high energies it is expected to show a cutoff, experimentally constrained to the range of 5-200 GeV. Its detection is important to discriminate between different pulsed VHE γ-ray emission models.

There are two major classes of models dealing with high energy γ-ray emission

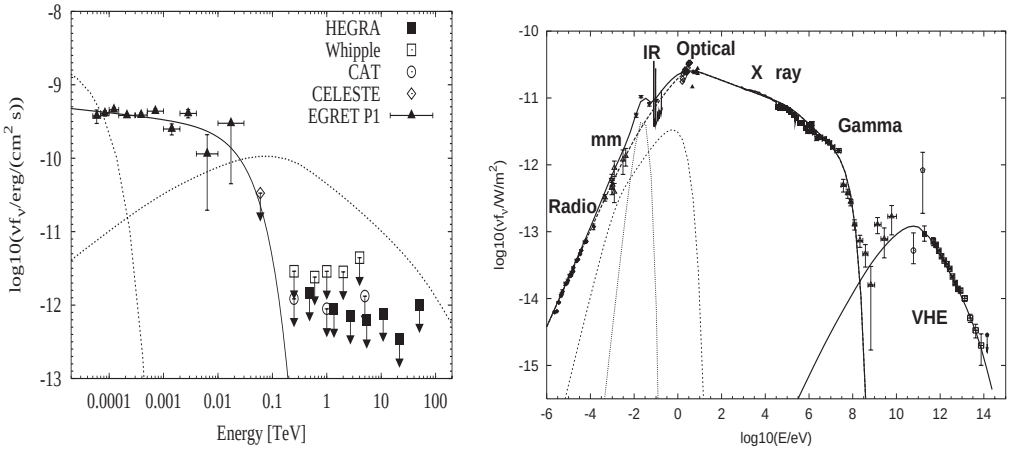

Figure 1.12: *Left: Crab pulsar spectrum, with the EGRET detection of the main pulse and the upper limits of CELESTE, HEGRA, Whipple and CAT. The solid line is a fit of a power law function with photon index of -2.08 and exponential cutoff at 25 GeV to EGRET data and CELESTE upper limit. Dotted lines are the synchrotron and IC predictions of a model for the emissions from the nebula. For detail, see [47]. Right: Overview of the Crab nebula spectrum, taken from [46]. Data shown are a compilation of results of many experiments at all accessible wavelengths, presented in different papers, as explained in [46] and references therein.*

from pulsars which differ in the assumption on where the particle acceleration takes place. A rotationally induced electric field drives pair cascades, producing the electrons that can escape in the regions where $\mathbf{E} \cdot \mathbf{B} \neq 0$. Those regions can be near the star surface, at the polar caps, or relatively distant from it.

Polar cap models [48] suppose that the acceleration and radiation processes take place near the surface of a neutron star, at its polar regions. They predict a strong cutoff at energies below 10 GeV, due to the absorption of the TeV γ-rays from the strong pulsar magnetic field. Millisecond pulsars, with their relatively low magnetic fields ($B \sim 10^8 - 10^9$ G) permit γ-rays to escape. In this case, the cutoff might occur at higher energies.

In *Outer gap* models [49] the acceleration zone is in the pulsar's outer magnetosphere, at a relatively large distance from the surface of the neutron star, where the magnetic field is reduced by several orders of magnitude in the region along the null-charge surface, called light cylinder. In this region no cascades absorption mechanism is possible. They predict a hard component of γ-rays in a narrow region around a few TeV [50], being the cutoff energy determined by the maximum energy of the accelerated electrons. TeV γ-rays can be produced via inverse-Compton (IC) scattering also in pulsars with relatively large magnetic field.

There are a few other models which completely differ from the previous ones, such as the *neutron star wind* model. Pulsar winds consist of electrons and positrons generated in the pulsar magnetosphere. Between the magnetosphere and the nebula

region there is a region where electrons of the wind are moving with the magnetic field (in figure 1.13 it is called *unshocked wind*), though no synchrotron emission is possible. This region can be observed via the bulk motion Comptonization caused by illumination of the wind region. The possible spectral features of the radiation produced in the wind would have features very much dependent on the Lorentz factor and geometry propagation of the wind, together with the characteristics of the 'particle dominated wind' site of origin.

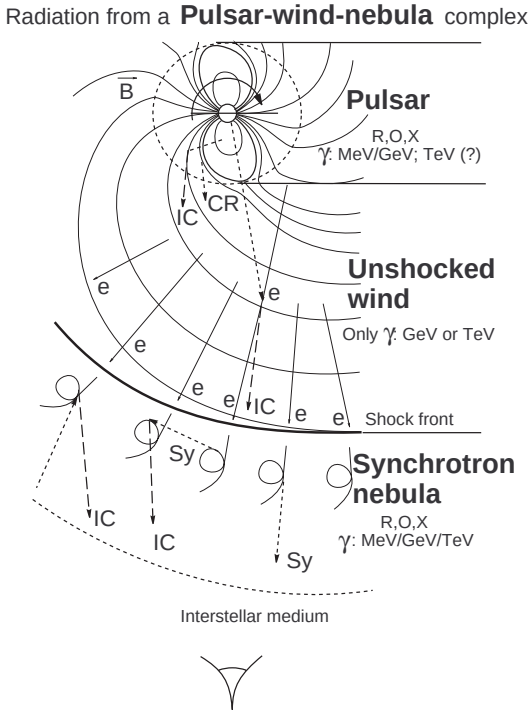

Figure 1.13: *Scheme of the three emitting regions of VHE γ-rays from a pulsar. Taken from [51].*

The emission from the Nebula

The spectrum of the Crab Nebula, shown in figure 1.12 right, is characterized by a continuum, from radio to TeV energies, of non-thermal origin. There are three spectral breaks and the four resulting branches are described by power-laws. The large lower energy bump, commonly interpreted as the synchrotron peak, extends to a few MeV. It indicates the presence of relativistic electrons up to 10^{16} eV that are effectively accelerated in a magnetic field ≥ 100 μG.

The first TeV detection dates back to 1989 by the Whipple collaboration [52]. Since then, it has been detected by more that 10 independent ground-based instruments for VHE γ-ray astronomy. It can be seen both from the northern and the

southern magnetic earth hemisphere and its steady emissions have made it the TeV standard candle.

The origin of the emitted photons of highest energy may be inverse Compton scattering of PeV electrons and π^0 decay. The pulsar accelerates a relativistic wind of particles that terminates in a shock, but the mechanism of acceleration can be explained with several possible models.

The most accepted model for the explanation of the non-thermal emission is known as the MHD model and was developed by Kennell and Coroniti in 1984 [53]. A spherical geometry is assumed, the electrons of the wind are accelerated at the wind termination shock and injected in the nebula. An additional component of radio electrons is introduced, whose location is determined by radio observations. TeV γ-rays would arise from IC scattering of relativistic electrons with target radiation fields, such as synchrotron, thermal IR or 2.7 K CMB radiation. The parameters of the model are calculated from the observational data. The result is the solid line shown in the spectrum of figure 1.12 right, in very good agreement with the experimental data.

Most models simplify the geometry of the nebula with a spherically symmetrical structure, despite of the complex cylindrical shape observed and shown in figure 1.11. The asymmetrical structure suggests that the rotational energy of the pulsar is released in form of wind, that flows along the pulsar equator. The interactions between the pulsar wind and the synchrotron nebula are not yet understood.

Studies on the emission region within the nebula have shown that the size of the emission region decreases with increasing energy, being spatially constant in radio wavelengths. The central region shows variabilities in radio, optical and X-rays, called *wisps*, with no clear explanation.

The observation of the Crab nebula from the astronomical observatories on La Palma is possible during winter time at nearly all zenith angles (Crab culminates at la Palma at 9° zenith angle).

Studies of γ-ray emissions, especially at GeV energies, should still reveal many interesting physics aspects, like the detection of the pulsed emission cutoff of the Crab pulsar and the expected IC peak [54, 55]. In addition, the general analysis of the Crab nebula flux and spectrum allows me to provide a solid cross calibration [6] for the 1ES1959 analysis. The lowest energies events are not subject of this work.

1.3 Active Galactic Nuclei

AGNs constitute the main population of extra galactic high energy (HE) and VHE γ-ray emitting sources found so far. They are one of the main targets to be observed

[6] It should be noted that there is no cosmic test beam to calibrate telescopes. The Crab is therefore the best available calibrator for MAGIC.

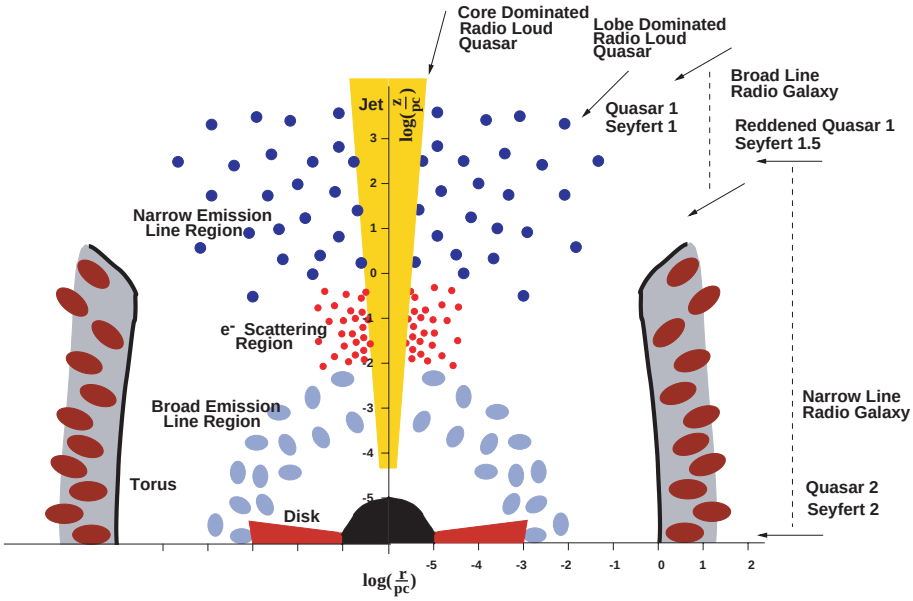

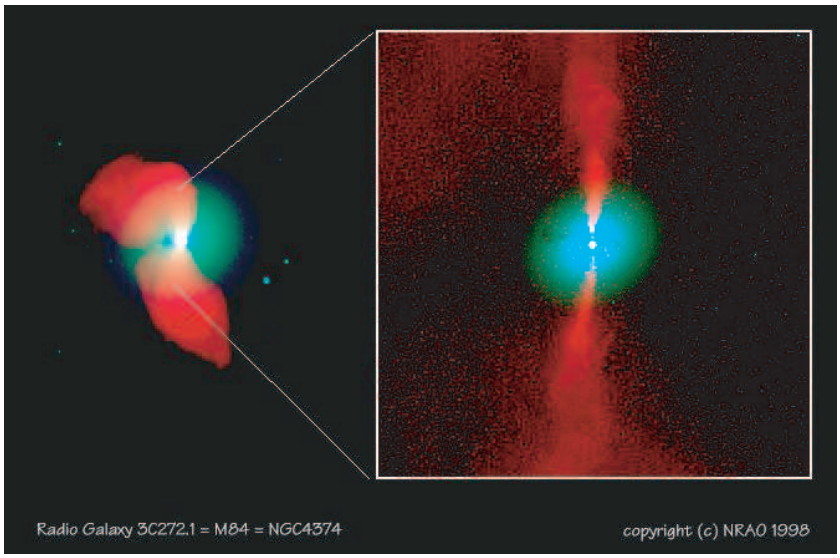

Figure 1.14: *Above: The unified schematic description of AGNs, taken from [56]. For the explanation, see text. Scales are logarithmic and geometry is not rigorously kept, to have a better view. Below: Fanaroff-Riley type I (FR I, double-plumed) radio galaxy at 17 Mpc distance. The overall size of radio source (red) is about 14 kpc. In blue-green: optical images of the elliptical host galaxy.*

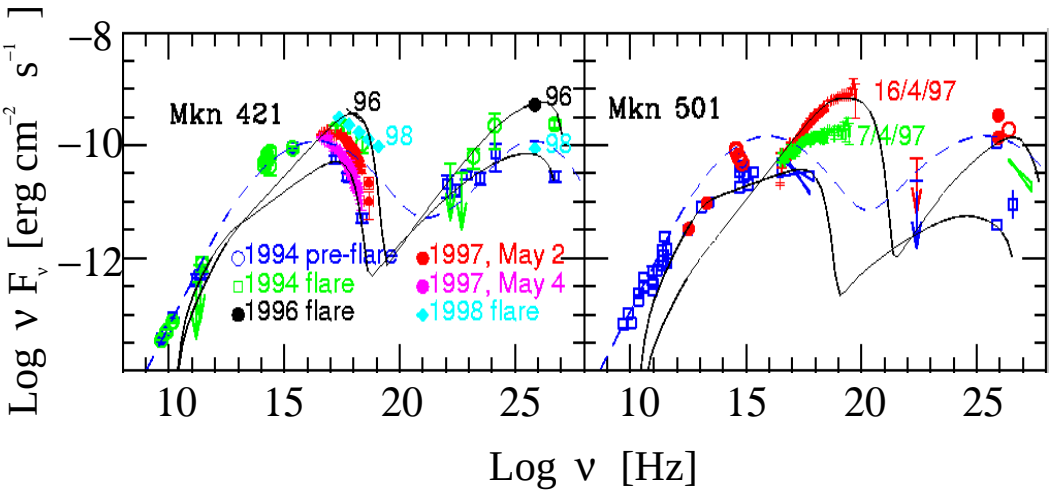

Figure 1.15: *Spectral energy distribution (SED) of the BL Lac objects Mkn421 and Mkn501. Solid and dashed lines refer to the SSC mode and to the SED constructed using the parameterization described in Fossati et al.,1998. Taken from [57].*

with IACTs. They include many different kinds of astronomical objects, such as Seyfert galaxies, radio loud quasars and quasi-stellar objects (QSOs).

An unified model has been introduced to explain what AGNs are (see figure 1.14, upper part): a central super-massive BH is surrounded by an accretion disc of hot plasma. From the BH, jets of ultra-relativistic particles arise basically orthogonal to the accretion disc and are beamed by the strong magnetic fields. Further out around the BH, a dusty torus can obscure the view to the central part, where there is a region producing broad lines in the spectrum. Molecular clouds could occupy the space between the torus and the jets (narrow line region). Differences between the observed spectra of AGNs depend on the orientation of the jet axis structure with the line of sight, the mass of the central compact object, the rate of accretion and the stage of evolution.

The variability of the highest energies emissions is related to infalling matter from the accretion disc to the black hole (BH).

Different models attempt to explain the jet formation and its connection to the accretion disk. One of the most accepted views is the extraction of energy and angular momentum from the accretion disk by means of a magnetic field, generating a flow of matter from the disk, as a consequence of momentum conservation. This matter is collimated at large distances by the action of a toroidal component of the magnetic field.

1.3.1 Comparison between models and observations

The first extragalactic source found to emit γ-rays in the TeV range was the AGN Mrk421 [28]. This blazar has also exhibited the fastest observed flux variations in

the TeV range [58].

The study of emission of VHE γ-rays by AGNs is related to the development of models trying to explain the physics processes causing the observations of different detectors.

Data and models are combined together to form a picture as coherent as possible, assuming that electron acceleration dominates. The shape of the spectrum of AGNs, as shown in figure 1.15, is characterized by 2 'humps'. The first hump is almost unanimously attributed to synchrotron radiation of electrons in the strong magnetic field inside the jet. The origin of the second hump is still under debate. Most likely, it is due to inverse Compton scattering, i.e. energetic electrons upscatter low energy photons, either those generated by synchrotron radiation (see SSC model [59]), or photons from the hot accretion disc or from hot spots.

Leptonic models These are the most popular among the models proposed. Relativistic electrons (and positrons) upscatter low energy photons and produce X-rays and γ-rays via an inverse Compton effect. Since the relativistic particles are moving inside the jet, the resulting radiation is also strongly beamed.

Evidence of correlation between big flares both in X-rays and γ-rays observed in Mkn421 [60, 61, 62] and in Mkn501 guided the formulation of a model that associates the origin of the very high energy (VHE) photons to the synchrotron photons. When the synchrotron photons are inverse Compton scattered by the same electrons that produced them, they acquire energy becoming γ-rays. This model is known as Synchrotron Self Compton (SSC) and it is the most accepted model to describe VHE γ-ray emissions from objects with weak accretion disc radiation, like BL Lac objects. For a numerical description, see [63, 64].

The target photons can have also other possible origins: they can be radiation from the central part of the accretion disc or reflected back to the jet after reprocessing by the molecular clouds between the torus and the jet. Objects like flat spectrum radio quasars (FSRQs) most probably emit γ-rays in this way.

Hadronic models Alternative models have been proposed to explain the higher energy γ-ray emission observed from AGNs. For a review, see [65]. According to those models, the blazar jets have a protonic component, which is accelerated inside the jet together with the leptonic component.

γ-rays can originate from the decay of neutral pions produced by the interaction of protons in the jet [66, 67] with low-energy photons (like synchrotron photons produced by accelerated electrons). The photons from the decay of neutral pions can interact with the soft synchrotron photons, with subsequent pair production, that initiates an electro-magnetic cascade in the jet. Photons from the cascade can escape from the jet and can be detected in the

TeV range or below. The target photons can be either synchrotron emissions of electrons produced in the strong magnetic field inside the jet, or photons produced outside the jet, as described for the leptonic model.

Another possibility is proton-proton scattering, occurring when a high-density matter target moves across the jet. Pion production follows the processes described above.

When protons are in a strong magnetic field ($\sim$100 G), they can produce γ-rays via synchrotron process [68].

In the case of the hadronic origin of the γ-ray radiation, one also expects to detect neutrinos, but at least km-square detectors are needed. Neutrinos would arise from the decay of mesons in photoproduction interactions. The detection of neutrinos would favour this model with respect to the leptonic one. On the other hand, one of the biggest problems of the hadronic models is that the acceleration and cool-down processes involved are rather slow, while in AGNs variations of flux has been observed during very short time spans (Mkn421 doubled its flux in less than 20 minutes [58, 69], Mkn501 in the order of a day).

At the moment, both models (with slight preferences for the SSC process in the AGNs Mkn421 and Mkn501) can describe the observational results, while the tuning of the parameters of the models is done on the data itself.

The physical parameters, which are usually derived from the spectral shape and the time variability of AGNs, are the size of the emission region, the strength of the magnetic field inside the jet, the Doppler factor and the Lorentz factor of, respectively, the accelerated particles and the density of the target photon field.

An important issue when observing AGNs of cosmological distances is the interaction of the background photon field with the emitted VHE photons (see section 1.1.3). What we observe is a combined effect of emission of AGNs and absorption. The VHE photon interaction with IR photons modifies the observed VHE spectra of blazars, which intrinsically follow a power law. The intrinsic AGN electromagnetic spectra might have a high energy cutoff (accelerators run out of energy). It is therefore difficult to distinguish the origin of an observational cutoff due to accelerator effect or IR interaction, but an upper limit of the IR column density can be set. The photon-photon absorption produces an exponential cutoff $e^{-\tau(E)}$, where $\tau(E)$ is the optical depth. The SED of AGNs is usually displayed in νF_ν graphs, using power law approximations and cut-off energy terms.

The comparison between different AGN spectra will allow us to understand whether the absorption due to the EBL (Extragalactic Background Light) is consistent with the distance of the AGN. Studies on the spectral features during different periods of activity of the sources are particularly interesting at different wavelengths, in order to have a global understanding of the physical processes involved in each phase of the emission.

Due to the expected number of $\gtrsim 50$ new sources at different red-shifts, observable with low energy threshold instruments, we should be able to disentangle the systematic effect of the EBL from the intrinsic characteristics of the individual sources.

Chapter 2

Observations of the AGN 1ES1959+650

This chapter adresses the recently confirmed VHE γ-ray source *1ES1959+650*. Multi-wavelength observations have shown interesting aspects, that will be covered in the following.

The HEGRA collaboration carried out observations of 1ES1959 both with the System and and the stand-alone Telescope CT1 in the years 2000, 2001 and 2002. The MAGIC collaboration program comprises the revisit of all known northern VHE γ-ray emitting AGNs, as well as a systematic search for new VHE γ-ray emitter objects. During the first year of operation the source 1ES1959 has been observed for few hours with MAGIC in the test phase.

2.1 Why look at the AGN 1ES1959+650?

1ES1959 is the name of an elliptical galaxy, that hosts a super-massive black hole (BH) in its nucleus. The mass of the central black hole has been evaluated in [70]. From the stellar velocity dispersion $logM_{\bullet}^{\sigma_v}/M_{\odot} = 8.12 \pm 0.13$ and from the luminosity of the galaxy bulge $logM_{\bullet}^{L_b}/M_{\odot} = 8.64$, the BH is considered to be the engine of the very energetic γ-ray emissions observed.

The emission is beamed along two jets and the orientation of one jet towards the earth allows us to observe the VHE photons boosted in the jet. Because of those properties the object is classified as a blazar (or BL Lac) type of Active Galactic Nucleus (AGN).

The discovery of 1ES1959 dates back to 1993, when radio, optical and X-ray observations lead to the identification of a new object at right ascension (Ra) 19h59m59.8s and declination (Dec) +65d08m54s. The name comes from the first catalog of the Einstein Slew Survey (1ES) [71], that performed observations in the X-ray band.

The first published suggestion to look at 1ES1959 with γ-ray telescopes dates back to 1996 [72]: a list of low-redshift XBLs was studied using SSC model as-

sumptions. Among the blazars, the most promising candidates were the ones with small redshift (z< 0.1), such that the photon absorption via pair production is limited. In BL Lac objects with a synchrotron radiation bump peaking at X-ray energies (called also XBLs or HBLs), inverse Compton scattering would generate photons that reach TeV energies according to the SSC scenario using simple scaling arguments. The inverse Compton peak would originate from the up-scattered synchrotron photons with the scaling factor calculated from the SED of Mkn421[1]. 1ES1959 was predicted to be one of the 23 best TeV low z AGN candidates, after Mkn 421, Mkn 501 and 1ES2344+514.

In 2001 the source was added as a TeV emitter candidate to the list by L. Costamante and G. Ghisellini [57], with estimates of the flux above 40 GeV, 300 GeV and 1 TeV. From a sample of 246 bright BL Lac objects, they selected the best likely TeV emitters candidates, requiring the presence of both high energy electrons (identified by intense and high X-ray emission) and a sufficient number of IR photons (identified by intense radio-optical emissions), to be the seed photons for inverse-Compton scattering.

According to the SSC model, the predicted fluxes from 1ES1959 at different energies are listed in table 2.1 [57], together with the results of a phenomenological parametrization of the SED by Fossati et al [73]. The SSC model used for the calculations has been modified assuming an homogeneous one-zone region of electron acceleration and that the injection of particles occurs for a limited time. The phenomenological model is based on the observed luminosity of blazars in radio wavelengths, determining its relation with the synchrotron peak and thus deriving the inverse Compton luminosity.

The SED of 1ES1959 with data available at TeV energies is shown in figure 2.1.

2.2 TeV observations

1ES1959 was detected for the first time as a TeV γ-ray emitter in 1998 by the Utah Seven Telescope Array [75], with an energy threshold of 600 GeV. After 56.7 hours, from May to August 1998, the total signal had a significance of 3.9 σ.

After this first experimental evidence, IACTs observed 1ES1959, but without any significant signal. The HEGRA collaboration performed a deep observation of the source between 1999 and 2001, using the Stereo System of 5 Cherenkov telescopes and the stand alone CT1 Cherenkov telescope. A large number of hours of observation were analyzed, but the signal was weak and not significant enough to claim a detection[2].

The final confirmation of the detection came only the year after. On May 2002 the VERITAS collaboration claimed a detection of a short flaring of the object [76].

[1]The shift factor was calculated as $\sim \gamma^2_{peak}$ in Thomson regime, equivalent to the Lorentz factor of the emitting electrons at the synchrotron peak. For Mkn421 this was $\sim 10^9$, with $L_C/L_{sync} \sim 1$ [72].

[2]There is a common agreement in the community that a *discovery claim* requires at least a 5σ excess.

Table 2.1: *Left: Predicted 1ES1959 integrated flux. The input parameters for the model are: intrinsic power (measured in the co-moving frame) of* $L' = 8 \cdot 10^{40}$ *erg* s^{-1}*, cross sectional radius of the emitting region* $R = 10^{16}$ *cm, bulk Lorentz factor* $\Gamma = 13$*, viewing angle* $\theta = 4°$ *(parameters of the SED by Fossati et al.). Right: SED of 1ES1959 showed in [57]. The solid line refers to the SSC model, dashed line refers to the phenomenological model by [73].*

Integr. Flux	Results from SED [73] $10^{-11}\,\gamma\,\mathrm{cm}^{-2}\mathrm{s}^{-1}$	Results from SSC [57] $10^{-11}\,\gamma\,\mathrm{cm}^{-2}\mathrm{s}^{-1}$
> 40 GeV	56.7	2.08
> 300 GeV	7.46	0.03
> 1 TeV	1.74	-

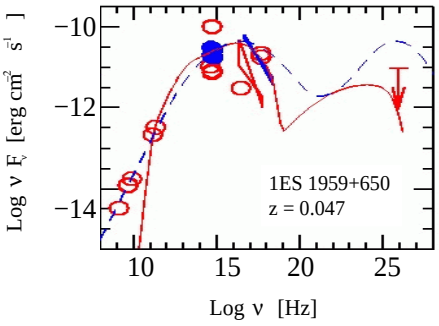

From then on, the attention on this object grew. A multiwavelength campaign was organized, with good results and encouraging outcomes. Other periods of high activity have been observed since the first one.

The study of the activity of 1ES1959 is challenging, especially due to the observation of a flare in γ-rays, during a quiet period of X-ray emission, in June 2002 [77]. The absence of a coinciding X-ray flare is a sign that the origin of the TeV flare was not due to high energy electrons and IC scattering. This effect, seen for the first time in a TeV γ-ray emitter was associated with hadronic products and such flares are called *orphan flares*. The hadronic emission models used to explain the phenomenon also make predictions of neutrino fluxes, which can be studied with very large neutrino telescopes located in the southern hemisphere.

The distance of 1ES1959 is of the same order of the two confirmed TeV sources Mkn 421 and Mkn 501. This also makes 1ES1959 a good candidate for studying interaction of γ-rays with the EBL and related cosmological problems. This is important as a single source spectrum cannot deliver unambiguous information on previously unknown EBL intensity, but only an upper limit.

2.3 Multi-wavelength properties of 1ES1959

The particularly intense activity and variability in the optic and X range makes 1ES1959 a good candidate for multiwavelength studies. In particular, finding a clear correlation between X-ray and TeV activity periods would imply that the radiation emitted in these two bands is produced by the same population of electrons. This would be an important constrain to the emission model.

The SSC model predicts, in its simplest form, that the change in IC scatter-

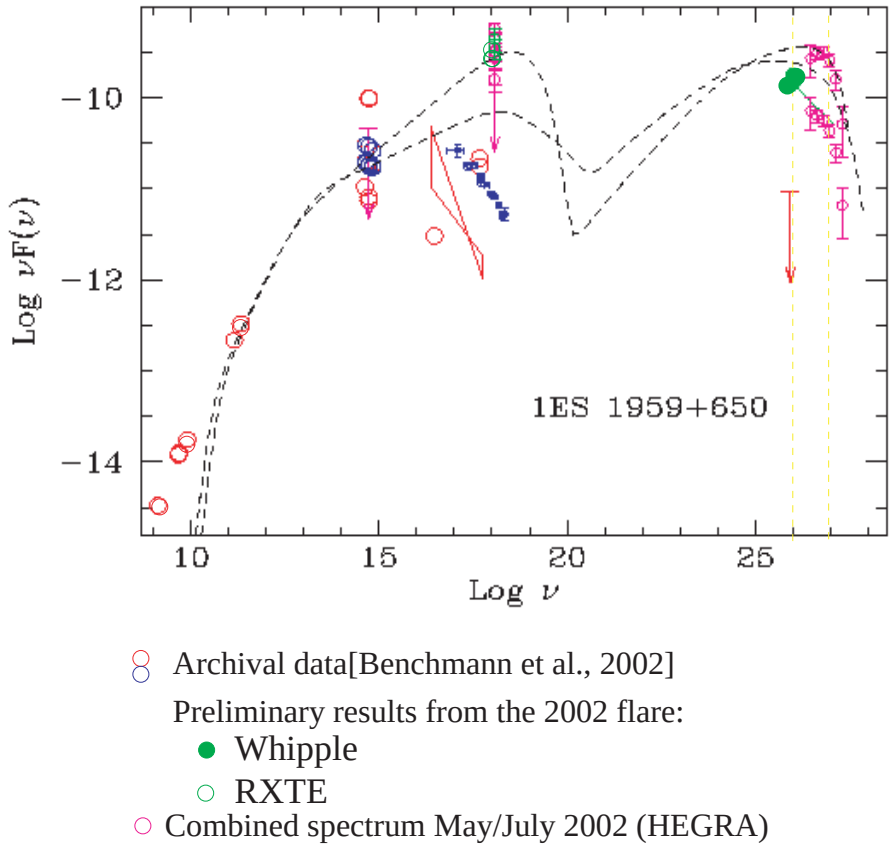

Figure 2.1: *SED of 1ES1959 with data at TeV energies recorded during the period of the 2002 flare and the low state reported by the HEGRA System. The black lines represent the predictions of the SSC model. Taken from [74].*

ing intensities is linked to the X-ray such that this intensity changes only with the square root of the TeV intensity. In addition, there is a strong correlation between the magnetic field and the intensities and slopes of the synchrotron and IC emissions.

A very interesting multi-wavelength campaign was carried out in 2002, during the period of major γ-ray activity and variability [78]. The results of the campaign will be compared and discussed together with the results of the analysis presented in this work (chapter 9).

2.3.1 The EGRET tentative detection

The Energetic Gamma Ray Experiment Telescope (EGRET) on board the Compton Gamma Ray Observatory, provided γ-ray observations from 20 MeV to 30 GeV during the years 1991 to 2000.

According to some papers (for example [79]), 1ES1959 is present in the third EGRET catalog with an average measured flux of 1.8×10^{-7} γ cm^{-2} s^{-1} for $E > 100$ MeV.

In contradiction, in the third EGRET catalog there is no source detected in the sky position inside the radius of confidence for 1ES1959. For this reason, some authors do not consider 1ES1959 as an EGRET source.

The non-detection in the energy range covered by EGRET, makes the study of the spectral distribution of the AGN even more interesting, supposing that the expected minimum between the synchrotron and the inverse Compton peaks would occur somewhere in that energy interval. The same happened to another well known TeV blazar, the AGN Mkn 501.

2.3.2 Studies of radio emission

1ES1959 was first observed in the 4.85 GHz survey with the 91 m NRAO Green Bank Telescope [80, 81]. Very Large Baseline Interferometry radio observations played a major role in understanding the different features of the central engine of the AGN.

The observation of the jet at radio frequencies is important to have an additional constraint to the model parameters describing the TeV blazars jet properties related to the emission of VHE γ-rays.

Interferometric observations have measured the jet's internal motions in AGNs with apparent superluminal velocities[3]. This is commonly related to the production of the VHE γ-rays, due to the presence of ultra-relativistic particles at sub-parsec scales. Radio measurement of AGN jets can constrain the Lorentz factor, the angle of the jet with respect to the observer line-of-sight and the jet opening angle.

The radio properties of the jets of AGN 1ES1959 have been studied with a series of 15GHz Very Long Baseline Array (VLBA) observations of the parsec-scale jet [82] (see figure 2.2). From observations of 1ES1959 at 5-15 GHz carried out in 1999 and 2000, no strong indications of the presence of a counterjet could be seen, the most plausible explanation being a very good alignment of the jet to the line of sight. Studies of possible motions inside the jet revealed a smooth decay of the jet profile. The VLBI studies of the core properties gave no indications of strong beaming emissions. The studies related to the apparent jet speed seems to be mostly subluminal. The VLBI measure gave only a lower limit consistent with no-motion (stationary components), due to the short exposure and relatively high redshift. The lack of superluminal components in the jet is puzzling, since this is considered a necessary condition for VHE γ-ray emission. One possible explanation is the very

[3]Such a physical paradox can be explained through models which imply a geometrical effect of relativistic motions of blobs of plasma towards the observer. When these blobs move with velocities close to the speed of light at small angles with respect to the observer's line-of-sight their brightness undergoes a process called *apparent enhancement*. For very small angles and very high blob speeds this process can render the luminosity of the blob up to hundreds of times greater than the actual luminosity.

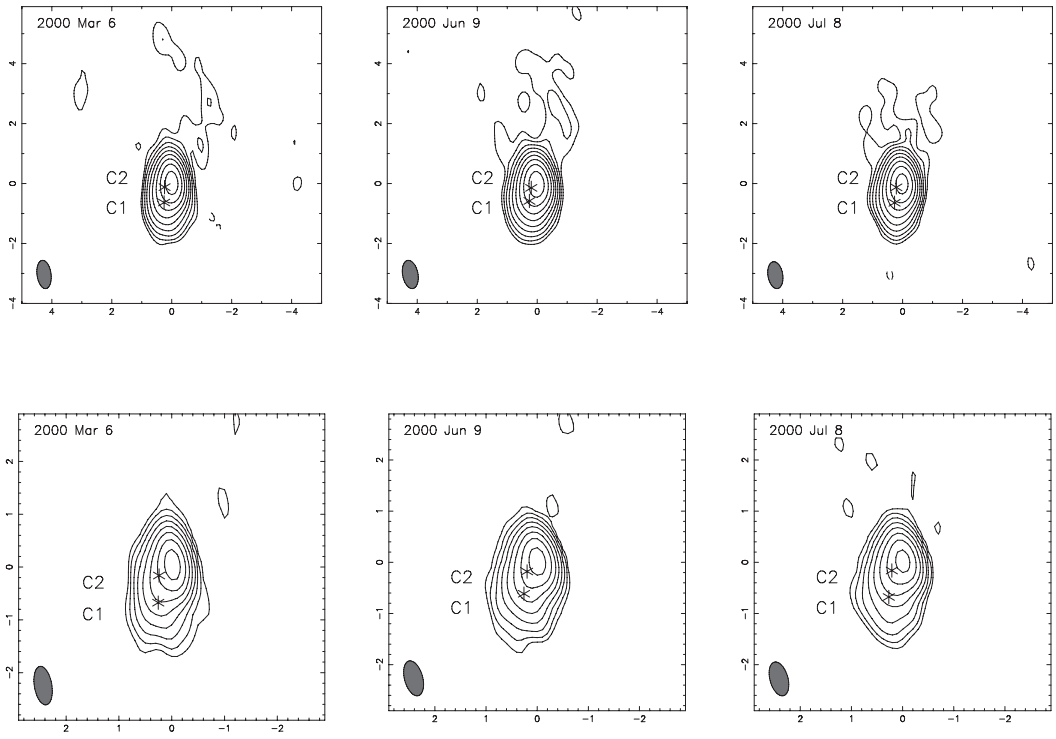

Figure 2.2: *VLBA radio images (15 GHz) of the parsec scale jet of 1ES1959+650, taken from [82]. The two rows show images obtained with different weightings, top: natural weighting (highest sensitivity, but low resolution), bottom: uniform weighting (low sensitivity, high resolution). Linear resolution:∼ 0.5 pc. Axes units are milliarcseconds (mas). Asteriscs represent the centers of the circular Gaussian fits, applied to the visibility data in order to identify any possible motions in the jet. The core is supposed to be the brightest, most compact and so the northernmost of the tree components of the image. The uniformly weighted images show a short jet, extending 1 mas to the south-east of the core. The naturally weighted images confirm the presence of the south-eastern jet, but in addition show a diffuse emission to the north of the core. The comparison with lower resolution images lead to the interpretation of a jet very close to the line of sight.*

small angle to the line of sight (0.8 deg), but the most favoured hypothesis considers the reduced bulk Lorentz factor between sub-parsec scale (highly relativistic and collimated, emitting TeV radiation) and parsec scale ($\Gamma \sim 2 \div 4$). At this scale the jet becomes also less collimated. This property puts new constrains to the jet models and new questions, such as the efficiency of models of shocks in the jet to reproduce the deceleration of the radio blobs observed in the jet.

2.3.3 Optical features of 1ES1959

Optical studies can give further information about the similarities and differences between AGNs. The study of 1ES1959 in the optical range is very interesting, due to the high variability of the emissions. The light of the jet is very strong; it is therefore not easy to observe the host galaxy.

In 1998 the Nordic Optical Telescope (La Palma) observed 1ES1959 for an exposition time of 990 s with excellent observational conditions (see figure 2.3). The astronomers found a complex host galaxy for 1ES1959 which may either be an elliptical galaxy with β=0.41 (significant deviation from a pure Vancouleurs law, used in the simulations), or an elliptical ($\beta = 0.25$) galaxy with an underlying disk [83].

Comparisons between optic and TeV emissions were carried out by the VERITAS collaboration.

During the May-July 2002 flare, 1ES1959 showed unusually faint optic activity compared to the light curves of previous years The magnitude and the variability were very dim [84].

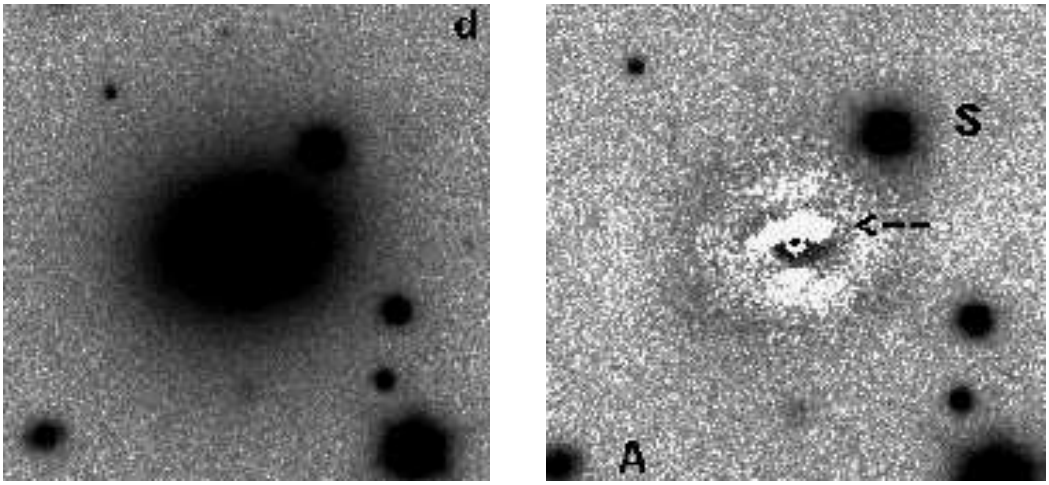

Figure 2.3: *Optical view of 1ES1959 (42"×42", 55×55 kpc). Data taken with the Nordic Optical Telescope (La Palma). The arrow indicates an absorption feature, about 1" to the north of the center, roughly oriented along the major axis of the galaxy in E-W direction. The closest galaxy is labeled with A (z= 0.048, 31 kpc far). None of the closest galaxies show signs of interaction with 1ES1959. Taken from [83].*

The Tuorla Observatory is working with the MAGIC collaboration with blazar optical monitoring, using the 60 cm KVA telescope on La Palma and the 1m telescope at Tuorla. The aim is to measure the variability properties of blazars and select possible interesting targets for follow-up studies, possibly involving also TeV observations. 1ES1959 is one of the targets of the project and data of the optical light curve since June 2002 is available[4].

2.3.4 Observations in the X-ray range

Confirmation of high X-ray emissions from 1ES1959 came with the Slew Survey performed by the Einstein-IPC X-ray detector [85]. The analysis of the X-ray activity of 1ES1959 showed periodic flare states, similar to the ones of Mkn501 [86].

The reports of the X-ray band observations carried out in 2000 with the USA and RXTE satellite detectors [87], permitted the study of source activity at different levels of activity.

The combined analysis of archival data from BeppoSAX (1997 data), USA and PCA satellite experiments show that in the X range (1-16 keV) the source spectrum is harder when the source is brighter. The X ray emission is most likely synchrotron radiation. Observations of the source in a flaring state indicates that the flux can double within a few days.

The magnetic field and the Lorentz factor Γ of radiating electrons were estimated from the variability of the spectrum. The magnetic field indicated a lower ($\sim$ mGauss) and a Γ factor being slightly higher ($\sim 10^7$) than the ones estimated from Mkn 421 data. The Doppler factor of the jet was estimated to be > 1.6[5].

The steady component of the X-ray emission may be due to bright knots in the relativistic jet, near the central engine and pointing very closely to our line of sight, with Lorentz factors of ~ 10.

In September 2001, 1ES1959 was observed with satellite BeppoSAX in the X-ray and optical bands during a period of high X-ray flux [79]. As is shown in light curves in figure 2.4, in X-rays the source was brighter than previously reported and the resulting spectrum harder, with the synchrotron peak moving to higher energies.

Simultaneous observations of TeV and X-rays during the period of the May-July 2002 flare were carried out. Studies of the spectra showed that the correlation in time was weak [84].

2.3.5 Previous TeV observations

On May 17th, 2002 the VERITAS collaboration reported a significant detection of VHE γ-rays range from 1ES1959, with an energy > 400GeV. The detection had

[4]See http://users.utu.fi/kani/1m/1ES1959+650 for the most recent lightcurve. The data are still preliminary and not published.

[5]The Doppler factor estimate from Mkn421 jet is not so precise and can be 1-10 in most estimates.

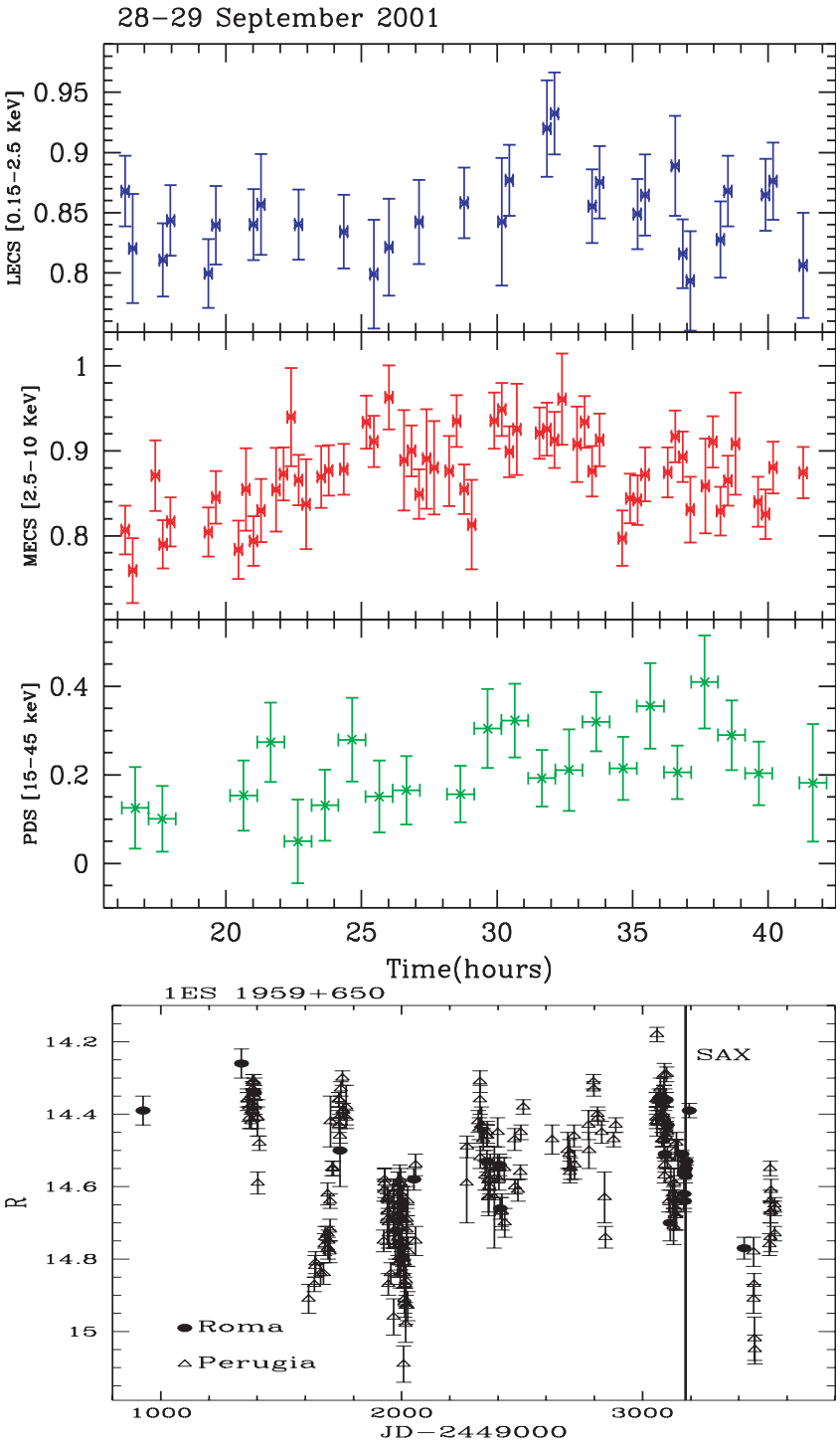

Figure 2.4: *Light curves of 1ES1959 taken between 28-29 September, 2001 with 3 instruments of the BeppoSAX satellite at different energy ranges. From top: [0.15-2.5keV] LECS 1000s binning, [2.5-10] keV MECS 1000s light curve, [15-45]keV PDS 3600s binned light curve. The bottom panel shows the optical R magnitude of 1ES1959 since August 1995. The vertical line indicates the period of the BeppoSAX observation. Taken from [79].*

a 13σ significance in 2 nights of observation. The rate doubled in the two nights of observation, reaching, at the end of the observation period, a maximum of 2.5 times the Crab flux. The preliminary analysis of the differential energy spectrum gave a slope index -2.4 ± 0.14 from 260 GeV to 5 TeV [76].

The detection and spectral features of 1ES1959 from Whipple observations in 2002 have been published, with a comparison between the flares with and without X-ray counterpart [88, 77].

The HEGRA collaboration observed 1ES1959 during 2000-2002 for 197.4 hours, using the CT System [74, 90, 91]. For ∼94 hours in 2000-2001 1ES1959 was found to be in low state. A signal at the significance level of 5.2σ was detected, for a mean flux $= 0.053 \pm 0.011$ Crab. The low state spectrum with a photon index of $\alpha = 3.18 \pm 0.17_{stat} \pm 0.08_{sys}$ was measured. During the May-July 2002 flaring time, they detected diurnal peak values of 1-2 times the flux from the Crab. The differential spectrum could be described with a power law and an exponential cut-off at $E_c = 4.2^{+0.8}_{-0.6} \pm 0.9$ TeV and a photon index of $1.83 \pm 0.15 \pm 0.08$.

The measurements with the Whipple telescope gave only an upper limit to the low state flux [88], to $1.3 \cdot 10^{-11}$ photons cm^{-2} s^{-1} above 350 GeV.

The 1ES1959 flux upper limit measured with CAT before 2002, when the source was not active, is $(4.1 \pm 0.9) \cdot 10^{-11}$ photons s^{-1} cm^{-2}, above 250 GeV [93].

Also the CAT (Cerenkov Array at Themis) detector observed 1ES1959 in 2002 with positive results [92, 93].

2.3.6 The *orphan flare* case and neutrino emissions

The June 2002 flare of 1ES1959 is the first clear and well documented case of a blazar that had a strong TeV emission without an X-ray counterpart. The observation of the orphan flare reported by Whipple collaboration stimulated the formulation of possible hadronic models to apply to 1ES1959.

A possible explanation of the phenomenon, with calculation of the physical parameters of the source can be found in [94]. The model, called hadronic synchrotron mirror model, correlates the fact that the orphan flare followed a TeV-X-ray correlated flare occurring briefly before. The first flare episode, of clear leptonic origin, would have produced the seeds soft photons. Ultrahigh energy protons would have scattered photons in a upward direction as they reentered the jet after reflecting off of a mirror cloud at a few pc from the central engine.

In principle, normal hadronic γ production via proton collision and subsequent π_0 decay is also possible (see section 1.1.2). This can be confirmed by neutrino detection, from the processes illustrated in equations 1.6 and 1.7. The possible hadronic scenario encourages the search for neutrinos which result from π^+ decay. The normal hadronic production model has a problem to explaining short flares, because proton acceleration is a slow process.

A recent calculation of the expected neutrino flux from 1ES1959 has been done in [95]. The AMANDA neutrino telescope detected two neutrinos spatially and temporally in coincident with 1ES1959 flares. The detection was not statistically

significant, however the authors conclude that a possible neutrino flux from proton-proton collisions in the jet of 1ES1959 is compatible with the observation of the AMANDA detector. According to their assumptions, the Lorentz factor of the jet should be close to $\Gamma \sim 1$ and the observed spectral index in good agreement with the HEGRA results. The estimates are however not fully conclusive: environmental conditions in the jet can have a big influence on the predicted neutrino flux.

2.4 Observational constraints of the data collected for this work

In my analysis I have considered data taken in 2002 with the HEGRA CT1 and the first data of MAGIC from 1ES1959 recorded in 2004.

Observations of 1ES1959 at TeV energies with the HEGRA CT1 telescope were carried out in 2002 and confirmed the high state of activity of the source. The result of the analysis of data taken will be presented in chapter 7.

The low threshold of MAGIC will allow us to study 1ES1959 during different states of source activity, especially during the low activity state. The study of the SED with a low energy threshold telescope can give information about the parameters of the emission model, on differences and similarities with other TeV blazars. The first hours of observation of 1ES1959 with MAGIC have been analyzed and compared with the Crab Nebula data and cosmic background (called also OFF) data, taken under the same zenith angle conditions, to be able to evaluate the performance of the telescope. The analysis will be presented in chapter 8.

Information about the position of 1ES1959 in the sky over La Palma and visibility are summarized in table 2.2.

Table 2.2: *Information about the sky position of 1ES1959 as seen from La Palma.*

Distance	z = 0.047
Position	RA 19h59m59.8s, Dec: +65°08m54s
Visibility from **El Roque de los Muchachos**	From April to November for 1650 hours per year (no moon).
Altitude above 45°	from May to October for 370 hours per year.

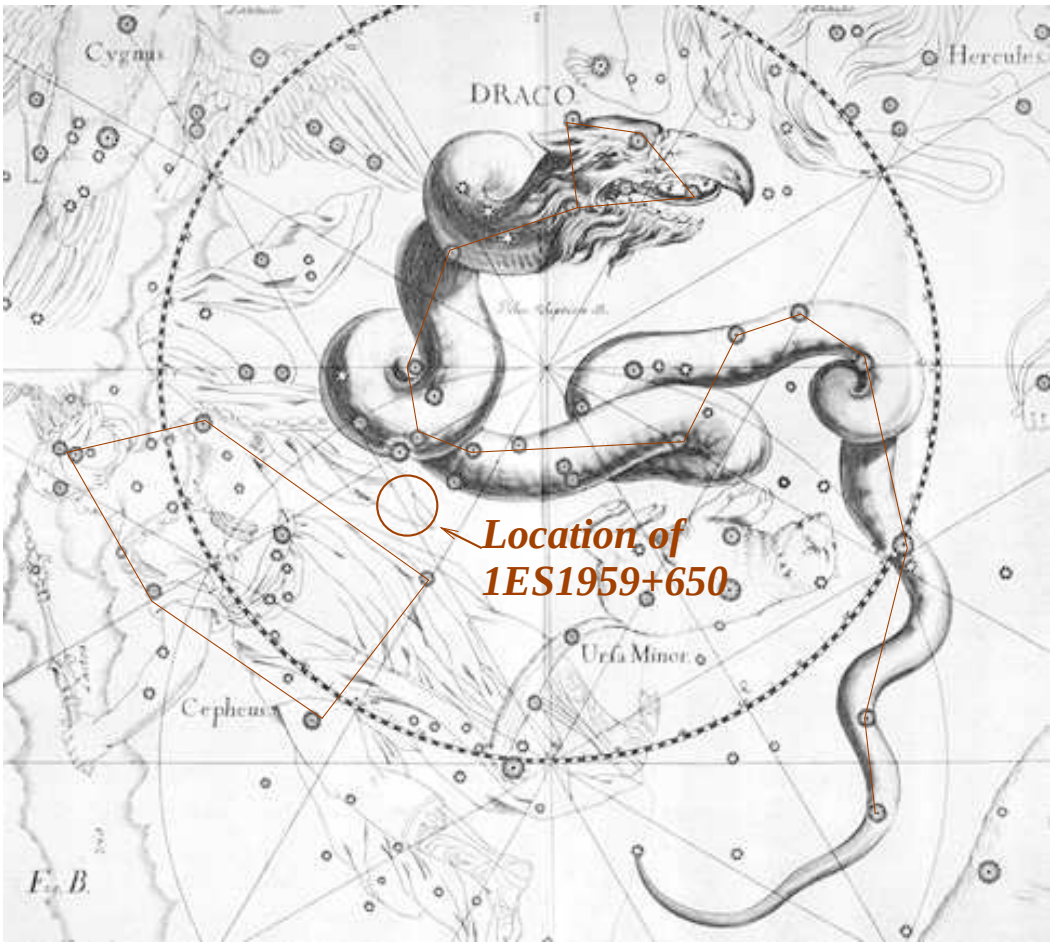

Figure 2.5: *1ES1959 is a galaxy between the constellations of Draco and Cepheus. It is a very faint galaxy discovered only in 1993. It is not included in the map by Johannes Hevelius: Draco, from Uranographia (1690) (*`http://chandra.harvard.edu/photo/constellations/draco.html`*). The superimposed brown circle indicates the approximate position of the source.*

Chapter 3

Cherenkov telescopes

In this thesis I present the results of my analysis of data taken with two different Cherenkov telescopes : HEGRA CT1 and MAGIC. They function basically on the same principle, but they were built in different epochs. Therefore they use different technologies. Here, I give a short description of the two telescopes and the technical details of these two instruments.

3.1 The HEGRA experiment on La Palma

The HEGRA experiment started in 1988 with a small scintillator array installed on the Canary Island La Palma (28.75° N, 17.89° W, 2225 m asl) by the Institut für Kernphysik of the University of Kiel. In the following years six other institutes from different countries joined and the detector was considerably enlarged. In 1997, the detector complex comprised 17 Geiger counters, 244 scintillator counters, 100 wide angle Cherenkov counters and 6 Cherenkov telescopes. Gradually, the experiment finished its operation because of rapid progress in technology. HEGRA CT1 was switched off at the beginning of 2003.

For this thesis, observations from only one of the HEGRA Cherenkov Telescopes have been used: this telescope is called CT1. It was operating as a stand-alone telescope, while the other HEGRA Cherenkov telescopes (CT2 to CT6) were operating in the so-called stereoscopic mode. CT2-CT6 were identical to each other, but differed from CT1 in many technical details[1]. In the following section CT1 will be described.

3.1.1 The HEGRA CT1 telescope

CT1 was the name of the first Cherenkov telescope of the HEGRA experiment. It was installed in 1992 at the Observatorio del Roque de los Muchachos and it

[1]The so-called CT-system denotes a set of 5 identical telescopes operating in stereoscopic mode. They were installed from 1993 and 1995 and they were dismounted in 2003. Their main features were: segmented glass mirror $\sim$8.5 m^2 and high resolution camera of 271 pixels and 4.9° FOV. For further technical details, see [96].

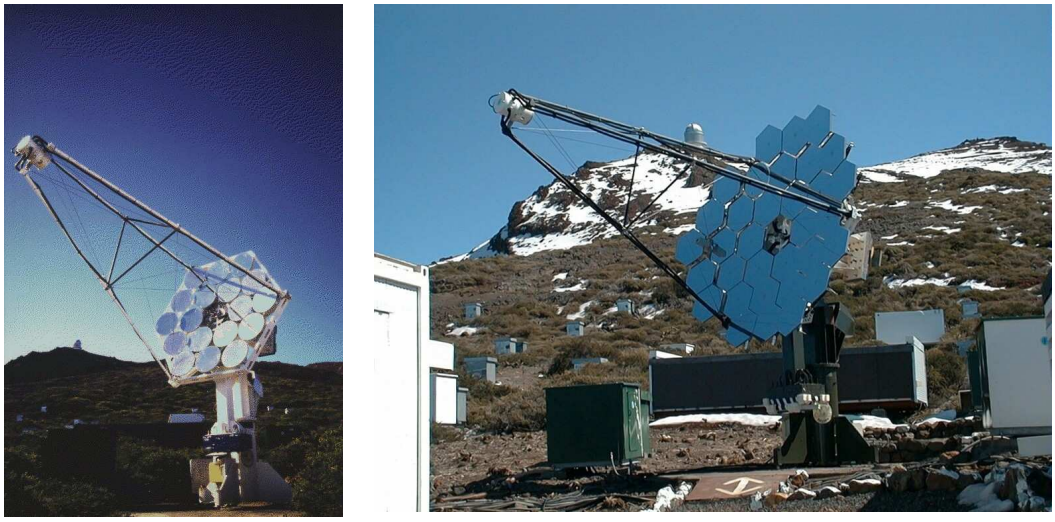

Figure 3.1: *Left: the original HEGRA CT1. Right: the same telscope after the upgrade of the mirror area.*

is sometimes referred to as the *prototype telescope* with respect to the so-called second generation HEGRA Cherenkov Telescopes (CT2-CT6). Originally, CT1 comprised a 5 m^2 segmented glass mirror and a 37 pixel camera with $\sim 3^\circ$ field of view (FOV) [97]. In December 1994 the camera was replaced by a higher resolution camera, with 127 pixels ($\sim 3^\circ$ FOV). In November 1997 the telescope was upgraded to ~ 10 m^2 mirror area using diamond-turned aluminum elements (figure 3.1). In its final configuration, the telescope has a threshold of about 750 GeV (at z.a. 0°). In contrast to most Cherenkov telescopes it has an equatorial mount instead of an alt-azimuth mount like the telescopes of the HEGRA-System and nearly all recently built telescopes worldwide. The motivations for an equatorial mount were:

- when tracking a source only one axis and one motor are necessay to rotate the telescope in order to counteract the rotation of the earth. This allows for a simplified steering;
- the FOV does not rotate with respect to the coordinate system of the sky. This simplifies the analysis and the simulations because bright stars always stay in the same position in the camera.

The disadvantages of equatorial mounts are:

- the aligment of the telescope axis with the earth's rotation axis is never perfect. This implies that the center of the camera does not always coincide with the coordinates of the pointed object, therefore data need a "pointing correction".
- heavy counterweights are needed to balance the structure. It requires a very stable and therefore expensive construction.

- the construction does, for practical reason, not allow access to the entire sky.

The technical details of the CT1 telescope are summarized in table 3.1.

Figure 3.2: *Left: the HEGRA site. Right: a view of MAGIC during construction on the HEGRA site.*

3.2 The MAGIC experiment

The Major Atmospheric Gamma ray Imaging Cherenkov (MAGIC) telescope is a new generation imaging air Cherenkov telescope designed for gamma ray astronomy in the energy range between 30 GeV and several TeV. The low threshold IACT project is the result of the collaboration between various institutes, some of which were already a part of the HEGRA collaboration. MAGIC is situated on the same observational site as the HEGRA experiment was. Data taking in the commissioning phase started in October 2003, with the observation of well established γ-ray sources, in order to have a full understanding of the telescope performance.

3.2.1 The MAGIC telescope: technical details

MAGIC incorporates many technological innovations so that it can fulfill the requirements imposed by the physics goals. The 17 m diameter tessellated reflector dish consists of 964 0.5×0.5 m^2 diamond milled aluminum reflecting elements. The parabolic reflector shape conserves the time structure of the Cherenkov pulses and allows the increase of the signal-to-noise ratio with respect to the night sky background. For a detailed description of the MAGIC reflector, see chapter 4.

Great care has been taken to reduce the overall weight of the telescope to allow for fast repositioning required for prompt reactions to GRB alerts. The telescope frame is made of light but stiff carbon fiber tubes and weighs less than 20 tons. The maximum repositioning time for a complete turnaround of the telescope has been measured to be 25 seconds at 70% of the maximum power of the motors. The design specification are 20 seconds at full power.

Table 3.1: *Technical details of the telescopes CT1 and MAGIC. (*) Currently the analysis of MAGIC data is restricted to 100 GeV.*

	HEGRA CT1	**MAGIC**
energy threshold(zenith)	∼750 GeV	∼50 GeV (classical PMTs)*
trigger rate at zenith	1.7 Hz	∼ 30-300 Hz
effective coll. area (0° z.a.)	few 10^4 m^2	few 10^4 m^2
f/d	1.7	1.05
mount type	equatorial	alt-azimutal
tracking error	0.03°	0.025°
pointing error	< 0.13°	0.05°
reflector shape	Davis-Cotton (spherical)	parabolic profile
mirror element shape	hexagonal	squared
mirror element surface	spherical	spherical
material	Al sandwich	Al sandwich,
	and protected by SiO_2	SiO_2 coated
diameter	60 cm	50 cm (side)
n. of mirror elements	34	964
mirror area	∼ 10 m^2	∼ 240 m^2
focal length	4.9 m	17 m
angular resolution	20 - 40 arcsec	0.1°
reflectivity	84%	85%
camera FOV	3.0°	3.5°
number of pixels	127	577
PMT type	10-stage EMI-9083A	6-stage ET 9116, 9117
quantum efficiency	26% at 375nm	∼30% with special coating
light cone	hollow Winston cones	hollow Winston cones
pixel diameter	0.25° (21mm)	inner: 0.1° outer: 0.2°
trigger condition	2/127neighbors	4 next-neighbors
		close-compact
	with signal ≥ 50mV in 13ns	with signal ≥ 4mV in 5ns
Digitization	CAMAC ADCs, 30 ns gate	300 MHz FADCs
dead time	2.5 ms	< 1 ms

The 3.5° field of view (FOV) camera is equipped with 576 photomultipliers (PMTs) of enhanced quantum efficiency. The inner section of the FOV is composed of 396 PMTs of 0.1° FOV surrounded by 180 0.2° FOV PMTs. The quantum efficiency is enhanced up to 20% by using a diffuse scattering, wavelength shifting coating which also extends the sensitivity to the ultra-violet (UV) range. A light collector allows the photon trajectory to pass often twice the hemispherical semitransparent photocathode.

In figure 6.1 a schematic description of the elements of the MAGIC hardware responsible for signal acquisition and digitization is given. The analog PMT signals are transferred via 162 m long optical fibers from the telescope camera to the counting house. The PMT signals are connected to the optical fibers using Vertical Cavity Surface Emitting Lasers (VCSELs).

In the electronics room, the signals are converted back and split. One branch is sent to a software adjustable threshold discriminator which generates a digital signal for the trigger system. In the other branch, the pulses are stretched to 6 ns and again split into a high and low gain channel. The high gain signal is amplified by a factor 10 while the low gain signal is delayed by 55 ns before it is merged again with the high gain signal using a fast GaAs analog switch. The combined signal is then digitized by a 8 bit 300 MHz Flash ADC. This method allows us to increase the dynamic range to $\sim$ 10 bits.

The trigger decision is generated by a 2-level system using the digital trigger signals generated by the 325 innermost camera pixels. The level-1 trigger is a fast next neighbor coincidence logic. The second level performs more complex topological filter algorithms.

The technical details of MAGIC compared with the previous generation telescope CT1 are summarized in table 3.1.

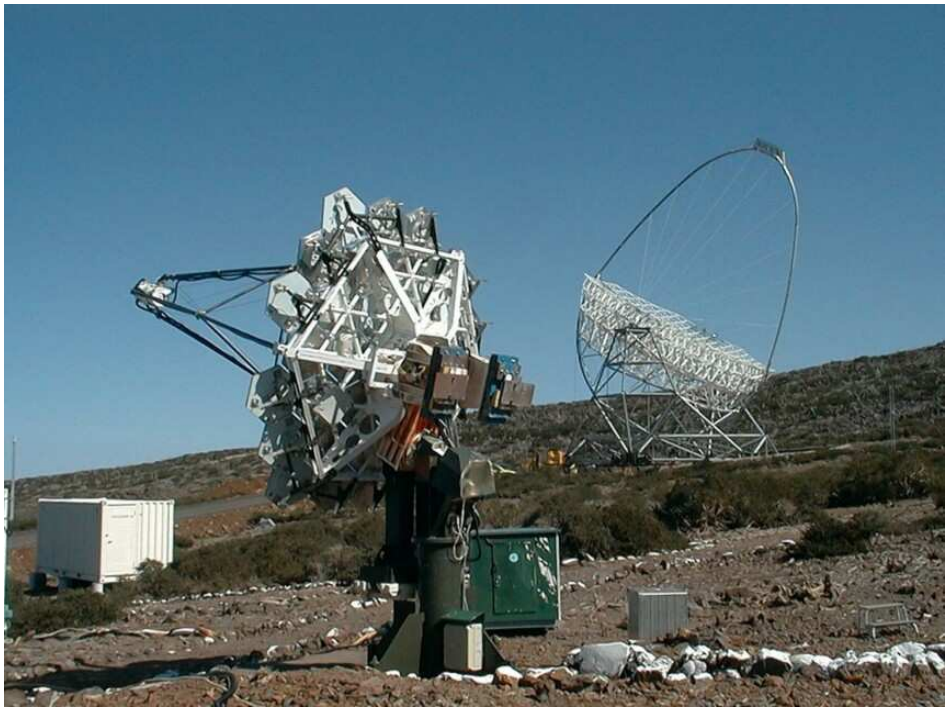

Figure 3.3: *The HEGRA CT1 telescope and MAGIC in construction in the background.*

Chapter 4

The reflector of the MAGIC telescope

Part of my Ph.D. work was spent on the production and the installation of the MAGIC reflector (figure 4.1). The structure and the characteristics of the mirror elements used for the reflector of the MAGIC telescope will be described here. I will describe the studies done to optimize the characteristics of the whole surface, with measurements of the effective radius of curvature and focusing power of each single mirror element. Some specific tests have been done in order to check the performances of the produced pieces and guide the next production.

4.1 Introduction

Round glass mirrors have been used in nearly all Cherenkov telescopes. The imaging performances of IACTs are modest compared to astronomical telescopes, but the reflecting system should be sensitive to very small light intensities. The reflector is a key element of a IACT and it represents a non-negligible percentage of the final cost.

The large reflecting surfaces needed for the imaging of atmospheric showers, the optical quality required and the cost are the reasons that IACTs have a reflector composed of a mosaic of smaller elements. Usually, glass mirror elements of nearly identical radius have been used to simplify the production. The elements then compose a spherical reflector. When f/d>1.5 and a small overall mirror diameter is used, the time dispersion of the Cherenkov light flashes can be neglected. In very large telescopes the arrival time dispersion induced by a spherical reflector can be quite large compared to the intrinsic shower light flash duration. In addition, glass mirrors are quite heavy and they need to be supported by a very stiff, heavy frame.

For the design of the reflecting surface of the MAGIC telescope for the study of VHE γ-rays, the following goals were taken into account.

- The study of short term phenomena (for example Gamma Ray Bursts) needs

a fast repositioning of the telescope. It is therefore necessary to limit the inertial momentum of the moving part of the telescope, with a lightweight structure.

- The detection of atmospheric showers initiated by low energy CR particles requires the maximization of the number of collected Cherenkov photons, with a large mirror surface.

- The fast development of showers in the atmosphere needs the minimization of the instrumental contribution to the time spread of the arrival time of Cherenkov photons, with a parabolic (= isochronous) mirror profile. The time spread of Cherenkov photons depends on the primary particle energy and nature.

Figure 4.1: *The MAGIC telescope in October 2003 (about 5% of the mirror elements is still missing).*

For these reasons, and after the experience of the aluminum mirror elements installed in the HEGRA CT1 (November 1997), the MAGIC collaboration decided to develop and adopt for the MAGIC design the following choices:

- the reflecting surface is a tessellated mirror. The total mirror area of the reflector is about 236 m^2, the largest mirror ever built for this kind of instrument;

- the mirror segments are aluminum sandwiches with diamond-milled surfaces,

with a high reflectivity and optimum optical quality. The lightweight sandwich construction ensures stiffness and low weight;

- the optical quality of the mirror elements is such that the point spread function (PSF) of the reflector, i.e. the light spot, is much smaller than a camera pixel. The diamond turned mirror elements have different radii, for the production of a reflector with parabolic mirror profile;

- the heating system integrated in the elements structure prevents dew deposition and/or icing during operation. Winters in the Roque de los Muchachos observatory can be characterized by periods of snow, with occasionally formation of thick layers of ice in the structures, that can damage the mirrors (in addition to prevent observations).

The reflecting surface is approximated by a paraboloid with an octagonal shape. The focal length is 17 m, with $\langle F/D \rangle = 1.05$.

4.2 Structure of the mirrors

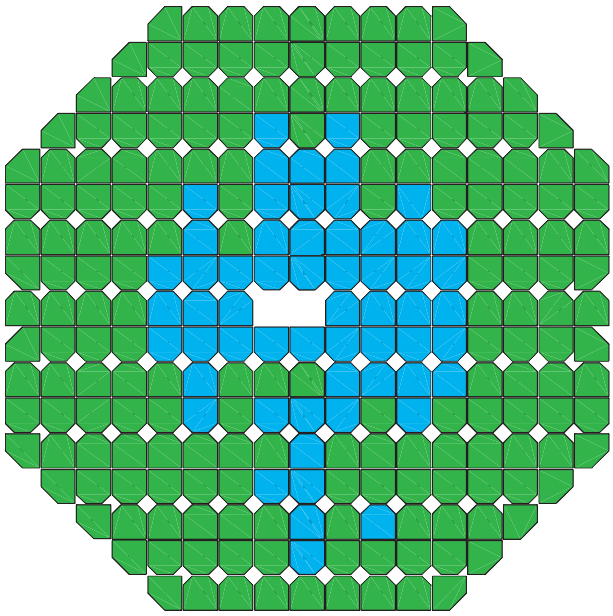

Figure 4.2: *The MAGIC telescope dish. In green: surface covered with mirrors made in Padua, in blue: surface covered with mirrors made in MPI Munich.*

The reflecting surface of the MAGIC Telescope consists of 964 mirrors with spherical surfaces. They were built in Padua, at the INFN Laboratories in Legnaro (70% of the total) and in Munich (the remaining 30%) at the workshop of the Max-Planck-Institut für Physik (see figure 4.2). The original design for the mirror elements comes from Munich. The first aluminum mirrors were tested and used for the HEGRA CT1. Important improvements in the production method were adopted in Padua. The description of the mirrors structure follows.

4.2.1 Munich mirrors (M)

The internal structure of the mirrors built in Munich is described in the MAGIC Proposal [98] and it is shown in figure 4.3. Each mirror element has a surface of 495×495 mm^2.

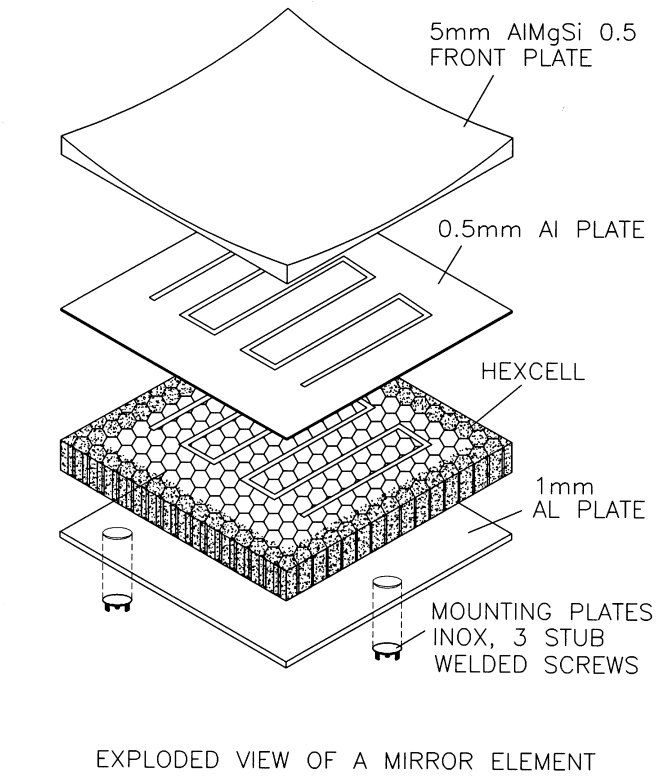

Figure 4.3: *Scheme of the internal structure of the mirrors built in Munich.*

The sandwich internal structure of the mirrors were constructed by two different companies: Euro-Composit in Luxemburg and Ederena-Concept in France. The sandwich sheets (HEXCELL panels) are made of AlMg3, glued with adhesive foils by Euro-Composit and with a spray glue by Ederena. Although the Euro-Composit panels were much stiffer and lighter, Eredena panels were bought and worked for economical reasons.

The enlarged view of a M mirror (figure 4.3) shows the site of an isolated heating wire. It is placed into a 5 mm wide channel milled into the top skin of the aluminum honey-comb structure.

The front surface plates are made of Al-alloys: AlMgSi0.5 or AlMgSi1.0. Most of the M mirrors have the AlMgSi0.5 alloy, which has a much higher corrosion resistance and a higher reflectivity compared to the AlMgSi1.0 alloy. The main

disadvantage of the AlMgSi0.5 alloy is the difficulty in machining the surface: the material is intrinsically harder and shows fine residual grooves from the diamond turning, resulting in some diffracting widening of the focal spot.

All front plates (both for Padua and Munich mirrors) were heat treated: for a few hours they were kept at $\sim 200°$C, to reduce the internal mechanical stresses.

The flatness of the frontal plate was tested and, when possible, mechanically corrected. About 5% of all plates could not be sufficiently corrected. The plates with best flatness were selected for the Padua production.

The plates were glued to the sandwich frame in the workshop of the MPI in Munich, with the following procedure.

- The corresponding surfaces to be glued, one of the aluminum plate and one of the sandwich body, were roughled with sand paper and cleaned to prepare them to stick (the Alu-skin of the Ederena cores is covered with an epoxi-primer).
- A two component glue (Araldite 420 A/B, 2:1 in volume) was spread on the surfaces with a rubber roller.
- The aluminum plate has been placed on top of the aluminum sandwich and an additional weight of 20 kg was uniformly distributed over the surface.
- After 3 days the glue reached its final strength.

The frontal plate was then pre-milled on a numerical controlled machine to produce the spherical shape to the surface. The precision was within 0.1 mm of the final curvature. Finally, the pre-machined mirror blanks were sent to the company for the diamond milling of the surface (see section 4.3).

4.2.2 Padua mirrors (P)

The internal structure of the mirrors built in Padua is shown in figure 4.4 and described here in detail. Data on the materials are listed in table 4.1.

Every single mirror has a squared shape 497×497 mm^2 and is 26-27 mm thick. The four corners of the mirrors are cut at 45 degrees (see figure 4.5).

The aluminum sandwiches were assembled in a facility of the INFN National Laboratories in Legnaro (Padua).

The honeycomb core structure is a 20 mm thick HEXCELL panel. At the four bottom corners, small aluminum blocks of $50 \times 50 \times 5$ mm^3 size are inserted in the honeycomb structure. They are used later to fix the mirrors on the support panel. The core is inserted into a 1 mm aluminum bottom skin, formed as a box.

The heating system is situated in the top layer, just under the frontal plate and consists of a printed circuit with embedded heating strips.

Some details of the P mirror structure are shown in figure 4.6.

The frontal surface is an AlMgSi1.0 alloy plate. After proper heat treatment, the plate is glued onto the sandwich body. The assembling and bonding, using 3M

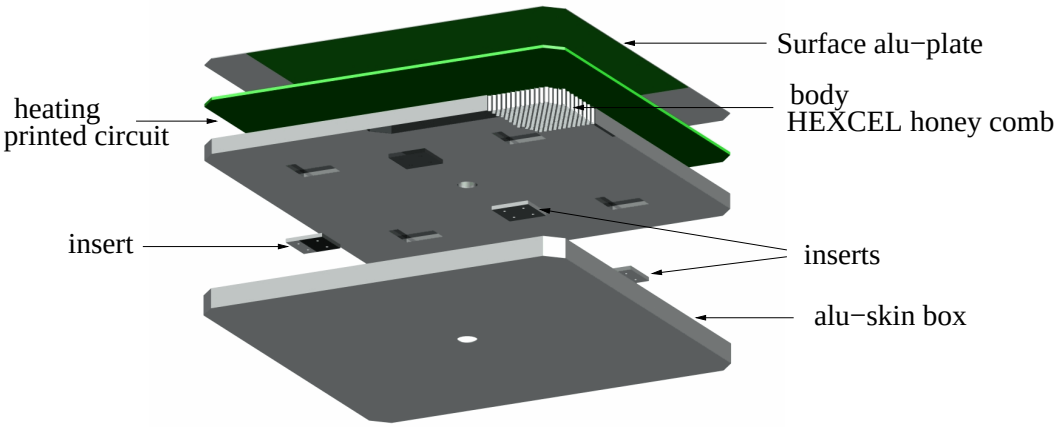

Figure 4.4: *Scheme of the internal structure of the mirrors built in Padua. The glue films are omitted in this figure.*

Scotch Weld adhesive, followed a technique adopted in the airline industry (Alenia), for the production of sandwich panels. In detail, the steps of the procedure are the following:

- the surfaces of the aluminum pieces are cleaned;

Table 4.1: *Technical details of the materials used to build the mirrors for MAGIC in Padua.*

Mirror part	Description
Boxes	Aluminum foil (Al 5754), adapted for cold deformations 1 mm thick, bended at the 4 sides
Honey-comb	HEXCEL composites: 5.2-1/4-003P-3003, Al panels, 20.7 mm thick
Glue	3M Scotch-Weld structural adhesive film AF-163 2K wt.06, specifics Boeing BMS 5-101 J Ty II
Upper plates	AlMgSi 1.0 F22, size :495x495 mm^2 ,tolerances to the required dimensions: +0.5/-0.3 mm thickness, $\pm$ 0.3 mm length, 0.5-1 mm flatness
Heating boards	Flexible foil of FR4 (*vetronite*), for the thermal coefficients: see *glass*), 0.3 mm thick, with two resistive circuits $\sim$ 42 Ω each, connected in parallel
Inserts	Al alloy (*anticorodal*)

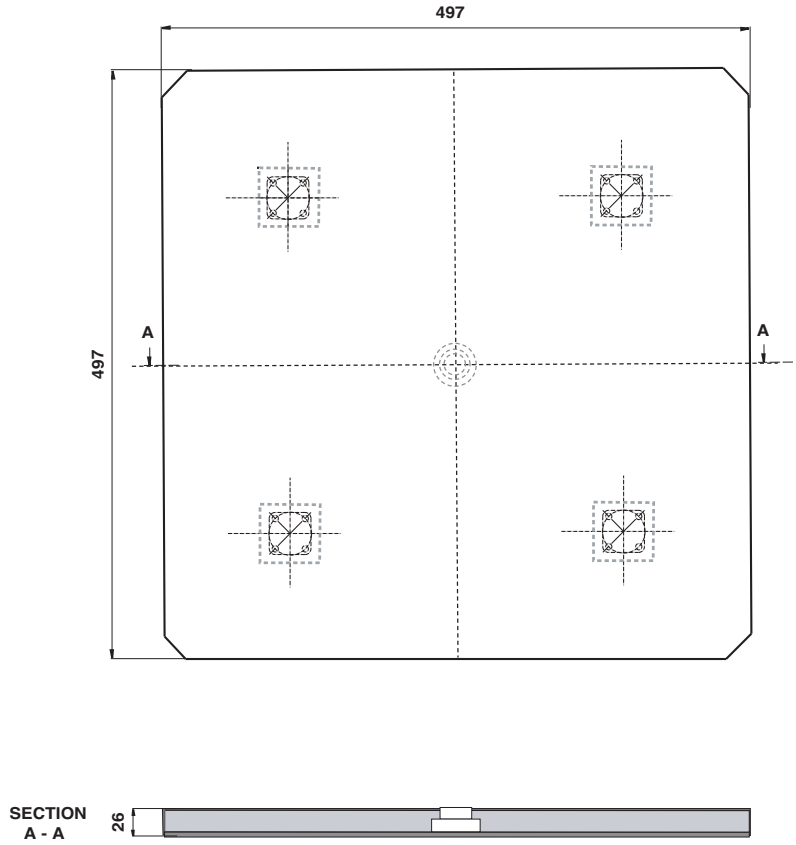

Figure 4.5: *Detailed design of a P mirror. The shape and the position of the inserts which fix the mirror to the panel structure, as well as the position of the connector to the heating card, can be seen.*

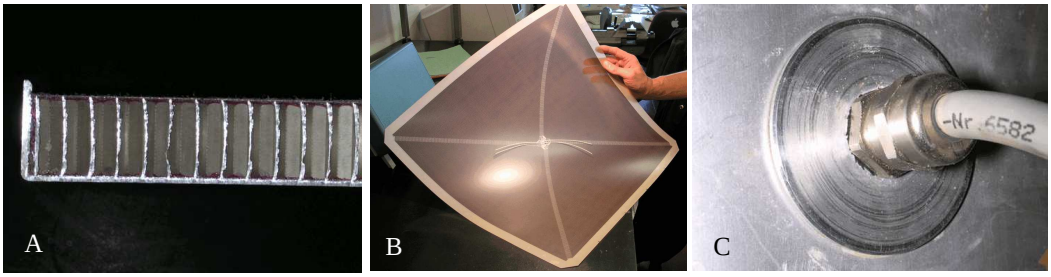

Figure 4.6: *Details of the structure of a P mirror. A: Cross section of a box and honeycomb. The upper aluminum plate is missing. B: The heating printed circuit. C: Enlarged view of the connector between the heating card and the outer cable, on the back side of the mirror.*

- the aluminum surfaces are treated with a primer;
- the mirror element components are assembled with glue film, to form the so-called raw blank;
- the raw blanks are put into a vacuum bag and placed in an autoclave;
- the thermal and pressure treatment for the glue reaction and bonding starts:
  - the thermic and pressure cycle goes from 20°C to 120°C with steps of 2°C per minute, and from 1 to 3 bar during the same time;
  - the final conditions are kept for about 90 minutes;
  - the conditions of temperature and pressure are taken back to normal following the same steps.
- Finally they are removed from the autoclave.

The top surface of the blanks were pre-milled in Padua in order to produce a spherical shape of the required radius of curvature, using a high precision computer controlled milling machine.

The deviation from the flatness of the back side (opposite to the surface plate) of the raw blank is less than 1 mm, necessary for the correct placement and blocking in the diamond milling machine (see section 4.3).

4.3 The diamond milling procedure

The premachined mirror blanks were sent to the company LT ULTRA Precision Technology Gmbf in Aftholderberg (Germany) for the diamond turning.

Figure 4.7 shows the machine used to polish the blanks surface. The blanks were placed on a moving support, that slowly approaches the cutter device. The diamond cutter rotates with an inclined axis with respect to the mirror support, in order to reproduce the required radius of curvature. The large radii of curvature to be produced ($\sim$ 34-37 m, see figure 4.8) imply a very small inclination of the rotational axis of the tools and therefore a great precision in the positioning and fixing of the mirror in the support. To avoid mechanical stresses, this is done applying a thin layer of liquid soap, uniformly distributed on the mirror support. The mirror is then fixed in its position using wax.

4.3.1 Required specifications

The requirements for our milled mirrors were:

- accuracy of the required radius of curvature: $\pm$ 0.5%
- accuracy of the surfaces: 5 μm or better

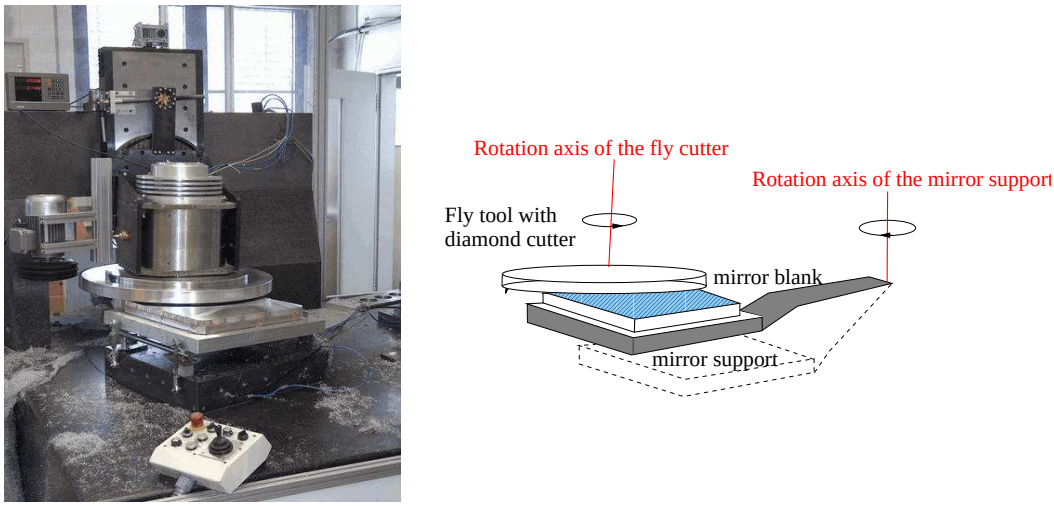

Figure 4.7: *The machine for the diamond milling of the mirrors at LT Ultra.*

- roughness of surface less than 20 nm RMS
- mean reflectivity greater than 90%
- 80% of the light of a source at infinity must stay within 5 mm ∅ at the focal spot.

After the diamond turning, all mirrors were checked to comply with the above listed specifications (see section 4.3.3 for the results of some measurements).

About 90% of all mirrors passed the acceptance criteria and were finally coated with a 200 nm layer of SiO_2 for surface protection. The protection layer is necessary because the telescope is not placed inside a protective dome. Based on the experience with the HEGRA CT1 mirrors, it is expected that the mirrors survive at least 5-7 years at the site. The coating was carried out by the Fraunhofer Institute for Material Research in Bremen (Germany).

4.3.2 Measurements of the effective radius of curvature of the mirrors

An apparatus (figure 4.9) for the measurement of the performances of the mirror elements was built in the INFN section of Padua. This instrument was used for testing the focusing power of the milled mirrors. At the same time, the effective radius of curvature is measured in order to select the best position of each mirror element in the dish.

Figure 4.9 shows the principle: a small structure, sliding on a track, hosts a screen and an ultra-bright blue LED (RS 235-9922) with angle of view of 15° and peak wavelength of 470 nm. They are kept at the same distance from the mirror

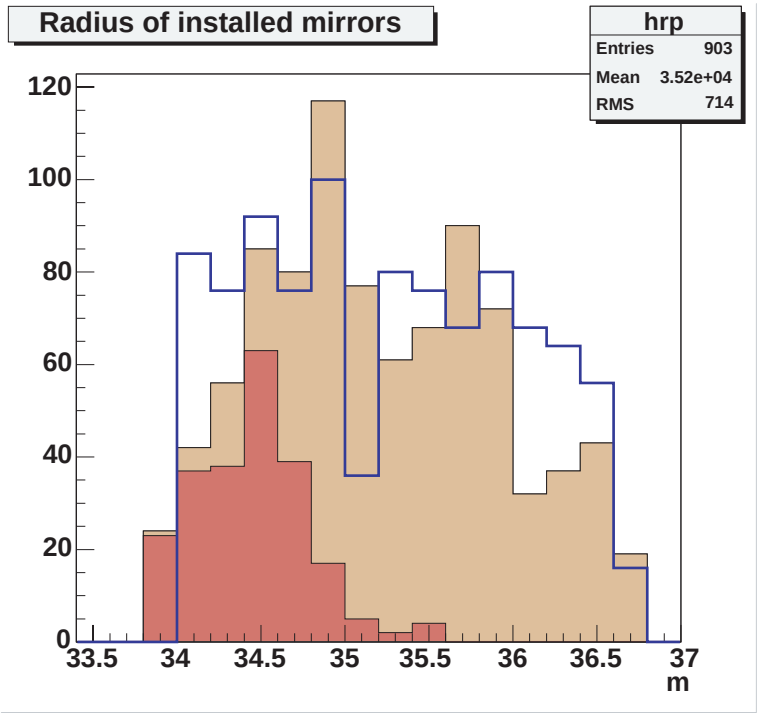

Figure 4.8: *Histograms showing the radius of the mirror elements produced for MAGIC. The dark distribution refers to mirror elements produced in Munich, the lighter colored distribution refers to the ones produced in Padua. The blue line demarks the distribution of the requested mirrors.*

and symmetrical with respect to its axis. The image of the LED, produced by the mirror under study on the screen, is recorded by a CCD camera (SBig ST5, 16 bits resolution), with a 10 nm interferometric filter (EDMUND OPTICS NT43-062), with the band-pass peak coinciding with the peak wavelength of the source (470 nm $\pm$ 2nm FWHM) also positioned on the sliding platform.

Moving the source-screen system, it is possible to find the distance to the mirror element where the minimum spot is produced. That distance corresponds to the radius of curvature of the spherical mirror element. The procedure used to take the image of the spot is:

- the LED is turned on and an image is grabbed, the time of exposure is 4 seconds;
- immediately after, the LED is turned off and a background image is taken (same exposure time);
- the images are transferred to a PC and analyzed with a C++ program, using ROOT [99].

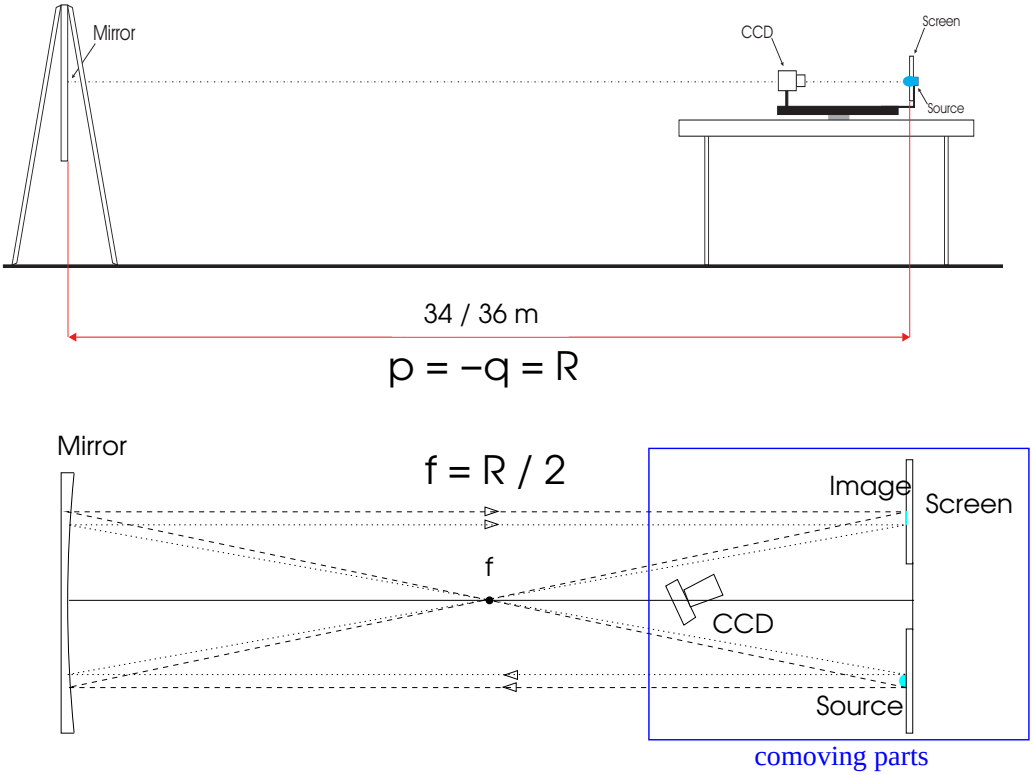

Figure 4.9: *Scheme of the apparatus and method used to measure the quality and radius of curvature of the mirror elements. The optical slide is at a distance equivalent to the nominal radius of the mirror. The source is an LED, that illuminates the mirror element. The image is focalized in the screen when the distance of the source is equal to the effective radius of the mirror element. The image is recorded by a CCD camera and analyzed.*

The procedure takes about 12 seconds and can also be done in presence of daylight. We first check the correct subtraction of the background from the spot image. If the difference of light values recorded by the CCD camera far from the spot in the 2 frames (image and background) is too big, the measurement must be repeated. We change the position of the source-screen system in steps of 10 cm. We determine the distance of the source-screen system from the mirror, where we record the minimum size of the reflected spot.

The light distribution around the center of gravity of the spot allows us to obtain its size (R_{90}) and thus derive the optical quality of the mirror element (see section 4.3.3). Figure 4.10 shows a sequence of pictures taken around the focal position, while measuring a mirror.

The production of the radii of curvature followed in first order the requirements given to reproduce the parabolic surface of the dish. Nevertheless, the precision of the machining could not be better than 0.5%. Therefore we measured the radius of each mirror element, in order to assign it to the best position in the parabolic dish.

4.3.3 Optical qualities of the mirror elements

The optical quality of each mirror element was evaluated during the measurement of the effective radius of curvature and by using the same instrument shown in figure 4.9. The result of the analysis is summarized with graphs and tables, as shown in figure 4.11.

The most important parameter checked was the radius of the circle that collects the 90% of the light grabbed by the CCD. This value is called R_{90}. The requirement is that the 90% of the light reflected by a mirror from a source at infinite is collected in an area smaller than a small pixel of the MAGIC camera, i.e. R_{90} <1.27 cm.

With the selected quality criterium, the light coming from very far (for example from stars) is concentrated in a single pixel. In this case, it will be easier to recognize the pixel affected by light from stars and thus reduce the number of noisy pixels (in the trigger or in the analysis). The good focusing power (small point spread function) is also necessary to record showers initiated by low energy particles, thus it is possible to lower the energy threshold of the Cherenkov telescope.

4.4 Tests of quality on mirror elements

All the mirrors installed in the telescope fulfilled our quality requirements. Each of them produces a spot from a source at infinite that covers about one quarter of the small MAGIC pixel area. However, the mirror elements produced in Munich show a systematically worse quality with respect to the mirror elements produced in Padua (see figure 4.12). The causes must be found in the combination of the used alloys, the mechanical structure and the diamond milling technique.

- The alloy AlMgSi0.5, used in M mirrors, gives higher reflectivity and it is much more corrosion resistent but much harder to machine. The original

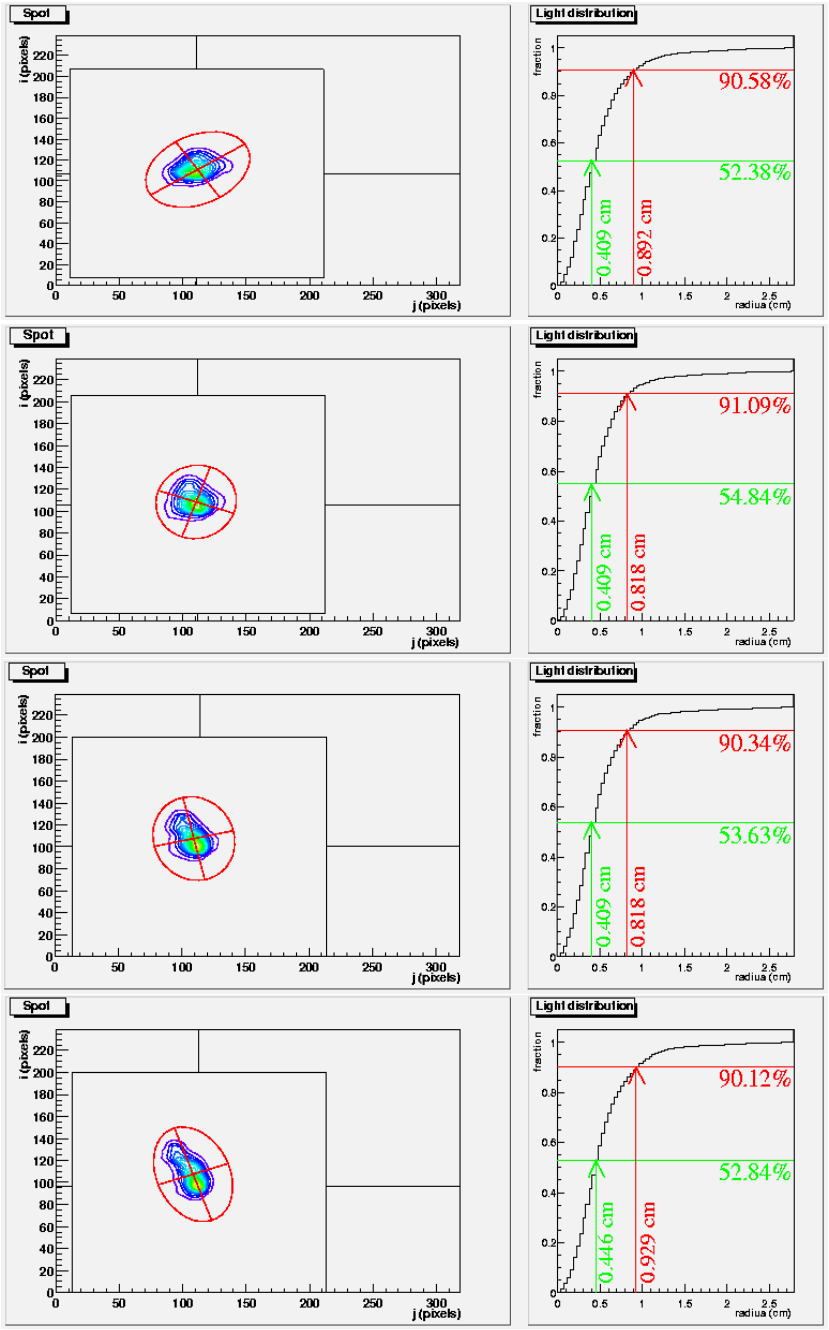

Figure 4.10: *Sequence of pictures of spots taken around the focal position of a mirror. Left:Histograms of the integral light distribution from the image center of gravity, for the calculation of the R_{90}, in red, and the R_{50}, in green.*

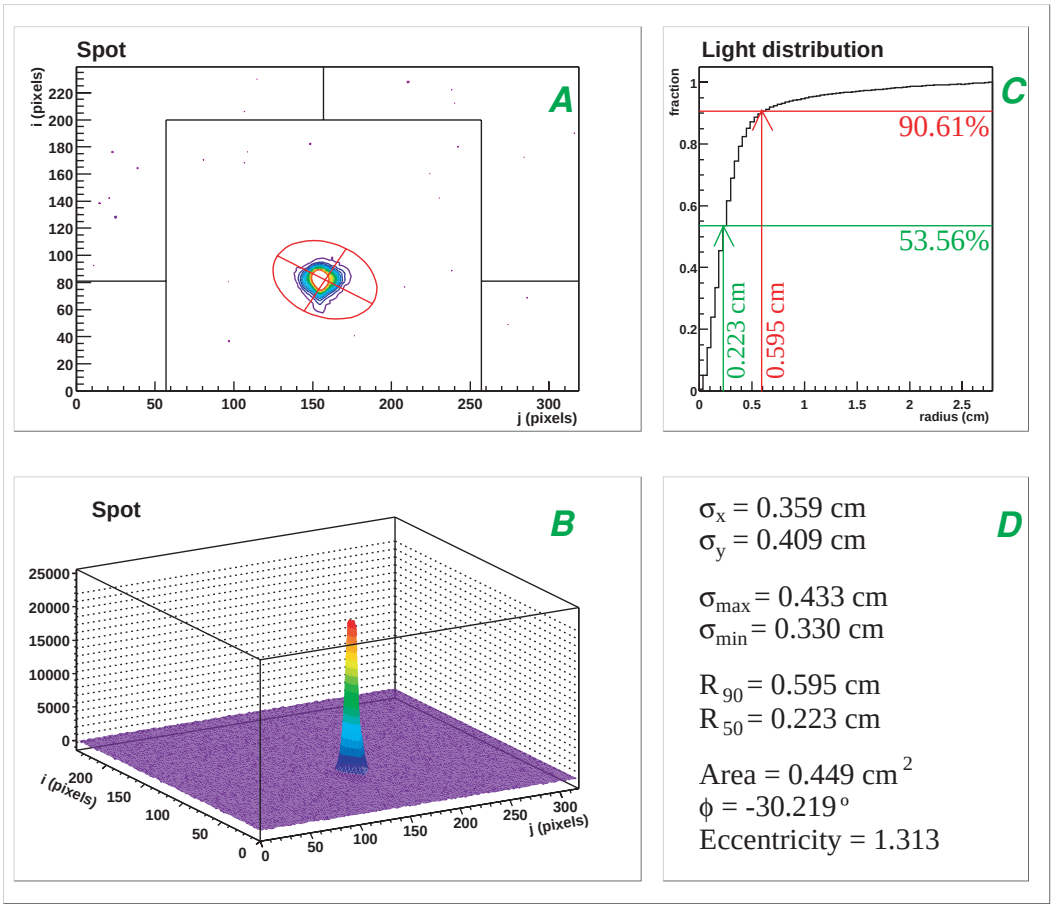

Figure 4.11: *Online graphs and tables summarizing the optical quality of the measured mirror element: example of a P mirror (serial number n071). The measurement was taken near the focal position. The graphs show the characteristics of the reflected spot, grabbed by the CCD camera. A: the 2-dimensional distribution of the light in the spot and, in red, the ellipse used to parameterize it (the major axis σ_{max} and minor axis σ_{min} of the fitting ellipse are multiplied by 3 and then plotted to better visualize it), B: the 3-dimensional distribution of light in the spot, C: the amount of light collected around the center of gravity of the spot, as a function of the radius of the circle whose center is the image center of gravity. D: Table that summarizes numerically some of the characteristics of the spot and of the ellipse that parameterize it. The value used to judge the quality of the mirror is the R_{90}, as explained in the text. This mirror, with its R_{90} of 6 mm, fulfilled our requirements of focusing and it was therefore possible to decide immediately after the measurement of its radius of curvature, the best position to assign to it in the telescope frame.*

mirror design used this alloy, but later the company that produced the mirrors' surface recommended switching to AlMgSi1.0, which is much easier to machine. It has a worse reflectivity and worse corrosion resistance. For the final production, 250 plates of AlMgSi0.5 were used for the M mirrors, while for the P mirrors the AlMgSi1.0 alloy was used. We checked the hardness of the alu-plates of some mirrors, as described in section 4.4.1.

- The two kinds of mirror have a different mechanical structure: the main differences are that in P mirrors the honeycomb structure is inserted in an aluminum box, and the heating system is embedded in a *vetronite* foil. The M mirrors are not contained in a box and their heating circuit is in aluminum. Additional mechanical stresses are therefore expected for the P mirrors. A test of the gluing procedure was done using a P mirror, that underwent some deformations after it was exposed in the telescope frame for some months (description in section 4.4.2).

- The different mechanical properties of the mirrors and the chemical compos-

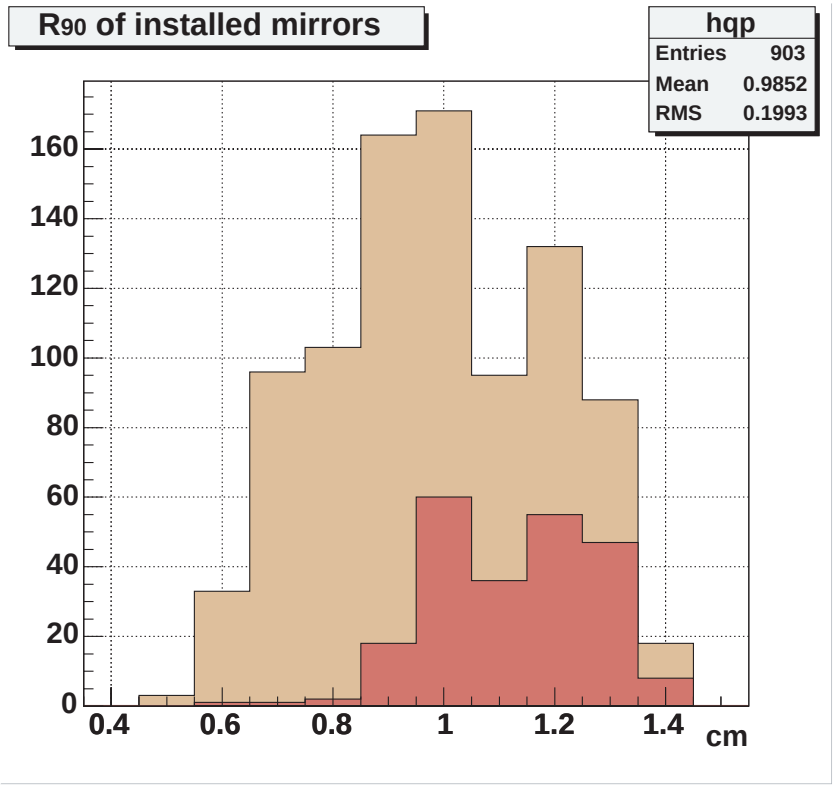

Figure 4.12: *Histogram showing the R_{90} values of the mirror elements produced for MAGIC. The dark distribution refers to mirror elements produced in Munich, the lighter colored distribution refers to the ones produced in Padua.*

ition of the plates influenced the quality of the machining. The microscope analysis of the mirrors surface after the machining and results of the scan of the surfaces will be presented in section 4.4.3.

The tests to check and compare the performances of the two approaches will be shortly described in the following.

4.4.1 Test on hardness of alu-plates alloys

Two different kinds of alu-plates have been used to produce the mirrors for MAGIC. The hardness of the upper aluminum plate was checked for P and M mirrors and compared. Only 3 M mirrors of low quality were compared with a standard P mirror. This test was performed in the MPI workshop, by hitting the plate with a steel sphere with a predefined force. The difference in hardness could be derived from the diameter produced from the sphere. The P mirror showed a bigger diameter (3mm) with respect to the M mirrors (2.2-2.5mm). It corresponds to a difference in absorbed pressure of about 50%; that means that the aluminum plates of the P mirrors are less rigid than those of the M ones. The hardness and alloy crystalline structure, as well as the chemical composition, has some influence on the milling procedure, since the tool in contact with the surface applies a small pressure to the surface of the mirror. With the P mirrors it was possible to reach a better focal quality, as shown in figure 4.12.

4.4.2 Test of the gluing procedure

Some P mirror elements showed a defect in the gluing of the upper aluminum plate. One of them has been cut and analyzed in the workshop of the University of Padua (see figure 4.6/A). The analysis of the glue showed that the process of fixing was correct in all the parts of the mirror (heating card, aluminum parts). The upper plate, that did not show any sign of gluing, was found to be a plate with a wax coated surface, and because of this, it was not sticking to the glue. The plate was accidentally introduced without surface cleaning in the production chain.

4.4.3 Analysis of the mirror element surface

Figure 4.13 shows the results of a measurement of roughness and reflectivity for a P coated mirror. The measurements were performed in the workshop of the University of Padua. The surface of the mirrors built in Padua resulted to be of good quality, with a reflectivity higher than 80% at all wave-lengths and a roughness of only $\sim$ 4 nm.

We analyzed the surface of an uncoated M and a coated P mirror with a microscope (see figure 4.14 and figure 4.15). While the M mirror showed signs of the diamond tool, we could not find any structure on the surface of the P mirror. The reason is likely the different hardness of the alloys used.

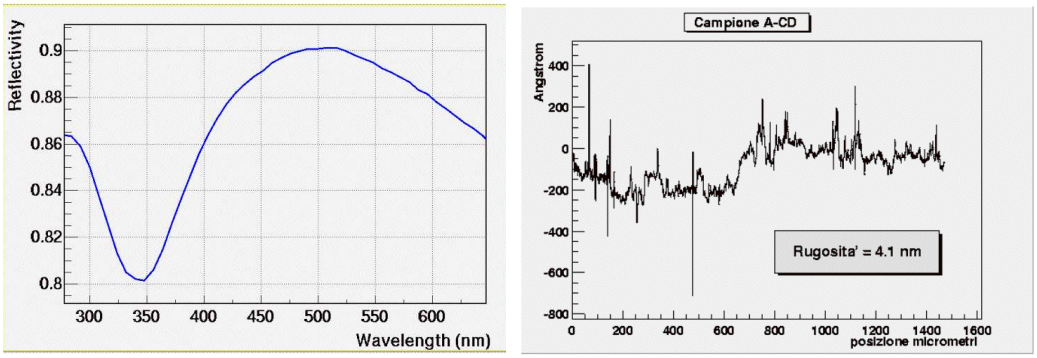

Figure 4.13: *Results of tests made in Padua to check the reflectivity and the roughness of coated mirror elements. The reflectivity is above 80% for every wavelength. The drop around 350 nm is an interference effect. The roughness (rugosità) is around 4 nm.*

The surface of an uncoated M mirror was scanned with a special 3D measuring machine (WENZEL LH 1210) in order to check if the surface imperfections had any relation to the internal structure of the blank (holes for screws, heating channel, ...). The same test was done for a P mirror of normal quality, after the coating procedure.

The mirrors were scanned along X and Y directions in steps of 2 cm. Figure 4.16 and 4.17 (top histograms) show the Z coordinate (left histogram) and their deviation from the spherical shape (right histogram). In the lower histograms of figure 4.16 and 4.17 we show the deviation from the spherical curve for the central X and Y scan lines. The M mirror shows a slight deviation in the center and the corners.

Results of a finer scan along 3 lines in X and Y directions are shown in figure 4.18 and 4.19. The mirror elements were scanned in 2 mm steps, at 17.5 mm from the borders and in the middle, in lines 230 mm apart from each other. We interpolated the measured points with circles. The parameters of the fit are not fixed, such that the radius of the fitting circle can be different from line to line. In this way, local systematic deviations should be found independently from the parameters of the global fit.

The M mirror shows, at the borders, systematic negative differences between measured value and fit circle. The scan in the center of the mirror reveals the presence of a pronounced deviation ($\sim$ 3 μm deep). These are the more likely reasons for the worse quality of the M mirrors. The P mirror scan does not show such strong systematic depressions at the borders. No hole in the center is visible. Deviations are confined on average to around $\pm$ 2 μm.

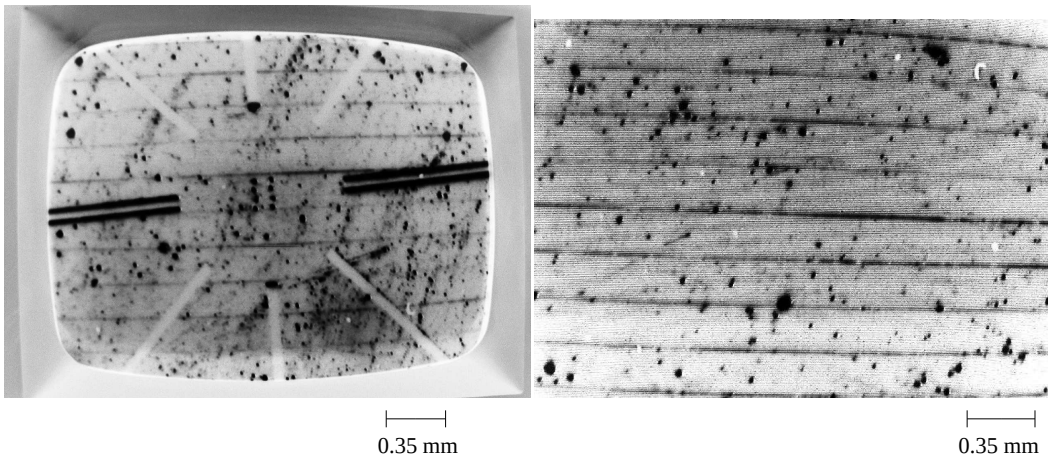

Figure 4.14: *A picture of a M mirror seen with the microscope (negative colors). The imperfections (spots) of the mirror surface are due to dust. The regular stripes are the result of the diamond milling procedure: it is possible to recognize the path of the diamond nail. The distance between 2 stripes is about 0.17 mm. On the left side: a piece of glass with small lines and dots at known distance from each other is overlaid to the mirror surface, as scale reference. On the right, the same picture, slightly enlarged and taken after removing from the mirror surface the glass with the reference lines, is shown.*

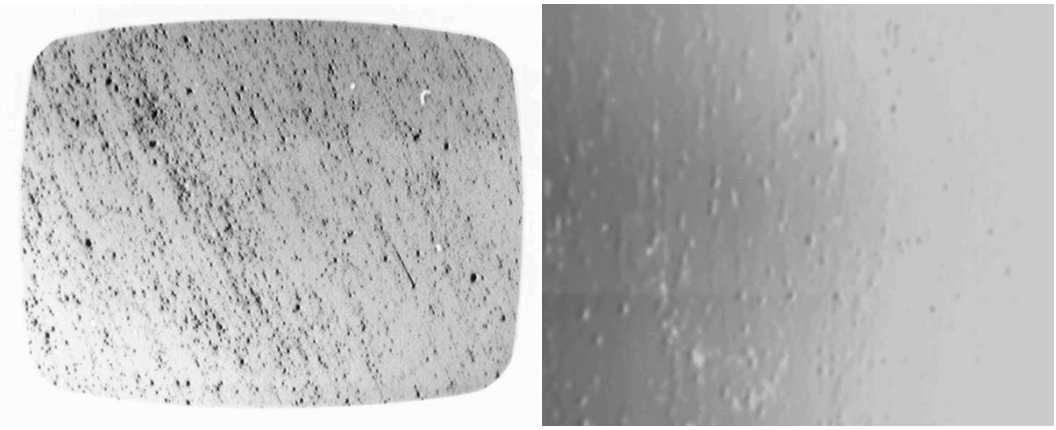

Figure 4.15: *A picture of a P mirror seen with the microscope (negative colors). The imperfections of the surface of the mirrors are due to dust. It was not possible to find and see the regularly striped structure present in the M mirror. On the right side, the surface of the mirror is shown with a different illumination.*

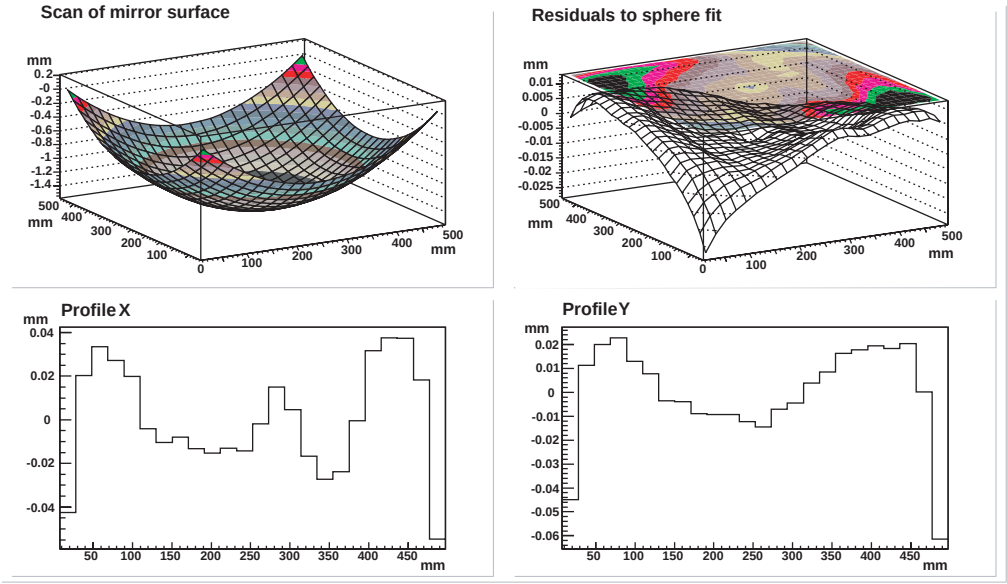

Figure 4.16: *Munich mirror: detailed scan of the surface using 2 cm space scan lines in X and Y. All dimensions are in mm. Deviation (in mm) from the spherical profile for the central X and Y scan lines.*

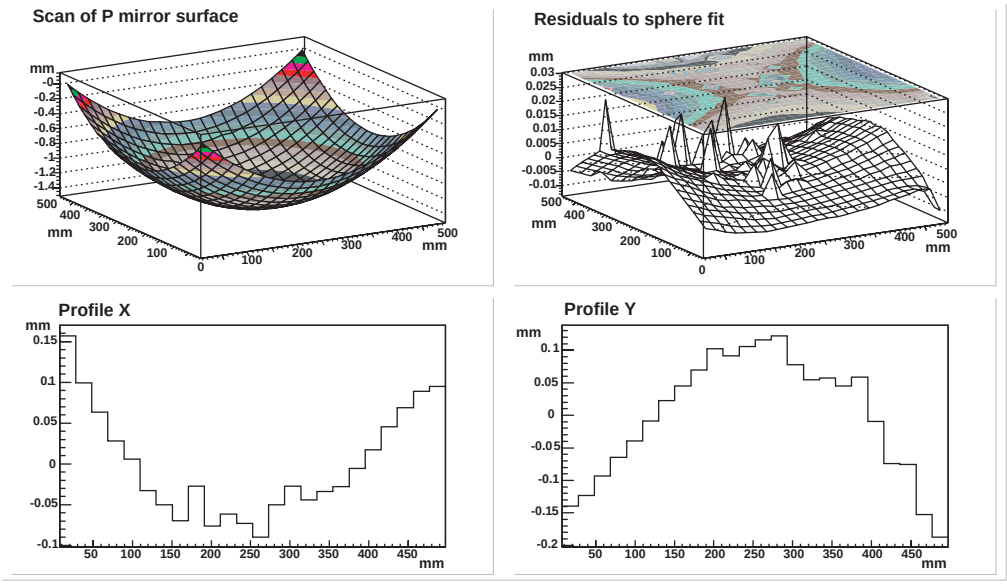

Figure 4.17: *Padua mirror: detailed scan of the surface using 2 cm space scan lines in X and Y. All dimensions are in mm. Deviation (in mm) from the spherical profile for the central X and Y scan lines.*

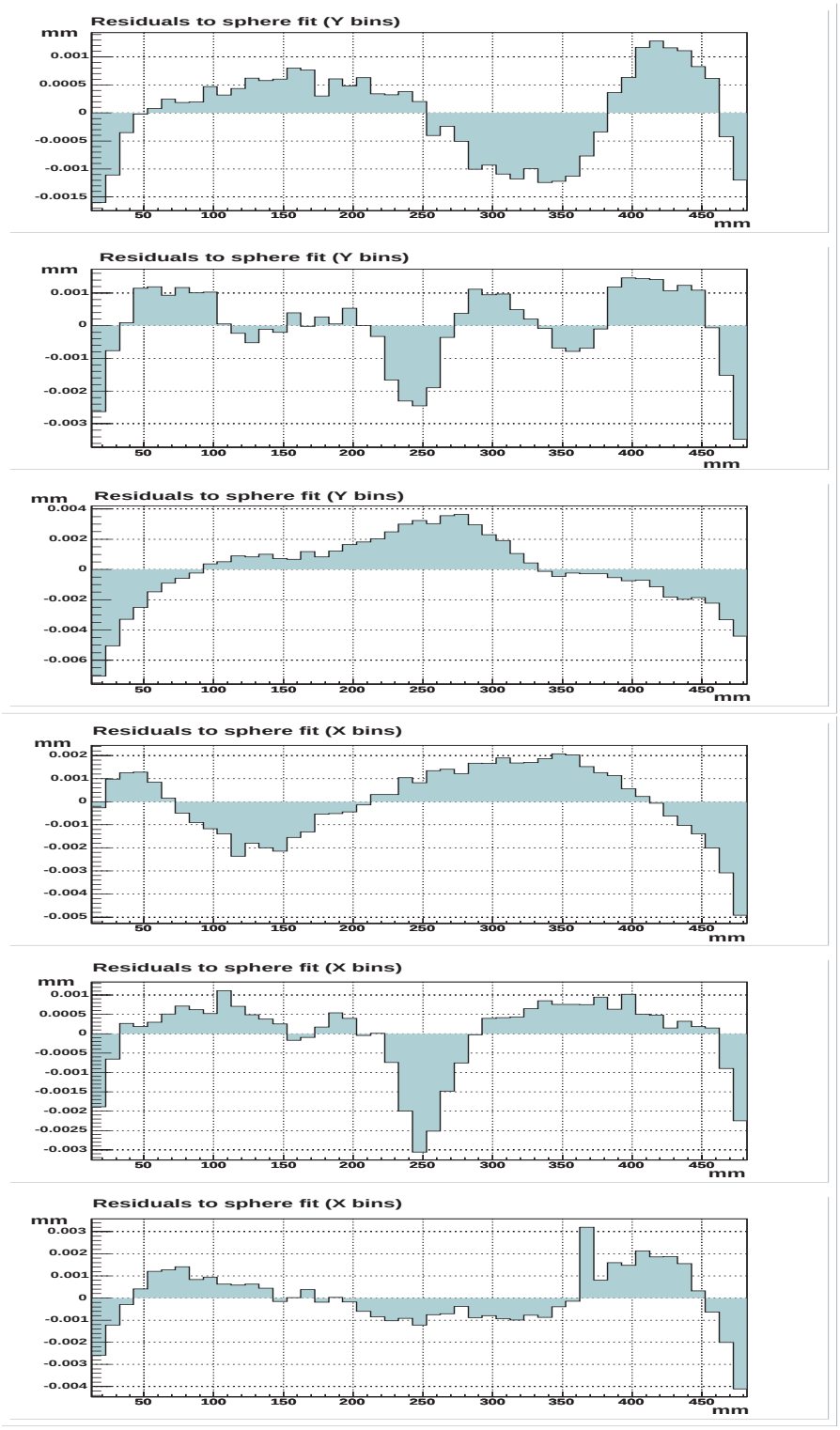

Figure 4.18: *Test on a Munich mirror, detailed scan of the surface. In these histograms the deviation from the sphericity is shown. All dimensions are in mm.*

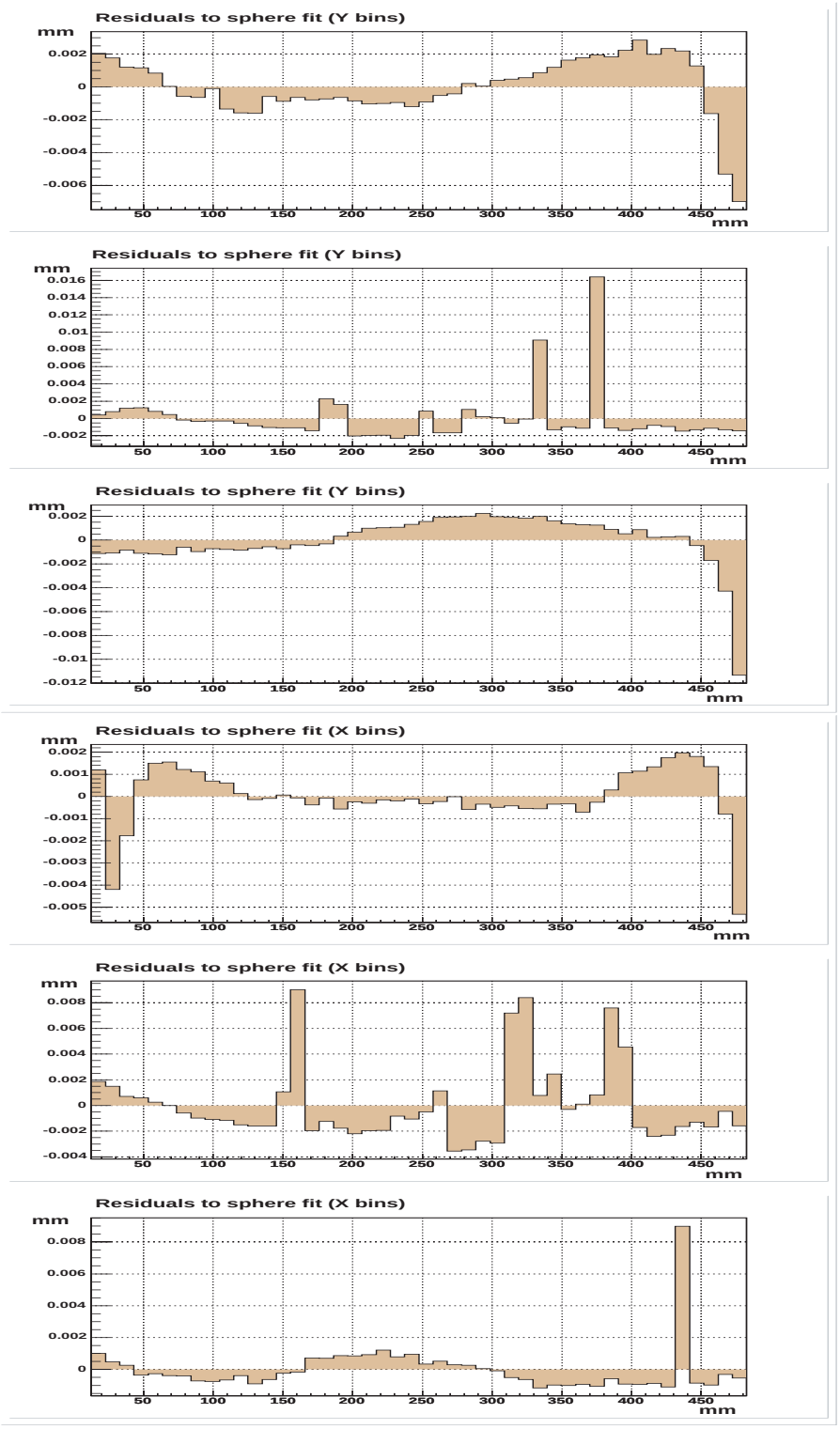

Figure 4.19: *Test on a Padua mirror, detailed scan of the surface. In these histograms the deviation from the sphericity is shown. All dimensions are in mm.*

4.5 Studies on the radius of curvature of the mirrors

The MAGIC mirror is composed of mirror elements of spherical shape forming an overall parabolic profile in order to minimize the differences on arrival time of the incident photons. A slight increase in the aberrations compared to a spheric mirror has to be tolerated.

In the design phase, two different ray-tracing programs were used to optimize the radii of curvature of each mirror element, minimizing the RMS of the spot produced by all the mirrors (see [98]).

The numerical method used for the optimization takes into account that the distance between the focal surface, where we can find the minimal dimension of the reflected spot, and the mirror is shorter than the focal length. This effect is called *shortening*.

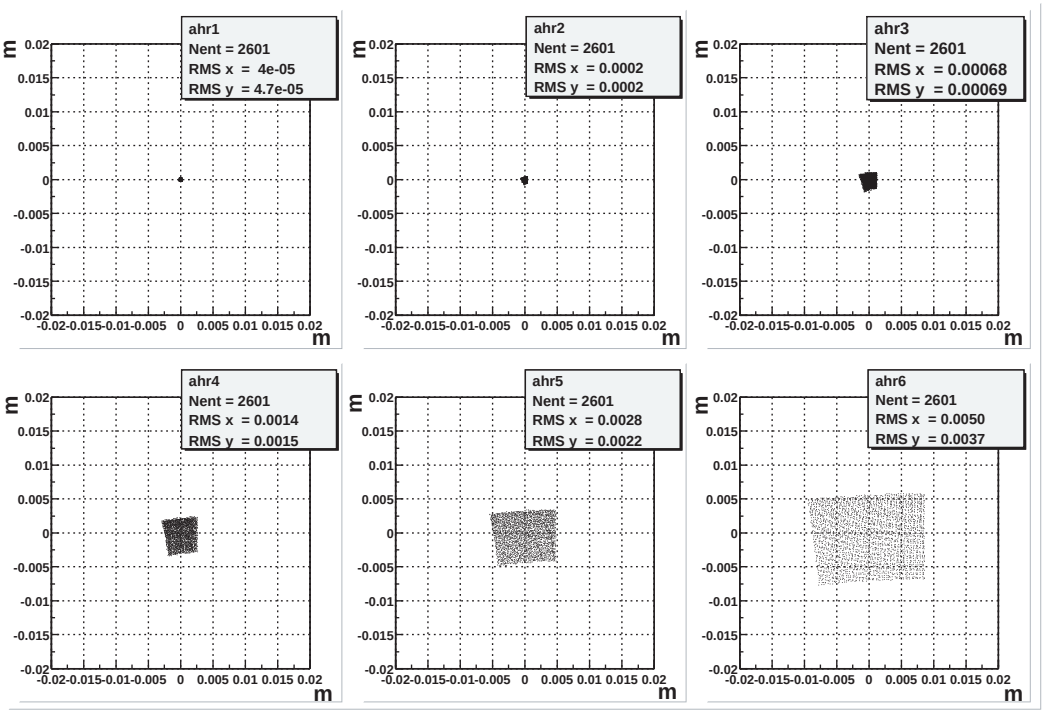

Figure 4.20: *Simulation of spots produced by single mirror elements in the MAGIC camera plane, depending on their position in the dish (from up-left to down-right the distance from the center increases from 1.5 m to 7.5 m). The simulation is done for ideal spherical mirrors. Distances are in metres from the telescope axis.*

The geometrical limits in focusing power of the telescope were tested using a ROOT [99] macro (see [100]) [1], that calculates the intersection point between the

[1]The macro, with some explanations of the algorithm, is available on the web address: `http://www.mppmu.mpg.de/~nadia/RayTracingMacro.html`

reflected light and the detector focal plane. The incident photons are simulated as a parallel beam and the angle between the incident direction and the telescope axis can be set. The reflector is composed of squared mirrors (50×50 cm^2) with a spherical surface. The radius of curvature of each mirror can be set by the user. The single mirror axis is perpendicular to the paraboloid surface on the central point of the mirror. The whole reflecting surface is composed of 964 mirror elements following the paraboloid reproducing the MAGIC reflector. One photon per cm^2 incises the surface. The graphical results obtained can be compared with the project solutions and to the first measurements on the produced mirrors.

The spherical approximation of the parabolic surface limits the focusing power of the telescope. The mirror elements produce spots of different shape and dimension depending on their off-axis position from the center of the dish (see figure 4.20). The optimal focusing power is reached by the mirrors with the same radius of curvature of the paraboloid as occurs in the central area. Far from the center of the dish, the difference between the shape of the paraboloid and the spherical mirrors increases and the dimension of the spot too.

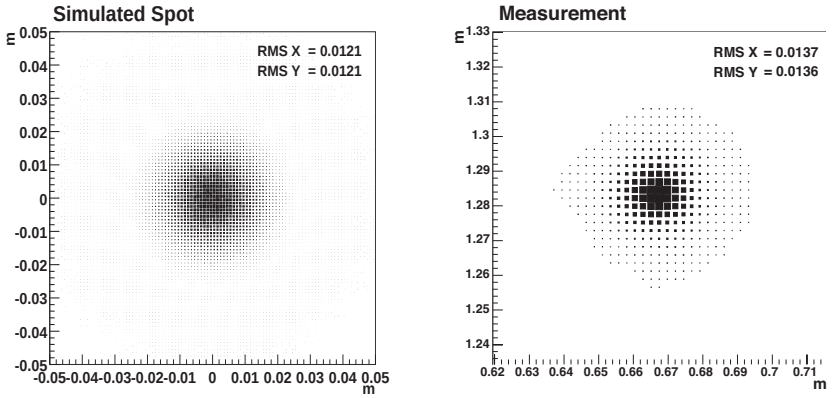

Figure 4.21: *Left: Result of the simulation of the reflection by the MAGIC dish, with the produced radius and minimum allowed quality parameter. The total spot produced has the dimensions of one inner pixel of the camera of the telescope. Right: Spot produced by the reflector, with the telescope pointing at the star Vega.*

The main causes of the enlargement of the spot produced by the outer mirror elements are: the spherical approximation of the surface, the *shortening* effect and the angle between the axis of the mirrors and the incident light.

The simulation shows the resulting spot for mirrors with the produced radius of curvature and for a perfect alignment of the system. The result is shown in figure 4.21, left. In this simulated case, all the mirrors produce a spot with R_{90} equal to 1.27 cm, the maximal accepted value in the production phase. The real quality (R_{90}) and the radius of curvature of the installed mirror elements is shown in the histogram of figure 4.12. Figure 4.21 (right) shows the spot produced by the mirrors

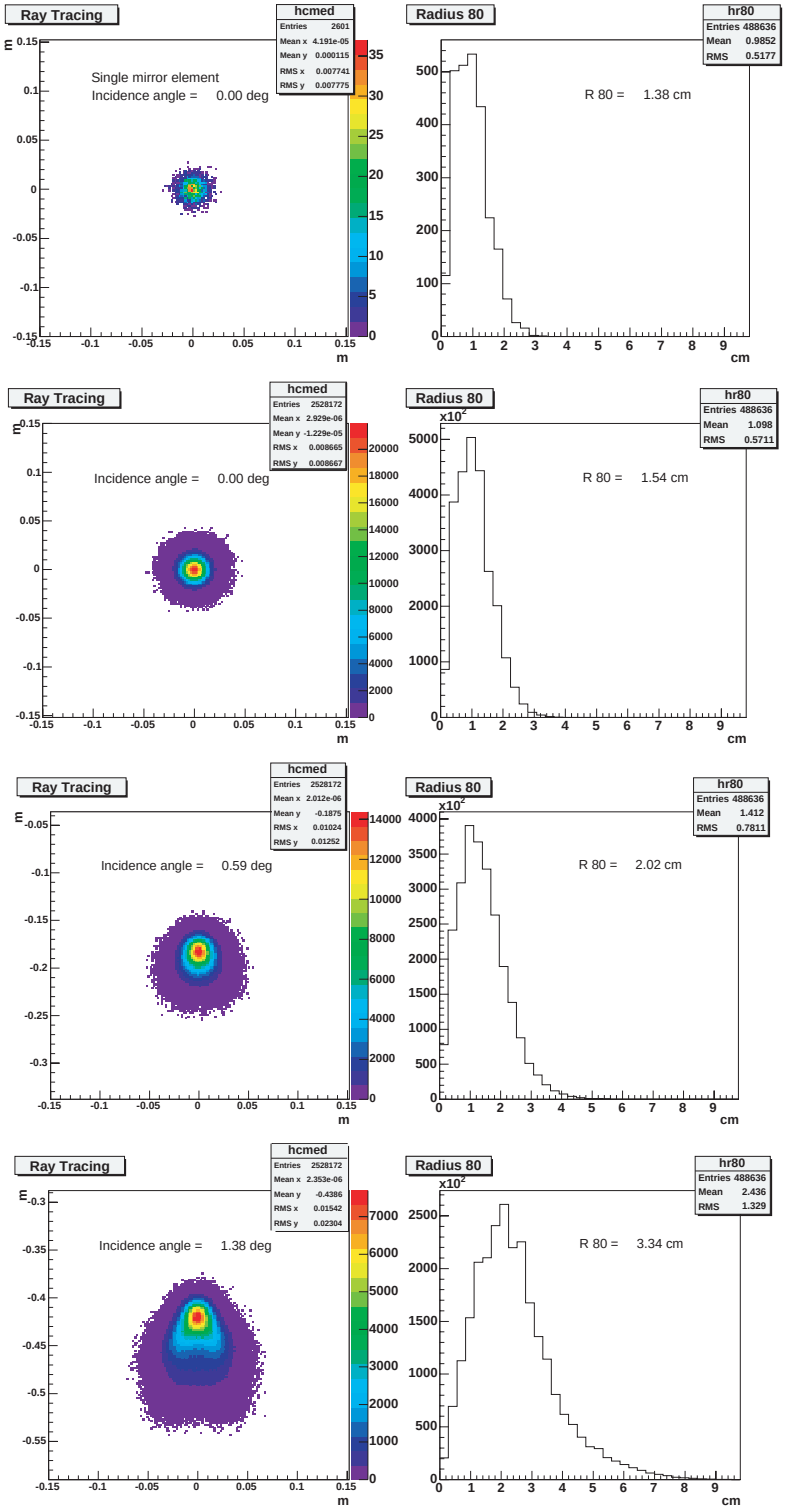

Figure 4.22: *Result of the simulation of the MAGIC dish, with the produced radius and quality parameter such to match the measured quality of the reflector. The noise in the spot has been obtained by smoothing the quality of the single mirror elements (first panel above) and maintaining the ideal alignment of the mirrors.*

installed on the telescope, as measured in La Palma, pointing to a bright star, with the mirrors focussed to infinity. The RMS of the real image is comparable with the result of the simulation. The point spread function (PSF) of the reflector is defined as the full width at half maximum (FWHM) of the 2-dimensional Gaussian function which interpolates the stellar light distribution on the focal plane; the measured PSF is $\sim 0.04^\circ$.

Figure 4.22 shows the result of the simulation for different angles of incidence of the light. In this case, the reference value is R80 (radius of the circle that collects 80% of the light). The quality of the single mirror (plotted on the top panel) is such to match the measured quality of the reflector (alignment error included).

4.5.1 Test of reproducibility of the measurements of radius of curvature

Measurements of the radius of curvature of 35 coated mirror elements (25 P mirrors, 10 M mirrors) were repeated some months after the coating. The method used for the measurement is slightly different from the one adopted before the coating. A white, strong, point-like source illuminates the mirror element and it is positioned at about 2 times the nominal focal length. The image is visualized on a movable screen near the light source and the distance to the mirror element is measured. The radius of curvature R is:

$$\frac{1}{p} + \frac{1}{q} = \frac{2}{R} \Rightarrow R = 2 \cdot \frac{p \cdot q}{p + q} \tag{4.1}$$

where p is the (fixed) distance between the lamp and the mirror and q is the distance between the mirror and the point where the spot (image of the lamp) is smallest on the screen. The measurement is not very accurate and can change somewhat from person to person. This simple method, used to determine the radius of curvature has an error on the evaluation of the focal point of about 10 cm. We checked that the temperature of the mirrors was in equilibrium with the room temperature ($\sim 20^\circ$) and that the screws that hold the mirror to the frame were not applying external stresses to the mirror.

The difference between the two measurements show a Gaussian distribution, which peaks around 0 and has a RMS of 15 cm (figure 4.23). From the result, we conclude that the radius of curvature of the mirror elements did not change systematically within few months and do not depend on the method used. Systematic behaviors could not be found on mirror elements milled at different periods.

4.5.2 Test of the surface deformation under the influence of temperature changes

The M mirrors are completely made of aluminum, while the P mirrors have a *vetronite* board (epoxy-fiberglass with a copper strip) for heating. The temperature expansion coefficients of the two components are different and we checked the behavior of the mirror elements when a sizeable gradient of temperature occurs. Three

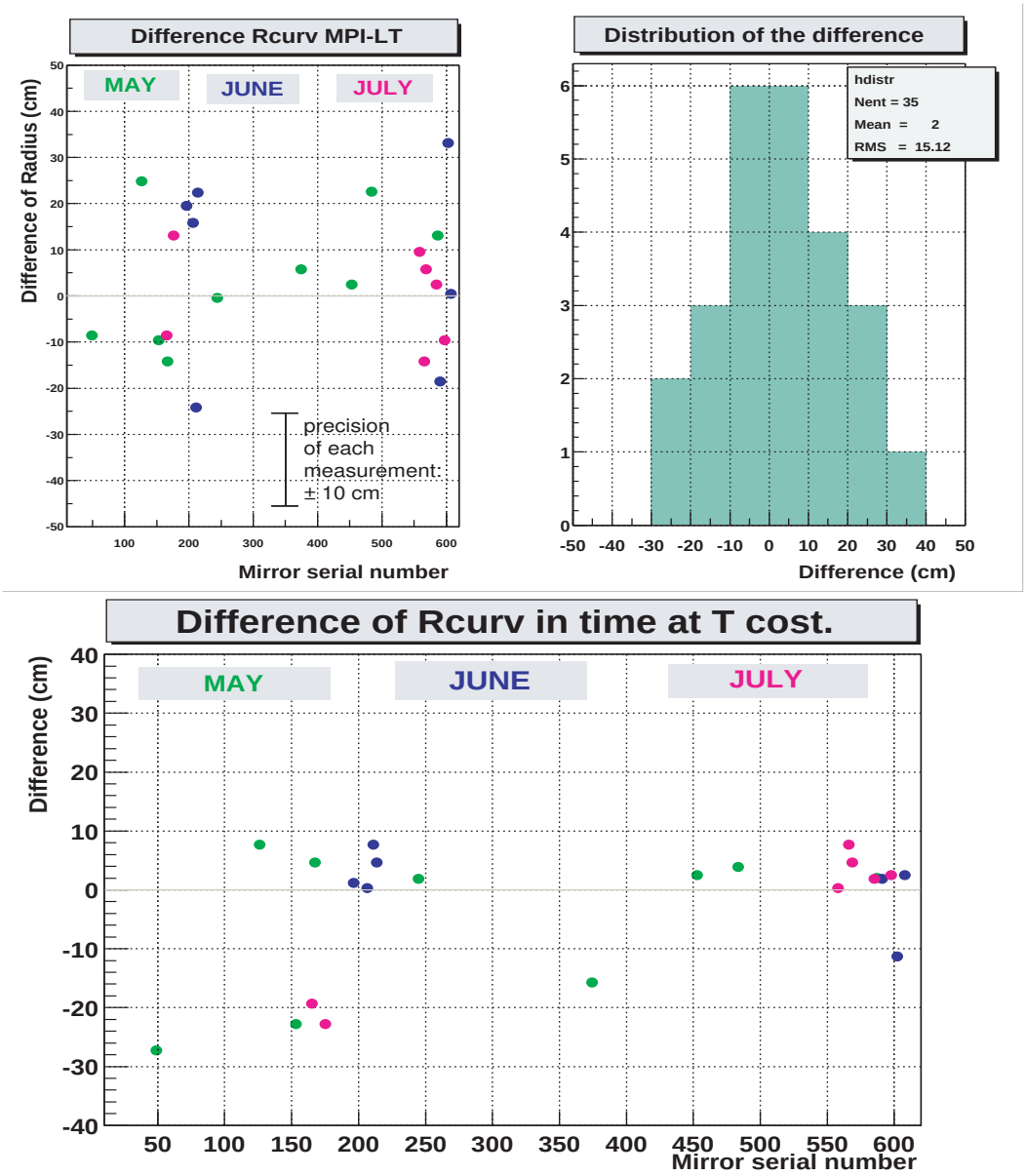

Figure 4.23: *Difference between measurements of radius of curvature done at LT-Ultra before the coating of the mirror and some months later, after the coating, at MPI by eye control. The error on each measurement is about 10 cm. The different color of the dots indicates different periods of production of the mirrors and measurement of the radius. Below: the difference of radius of curvature measured at MPI, just after the positioning on the frame and after 10 minutes.*

mirror elements (2 P and 1 M) were kept at about 0°C for some hours, then they were put into a room at ∼22°C. The radius of curvature of each mirror was measured every 5 minutes during the reheating period. The method used to measure the radius of curvature is the same as described for the previous test.

The behavior of the three mirror elements is displayed in figure 4.24. The P mirror n167 shows a very strong temporary change in radius of curvature, but settles eventually to the referring value. The calculated excursion corresponds to a variation of 2.4 m in radius of curvature. The temperature difference was about 20°C. The P mirror n374 shows no monotonic variations, but at the end, the radius value is the reference one. The maximum registered variation from the nominal radius of curvature was about 50 cm. The M mirror showed fewer variations (30 cm), but the structure of the mirror did not allow us to easily check the temperature. The heating system was activated to provide a higher variation of temperature in less time.

The measurements show that sudden increase in temperature causes a variation of the radius of curvature of the P mirrors, that in some cases can be considerable (∼ 7%). The mirrors reach the equilibrium in around 15 minutes and the radius of curvature tends to the nominal one.

The validity of this test is limited, since only 3 mirror elements were measured during controlled variations of temperature and the methods to measure the temperature were different and not completely reproducible.

We suggest as an additional test to check the behaviour of the radius of curvature at different (stable) temperature levels.

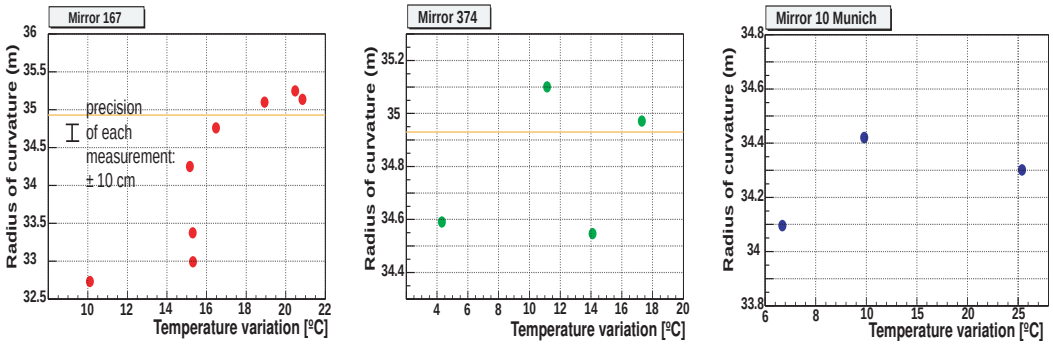

Figure 4.24: *Variation of the radius of curvature of some mirror elements with a fast changing of temperature.*

4.6 The layout of the MAGIC reflector

The main parameters of the MAGIC reflector are:

- a total mirror surface of 236 m^2, composed of 964 mirror elements of position-dependent spherical shape.

- an overall parabolic profile, locally approximated by spherical mirror elements;
- a stiff and lightweight carbon fiber structure;
- an active mirror control (AMC) system to counteract deformation of the reflector support frame as a function of the declination angle.

For cost reasons it was not possible to install an active mirror control (AMC) for each mirror element. It was decided to mount 4 (or 3) mirror elements, selected according to their best position on the dish, onto a panel. The mirror elements are linked to the panel at 3 points with finely treaded adjustment screws.

The panels, shown in figure 4.25, are lightweight 60 mm thick sandwich plates (6.35 mm cell size Al HEXCELL with a top and a bottom Al skin of 1.5 mm thickness).

The panels are then connected to the motors of the AMC, that adjust their orientation when installed in the telescope frame. The lasers in the middle of the panels are part of the AMC, necessary to recognize the orientation of the panels.

Panel production and alignment

Each mirror is mounted on the panel through three connection points. The blueprint of a panel and of the mirror fixing points is shown in figure 4.25.

Once the mirrors are fixed on the panel, they have to be aligned to form a common focal spot.

A parallel beam of light is produced using 4 prototype mirrors. A strong light source is positioned at the common focal distance. The system used for the alignment is shown in figure 4.26 and the steps to align the mirrors in a panel follow:

- The position of the panel in the telescope dish with respect to the camera is calculated. A white screen, with the drawing of a 0.1° MAGIC pixel is positioned at the position of the camera.
- The parallel beam of light illuminates the mirrors to align them. On the screen the focal spots produced by the mirror elements are seen at random positions.
- On the back of the panel, long screws, one for each fixing point, allow us to modify the distance between every single mirror and the panel. By adjusting the screws, the spot of each individual mirror is adjusted onto the center of the drawn pixel in the screen.
- A video-camera, positioned near the screen, displays a magnified picture of the central part of the screen. This allows us to easily superimpose the 4 spots to the panel focus with good precision.

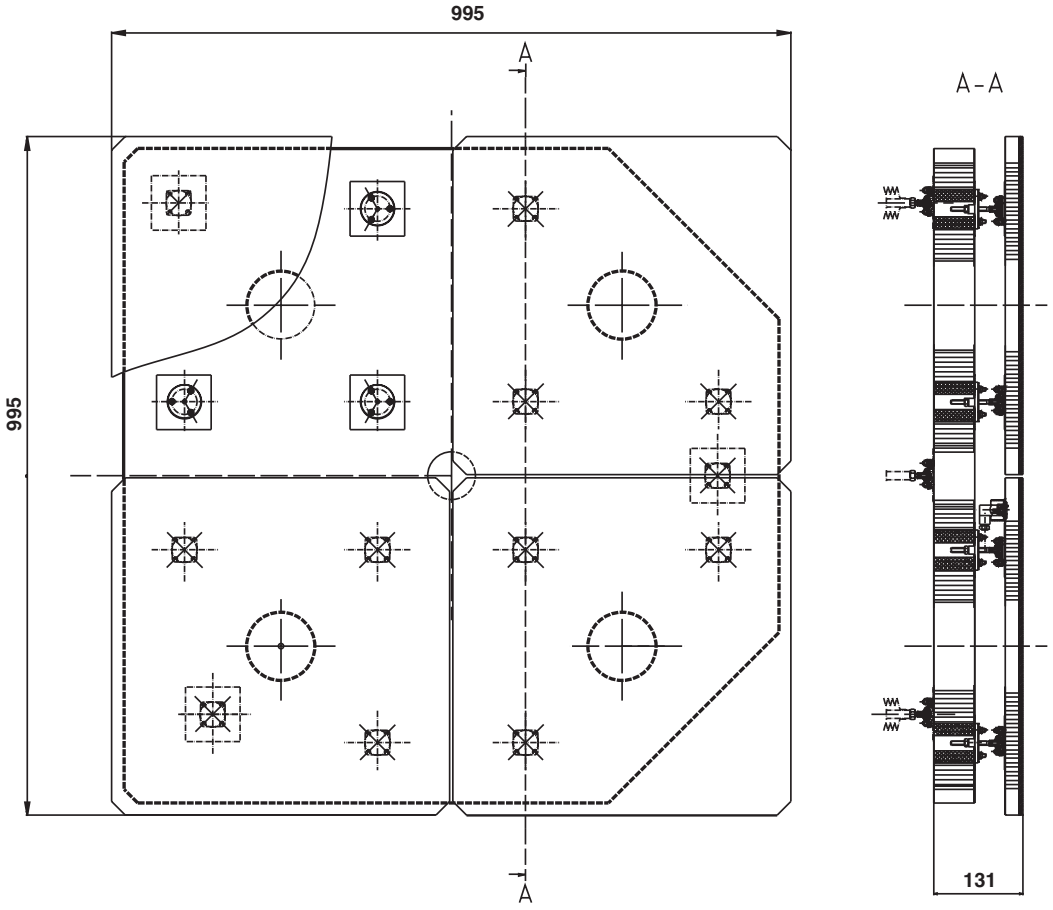

Figure 4.25: *Design of panels for the MAGIC telescope.*

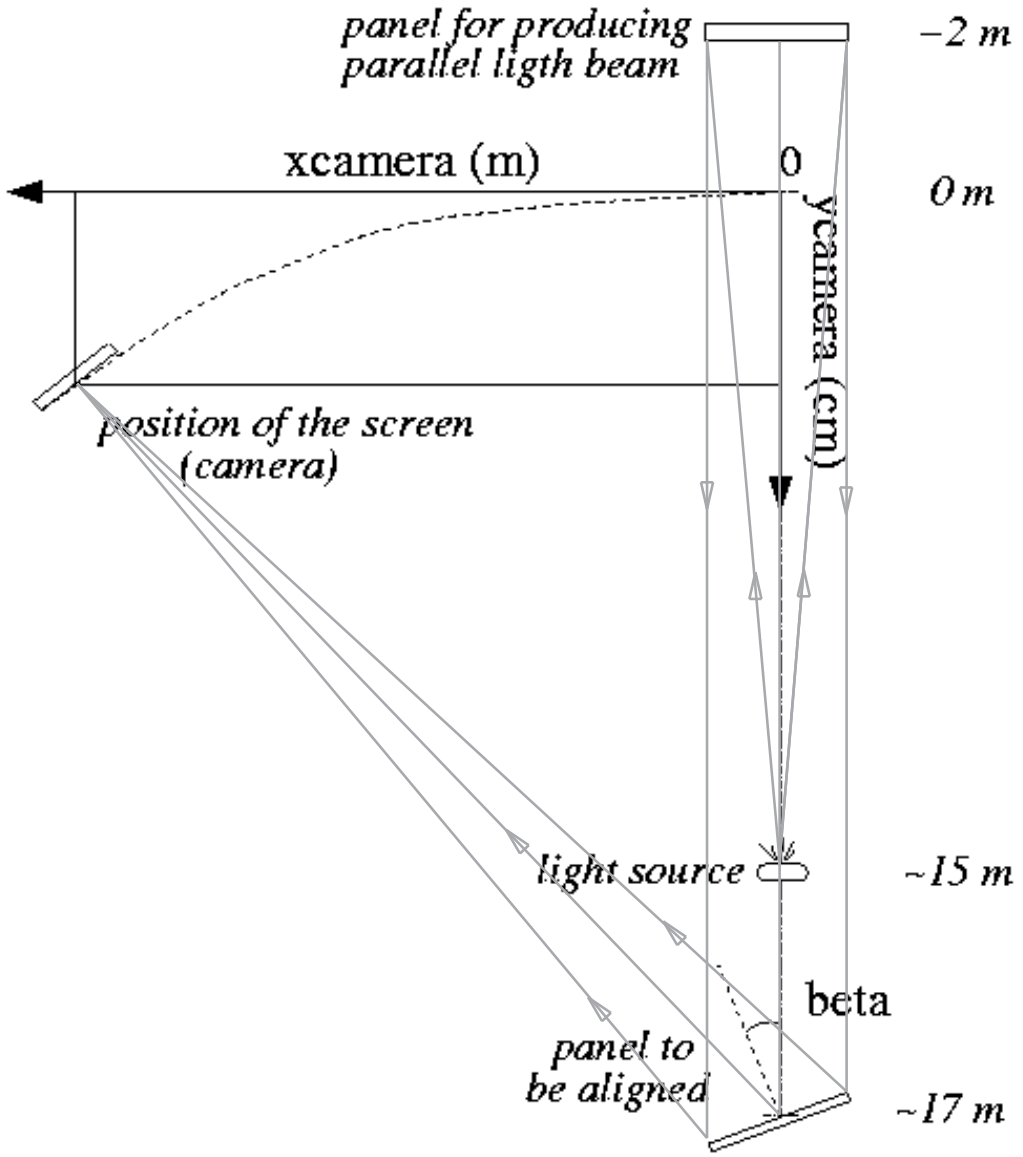

Figure 4.26: *Scheme of the system used for the alignment of the mirrors of one panel. The grey lines represent the light path. The innermost panels were adjusted with a small offset in order not to obscure the parallel beam by the screen representing the camera plane. The induced error is negligible.*

- Finally, the laser positioned at the center of the panel is adjusted to send light to the same position of the resulting spot. The laser pointer is fixed in this position.

The pre-alignment of the mirror elements in each panel did not worsen during the transportation to the telescope site. Anyway, a fine tuning of the alignment is also possible after the panels are installed on the frame.

The focusing power of the telescope is then determined by the AMC performances. The motors connected to the panels allow us to change the orientation of the focal system, guided by the lasers installed in the middle of the panels. It is absolutely necessary to adopt such a system because of the huge structure, that can slightly deform under the weight (even though limited) of the mirror panels.

During normal telescope operation, the AMC adjustment is done every time one points a new source or when tracking a source whose position changes significantly in zenith angle. The power of the AMC alignment, together with the PSF, can be guessed from the root mean square (RMS) of the light distribution shown in figure 4.21.

The panels were installed on the MAGIC telescope frame, following a so-called *chess board* structure. They have a difference of $\sim$ 6 cm in height with respect to their nominal position. This operation was found to be necessary to guarantee enough space between the panels [2].

The staggering does not spoil the optical characteristics of the reflector. It influences, however, the Cherenkov light pulse time spread.

[2]The space between the panels was calculated taking into account a smaller height between the frame and the mirrors' surface and a smaller space between the mirror elements. The changes of some assembling parts caused the lack of space between the mirrors.

4.7 Conclusions on the novel mirror system

The reflector of the MAGIC telescope is unique among Cherenkov telescopes: new technologies have been employed, from the materials adopted (Al alloys mirror elements, carbon fiber frame), to the control systems (AMC, internal heating). Nowadays, the precision of cuts and treatments for metals available on the market have been tested to give good reliability. New features and much progress, with respect to the previously adopted mirrors, are expected.

The low weight of the materials employed allows the construction of such a large mirror area. The technology adopted gives impulse to new possible studies, i.e. the possibility to detect lower energy γ-rays with respect to the past and to study some of the most enigmatic phenomena happening in the γ-ray universe, like GRBs.

At the same time, a certain dose of hazard has to be taken into account. The many tests on the new mirrors could not reproduce all the possible situations a mirror in a telescope has to confront. The experience with the installation of aluminum mirrors on the HEGRA CT1 telescope was certainly a great advantage.

After some months of installation, defects on some elements started to show up and some replacements were needed. They were taken into account at the beginning of the production. The installation of the panels on the telescope was carried out for almost two years, between the summer of 2002 to the summer the 2004. This time was also used to get experience and feedback from the first mirrors installed.

At the moment, some systems which constantly check the conditions of the reflector are being tested: the total reflectivity has been measured to be $\sim 73\%$ and the knowledge of its evolution in time determines our capability to calibrate the instrument.

The experience acquired is now a source of new ideas for the development of the mirrors for MAGIC phase II: a clone of the MAGIC telescope will be built soon near the original one, to form a stereoscopic system. The new mirrors will be made of Al alloys, as the previous ones, but probably they will be bigger (~ 1 m^2). Different solutions for the mirror structure are being tested in order to guarantee good milling, i.e. good precision in the radius of curvature and reflectivity, good stiffness, without mechanical stresses and good stability of the performance.

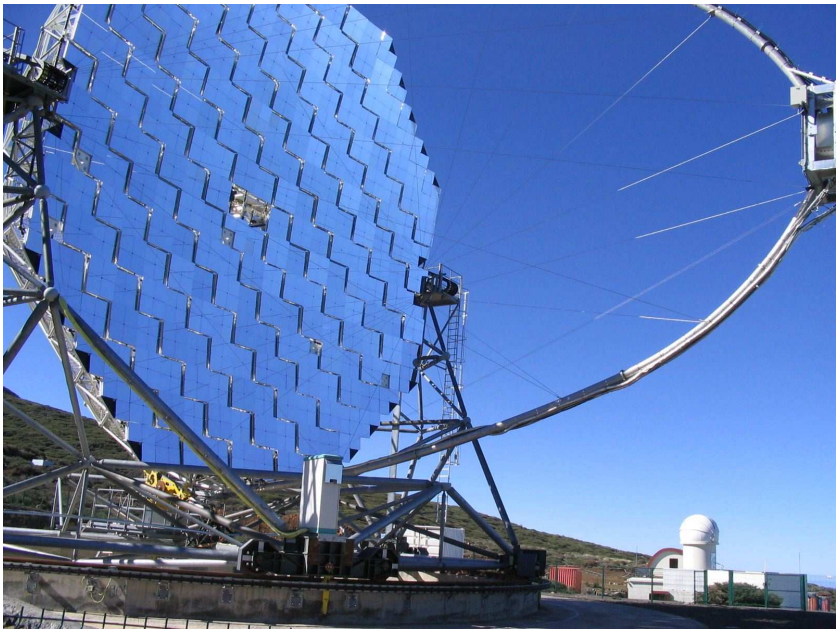

Figure 4.27: *The MAGIC telescope in October 2005.*

Figure 4.28: *The mirror elements seen from the camera access tower, i.e. around the focal distance. The position is optimal to visualize the tiny imperfections of the surface of the mirrors.The ones on the right are M mirrors; it is possible to recognize the channel for the heating and the small central depression.*

Chapter 5

Extended atmospheric showers and the imaging technique

Cherenkov telescopes record the effects of the impact between CRs and the earth's atmosphere. The electromagnetic interactions involved are known but not easy to describe, due to the high number of particles and variables. On the other hand, nucleus-nucleus collisions at very high energies are only known with some uncertainties. For this reason, Monte Carlo simulations are very important to understand which observational effect to expect from such interactions and the possible response of the detectors. In this session I will describe the main characteristics of extended air showers (EAS) and of the Cherenkov light they produce.

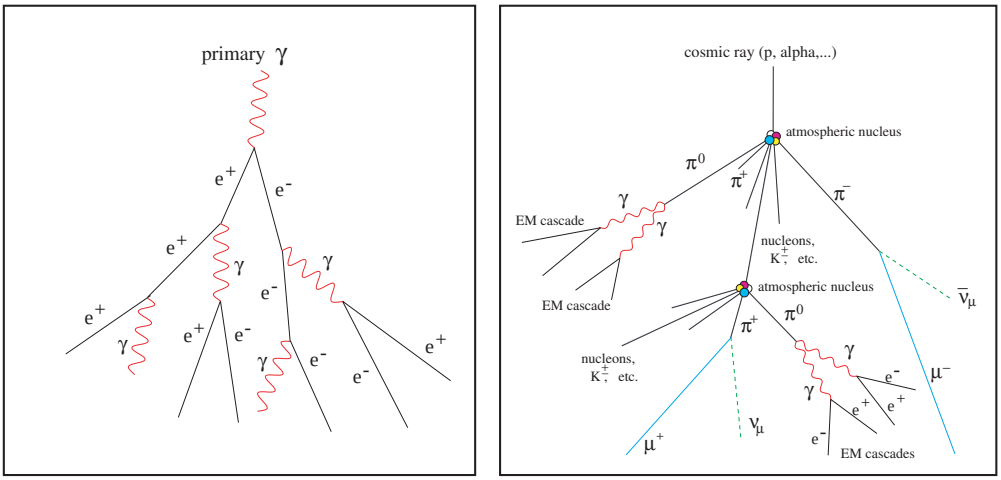

Figure 5.1: *Schematic description of EAS. Left: electromagnetic (EM) shower. Right: hadronic shower. For the description, see text.*

5.0.1 Electromagnetic showers

When a γ-ray hits the atmosphere, it initiates a cascade (see figure 5.1, left) with the production of an electron/positron pair in presence of a nucleus of the earth atmosphere. Each electron/positron generates high energy photons via Bremsstrahlung, the secondary photons produce $e^{\pm}$ pairs and so on. The energy of the particles and photons involved in the cascade becomes progressively lower, while the number of particles increases. Such a cascade of particles is called an electromagnetic (EM) shower, due to the physics processes sustaining the shower development. Electrons and positrons can lose energy by ionization ($\simeq 1.85$ MeV/(g/cm^2) = 67 MeV/ radiation length). Once the energy losses due to Bremsstrahlung and pair production become lower than the ionization losses, the multiplication process slows down and eventually stops.

A simple model by Heitler [20] describes with good approximation some properties of EM showers. Supposing that the energy of the primary particle is equally distributed into the products, we can easily derive the position of the maximum development of the shower. The radiation length ξ_0 of an ultrarelativistic electron is defined as the mean distance it travels before losing its energy by a factor e. In air $\xi_0 \simeq 36.7$ g/cm^2. Let's define $R = \xi_0 \ln 2$. The probability of having interactions in the space R is $\exp(-R/\xi_0) = 1/2$. The number of particles after n interactions, occurring in the travelled length nR will be 2^n, each particle having mean energy $E_0/2^n$. The position of the shower maximum is then:

$$X_{max} = R \cdot \ln \frac{E_0}{E_c} / \ln 2 = \ln \frac{E_0}{E_c} \cdot \xi_0 \tag{5.1}$$

with E_c being the critical energy ($\simeq 100$ MeV) below which the production of particles is highly reduced. More complicated models, but again with strong approximations, have been developed by Rossi and Greisen [101]. They derived the total number of $e^{\pm}$ in the shower at a given time as:

$$\begin{aligned} N_e(t) &= \frac{0.31}{\sqrt{\ln(E_0/E_c)}} \cdot \exp\left[t \cdot (1 - 1.5 \ln s)\right] \\ s &= \frac{3t}{t + 2\ln(E_0/E_c)} \end{aligned} \tag{5.2}$$

The variation of N_e with the atmospheric depth t is called longitudinal development and it is shown in figure 5.2. The parameter s is called age parameter and indicates the development level of the shower: it goes from a value of 0 in the point of first interaction, 1 at the maximum and 2 at the point where the shower dies.

The lateral distribution of a shower is described with the formula of Nishimura-Kamata-Greisen (NKG) [102]:

$$\rho_e = \frac{N_e}{r_M^2} \cdot \left(\frac{r}{r_M}\right)^{s-2} \cdot \left(1 + \frac{r}{r_M}\right)^{s-4.5} \cdot \frac{\Gamma(4.5 - s)}{2\pi \cdot \Gamma(s) \cdot \Gamma(4.5 - 2s)} \tag{5.3}$$

where r_M is the Moliere radius ($\simeq$ 79 m asl).

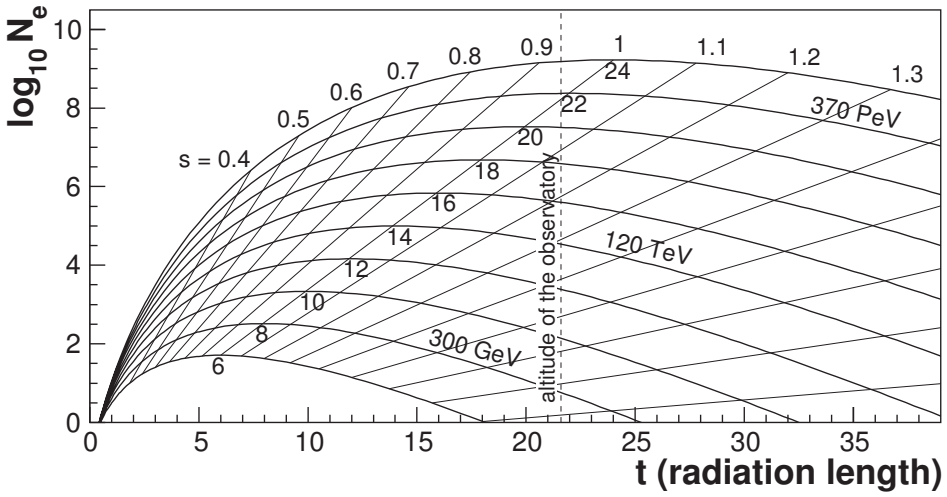

Figure 5.2: *Longitudinal development of an EM shower. The x axis corresponds to the atmospheric depth, the curves correspond to different energies of the primary photon (the value* $\ln E_0/E_c$ *is written below each curve) [103].*

The hadronic component of EM showers is produced by photo-production, i.e. the interaction of a photon with an atmospheric nucleus. The photo-production cross-section is very small: 100 μb/nucleon (in air: A = 14.5 corresponds to 1.5 mb), with respect to the cross section for pair production ($\sim$ 500 mb). For this reason, the hadronic component of an EM shower can be neglected.

The muon component of an EM shower has been analyzed using Monte Carlo simulations in [104]. For an energy threshold for muons of $E_\mu = 100$ MeV, inside a radius of 1 km around the detector, an average of 2 muons (with large fluctuation) are produced by a 10 TeV γ-initiated shower, while a 10 TeV proton initiated shower contains on average 156 muons. The muon component of a shower increases with increasing energy of the initial particle. Therefore, we do not expect a significant muon component in EM showers detected by Cherenkov telescopes.

Electrons and positrons can also initiate EM showers. They will be identical to γ-initiated showers.

The characteristic of the Cherenkov light produced by EAS in the atmosphere will be described in section 5.1.

5.0.2 Atmospheric showers induced by hadrons

The majority of particles hitting the top layers of the atmosphere are of hadronic origin. A charged CR particle interacts with an atmospheric nucleus, creating pions, kaons and other nucleons (see figure 5.1, right). The hadronic interactions of the products continue until the energy is still sufficient to create pions ($E_c \sim 1$ GeV).

A hadronic shower has also an EM component: the decay $\pi_0 \rightarrow \gamma\,\gamma$ starts an EM subshower, as described in section 1.1.2. Since pions of the three charges are produced with about the same probability in hadronic collisions, about one third of the energy in inelastic interactions is transferred to EM subshowers. This process is basically irreversible, therefore most of the initial energy is transferred at the shower end to the EM component.

As described in section 1.1.2, charged pions can decay by producing $\mu^{\pm}$ and neutrinos, according to Eq. 1.6 and Eq. 1.7. Muons can either decay into $e^{\pm}\nu\bar{\nu}$ or lose energy by ionization. Due to the high initial muon energy, only a few of them decay. Therefore, most of the muons produced in hadronic cascades arrive at the ground, unless they lose all their energy via ionization processes.

Besides protons, charged cosmic rays also consist of nuclei (dominantly He nuclei, up to Fe). We can describe heavy ion induced showers using a simple superposition model [105], assuming that a nucleus of mass A and energy E_0 is equivalent to A nucleons of energy E_0/A. The position of the shower maximum (in analogy with Eq. 5.1) is:

$$X_{max} \propto \ln[E_0/(AE_c)] \cdot \xi_N \tag{5.4}$$

where ξ_N is the nuclear interaction length of a nucleon in the air. From this simple model it is easy to understand how heavier nuclei can create showers of a larger number of particles and with a development higher in the atmosphere.

A detailed study of the hadronic shower development implies the application of models of nuclear interaction to a huge number of particles. Monte Carlo simulations are the best tools for the study of hadronic showers behaviour. The nucleus-nucleus cross-sections for high energy interactions in the atmosphere are extrapolated from accelerator experiment results at lower energies, though containing some uncertainties.

5.1 Production of Cherenkov light in the atmosphere

Atmospheric showers are composed of a large number of energetic, charged particles, of a speed close to the speed of light in vacuum, c. Travelling through the atmosphere, many of them produce Cherenkov light, whose detection is the key element for the γ-ray astronomy with ground-based detectors. The phenomenon of Cherenkov light production will be described in the following.

5.1.1 Physics principle of Cherenkov light production

A charged particle travelling in a dielectric with refractive index n with a speed exceeding the speed of light in the medium, can produce Cherenkov light. A charged particle at rest causes a static polarization of the medium around it and there is no radiation propagation at big distances, as illustrated in figure 5.3 (a).

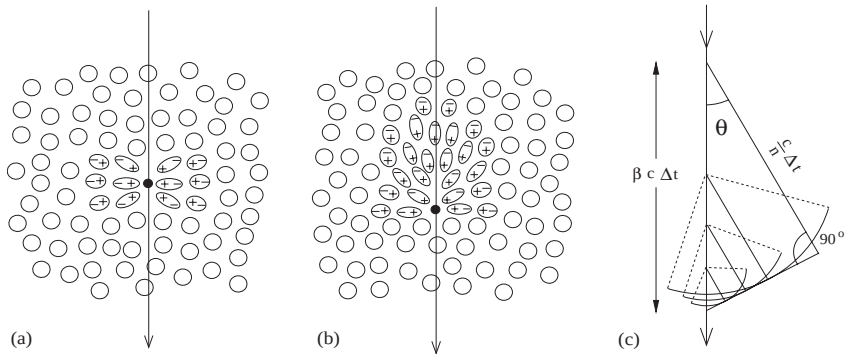

Figure 5.3: *Left (a): when a charged particle crosses a dielectric medium, it polarizes it. Center (b): If the speed of the particle exceeds the light velocity in the same medium, a wave of radiation, called Cherenkov light, can propagate. Right (c): geometrical description of the Cherenkov angle θ.*

The speed of light in that medium is c/n. When the speed v of the charged particle is larger than c/n, the dielectric medium polarizes non-uniformly, as illustrated in figure 5.3 (b). The particle is, in fact, moving faster than the electromagnetic information that induces the polarization. In this case, a coherent wave front appears at an angle θ and the radiation is called Cherenkov light. The angle of emission θ can be derived with simple geometrical arguments (see right figure 5.3) and it is:

$$\cos\theta = \frac{1}{\beta n} \tag{5.5}$$

where $\beta = v/c$. It is easy to see also that:

- the threshold velocity for a particle for producing Cherenkov light is c/n ($\beta = n^{-1}$), below which no radiation can be produced;
- the maximum Cherenkov angle is $\theta_{max} = \arccos n^{-1}$, occurring for ultra-relativistic particles ($\beta = 1$);
- the Cherenkov radiation can occur only at frequencies for which $n > 1$, i.e. from microwave to UV, but not in the X-ray or γ-ray parts of the EM spectrum.

In the following, the characteristics of the Cherenkov light produced in air by EAS charged particles are described.

Propagation of Cherenkov light in the atmosphere

The Cherenkov light produced in air has typical features, due to the refractive index of the medium close to 1 ($n_{air} \simeq 1.00029$ at sea level). In general, for air mass 1 [1]:

- the threshold kinetic energies are 21 MeV for $e^{\pm}$ and 4.3 GeV for μ; the threshold for heavier particles scales with the mass.
- $\theta_{max} = 1.3^{\circ}$
- the rate of production of radiation W with path length l is $dW/dl = 30$ photons/m, between 350 and 550 nm and for particles with $\beta = 1$ [106].

When considering Cherenkov radiation produced in the atmosphere, we must take into account the exponential variation of air pressure p with the height (the following description model is taken from [107]). We can write the refractive index

$$n = 1 + \eta_h = 1 + \eta_0 \exp(-h/h_0) = 1 + 2.9 \cdot 10^{-4} \exp(-h/h_0) \tag{5.6}$$

where $h_0 = mg/RT \approx 7.1$ Km (called also scale-height). All the values derived above will be then p (and h) dependent.

The threshold energy for electrons is:

$$\begin{aligned} E_{min}(h) &= \frac{m_e c^2}{\sqrt{1 - \beta_{min}^2}} \\ &= \frac{m_e c^2}{\sqrt{1 - n^{-2}}} \\ &\simeq \frac{0.511 \text{ MeV}}{\sqrt{2\eta_h}} \\ &\simeq \frac{0.511 \text{ MeV}}{\sqrt{2\eta_0 \exp(-h/h_0)}} \end{aligned} \tag{5.7}$$

for $\eta_h \ll 1$. The angle θ_{max} can be written as:

$$cos\theta_{max}(h) = \frac{1}{1 + \eta_h} \simeq 1 - \eta_h \simeq 1 - \eta_0 \exp(-h/h_0) \tag{5.8}$$

Using this formula, we can derive the distance R_c to the shower axis of the photons emitted from on-axis particles at a height h and observed at h_{obs}:

$$R_c = (h - h_{obs}) \cdot \tan\theta_{max} \tag{5.9}$$

[1] The air mass is defined as the path length of light in the atmosphere, with respect to the length at zenith. For vertical observations (z.a. $= 0^{\circ}$) the air mass is 1, for small zenith angles the air mass goes as sec(z.a.) (valid for the plane parallel atmosphere approximation).

The radius R_c(h) has a maximum between 10 and 20 km, such that the Cherenkov light produced at this height range arrives at $h_{obs} \simeq 2200$ m (corresponding roughly to La Palma observatory altitude) forming a ring of ∼120 m radius and ∼10 m width (see figure 5.4). The light from the shower tail is emitted with a larger Cherenkov angle θ, but due to the lower height its distance is less.

The number of Cherenkov photons emitted for a unit path length (in g/cm^2) by an electron, is :

$$\begin{aligned} \frac{d^2N}{dxd\lambda} &\propto \frac{1}{\lambda^2} \\ \frac{dN}{dx} &= 2\pi\alpha \cdot \left(\frac{1}{\lambda_1} - \frac{1}{\lambda_2}\right) \cdot \left(1 - \frac{1}{\beta^2 n^2}\right) \end{aligned} \tag{5.10}$$

with $\alpha = e^2/(\hbar c) = 1/137$. The largest amount of the Cherenkov light is emitted in the UV range (see next section).

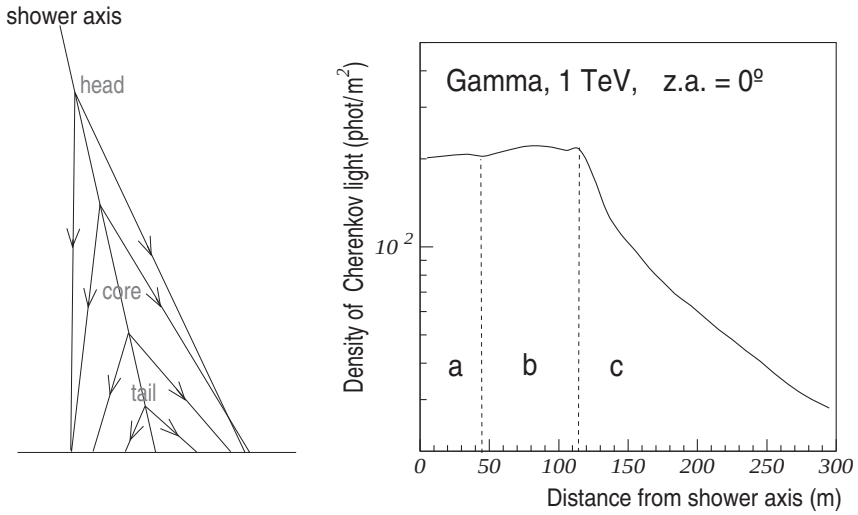

Figure 5.4: *Left: Schematic view of a shower with different Cherenkov angles at different altitudes. Right: lateral distribution of Cherenkov photons from the shower axis. The region (a) closer to the impact of the shower axis collects the light principally from the shower tail, while the region up to about 120 m from the shower axis is dominated by light coming from the shower core. Light produced by the shower halo particles contributes to region (c).*

Attenuation of Cherenkov light in the atmosphere

Possible processes that modify and characterize the features of Cherenkov light propagating in the atmosphere are:

- Diffraction and dispersion. Their effects can be neglected, due to the low air density and the small variations of n with height and wavelength.

- Absorption. It is strongly proportional to the thickness of atmosphere crossed by Cherenkov photons or, in other terms, to the zenith angle of observation. It is due to O_3 molecules for photons of $\lambda < 290$ nm and to molecules of H_2O and CO_2 for photons of $\lambda > 800$ nm.

- Scattering of shower particles. The scattering angles are of the same order or larger than the Cherenkov angles ($\langle\theta_s\rangle_{rms} \sim E_s/E \sim 12^\circ$ for E = 100 MeV, typical energy of electrons in EAS). The scattering of the electrons makes the ring structure rather washed out.

- Scattering of light. *Raileygh scattering* is the effect due to the molecules of air, with diameters smaller than the wavelength of the scattered light. The cross section varies with the wavelength and is proportional to λ^{-4}, having a bigger effect on blue and violet light.

  The dispersion due to particles of diameter about 10^{-3} and 10^{-2} μm present in the atmosphere (for example dust) is called *Mie scattering*. There is not strong dependence on the wavelength of the light in the optical range, where the light wavelength is comparable to the particles diameter. The effect is concentrated in the lower part of the atmosphere.

The lateral distribution of a typical EM shower initiated by a photon of 1TeV (figure 5.4, right) shows a characteristic hump at ∼115 m that does not disappear after the scattering effects. In a hadronic shower, this effect is less visible, due to the large transversal momentum spread of the secondary particles produced in nuclear reactions.

The final spectrum of Cherenkov light seen by an observer at ∼2 km of altitude is shown in figure 5.5. For particles from showers halo, the Cherenkov light peaks in the UV wavelength.

Sources of background light in the night sky

In 1948 Blackett studied, for the first time, the contribution of Cherenkov light to the brightness of the night sky. It was estimated that Cherenkov light contributes with a factor $\sim 10^{-4}$ to the total light of the night sky. Therefore, when observing the Cherenkov light produced by EAS, we have to consider all the other sources of light that can interfere with the detection of the shower images.

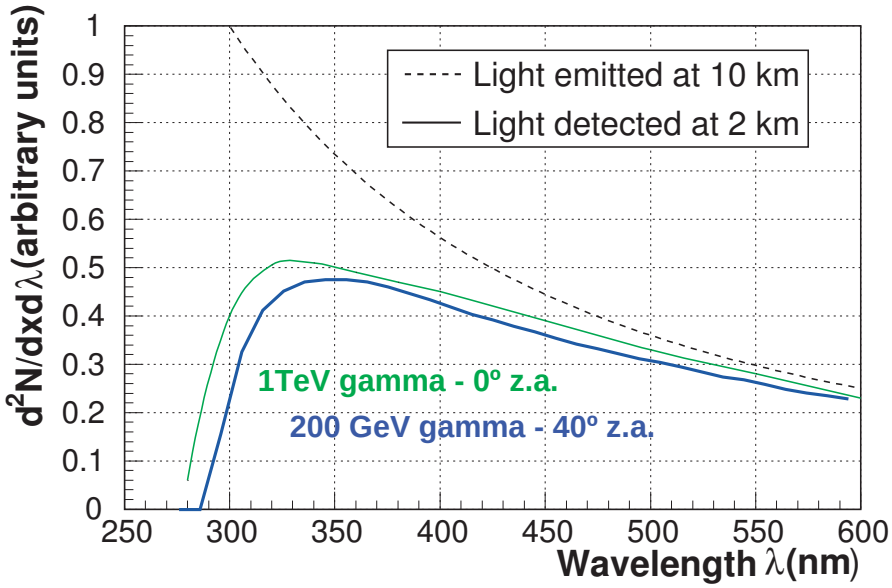

Figure 5.5: *Effect of the absorption of the atmosphere in the spectrum of the light detected at 2.2 km altitude, with respect to the total light produced at 10 km of height. The shower was initiated by a 1TeV photon of vertical incidence, in green, and a 200 GeV photon initiated shower at a zenith angle of 40° in blue.*

The light of the night sky (LONS) has different origins, both artificial (man-made light pollution, usually low near astronomical observatories [2]) and natural (light of bright stars, diffuse sunlight scattered by interplanetary dust, zodiacal light, ionospheric fluorescence, moonlight, aurora borealis [3], etc.). The intensity of the LONS depends on the sky position: it decreases with increasing galactic latitude and the zenith distance. The local concentration of faint stars and galaxies can considerably modify the background light level.

The intensity of the continuum component of the LONS rises by a factor of 6 between 360 and 650 nm, while the Cherenkov light spectrum is decreasing as $\lambda^{-2}d\lambda$. Diffuse galactic light, zodiacal light and faint starlight contribute to the continuum background level [4].

The spectrum of the LONS in La Palma has been measured [108] in the visible range to be ∼0.12 photons/(s m^2 nm arcsec^2) in the U and B band. During moonless nights, far from the bright galactic plane, the background light flux in the visible range (300-600 nm) has been calculated in [109] to produce an average

[2]On the island of La Palma the light pollution is controlled by the local law called 'Ley del Cielo'.

[3]The auroral light is important at geomagnetic latitudes >40°. The island of La Palma is located at geomagnetic latitude ∼20° N.

[4]There are only few lines composing the discrete part of the LONS spectrum in the visible wavelength range, due to molecules of O_2 (557.7 nm line) and OH band at ∼560-590 nm

of ∼0.15 phe/ns for a 0.1°∅ pixel of the inner part of the MAGIC camera. In the calculation, the LONS spectrum has been convoluted with the PMT quantum efficiency, as a function of the wavelength.

The presence of the moon and its phase increase the brightness of the night sky. Observations during the presence of the moon are nevertheless possible depending on the moon phase and angular distance to the telescope FOV. The influence of the moonlight is minimum at $\sim 90^\circ$ distance.

The background light level can affect the shape of the recorded events and the energy threshold of the telescope. The shower images appear as a fast pulse of light, on top of the background level. The pixels containing Cherenkov photons must be distinguished from those with just background light. This operation is called image-cleaning and will be described in chapter 6, together with the effect of background light in the image parameters.

Observations during moonlight have been successfully carried out with the HEGRA CT1 telescope. Different levels of background must be treated separately, having different characteristics. They will be described later. MAGIC observed the Crab Nebula, located inside the galactic plane (high diffuse background light). 1ES1959, on the other hand, is located at high galactic altitudes. This must be taken into account when comparing results.

5.2 Monte Carlo simulation of EAS and the detector response

The main goal of the analysis of data of IACTs is the reconstruction of the characteristics of the detected γs, after their selection among the hadronic background images. The small ratio between gammas and hadrons in the cosmic ray composition makes the analysis of data recorded with IACTs like looking for a needle in a haystack.

The processes going on in the atmosphere during the development of EAS have a high degree of complexity. The huge number of parameters involved in the detection makes the Monte Carlo simulation a key point for the study of the EAS of different origin.

What do γ-ray-initiated showers look like when seen by the camera of a IACT? It is not possible to calibrate and characterize the response of the detector with a *test beam*, a controlled flux of known particles, to study, in controlled conditions, the reconstruction power of the analysis. The Monte Carlo simulation of the detector response is the essential tool to understand the capabilities for γ-hadron separation and parameter reconstruction.

The simulation of EAS is based upon a program called CORSIKA [110] (version 6.019 for MAGIC, version 5.62, 5.94 and 6.1 for CT1 [5], VENUS and Ghe-

[5]Showers at 15°, 30° were simulated with CORSIKA version 5.62 , at 45° were simulated with CORSIKA version 5.94 while for showers simulated at 20°, 27°, 32°, 55° and 65° the version 6.1 was used.

isha for hadronic interactions, EGS for EM showers, earth magnetic field effect included), which uses experimental cross-sections and complex atmospheric models. Each particle is treated individually, when calculating tracks and interactions. We can therefore take advantage of the information delivered regarding the number of Cherenkov photons arriving at the detector height. In table 5.1 it is possible to find informations about the simulated events used in this work.

Table 5.1: *Parameters of the simulations used for the analysis of the data presented in this work. (*) In the final analysis, the energy spectrum has been weighted with the correct coefficient.*

MC simulation parameter	HEGRA CT1	MAGIC
Primary particles	photons	photons
Energy range	50 GeV - 30 TeV	10 GeV - 30 TeV
Spectrum	$E^{-1.5}$ (*)	$E^{-2.6}$ (*)
Zenith angle range	15° - 55° (discrete)	36° - 46° (continuum)
Max. impact parameter	250 m - 550 m	300 m
N. of simulated showers	$\sim$ 260 k	$\sim$ 4.8 M
N. of events after trigger	$\sim$ 40 k	$\sim$ 127 k

Detector simulations include the effect of the mirror reflectivity, of light collectors, the gain of PMTs and the full electronic chain and electronic noise. The background light (LONS and bright stars) can also be added to the image of the simulated shower as it appears in the detector. The simulation of the noise is done so that it matches the actual observation conditions of the data to be analyzed.

5.2.1 Differences between simulated γ and hadron induced showers

The MC simulation allows us to study in detail the characteristics of the showers and their detection by the telescope, in order to be able to identify the primary particles. As described in section 5.0.1 and 5.0.2, the physical processes involved in EM and hadronic showers are different. This fact shows up also in the geometrical shapes of the showers and their images.

For hadronic showers:

- the interaction length for protons and mesons in air is about 3 times longer than for photons. Hadronic showers develop deeper into the atmosphere.
- the mean transversal momentum of secondary particles of hadronic interactions is 0.3 GeV/c, significantly larger than in EM showers
- there are large fluctuations in the shower development, due to the large interaction length, the number of particles involved and their large transverse momentum variation

- about one third of the total energy goes into EM sub-showers in each hadronic interaction
- muons are present, while they are mainly absent in photon-initiated showers
- elastic scattering processes can be neglected as they do not basically change the direction and do not contribute to secondary particle production.

For EM showers:

- there is a limited variety of particles that compose the showers (e^+, e^-, γ, rarely hadrons), with very small transverse momentum (particles close to the Cherenkov threshold), thus the EM showers are laterally much more compact
- the main processes that widen the showers are the multiple scattering with the atmospheric particles and the effect of the earth magnetic field
- the energy threshold for EM showers is, in general, lower than for hadron induced showers, since a larger fraction of the primary energy is transformed into Cherenkov light
- EM showers have the same direction as the emitting source, while hadronic showers ($E<10^{19}$) are isotropically distributed, because they are randomly deflected by the galactic (or extra-galactic) magnetic fields,
- the fluctuations in the shower are, in general, much smaller than that in proton showers.

As previously mentioned, not only photons can produce EM showers: cosmic electrons and positrons induce EAS with the same characteristics of photon induced EAS. They can be considered therefore a dangerous background for γ-astronomy with IACTs. The situation is not so critical because the spectrum of electrons and positrons incident at the top of the atmosphere is steeper than the spectra of protons and nuclei, as shown in figure 5.6 [113] (the positron fraction is about 10 % in the region <20 GeV). In addition to the small expected rate, as charged particles they are also deviated by magnetic fields; thus they have the same isotropic arrival distribution of hadrons.

5.2.2 The imaging technique

CR are producing flashes of Cherenkov light in the presence of the night sky background light. The quasi light speed development of the EAS produces a very short Cherenkov pulse, in the order of ns, dependent on the number and kind of particles involved. Typically, the photons of an EM shower have a time spread of $\sim$3 ns (FWHM), while the light from hadron-initiated showers have a slightly wider time spread, up to 10 ns. On the other hand the LONS has a steady flux, with only statistical fluctuations. Therefore it is possible to detect the weak but fast Cherenkov light flashes in the presence of the large LONS flux.

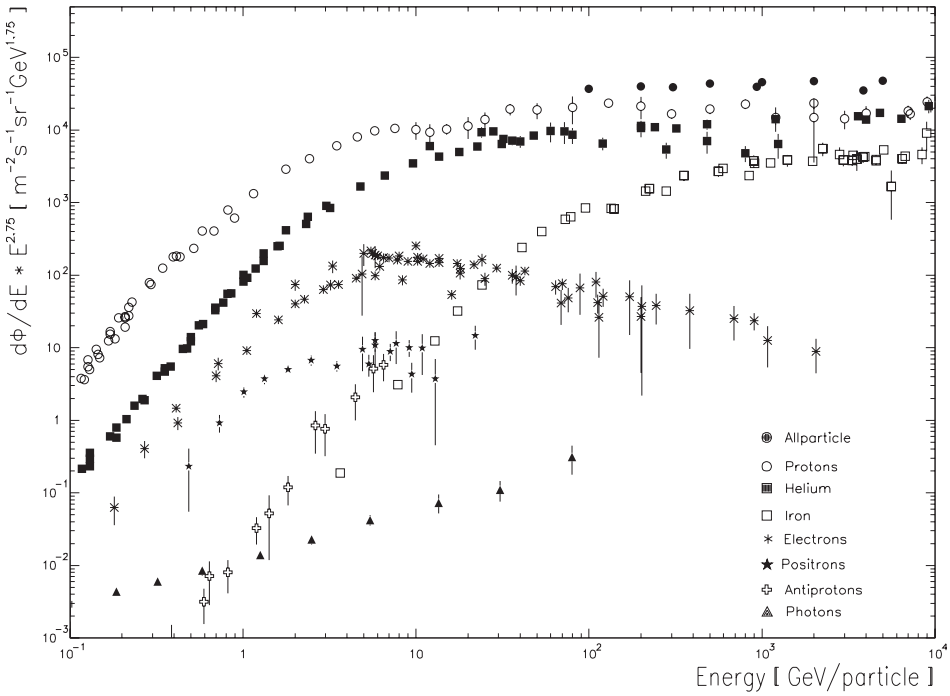

Figure 5.6: *Combined differential spectrum of electrons and positrons, compared with the spectrum of protons and other CR particles, multiplied by $E^{2.75}$ (taken from [114]). For a more recent measurement of the $e^{\pm}$ differential spectrum in cosmic rays, see [115].*

The detection of Cherenkov pulses is possible with a simple light collector and a PMT. Such a simple detector has a high energy threshold, it can only trigger on some hundreds of TeV CR showers, where hadronic particles largely dominate the detected events. The most challenging task consists of identifying the shower original particle.

The lack of discrimination power between γ-showers and hadronic showers made the identification of γ-ray sources only from the anisotropy in the showers' arrival direction impossible for almost 40 years, i.e., from the first detection of CR showers in Cherenkov light by Galbraith and Jelley, until the identification of the first γ-ray source in 1989 [2].

The first source that broke the threshold of the 5σ of signal significance above the background, necessary to claim a discovery, was the Crab Nebula, the strongest steady γ-ray source in the northern sky. The detection of CR showers with the imaging technique is a relatively easy task, but it required many years of experience with scarce results and continuous technological improvements. With the new generation of Cherenkov telescopes it is possible to reach this level in few minutes of observation [6].

[6]The search of γ-rays from the Crab Nebula was unsuccessful for about 20 years. In 1988 it took a few 100 hours of observation to extract an 8 σ signal. In the mid '90s it took about half an

The biggest technical improvement in the telescopes, that marked the step into the new generation of IACTs, was the use of matrices of PMTs in the focal plane of a large light reflector. This permitted the study of the structure of showers initiated by particles of energies lower than some hundreds TeV, in a range of energy where the ratio between γ-showers and hadronic showers is larger.

The main potential of the technique comes from the proportionality between the light intensity and the number of secondary particles of the shower, which is, in first order, proportional to the incident energy. Another big advantage of the technique is that the axis of the shower image aligns with the direction of the initiating particle. The simulation of the reflector and the electronics of the detector makes possible the study of the correspondence between the shower features and the shower image parameters.

As illustrated in figure 5.7, photon positions on the camera correspond to directions of the incident Cherenkov photons. For a γ-initiated shower, whose axis is usually parallel to the telescope axis, photons emitted high in the atmosphere are reflected close to the camera center, while the shower tail image extends towards the camera edges. The quantity of collected light is then correlated in first order to the number of particles producing Cherenkov light of the EAS, falling inside the FOV of the detector.

The features of the detectors have to take into account all the mentioned properties of EAS. The size of the pixels in the camera have to be small enough to resolve the different shower shapes. The study of the shower shape can also guide the design of a topological trigger, in order to limit the accidental triggers coming from fluctuations of the LONS.

The characteristics of the shower image can be washed out by many factors, both due to the detector (pixels size, limited FOV, limited trigger capability, imperfections of the reflector, etc.) and due to environmental conditions, such as the presence of background light in the galactic plane or bright stars in the FOV. Fluctuations therefore influence the widening of the possible values a shower development can deliver and its identification becomes more difficult. To cope with all these factors, Monte Carlo studies on the shape of images of different origins are carried out and used for the optimization of the main parameter reconstruction, like the detector effective area, the energy and the impact parameter of the primary particle. The detection of strong γ-ray sources allows us to obtain quite pure samples of γ-shower images from recorded data, improving the analysis potential.

The discrimination power of the first Cherenkov detectors improved when the image resolution reached the point where it was possible to find differences between γ-images and hadronic showers. The main shower parameters used for the γ-hadron separation are described in the following section.

---

hour for a 5σ signal with the HEGRA CT System. This time is now reduced to 2-3 minutes with MAGIC.

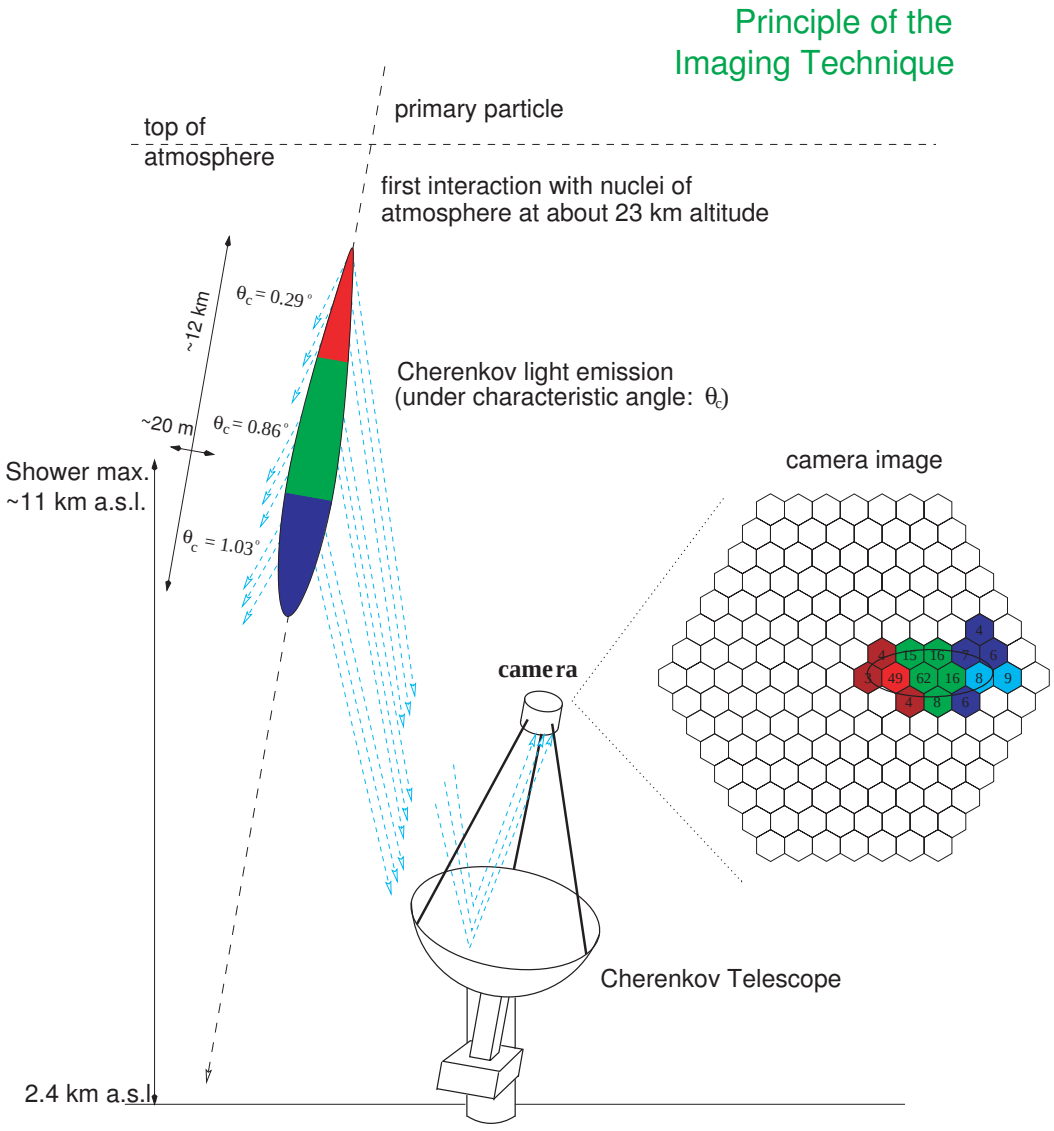

Figure 5.7: *Sketch of the imaging technique and the formation of the shower image in the HEGRA CT1 camera.*

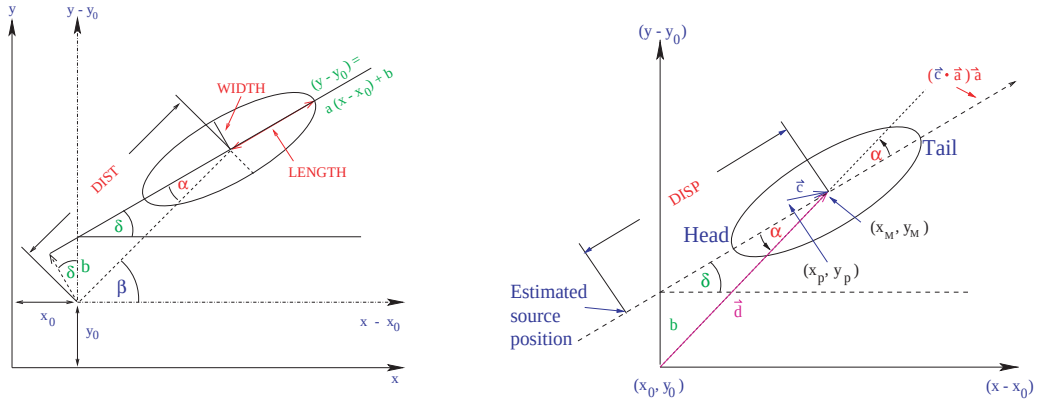

Figure 5.8: *Scheme of the parameterization of the shower image.*

How to describe showers images: the parameterization

Images recorded with IACTs are first analyzed by calculating the moments of the light distribution. The signal, expressed in number of photons N_i in every pixel of coordinates (x_i, y_i) in the camera system, is weighted according to the total signal in the image: $w_i = \frac{N_i}{\sum_k N_k}$. The shower image is parameterized as an ellipse, as shown in figure 5.7 . The moments of the image are calculated after rotating the system of coordinates to an angle δ, in order to have the coordinates along the axis of the ellipse (see figure 5.8).

The most commonly used image parameters are:

SIZE number of photons (or photo-electrons) in the shower image [7]. In the first approximation, the number of photons detected is directly proportional to the primary particle energy. The proportionality is a function of the impact parameter. Up to 120 m, the dependence on the impact parameter is very weak for energies up to a few TeV.

LENGTH half length of the major axis of the shower ellipse. The length of the image is correlated with the longitudinal development of the shower.

WIDTH half width of the minor axis of the shower ellipse. It is a parameter correlated with the transversal development of the shower. The larger transversal momentum in hadronic interactions increases the width of the images of hadronic showers. It is therefore an important parameter for γ-hadron separation.

CONCn $(n = 1, ..., 7)$ fraction of photons contained in the n brightest pixels. It provides information about the shower core.

[7] The number of photo-electrons is a good estimate of the number of incident photons. In a inner pixel of MAGIC 1 photon = 0.18 photo-electrons.

M3LONG third moment of the image along the shower axis. It is positive when the image of the upper part of the shower (head) is closer to the camera center than the image of the lower part of the shower (tail).

ASYM asymmetry of the distribution of photons along the major shower axis. This parameter can help in the identification of the part of the shower corresponding to the maximum development and the shower head-tail orientation. It represents a vector between the image center of gravity and the pixel with the strongest signal.

LEAKAGE fraction of signal distributed in the most external camera pixels ring, with respect to the total SIZE of the image. High LEAKAGE values indicate a truncation of the shower image, with losses of information: when the shower image is entirely contained in the camera (small impact parameter), the LEAKAGE value is near to 0. This parameter is important for the energy estimation.

Some parameters are calculated with respect to a defined position in the camera, usually the camera center or, in general, the position of the source in the camera FOV. The most commonly used source dependent parameters are:

DIST distance of the shower center of gravity with respect to the reference point. It is in first order the information of the distance between the shower maximum and the telescope axis, correlated to the shower impact parameter. This information is very important to be able to determine the energy of the primary particle.

ALPHA angle between the shower axis and the direction determined by the image center of gravity and the reference point (see figure 5.8). It is one of the most powerful tools for the γ-hadron separation: the images induced by the γ-rays coming from the source point towards the position of the source in the camera.

The combination of parameters is also commonly used to enhance the γ-hadron separation. In figure 5.9 some distributions of the above listed parameters for MC gammas and hadrons simulated for the MAGIC telescope are shown (zenith angle 15°- 30°). The parameters WIDTH and LENGTH have been scaled with the corresponding log(SIZE) value. In plots *a* and *b*, the parameters after the image cleaning are shown for 2 different SIZE bins. Images with large SIZE present, in general, bigger differences between $\gamma$and hadrons.

The difference in parameter distributions between hadrons and γ is used for hadronic background rejection. From the plots, it is easy to see that the parameter with the highest γ-hadron separation power is the parameter ALPHA . In the figure, the absolute value of ALPHA is plotted. Usually, the γ-hadron separation methods take into account, at first, all the parameters, except ALPHA. In figure 5.9(c), the ALPHA distribution is plotted, after applying the optimal cuts for the γ-hadron separation in all other parameters.

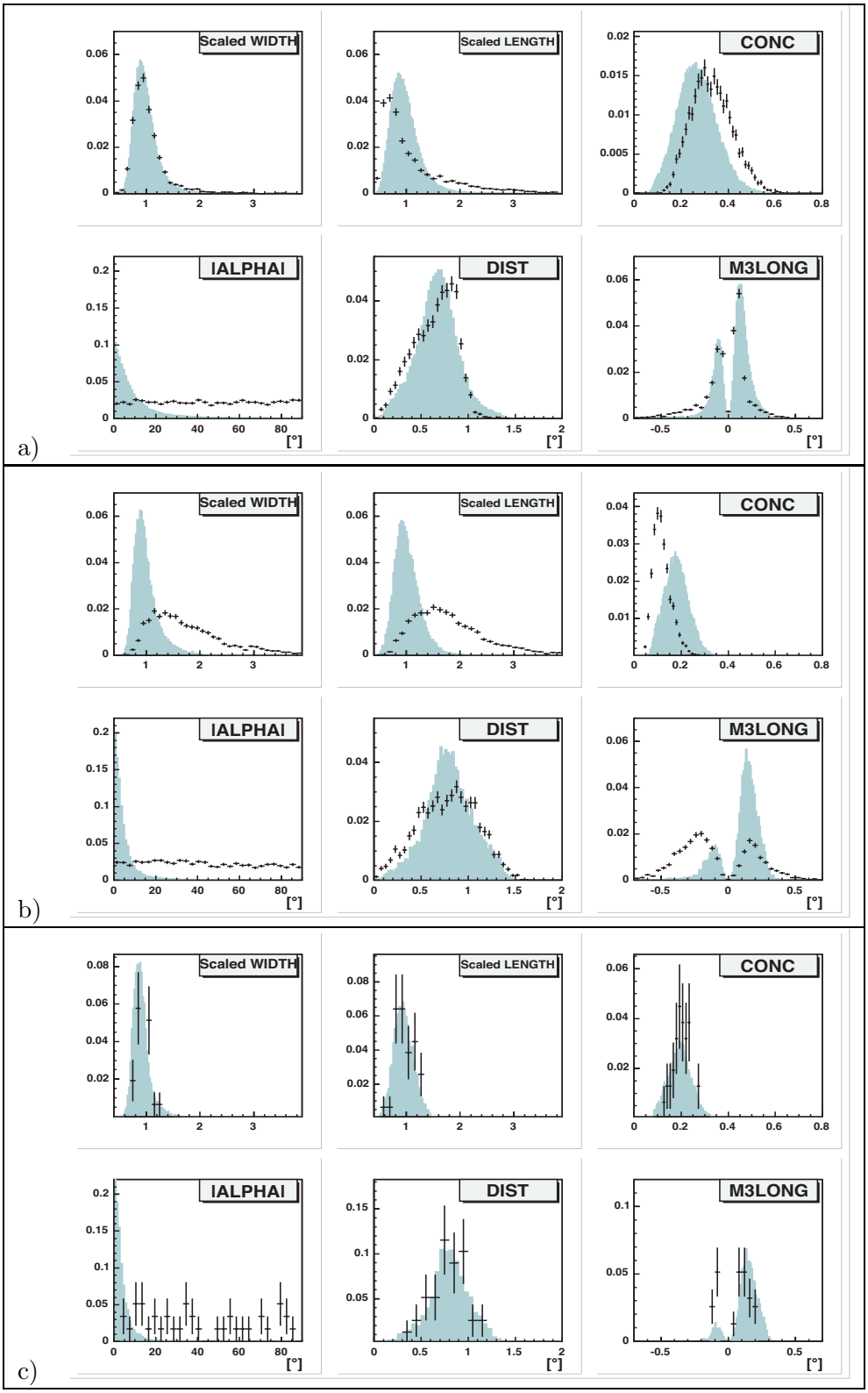

Figure 5.9: *Comparison between MAGIC MC simulated protons (black crosses) and γ(filled histograms) image parameters for different SIZE ranges after image cleaning: a) 500<SIZE<1000 photons, before γ-hadron separation, b) 2000<SIZE<4000 photons before γ-hadron separation, c) 2000<SIZE<4000 photons after γ-hadron separation. MC simulation, taken from internal MAGIC technical note (A. Moralejo , 2004).*

Effective area and flux estimation

The γ-ray flux F seen by an IACT is calculated out of the measured event rate and takes into account the efficiencies of hardware selections and analysis cuts.

The differential flux is defined as:

$$\frac{dF}{dE} = \frac{dN}{dE\, dA\, dt} \tag{5.11}$$

where E is the energy, A is the area and t is effective observation time. N indicates the number of particles recorded from the source, whose emitting flux we want to determine. The number of estimated photon showers surviving the parameter cuts are called *excess events* and their number, with respect to the total number of γevents recorded during the observation time t, defines the telescope efficiency ϵ_{tot}. This number can be obtained with MC simulations, because it is not possible to calibrate the detector with a test beam, as already mentioned.

From the number of simulated showers N_{sim} and the number of selected events N_{sel} surviving the whole analysis chain, we can obtain the total efficiency (E = incident energy; θ = zenith angle; I = impact parameter):

$$\begin{aligned} \epsilon_T(E,\theta,I) &= \epsilon_{trigger}(E,\theta,I) \cdot \epsilon_{cuts}(E,\theta,I) \\ &= \frac{dN_{sel}(E,\theta,I)}{dN_{sim}(E,\theta,I)} \end{aligned} \tag{5.12}$$

where the two components (hardware dependent and software dependent) of the total calculated efficiency have been evidenced.

The effective area A_{eff} is one of the parameters characterizing the sensitivity of a telescope. It is a function of the energy and zenith angle, thus it can be calculated in the impact parameter range (I_{up}, I_{low}) as:

$$A_{eff}(E_k,\theta_l) = \pi \sum_{i=1....N} \frac{N_{sel}(E_k,\theta_l,I_i)}{N_{sim}(E_k,\theta_l,I_i)} (I^2_{up}(i) - I^2_{low}(i)) \tag{5.13}$$

The relation between the number of excess events in a certain energy bin dE and the differential flux dF/dE is:

$$\frac{dN}{dE} = \frac{dF}{dE} \sum_{\theta_i} T^{\theta_i}_{obs} A_{eff}(E,\theta_i) \tag{5.14}$$

where the observations have been subdivided in bins of zenith angle and T_{obs} is the observation time corrected for the dead time (assuming that there are not detector inefficiencies or losses, that are not included in the MC simulation). Inverting this last formula is therefore possible to obtain the differential flux.

Energy estimation

The energy of the recorded events can be evaluated using the image parameters SIZE, WIDTH, LENGTH, zenith angle (and their relations with the impact parameter I), using the Monte Carlo simulated showers, whose energy is known.

The first problem is the determination of the impact parameter that, for a single telescope, can be done in different (not univoque) ways. The assignment of the impact parameter permits the determination of the relative position of the telescope on the ground with respect to the shower axis. The energy is then evaluated as a function of the parameters I, SIZE, WIDTH, LENGTH, θ, with a parameterization defined using Monte Carlo simulated showers.

The parameterization method was used in the analysis of CT1 data, while for the analysis of the MAGIC telescope data, the image parameters were processed using the Random Forest method (see section 6.8.3). The image parameters used in this case are: log(SIZE), DIST, WIDTH, LENGTH, log(SIZE/(WIDTH*LENGTH)), CONC2, LEAKAGE, zenith angle.

The assignment of a value of estimated energy is not the last step before the compilation of the differential spectrum of the data sample analyzed. From the estimated (measured) energy, we have to derive the real energy distribution. Inside one range of estimated energy, we can have contribution from events having a different true energy, as a consequence of fluctuations. The so-called *unfolding* procedure permits the recovery of the original energy distribution from the one that the energy estimator is giving.

The unfolding procedure is supported by so-called regularization procedures, that add constrains to the convolution and limit the fluctuations of the result. The methods of regularization introduce a bias to the unfolded distribution. Some methods are described in [116, 117, 118] and they do not need any assumption on the final shape of the spectrum. The method used in this work, called *forward unfolding*, needs an assumption on the shape of the final distribution (parameterization) and returns the parameter values.

5.3 Dependency of γ-image parameters on the zenith and azimuthal angles of observation

Observations at high zenith angles imply a larger path from the point of first impact of the primary particle with the top layers of the atmosphere to the detector. The EAS can be the subject of larger fluctuations and light losses with respect to EAS, observed when pointing the telescope vertically (zenith angle = 0°). Thus the observation angle has to be taken into account when analyzing the image parameters of the showers recorded.

The dependence of some parameters on the zenith angle is especially strong when calculating the cut efficiency. Usually, the dependence on the zenith angle is negligible for observations between 0° and 30°. Above this angle, the dependence

of the parameters of the image showers to the zenith angle of observation becomes stronger.

In this work I analyzed data at a mean zenith angle of 40°. The range in zenith angle of the observations is only 10° wide, therefore we do not expect a strong difference in the image parameters distributions for the analyzed zenith angles.

In figure 5.10 the simulated Cherenkov photons for the MAGIC analysis at two extreme zenith angles have been analyzed and the image parameters compared. Even though a small difference is already present, the following analysis considers the range 35°-46° as a single bin where image parameters can be optimized for the γ-hadron separation.

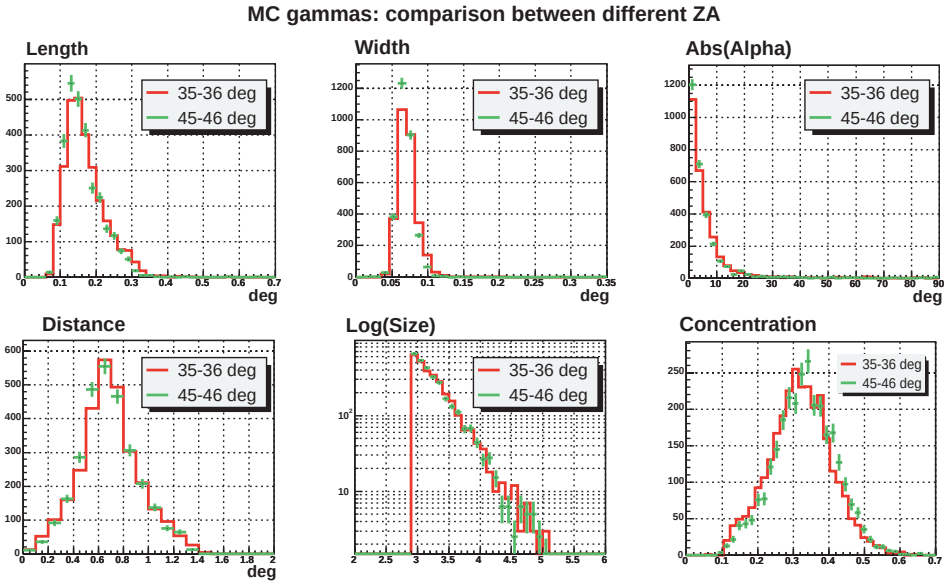

Figure 5.10: *MC gammas simulated at different zenith angles, as indicated in the legend. The image parameters distributions depend on the zenith angle. For the analysis in this work the difference in zenith angle is quite small and the differences in the parameter distributions can be neglected.*

In order to avoid possible biases, we decided to use only data with zenith angle $\sim$36° to $\sim$46° in the optimization of the analysis cuts and for the comparison between the results obtained analyzing the Crab Nebula, a sample of OFF data and 1ES1959 sample.

The azimuthal angle of observation determines the angle between the telescope optical axis (i.e. the axis of the γ-showers produced in the pointed source) and the earth magnetic field. Charged particles, producing Cherenkov light, are deviated from their straight path when their energy is not too high and when their velocity direction has a component perpendicular to the magnetic field. The distribution of Cherenkov light from shower particles traveling in East-West direction is therefore

influenced by the earth's magnetic field. MC studies using showers simulated for MAGIC (internal note) show that the effect is negligible when the energy of the primary particle is >100 GeV for observations at small zenith angles. In the absence of better choices, in the analysis of the MAGIC data presented in this thesis, the MC γ-showers produced at azimuthal angle 0° have been used for the analysis of 1ES1959 (mean azimuthal angle -15°), and for the optimization of the cuts to the Crab Nebula sample, even though the mean azimuthal angle in this case is $\sim$90°. The effect of this discrepancy in the Crab Nebula result has not been taken fully into account, since the main goal of the work is the analysis of the AGN 1ES1959.

Studies regarding the influence on zenith and azimuthal angle observational conditions of the telescope in the analysis results are beyond the scope of this work. In this thesis the MC simulated images are considered to contain all the necessary information to perform a correct analysis of 1ES1959.

Chapter 6

Analysis of data taken with Cherenkov telescopes HEGRA CT1 and MAGIC

In this chapter I will give an overview of the analysis technique for the stand alone Cherenkov telescope MAGIC, which can also be applied to HEGRA CT1 data. The technical details of the analysis of HEGRA CT1 data are described in [96] and here only some of the main points of difference with MAGIC will be given. The data analysis techniques used for the MAGIC telescope data will be described here in more detail. The standard programs for the analysis of the MAGIC data are collected in a package called *MARS* (MAGIC Analysis and Reconstruction Software), working in the ROOT [99] framework. The results presented in my thesis have been obtained analyzing data of two different telescopes and applying to each data set the related analysis programs.

6.1 Introduction

When we observe the sky with a Cherenkov telescope pointing to a γ-ray source, we do not see the high energy photons coming from the celestial object we are looking at.

The way that leads from the digitized signal of air showers to the physics of the source of VHE γ-rays consists of steps that can technically differ from detector to detector, but have a basic common target: the reconstruction of the quantities of the initial messenger particles that generated the recorded images. The strategies followed also have a common base.

The technical elements in use in the MAGIC telescope are schematically presented in figure 6.1. The steps that return the digitized signal are the following.

- The Cherenkov light falling onto the main mirror is focussed on the matrix of PMTs in the focal plane.

- The light that hits the PMT photocathode is converted into an electrical pulse and amplified inside the MAGIC telescope camera.
- The electric pulse from each PMT is converted back into a light pulse and sent through an optical fiber to the data acquisition system.
- The signal is converted back into current by the receiver boards and split into 2 parts: one goes to the discriminator of the trigger system and the other is directed to the FADC system.
  - The trigger system compares the signal level in different pixels: the discriminators fire if the PMT signal exceed a preset value. The trigger then compares the topology of the pixels with a signal above threshold. If the trigger conditions are fulfilled, the recording of the signal can start.
  - The second part of the signal, before reaching the FADC system, is again split into 2 parts: the so-called *high gain* part is amplified ∼10 times and sent to the digitization by the FADCs. The high gain part of the signal saturates when reaches the 250 FADC counts in amplitude (see fig 6.3, the red curve of the left panel). In this case, the second, delayed part, called *low gain*, is recorded. It contains the signal without amplification.
- The signal that reaches the FADC system is recorded: the FADCs signal consists of 30 samples, taken every 3.3 ns and whose amplitude is expressed in digital counts, to be calibrated and analyzed.

The data analysis chain for the MAGIC Cherenkov telescope consists of:

- extraction of the charge contained in the pulsed signal from the recorded 30 FADC time slices;
- conversion of the digitized signal into number of photo-electrons (resp. photons), using the recorded events produced by the calibration light pulser;
- image cleaning, i.e. selection of the pixels containing light which belongs to the shower event. The pixels affected by LONS fluctuations are recognized (see section 6.5) and rejected;
- image parameter calculation (described in 5.2.2);
- γ-hadron separation: the image parameters are analyzed to distinguish γ and hadronic shower images. The images induced by cosmic, charged particles, that are background for us, are much more numerous than those induced by γ-rays;
- extraction of the excess signal over the background, using statistical methods.

The final step consists of the energy estimation which is needed for spectrum calculations and the evaluation of γ-ray flux as a function of time. The calculation makes extensive use of MC simulation and is described in section 5.2.2.

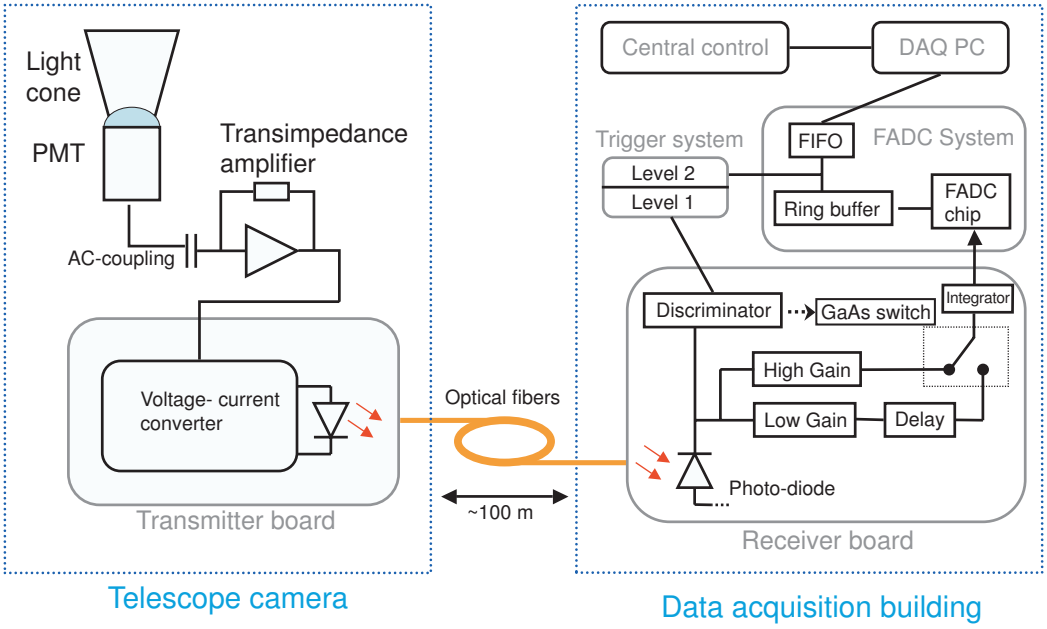

Figure 6.1: *Schematic description of the chain from the light collected at the PMT photocathode of the MAGIC telescope camera to the recorded digitized signal corresponding to the initial light pulse. For the description, see text.*

6.2 Format and classification of data

During the normal operation of the Cherenkov Telescopes MAGIC and CT1, raw data are stored in three different kind of files: *calibration, pedestal* and *data* files, filled during telescope operation.

Data runs The telescope is pointed to the source under study and data are recorded when a trigger occurs. The trigger of MAGIC is activated when the signal in a group of 4 next-neighbor pixels exceeds a fixed value within 5 ns. The data of 30 time slices are stored in units of digital counts (see section 6.3.1).

Pedestal runs The information on the LONS fast fluctuations is essential to catch the rapid and high variations of the signal induced by atmospheric showers. Due to the AC-coupling (see figure 6.1), the part of the noise producing continuous current in the electronic chain is suppressed; only the fast variations produced by the noise sources are recorded.

Information of the light of the night sky (LONS) and other sources of noise is taken during a so-called pedestal run. The trigger is activated randomly, when there are not showers in the observed FOV. The analysis of those data,

allow us to determine the baseline of the signal and its fluctuations (see section 6.3.2).

Calibration runs The photon sensors and the electronics readout chain is not perfectly stable. The conversion factors can vary by up to 10% over a night and thus needs to be calibrated [1]. To determine the conversion factor of the recorded signal from ADC counts to photo-electrons and finally to photons, a light pulser with a series of ultra-bright LEDs, installed in the center of the telescope reflector, emits short pulses of light of a known wave-length (UV, blue, green or red). The response of the camera to the known light intensity from the calibration box is evaluated. In addition, the short pulses allow us to synchronize the different channels of the FADCs, which is essential for timing studies and trigger coincidences (see section 6.3.3).

In CT1 and during the commissioning phase of MAGIC, data, calibration and pedestal runs were taken at fixed time intervals and analyzed.

The readout of MAGIC allows us to extract the pedestals directly from data runs. As can be seen in figure 6.2, only part of the available FACD slices contain the signal. The other part of the total recorded time can be used to extract the pedestal information, as explained in section 6.3.2.

During data taking, calibration flashes are periodically generated at a given frequency and recorded. Later, they can be extracted from the data files and analyzed during the offline analysis, as explained in section 6.3.3.

In this work, the analysis of data taken at the end of commissioning phase of the MAGIC telescope is presented: different types of runs have been taken and analyzed. As the readout system was still undergoing fine tuning, the trigger conditions and calibration procedures were frequently changed without proper documentation, because a standard procedure for data taking and analysis was not yet defined.

At the moment the MAGIC telescope is taking only data runs, which, however, also contain the calibration and pedestal information.

In CT1, the signal of every pixel was integrated over 30 ns, thus it was not possible to extract time information. Dedicated laser pulse runs to calibrate the signal and pedestal runs were taken before every data run.

6.3 Calibration of the signal

The digitized signal for each PMT must be converted from FADC counts to the number of photons that produced the signal. We need to know the *charge*, in FADC counts, produced by the photons hitting the PMTs, and the conversion factors.

[1] Dominant sources of drift are the gain of the PMTs, the preamplifiers and the analog signal transmission, all being sensitive to temperature changes.

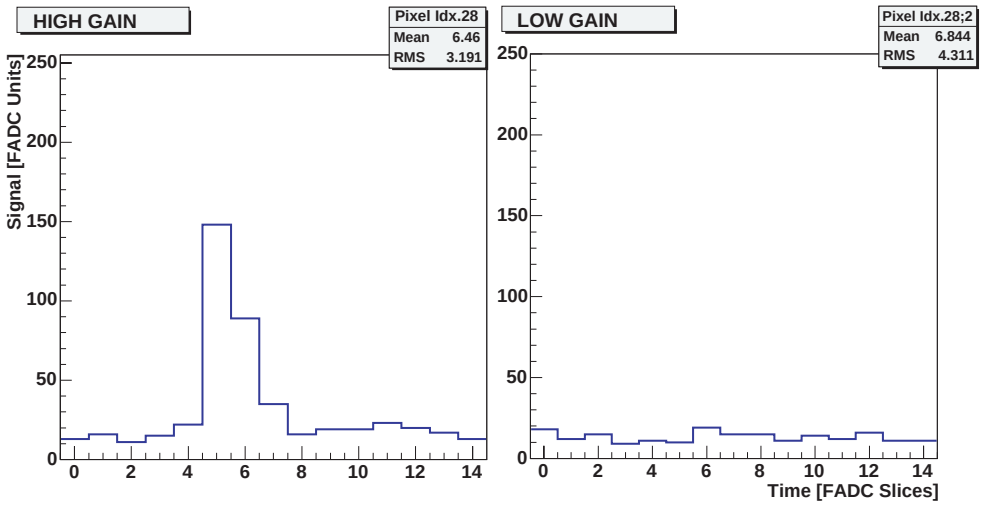

Figure 6.2: *MAGIC: FADC sampling of the signal recorded at one pixel. The sampling consists of 30 slices. Left: High gain signal, in the first 15 slices. Right: low gain signal, in the second 15 slices. Since the high gain signal does not reach the saturation level of 250 FADC counts in amplitude, the low gain section only contains information about the pedestal. These data are therefore used to calculate the rapid fluctuations of the FADC baseline. Note that in case no saturation occurs, the trigger logic does not switch over to the low gain branch, but still records the high gain branch, in this case the noise.*

6.3.1 Extraction of the signal

The raw data contain the digital information about the photon-induced PMT pulses for each pixel and triggered event. In the raw MAGIC data format, this information is not recorded in the identical format as of CT1: the electrical pulse generated by every PMT is amplified, stretched and, when the saturation limit is reached, the no-amplified signal is delayed, as previously mentioned. The 300 MHz FADC operates 30 sampling of the signal in a time window including the trigger and the eventual low gain signal. It is important to notice that this information allows us to reconstruct the time-dependent signal in different PMTs, which can be used to discriminate between the shower image from different generating particles. The time information has not been used in the analysis presented in this work.

There are different methods in the MARS analysis software that can be used to extract the information from the FADC signals. The different methods aim to minimize the effect of the night sky background (NSB) light on the estimate of the integrated FADC signal. In this work, two different methods of signal extraction have been used. They are called *sliding window* and *digital filter* [119]. The reader is referred to figures 6.2 and 6.3 for illustration.

Sliding window The extracted signal is the sum of the content of the n consecutive FADC slices around the slice with the maximum signal. The position

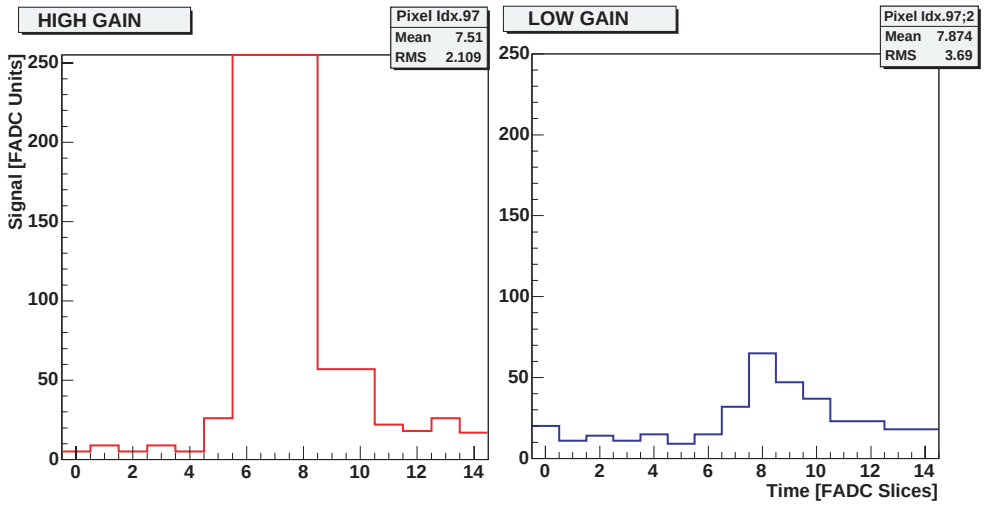

Figure 6.3: *FADC sampling of a large signal from one pixel of the MAGIC telescope. Left: high gain signal. The signal reaches the maximum of 250 FADC digital counts. Right: low gain signal: the same signal is recorded after a certain delay and with a reduced amplification. Note that the high gain signal (left) is amplified by a factor 10 with respect to the low-gain signal (right).*

of the signal is not fixed and it can change from pixel to pixel and from event to event, depending on the arrival time of the Cherenkov light in different regions of the camera. The number of integrated slices n can be chosen in advance and represents the width of the time window where we expect to find the pulse.

Digital filter Also in this case, the number of slices to be summed up can be chosen as a variable parameter. The extracted signal is calculated as the weighted sum of n consecutive FADC slices. The weights are determined by taking into account the expected pulse shape, known by the pulse shaper and from MC simulation. In this way, the effect of a possible noise contamination on the extracted signal is strongly reduced.

It should be noted that the search for the maximum signal in the 30 FADC slices introduces a bias in the small signals, since positive fluctuation of the background LONS are favoured. The signal produced by the calibration pulse in MAGIC is typically 4-6 FADC slices long.

6.3.2 Pedestal evaluation

Not only Cherenkov photons contribute to the recorded signal: light coming from the stars and diffuse light of the night sky, as well as artificial light accidentally produced near the telescope, contribute to the pedestal fluctuations. At the final

signal level there is also another source of pedestal RMS: the noise of the electronic chain.

The pedestal value can be calculated in different ways. The mean pedestal can be evaluated as the mean signal (with its corresponding RMS) per FADC slice recorded during dedicated pedestal runs. The pedestal can also be evaluated from the recorded FADC signal in the low gain region; if not, switch-over occurs, i.e. the high gain signal is small.

For a correct subtraction of the pedestal, the evaluation should be done often during data taking (in CT1 data: after every 20 minutes long data run, in MAGIC at least every time a calibration run is taken). As already mentioned, in MAGIC the pedestal and its fluctuations can be derived directly from data runs. In fact, as figure 6.2 shows, only a few ns of the total time recorded contains the signal we want to analyze: in the presented example, the signal is located between slice number 4 and number 8 of the high gain part. The remaining FADC channels, outside the slices affected by the signal, can be used to extract information related to the pedestal RMS. Technically, we extract the mean pedestal for each pixel on average over 500 measurements in the low gain region when the high gain signal is not saturated (see the left panel of figure 6.2).

The LONS affects the observations, as explained in the previous chapter. In particular, moonlight significantly limits the duty cycle of a Cherenkov telescope. However, CT1 was able to operate during nights with partial moonlight. This was possible by reducing the high voltage (HV) setting of the PMTs in the camera, so as to avoid increasing the PMT direct currents (DC), caused by the higher background light. This reduction of HV in CT1 maintained the linear response of the PMTs, but strongly reduced the signal from fluctuations of the continuous light. Therefore, the energy threshold of the recorded events rises with respect to normal observational conditions. A separate analysis is followed for the subset of data taken during the presence of moonlight.

6.3.3 Calculation of conversion factors

The integrated signal, recorded in FADC counts (here also called *charge*), has to be converted to the number of photons that hit the PMT. This is done in the calibration process.

The calibration starts with the so-called *flat fielding*: the same amount of light per pixel should give the same reconstructed signal output in each pixel. This is done by illuminating the camera with pulses of strong uniform light and adjusting the output amplitude of each pixel with respect to the others [2].

The absolute calibration consists of calculating the conversion factor from digital charge (in FADC counts) to photons. The conversion factor is given by two values: the quantum efficiency (QE) of each PMT (QE: ratio of photons that are converted

[2]This is performed at first order at the 'hardware' level, by changing the bias voltage of the PMTs and, in a second moment, by applying a software correction factor in order to adjust the remaining small variations.

to photo-electrons by the photo-cathode and focused to the surface of the first dynode) and the PMT gain. The gain of each PMT depends on the applied HV and decreases slightly with time and has to be frequently readjusted.

In MAGIC we used also different methods to derive the conversion factor: F-factor (also used in CT1), muon events, or using a *blind pixel*, currently under installation.

The currently used method is based on the excess-noise factor, also called F-factor. We convert the signal charge in number of photo-electrons (phel) using the formula:

$$N_{phel} = \frac{\langle Q \rangle^2}{\sigma^2} F^2 \tag{6.1}$$

F is a quantity representing the specific excess noise of the used PMTs (F = 1.15). $\langle Q \rangle$ is the mean digital charge for a pixel (in FADC counts) calculated after pedestal subtraction from the recorded calibration pulses and σ^2 is the reduced variance, calculated from the charge distribution and corrected for the contribution of the pedestal variance: $\sigma^2 = \sigma^2_{\langle Q \rangle} - \sigma^2_{ped}$.

In this way, it is possible to calibrate the gain of the PMTs. Finally the conversion factor ($c.f.$), is obtained:

$$c.f. = \frac{N_{phel}}{\langle Q \rangle} = \frac{\langle Q \rangle}{\sigma^2} F^2 \tag{6.2}$$

While for CT1 data the signal is finally given in terms of photo-electrons, in MAGIC the signal content is given in terms of photons hitting the PMTs. The conversion factor between number of photo-electrons and photons is applied as a general factor for all pixels. This factor takes the losses of all the optical elements (mirror, protection window of the camera, light cones, and focusing losses of electrons inside the PMTs) into account. For MAGIC it has been estimated that the number of photo-electrons is 18% of the number of initial photons reaching the PMT cathodes.

6.4 *Bad pixels*: definition and treatment

Some pixels cannot be calibrated, due, for example, to hardware problems in the PMTs or in the electronics. Those pixels have to be somehow recognized in order to find possible major problems in the hardware, and be treated in order to avoid biases in the analysis results.

The pixels affected by hardware problems show an extracted digital charge Q from a calibration run with too large fluctuations. Too few measurements or too low extracted mean charges are also signs of hardware problems. Software filters can flag the pixels that cannot be calibrated and they are called *bad* pixels.

After calibration of the data, there are other anomalous conditions that can induce us to define the pixels as *bad*. When the response of a PMT is very different from the others, due to small fluctuations in the hardware behaviour, a deviation of the pedestal RMS from the mean value in the camera will show up. When a star illuminates a pixel (usually not more than 2 pixels are affected by the light of one single star), the DC in the pixel increases, together with the pedestal RMS. Those pixels can also be included in the list of *bad* pixels.

In order to cope with these problems a dedicated software (classes of MARS) was developed:

- after calibration, the mean pedestal RMS for each pixel is calculated;
- a lower and an upper threshold can be set for the definition of the *bad* pixels: if the pedestal RMS of a pixel does not fulfill the requirements, the flag is set as ON ($\equiv$ bad pixel);
- some pixels are also included in the *bad* pixels list if they are used for special purposes (for example, the central pixel), or when known that they are broken.

The *bad* pixels can be treated in two different ways:

- they can be excluded from the calculation of the image parameters. Their signal is therefore ignored in the following analysis steps;
- their signal, pedestal and pedestal RMS can be substituted with the average quantities, calculated from the surrounding pixels (if none of them classified as *bad*). The pixels with their new content are then included in the regular analysis chain.

The software check of bad pixels has to be strictly correlated with the hardware check of the problems.

The software check on the pedestal RMS gave good results in recognizing the pixels affected by problems or star light. In the 1ES1959 field of view, for example, there are two faint stars, quite close to each other, whose position could be critical if causing accidental trigger, because they are aligned and pointing to the camera center, thus simulating γ-showers [3]. The camera images in figure 6.4 show the MAGIC camera with DC signals, the position of the stars in the field of view of 1ES1959 during data taking and finally the automatically recognized bad pixels superimposed.

6.5 Image cleaning

After calibration, the next analysis step is to recognize the pixels that contain information about the shower and to reject those pixels where the signal is most

[3] The stars, belonging to the constellation of Draco, have magnitude larger than 5. Their effect in the data has been checked to be negligible.

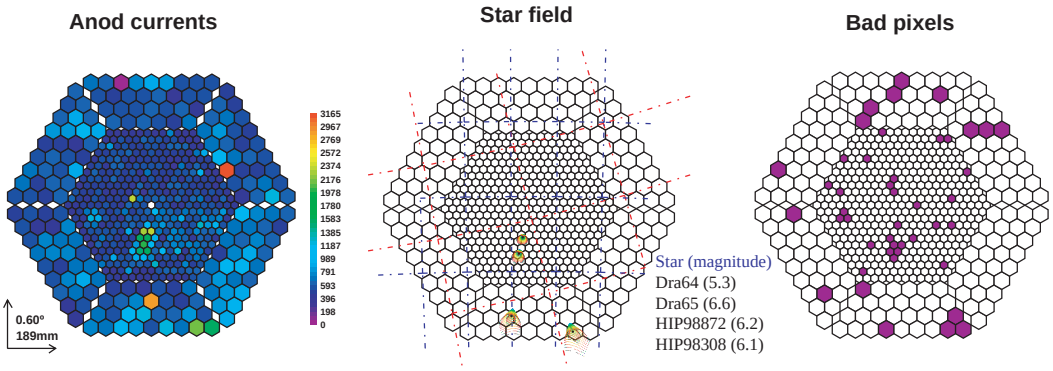

Figure 6.4: *MAGIC camera display. Left: DC signals(real data). Center: Star field, as read from catalog and projected in the camera plane. Right: Bad pixels recognized by the software by reading the pedestal RMS of the pixels (in this case, a very strict condition was chosen, in order to show the effect of the stars in the FOV: the stars are too faint to interfere with the data analysis).*

likely due to fluctuations of the night sky background light. This operation is called *image cleaning* or *tail-cut* (see figure 6.5). The surviving pixels are classified as *core* pixels, that pass a preset threshold and compose the main part of the shower, and *boundary* pixels, for which a lower signal level is allowed, but, as the name says, are part of the image edges connected to the main image.

The following image cleaning methods are applied in CT1 and MAGIC data analysis:

Standard In the standard CT1 analysis, the signal-to-noise ratio is used for the image cleaning. The noise is expressed in pedestal RMS units (called also σ_p). The standard image cleaning procedure consists of defining the *core* pixels as the ones whose signal is more than $3\sigma_p$ above pedestal and which have at least one core pixel neighbor. *Boundary* pixels are kept if they have a signal above $2.5\sigma_p$.

Absolute The easiest way to clean the image is to define a fixed threshold (in number of photons or photo-electrons) for a pixel in order to be part of the image core, and a lower threshold for the surrounding pixels, to be accepted. This method is very simple and does not require the pedestal RMS calculation. It is applied in the MAGIC data analysis.

The general rule applied in the cleaning of CT1 and MAGIC images is that a core pixel will be rejected if it is isolated from other core pixels, i.e. a minimum of two neighboring core pixels are required.

The image cleaning procedure is currently not yet fixed and can have numerous variants, the most common one is to change the required thresholds. Additional

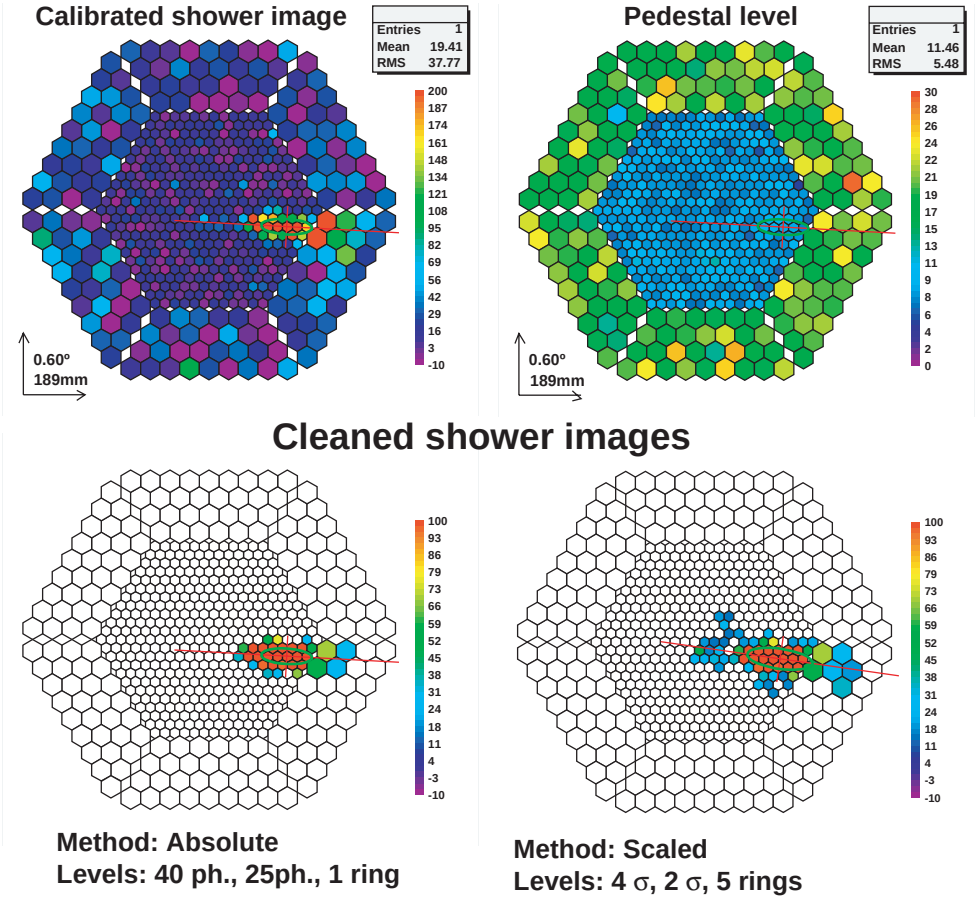

Figure 6.5: *Example of the image cleaning procedure: an event recorded by MAGIC after calibration in the upper left panel, with the corresponding pedestal values for each pixel displayed to the right. The two camera pictures below represent the same event for two different image cleaning methods. As can be noted, the image cleaning procedure clearly affects the image parameters values.*

selections can be done by taking into account the arrival time of the signal in the pixel, or the composition of the shower image in unconnected parts, called *islands*.

Due to the lower trigger threshold of MAGIC with respect to other telescopes, fluctuations of lower energy shower images can easily arise when cleaning thresholds which are too low are applied, thus spoiling the expected compactness of the γ-images. Genuine signal from low energy showers is also expected at a larger distance (in number of pixels) from the image core region, even if the signal is only $2.5\sigma_p$ or less above the pedestals fluctuations [4]. For those events, new analysis features are

[4] A $2.5\sigma_p$ cut seems normally very safe as only one out of $\sim$150 pixels should have a statistical fluctuation in order to pass the acceptance threshold. Studies have shown that the noise is not

needed. Here I describe the new criteria I have implemented in the code for the MAGIC data analysis:

Number of rings The standard procedure consists of checking only the closest neighbors of core pixels. We can check the signal level of boundary pixels a selected number of times, progressively increasing the distance around the core pixels. This allows us to analyze a bigger area around the core of the image.

Democratic cleaning The calculation of the pedestal RMS, needed for the calculation of the signal-to-noise ratio, can be done estimating the average noise of the pixels in the camera (divided in inner and outer pixels in case of MAGIC), and not pixel by pixel, as in the standard procedure.

In case the arrival time information of the signal in a pixel is available, it can be taken into account to reject the pixels' content that do not fulfill the expected timing of the atmospheric shower development.

The method based on the calculation of signal-to-pedestal RMS ratio is effective, but the RMS can be quite different for data taken from sources that are located in the galactic plane [5], like the Crab Nebula, compared to extra-galactic sources, like 1ES1959. Large differences in the pedestal conditions lead to different image parameter distributions, as described in section 6.7. This holds in particular for observations during moonlight. In this case, for CT1 data, the image cleaning is applied with different cleaning levels, empirically derived, in order to obtain the same image parameter distributions, independent from the pedestal noise.

A hard image cleaning (i.e. high threshold values or high pedestal RMS), produces, on average, smaller images than less stringent conditions of cleaning, as shown in the example of figure 6.5.

6.6 Pre-selection of data: filter cuts

After the image cleaning, a first selection of image showers is done, in order to reject data runs or shower events that do not satisfy the selected analysis conditions.

- Event rate: a low rate is an indication of the adverse weather conditions.
- The minimum and maximum number of pixels (core or used) of an image: too few or too many pixels in the image give poor information on the original shower.
- Special software trigger conditions: it is possible to select (for example) calibration events from shower images.

purely Gaussian distributed and large tails are present.

[5] In case of persistent stellar illumination, the HV controller ramps down all PMT voltages and automatically closes the camera lids.

- Muon ring events: the sharpness of the images can be used to check the PSF and to calibrate the telescope.
- Rejection of images accidentally produced by cars illuminating the camera.

6.7 Image parameters calculation

As described in section 5.2.2, the parameterization of the image is done in terms of first, second and third moments of the light distribution, called Hillas parameters [120], from the author that first introduced them in the analysis of IACT data.

From the image shape we can reconstruct the energy and impact parameter of the original shower and also perform the rejection of the hadronic background. The ALPHA parameter has an especially high rejection power: when the telescope is pointing to the source, the γ-rays coming from that direction will produce showers that develop parallel to the telescope axis. They will appear in the camera plane as images with the major axis pointing towards the center of the camera, i.e. they have a small ALPHA angle.

High order moments of the light distribution are also calculated, but they are less efficient in terms of discrimination power.

Low energy particles, close to the energy threshold (under (100 GeV) / (cos $\theta)^{2.7}$) produce images that are not so well structured: the light distribution in the camera is more scattered and the total number of photons in the image is small. In addition, fluctuations from shower to shower are much larger than for higher energy showers. The image parameters have large fluctuations (for example: the orientation with respect to the source position in case of an image consisting of few pixels) and the γ-hadron discrimination power becomes less efficient. New analysis techniques are under investigation to improve the analysis in the interesting energy range below 100 GeV but are beyond the scope of this thesis.

6.7.1 Source position evaluation

The correct calculation of the parameters that depend on the source position in the camera plane, like DIST and ALPHA, needs information on the mis-pointing of the telescope and on the precision of tracking. The mis-pointing must be monitored and checked, both from the hardware and software point of view. This holds in particular for the commissioning phase of telescope operation.

In CT1, a bending correction is applied to 1ES1959 data, depending on the hour angle of observation (see p.xxiv for the definition):

$$\begin{aligned} cx &= (-0.086 - 0.00091 \cdot \text{hour angle}) \ \text{mm} \\ cy &= (-0.083 - 0.001 \cdot \text{hour angle}) \ \text{mm} \end{aligned} \tag{6.3}$$

where the parameters of the functions are empirically determined from the recorded data.

A so-called *star guider* system, which allows us to monitor and correct the pointing is currently being installed in MAGIC. It consists of a high sensitivity CCD camera, installed at the center of the telescope dish. It displays both the section of the sky containing the source and some reference LEDs on the telescope camera. From the many stars in the CCD FOV, the pointing of the telescope is calculated with a precision better than 0.01°.

During the commissioning phase, a different procedure was used: we corrected for the bending of the structure causing mis-pointing by applying a model [121] that uses the star signals in the camera pixels. When the image of a star is focused on a pixel, the anode current of that pixel is larger with respect to the others. We can compare this star map with catalogs and by triangulation, determine the mis-pointing. The anode current information is updated every 10 seconds. The results of the anode currents analysis show that the determination of the source position has a statistical error of $\sim 0.01°$ and that we are able to find stars up to magnitude 8 in the inner part of the camera.

The *false source* method

In the method called *false-source* [122], the camera FOV is divided in a grid and the image parameters that depend on the source position are calculated for each grid point. We analyze both data taken when the telescope points to the source (ON-data) and data taken when there are no γ-ray sources in the telescope FOV (OFF-data). The ALPHA plot of the data sets allows us to calculate number of excess events and significance. In this way we can determine the original arrival direction distribution of the γ candidate events. The disadvantage of the method is that one cannot check short time deviations as from the star images. The advantage is a higher precision of the mean deviation.

The DISP analysis method

Another powerful technique to analyze the recorded images without *a priori* assumptions of the source position in the camera plane of a single IACT is the so-called DISP method. This method is especially convenient in the analysis of extended sources and was successfully applied by the Whipple collaboration [123] and the HEGRA collaboration for the CT1 analysis [124].

The shower image is used to estimate the arrival direction of the shower event (see figure 5.8). The position of the γ-ray source in the camera plane lies on the major axis of the Hillas ellipse at a certain distance to the image center of gravity. The distance, called DISP, is a function of the image elongation and denotes the source position of the initial particle on the sky map (neglecting deflections of the charged particles track by the galactic magnetic field). The elongation is defined as WIDTH/LENGTH. The parameter DISP used in this work for the MAGIC data also takes the SIZE of the image into account:

$$\begin{aligned} \text{DISP} &= \left(1 - \frac{\text{WIDTH}}{\text{LENGTH}}\right) \cdot (a + b \cdot \log \text{SIZE} + c \cdot (\log \text{SIZE})^2) \\ a &= 261 \\ b &= -34 \\ c &= 24.13 \end{aligned} \tag{6.4}$$

(parameters in mm on the MAGIC camera) where the parameters a, b, c are determined with a MC γ sample. For the CT1 data, the parameterization also includes the LEAKAGE parameter as determined by D.Kranich in [124] and used in [125].

The determination of the source position along the image major axis with the DISP is not univoque, because of the *head-tail* ambiguity. The head of the shower is the part that initially develops, high in the atmosphere. The part called tail is the final developmental stage of the shower, closer to ground level and characterized by a larger angular spread of photons. Parameters like ASYM or M3LONG (multiplied by the sign that defines its orientation with respect to the camera center) can help to identify the head of the shower and is, therefore, the favorable one of the two possible solutions. Unfortunately, the asymmetry does not always allows us to completely eliminate the head-tail ambiguity.

The result of the DISP analysis is displayed on a map, indicating the most probable source position in the sky for each event. The excess of γ-ray events would create a peak at the position of the source in the camera plane. The use of the DISP method for the analysis of the MAGIC data is under study but has already given promising results [126].

In the following chapters the DISP method has been applied in its original version (equation 6.4), in order to cross-check the classical analysis result and to identify and correct a possible mis-pointing of the telescope.

6.8 γ/hadron separation methods

In the γ/hadron separation procedure, the images generated by EM showers are selected by means of cuts on image parameter distributions. The technique to distinguish images generated by γ from the ones generated by hadrons is based on the different shower development of γ and hadronic induced showers, which leads to different image parameter distributions (see section 5.2.1). The optimization uses Monte Carlo data, correctly tuned to describe the observed events, or a data sample, particularly rich of γ-showers (typically from the Crab Nebula data or from flaring AGNs).

For the training of the cuts, a sample of γ-induced showers must be compared with hadronic showers. The hadronic sample is normally taken from real observations, i.e. OFF source data. The γ-showers are normally Monte Carlo simulated, because the content in real ON source data is too small and not well known. In

case of having a very strong γ-source, the previously selected γ candidate events can be used for further optimization of the selection criteria.

6.8.1 Static cuts

The easiest way to select γ events is to use the so-called static Supercuts, derived by the Whipple collaboration from MC data [127]. These cuts have also been used for CT1 data and are listed in table 6.1. The cuts take into account the characteristics of the detector.

Table 6.1: *Supercuts applied to CT1 data.*

Parameter	Minimum	Maximum
DIST	0.51°	1.1°
WIDTH	0.07°	0.15°
LENGTH	0.16°	0.3°
CONC	0.4	
ALPHA		10°

Because they select showers with parameter values in intervals with fixed edges, they are optimized for the most frequent showers, which occur at low zenith angle (z.a.) and have small energies. The efficiency of the cuts worsen in different conditions (large z.a., large energies). These cuts can therefore be improved by taking into account the dependency on the energy (like SIZE), the z.a. or the impact parameter of the shower (like DIST).

6.8.2 Dynamical cuts

The shape of the shower images depends on the energy of the primary particle, on the impact parameter and on the observational z.a. The width and length of the shower image are directly proportional to the energy of the shower. For observations at large z.a., the showers develop far away from the telescope and the amount of collected Cherenkov light is reduced as a function of the z.a., because the light is spread over a larger area on the ground level and because of atmospheric losses. Above an impact parameter of about 120 m the image does not more contain light from the shower core. Only light from the shower halo is detectable and the proportionality between SIZE and initial energy degrades rapidly. The distance of the shower image is also far away from the camera center.

The different parameter dependencies are taken into account in the so-called dynamical cuts, listed in table 6.2. The dependencies between the parameters can also be of second order, (Supercuts [128]), such as the ones applied to CT1 data. The limits on the cuts are functions of the parameter SIZE (related in first order with the energy), DIST (in first order proportional to the impact parameter) and

of the z.a. of observation. The three mentioned parameters are independent and they influence the shape of the image in different ways.

Table 6.2: *General formulas for the dynamical cuts applied in CT1 data.*

Parameter	Minimum	Maximum
DIST	D_{low}(SIZE,θ)	D_{up}(SIZE,θ)
WIDTH	W_{low}(SIZE, DIST, θ)	W_{up}(SIZE, DIST, θ)
LENGTH	L_{low}(SIZE, DIST, θ)	L_{up}(SIZE, DIST, θ)
ALPHA		const.

One can either scale the cuts taking into account the parameters' dependence or scale the image parameters WITH, LENGHT and DIST and leave the cuts constant. For this last approach, one calculates the mean value of some image parameters (mainly LENGTH and WIDTH) for every SIZE bin. The parameters are then scaled to the MC derived mean value and the (now static) cuts are optimized in the new variable distribution (Scaled cuts [129]).

6.8.3 The Random Forest method

The multi-parameter space that delimits the γ region can be defined with more sophisticated techniques, using classification methods, now widely adopted in high energy physics. Random Forest (RF) [130] is one of them and has been used in this work for the analysis of MAGIC data for the γ-hadron separation.

- The training of cuts with the RF method consists of using two samples of data, each of them corresponding to one of the categories to distinguish: in our case, a sample of pure photon showers and a hadronic shower sample (usually MC data for γ-showers and real OFF data for hadronic showers [6]).

- The classification of the events is done using a certain number (in our case between 6 and 9) of image parameters, that the user can choose. The parameters must be at least partially independent.

- The RF is then composed of 100 decisional trees, each of them uses 3 parameters, randomly chosen among the selected ones. The trees *grow* in the training, so as to completely distinguish the training samples.

- The events are labelled with a number between 0 and 1 indicating how similar they are to hadronic showers. In our case this label is called *hadronness*. In the training samples, all MC γ have (by definition) hadronness 0, all hadrons

[6] A certain degree of contamination of the samples with events of the other category does not affect the procedure.

1. The hadronness value assigned to the analyzed data depends also on the ratio between γ and hadronic events using for the training samples.

A comparison between RF and other analysis methods such as Supercuts and neural networks has been done by J. Zimmermann [131]. In that analysis, the 1ES1959 and Crab data presented in my thesis were used. RF gave comparable results as neural networks in terms of γ-hadron separation power, and improved results compared to Supercuts, especially at low energies.

6.8.4 Calculation of the significance of the signal

The strongest discrimination power comes from the parameter ALPHA, whose typical distribution after γ-hadron separation is shown in figure 5.9.

The optimization of the cuts in the image parameters is usually done excluding ALPHA. From the ALPHA plot, after cuts in all the other parameters, it is possible to calculate the residual background and the number of γ events surviving the cuts. The γ events normally pop up in the ALPHA distribution as a peak at small angles, as explained in the previous section. Typically, we expect the signal events to have ALPHA $\leq$10-15°.

The behavior of γ images and background can be studied by comparing data taken with direct observations of the source (ON) and OFF-source observations, i.e. with no sources in the FOV. The final number of γ (excess) events is calculated after a cut in ALPHA, by subtracting the number of OFF data, normalized in the region far from the ALPHA peak, from the number of ON data.

The significance S of the signal is calculated by the Li and Ma formula (n. 17 of [132]):

$$S = \sqrt{2}\left[N_{ON}\ln\left[\frac{1+\alpha}{\alpha}\left(\frac{N_{ON}}{N_{ON}+N_{OFF}}\right)\right] + N_{OFF}\ln\left[(1+\alpha)\left(\frac{N_{OFF}}{N_{ON}+N_{OFF}}\right)\right]\right]^{1/2} \tag{6.5}$$

where N_{ON} and N_{OFF} are the number of ON and OFF events respectively and α is the ratio between the ON and OFF observation time.

The availability of OFF data is often limited by the preferred ON source observations. The procedure adopted consists of normalizing the distribution of OFF-data to match the observation time spent looking at the source. This procedure works quite well when the time difference is not big, but is not always the case. Large normalization factors applied to OFF-data cause the amplification of statistical fluctuations.

When looking at the source position, a huge number of events, normally background events, are recorded, but only a very small minority are real photons emitted by the source. The background can therefore be studied analyzing the ON-data themselves. The HEGRA Collaboration widely and successfully used this method in the CT1 data.

The technique is based on the fact that charged cosmic rays are completely isotropic. Therefore the ALPHA distribution is smooth and has a known shape, described by a simple, empirically determined polynomial function. The assumption is that one is able to describe the background shape directly from the ON-data ALPHA plot by fitting the distribution far from the signal region (between $\sim 30°$ and $80°$). The background level is described, extending the fit to small ALPHA values (signal region). The error on the fit can also be taken into account in the calculation of the significance of the signal.

The application of this method and the comparison to the OFF data gave good results, shown in figures 7.2 and B.5. There are some *a priori* uncertainties in determining which function the ALPHA plot for background events should look like. This is a controversial point, since, in principle, the shape of the ALPHA plot can vary with the cuts applied to the data and with the characteristics of the detector, in particular with the camera geometry and the trigger area. In all the measurements that we have done, we tested the quality of the fit for the extrapolation of the BG from the ON-data with a suitable parameterization of the OFF-data sample (selected according to z.a., period of observation, telescope conditions,...). The significance is then calculated with the Li and Ma formula using information only of the ON-source: the number of excess events is determined directly from the histogram entries, while the number of OFF-events are determined by the fit (with its uncertainty).

Chapter 7

Results of the analysis of HEGRA CT1 data

The results presented here were produced using existing programs developed and extensively tested by Daniel Kranich and the HEGRA collaboration. Analysis of Mkn 421 and Mkn 501 data taken during periods of intense γ-ray activity with CT1, were published using the same analysis chain (see [96] for the Mkn 501 analysis and [133] for Mkn 421 analysis).

7.1 Data taken with HEGRA CT1 telescope

The HEGRA CT1 telescope collected a large amount of data from 1ES1959, starting from the year 2000.

The observation times and conditions are listed in table 7.1. All the data were taken at a zenith angle between 36° and 52°, but only a small fraction of events above 45° [1], as can be seen from the plot of table 7.1, related to data taken in 2002. Data taken during nights without moon and with weak moonlight (nominal HV setting) have been analyzed, as well as data taken with 4% reduced HV.

In the following sections the results of the data analysis in the different years will be presented. Particular emphasis is put on the year 2002 data, when for the first time 1ES1959 was observed with high significance by several Cherenkov telescopes, CT1 included, during a period of flaring activity.

7.2 Years 2000-2001: the low state

Before the first big flare reported in May 2002, the γ-ray emission from 1ES1959 was very faint. The detection of the Seven Telescope Array [75] caused an increase in interest on this object. Although a lot of observation time was spent on 1ES1959,

[1] The preliminary analysis results for the 2002 subsample of data at zenith angles below 45° ($\sim$ 150 hours) were presented at the 28^{th} ICRC [134].

Table 7.1: *Statistics of the raw data taken with the HEGRA CT1 telescope: observation time and conditions of the high voltage (HV) setting. Right: Observation time vs. zenith angle of the data taken during the year 2002.*

Observation conditions	**2000**	**2001**	**2002**
Dark nights, nom. HV (*nom*)	58 h	86 h	174.2 h
Weak moonlight, no HV red.(*hv00*)		24 h	8.1 h
Moonlight 4% HV red.(*hv04*)		12 h	16.1 h
Moonlight 8% HV red.(*hv08*)		8 h	6.1 h
Moonlight 12% HV red.(*hv12*)		7 h	2.9 h

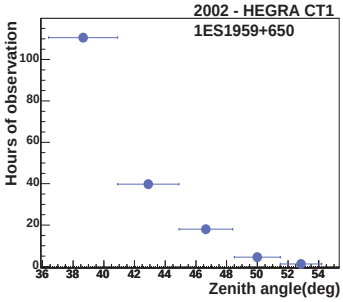

no Cherenkov telescope was able to monitor the short time variations of γ-ray flux from the source in its low state [2].

The data taken with CT1 in 2000 and 2001 showed no significant signal. Despite the long observation time (58 hours in 2000 and 84 hours in 2001), the number of excess events after the analysis of the CT1 data was not significant. The estimated mean integral γ-ray flux above 1TeV was calculated for the data taken during good moonless nights (high quality data). The derived average integrated flux was $\sim$ 6.5% of that of the Crab flux in 2000 and $\sim$ 5.3% in 2001 (see the light curves of figure 7.1). The calculated average flux has big uncertainties, due to the very weak recorded signal.

The slightly higher flux in 2000 can be explained by the points at MJD 51724-25 (June 29-30th, 2000). The average flux was 0.5 Crab for a total time of 5 hours, accumulated over two subsequent nights. The significance of the recorded signal in the two nights hardly reached 3σ significance, too low to claim a detection. If we consider this low flux enhancement as a modest flaring state, we can also notice that the state lasted at least 24 hours. It is another indication of the slow changes of state during the considered period of time.

The CT1 measurements of the 1ES1959 flux during low γ-ray emissions show that the flux variability above 1 TeV is low and slow, with a mean flux of 5.8% the Crab flux [3].

No spectral analysis was possible, due to the very limited statistics.

[2]The only published result regarding the detection of the low state of the source was obtained with the HEGRA System, after accumulation of 93.8 hours of observation during 2 years, [91]. The Whipple and CAT telescopes could obtain only upper limits to the integral γ-ray flux (see section 2.3.5).

[3]The integral Crab flux above 1 TeV, from data taken under similar conditions of observation is 1.7 $\cdot 10^{-11}$ photons cm^{-2} s^{-1}.

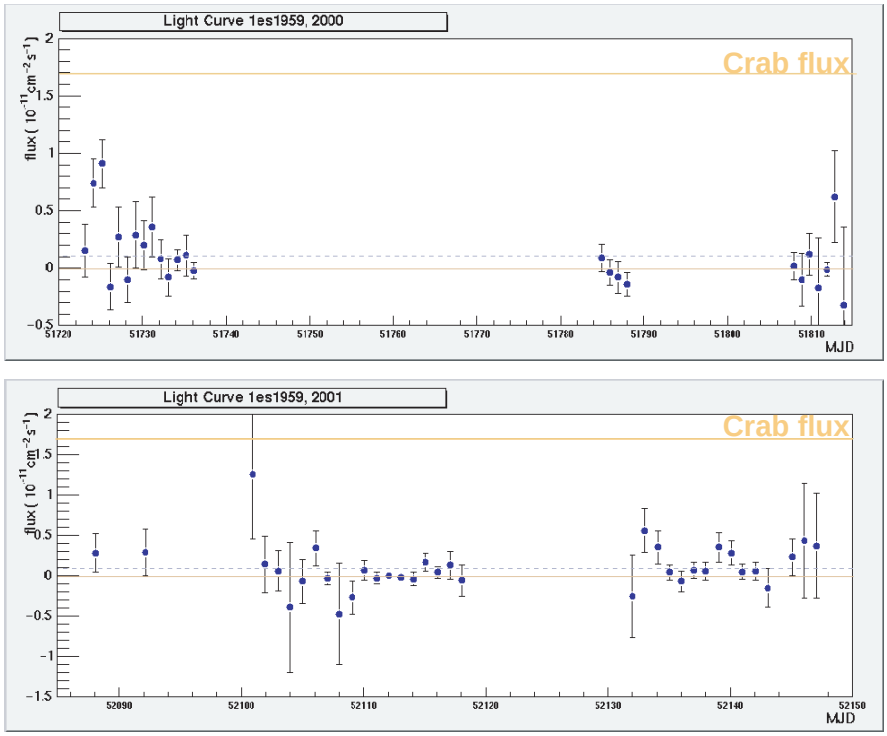

Figure 7.1: *Light curve (integral flux) of 1ES1959, as calculated with the program jacuzzi, for the data taken with CT1 during the years 2000 (above) and 2001 (below). In this period of time, the γ-ray emissions were very low and the accumulated signal is not significant. The corresponding data are listed in Appendix A, table A.1 and table A.2. For the definition of MJD (Modified Julian Day), see p.xxiv.*

7.3 The first signals of strong γ-ray emissions from 1ES1959

After a circular sent by the Veritas collaboration in May 2002 [76], the 1ES1959 observations with CT1 gave positive detection results. The data were analyzed by applying the dynamical supercuts, as described in the previous chapter (section 6.8).

The overall signal accumulated by CT1 in the almost 200 hours of moonless observation in the year 2002 (MJD: 52412 - 52584) is shown in the ALPHA plot of figure 7.2, left. In the energy range 1 - 10 TeV, we recorded 691 $\pm$ 42 excess events, over 1826 $\pm$ 38 events of background after a cut in the parameter ALPHA of 13.1°. The region below this value is also called *signal region*. According to formula 17 of the Li and Ma paper [132], the significance of the signal amounts to 11.1 σ. The number of background events and the errors are calculated fitting the region of the ALPHA plot above 20°, far from the signal region. As a check, we applied the fit

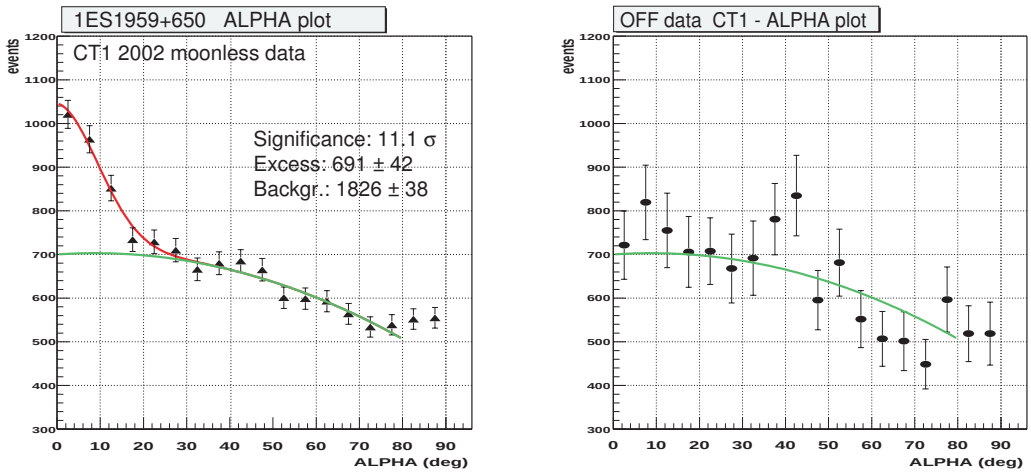

Figure 7.2: *Left: ALPHA plot of 1ES1959 from data taken with nom high voltage in 2002. Right: The same plot for OFF data, after the same analysis, shown for comparison. The green fit line on the left has been superimposed to the data to show the quality of the background estimate.*

that defines the background to a normalized (because smaller) sample of data taken when there were no γ-ray sources in the telescope FOV (OFF source). The fit is a good description of the shape of the OFF source data, after the same analysis applied to the ON source data (figure 7.2, right).

In figure 7.3, the histogram of the arrival direction of the excess events (calculated with the DISP method [124]) is plotted in sky coordinates. A peak occurs at the expected position of 1ES1959 .

Together with the Whipple, the HEGRA System and the CAT telescopes results, this is another confirmation of the detection of strong γ-ray emission from 1ES1959 in 2002.

7.3.1 Light curve of 1ES1959 in 2002

The emission of 1ES1959 was studied as a function of time and the results are presented in the light curve in figure 7.4 and 7.5 together with the mean integral γ-ray flux of the Crab Nebula, as a reference. In the plot, dots of different colors represent the HV setting of the telescope when the data were recorded. The analysis of the different data sets was done separately and then combined together in the light curve, to have the larger observation covering. The plotted values are listed in the tables A.3 of Appendice A.

The special operation mode with partially reduced HV for the PMTs or observations during weak moonlight (although for a limited time) is one of the special features of CT1. The sensitivity of the telescope is reduced and the energy threshold

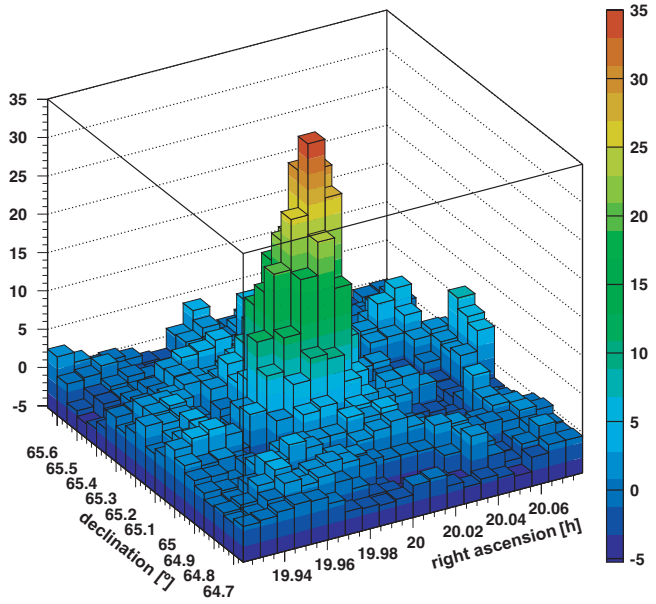

Figure 7.3: *Events incoming direction, after background subtraction, calculated as explained in [124]. The recorded γ-ray showers have been analyzed to reconstruct their arrival direction in the sky. The peak has been analyzed with a Gaussian fit. The difference between the reconstructed source position and the nominal one is 0.035 h in RA and 0.001° in DEC. The angular resolution, defined as the σ of the fitted Gauss function is 0.077 h in RA and 0.085° in DEC. The accuracy of the shaft encoders steps of CT1 is 0.02°.*

is higher when the background light is enhanced by the presence of moonlight. The larger error bars reflect the limited statistics.

It is easy to see that variability is one of the main characteristics of the γ-ray emissions of this AGN in 2002. The periods of enhanced activity during the year 2002 were recorded on May 20th (MJD52414), June 2nd (MJD52427) and July 14th-15th (MJD52469-70). It is worth noticing that both in May and in June, the flares occurred at the edge of a full-moon period.

All the light curve points in May appear at a higher level, i.e. $\sim$50% the Crab Nebula flux, with respect to the average flux recorded in the previous years. On the other hand, the flare at the beginning of June is a single peak on the light curve, but very strong. The limited number of events allows us to quote only a mean flux of $\sim$2 times the mean Crab flux. The July flares were somewhat less strong, hardly reaching the 0.5 Crab flux, but the variability with respect to the previous and later observations is clear.

A period of enhanced activity was also found in August 2002 (MJD 52492-52495), but the maximum flux of this period hardly exceeded half the Crab flux.

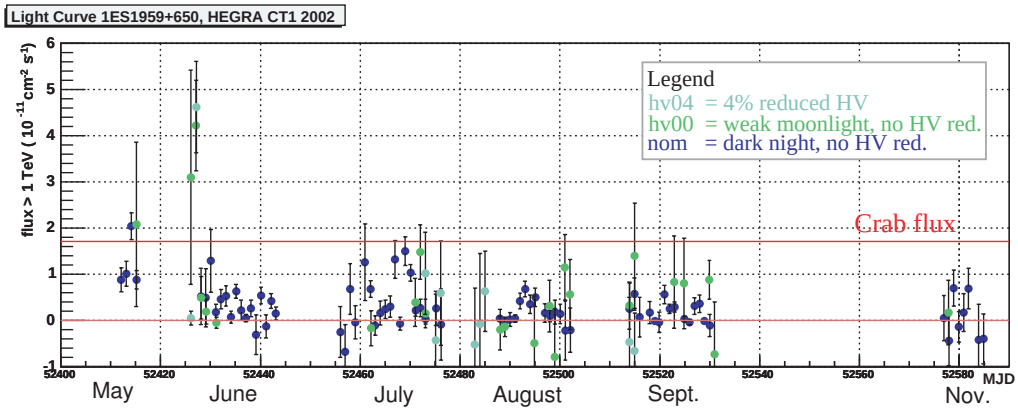

Figure 7.4: *Light curve of 1ES1959, with CT1, for the year 2002. Data taken with different HV settings are plotted in different colors. Negative fluxes must be interpreted as as no-detection.*

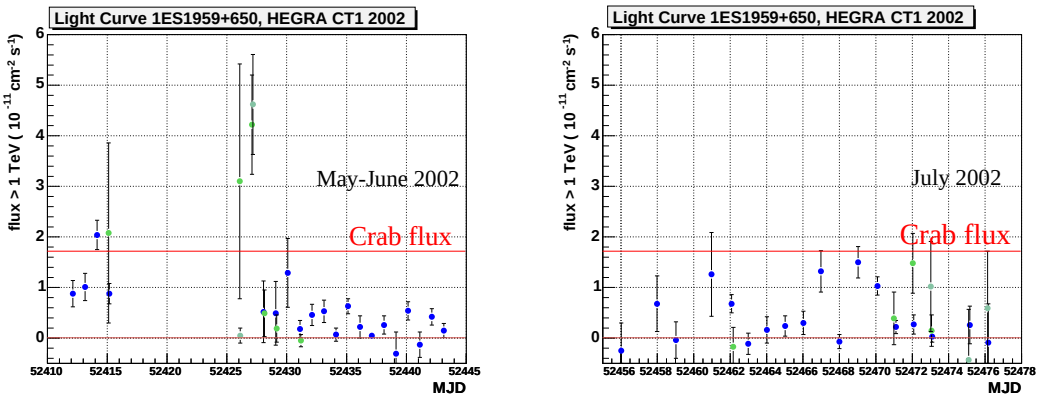

Figure 7.5: *Light curve of 1ES1959, with CT1, for the year 2002, zoomed for the periods of increased γ-ray emissions. Data taken with different HV settings are plotted in different colors (see legend of figure 7.4). Negative fluxes must be interpreted as as no-detection.*

7.4 Differential spectrum of 1ES1959 from data recorded in 2002

The moonless data collected in 2002 have been used to calculate the differential energy spectrum. The data related to the strong γ-ray flare recorded at the beginning of June is not included. The results are plotted in figure 7.6.

Both periods of low activity and high activity are combined together. The limited statistics did not allow us to divide the available data and to obtain a differential spectrum for the low emission and another one for the high emission state. The plot of the spectrum has large error bars (only statistical uncertainty). The fitting of the spectrum between 1 TeV and 20 TeV using a power law gives acceptable results:

$$\begin{aligned}\frac{dF}{dE} &= f_0 \left(\frac{E}{TeV}\right)^{-a} \\ &= (0.83 \pm 0.13) \left(\frac{E}{\mathrm{TeV}}\right)^{-(3.60\pm0.17)} \cdot 10^{-11} \quad \mathrm{cm}^{-2}\mathrm{s}^{-1}\mathrm{TeV}^{-1} \quad (7.1)\end{aligned}$$

with a $\dfrac{\chi^2}{d.o.f.} = \dfrac{11.3}{5} = 2.26$

as well for a fit with a power law with an exponential cutoff approach:

$$\begin{aligned}\frac{dF}{dE} &= f_0 \left(\frac{E}{\mathrm{TeV}}\right)^{-a} \exp\left(\frac{E}{E_0}\right) \\ &= (1.32 \pm 0.34) \left(\frac{E}{\mathrm{TeV}}\right)^{-1.8_{fixed}} \exp\left(\frac{E}{(1.28 \pm 0.18)}\right) \cdot 10^{-11} \quad \mathrm{cm}^{-2}\mathrm{s}^{-1}\mathrm{TeV}^{-1}\end{aligned}$$

with a $\dfrac{\chi^2}{d.o.f.} = \dfrac{5.13}{5} = 1.03$

(7.2)

In this last case, the spectral index has been fixed, according to the HEGRA System results for the description of the low state spectrum.

A conclusion regarding the presence of a cutoff is not possible because of the large statistical errors of the last data points.

7.5 Discussion of systematic errors

The systematic errors in the analysis of the CT1 data are listed in the following, as discussed in [125].

- The calibration method, using the excess-noise factor, can be a source of systematic error in the absolute energy scale. It has been estimated to be

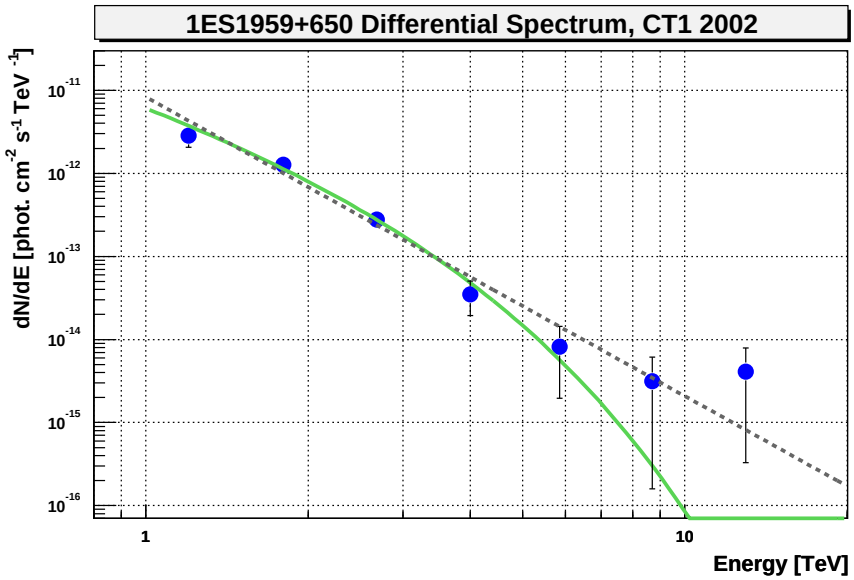

Figure 7.6: *Averaged 1ES1959+650 energy spectrum for the complete CT1 nom HV dataset (moonless nights). The fitting lines represent a pure power law (dashed line) and a power law with exponential cutoff (solid line). For the parameters of the fit, see text (equations 7.1 and 7.2).*

Table 7.2: *Differential spectrum of 1ES1959, as measured by HEGRA CT1 in 2002 moonless nights of observation.*

Energy TeV	Flux 10^{-11} cm^{-2}s^{-1}TeV^{-1}		
1.20	2.85e-01	±	7.86e-02
1.80	1.27e-01	±	1.51e-02
2.68	2.79e-02	±	3.91e-03
4.00	3.49e-03	±	1.56e-03
5.86	8.18e-04	±	6.21e-04
8.71	3.15e-04	±	2.99e-04
12.98	4.12e-04	±	3.79e-04

up to 10%. The change of spectral shape of 1ES1959 due to a possible error in the energy scale is not considered relevant, since the determination of the spectrum is dominated by the large statistical errors.

- The algorithm used for the estimation of the background can cause a systematic error on the integral flux of less than 10%. Studies on the changes of the spectral shape due to the under-overestimate of the background reveal that the changes in the spectrum parameters are inside the statistical error range. In the light curve, however, the statistical information of each point is, in general, poor and the systematic error can affect the calculation of the daily flux variation.

- The absolute γ-ray flux estimate is based on the fact that the MC sample used for the calculation of the effective area describes the data reasonably well. The systematic error of the flux level introduced by possible differences between MC and data has been estimated to be 10%.

The total systematic error on the flux level was calculated summing up quadratically the errors listed above, resulting in 17%. A dependency of the systematic error on the energy is present, but impossible to evaluate with the present knowledge.

Chapter 8

Results of the analysis of MAGIC telescope data

In this chapter I will present the results of the analysis of the data taken with the MAGIC telescope in 2004 [1]. For the detailed description of the analysis method see chapter 6.

The telescope has only been operating in its final configuration for a short time before the data were taken, therefore the analysis method has been tested and optimized with the TeV standard candle, i.e. the Crab Nebula. As the analysis programs were, at that time, still undergoing improvements and, also, not all light losses were fully understood, many of the data from 1ES1959 were calibrated with respect to those of the Crab Nebula.

The same analysis procedure optimized to the Crab data has also been applied to the OFF and the 1ES1959 data sets.

The raw data statistics are summarized in table 8.1.

Table 8.1: *MAGIC 2004: statistics of the raw data analyzed.*

Source	**Days (2004)**	**N. events**	**Total obs. time**
1ES1959	Sept. 6, 7, Oct. 7, 10 15, 16, 17	4.4 M	6 h 55 min
Crab Nebula	Sept. 13, 14, 15, 16, 21, 22, 23	1.7 M	2h 17 min
OFFData	Sept. 8, 10, 11, 12, 13, 14, 16, 17	2.3 M	2 h 49 min

The selection of the Crab and OFF data is based on the 1ES1959 observations,

[1] The results of this analysis are the subject of a paper accepted for publication in the Astrophysical Journal.

so as to have the same telescope conditions, within a few days of stable atmospheric conditions and at nearly the same z.a. range.

MC studies showed that the image parameters' distribution of events observed at $\geq 30^\circ$ z.a. change quite substantially as a function of the z.a. The z.a. range of the observations of 1ES1959 was rather limited, only $\sim 10^\circ$ wide. This allows us to use a mean value for θ and to neglect its change on the cuts, as shown in figure 5.10, but, on the other hand, it requires a comparison with data matching the same z.a. observation conditions. We tried to fulfill this requirement, according to the available data recorded by MAGIC during the same period of year 2004, as can be see in figure 8.1.

8.1 Analysis of the data

The same method of data analysis, whose options will be described in this section, was applied to the Crab Nebula data, to the OFF data sample and to the entire 1ES1959 data set. When the available analysis programs were not prepared to handle MC files, macros which reproduce the same analysis applied to data have been applied to the MC data set [2].

8.1.1 Data quality check

The telescope was still in the testing and improvement phase when the data were recorded. A set of automatic checks to define the quality of data was, at that time, not available. The following tests have been applied to select high quality data.

- The minimum size of data files was required to be 35 MB. Files which are too small with respect to the standard file size are a sign of possible data corruption and were therefore discarted.

- The eventual failure of the calibration pulser is the cause of missing calibration constants for the data which is to be analyzed (see definition of calibration runs p. 110). Calibration run files have been checked (see figure 8.2): the requirement to define a calibration run as *good* was that the mean calibration constant should follow the average trend of all the calibration constants of the whole period ($\pm$ 10%). Data files have been calibrated by using the *good* calibration run closest in time.

- After calibration, the recorded events rate was checked to be consistent with the expected rate for the given z.a. In figure 8.3, the plots for the check of 1ES1959 data are shown. Runs with a rate which is too low with respect to the mean, as a function of the z.a., were excluded from the analysis.

[2]The MC data for MAGIC were analyzed using macros that reproduced the calibration and the calculation of image parameters applied to the telescope data. For the γ-hadron separation it was possible to use exactly the same programs for the treatment of MC data and real data.

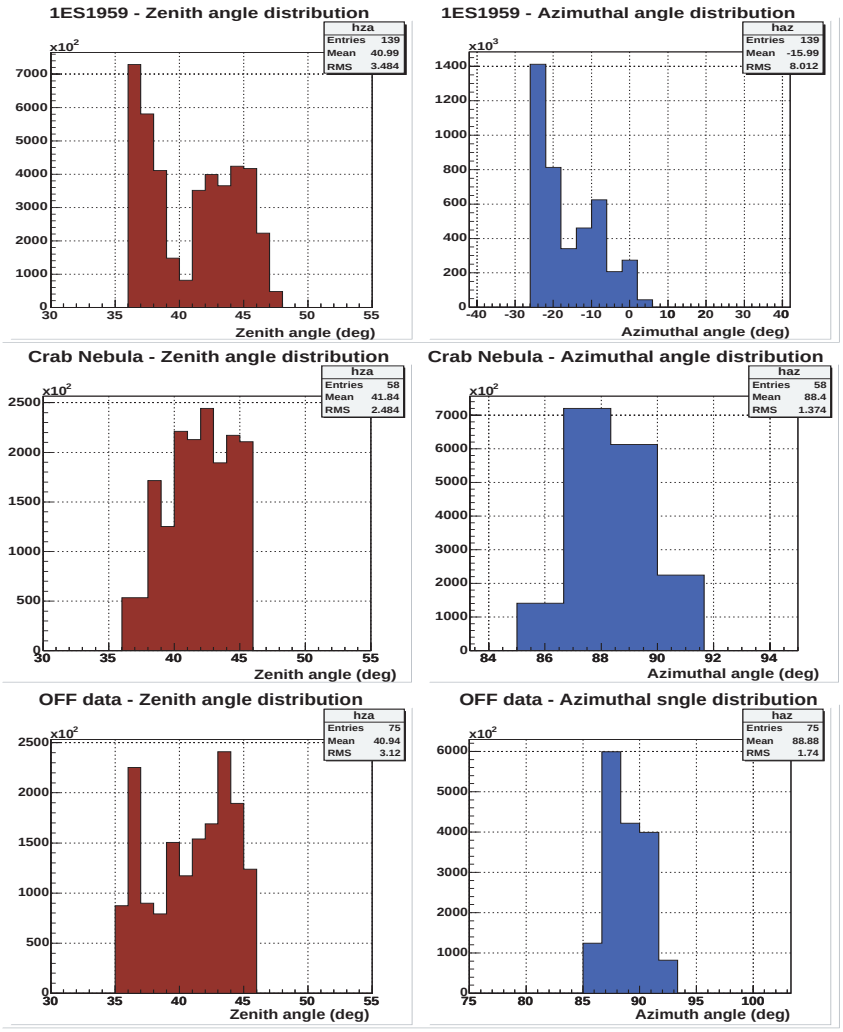

Figure 8.1: *Zenith (left) and azimuthal (right) angles distributions of the 1ES1959 data, Crab data and OFF data selected for the analysis. The azimuthal angle distributions for Crab data and OFF data are very much comparable, while 1ES1959 data have a ∼90° shift in azimuthal angle.*

8.1.2 Analysis options

The data recorded by MAGIC and selected for this work were analyzed using the following analysis options [3].

- The Digital Filter as signal extractor (see section 6.3.1 for the desctiption) was used, integrating the signals of 6 slices, both for high and low gain.

[3] A preliminary analysis using different methods of signal extraction, image cleaning, etc. was also performed. A short report about it can be found in Appendix B.1. The results were found to be in good agreement with the analysis results obtained with the options listed above.

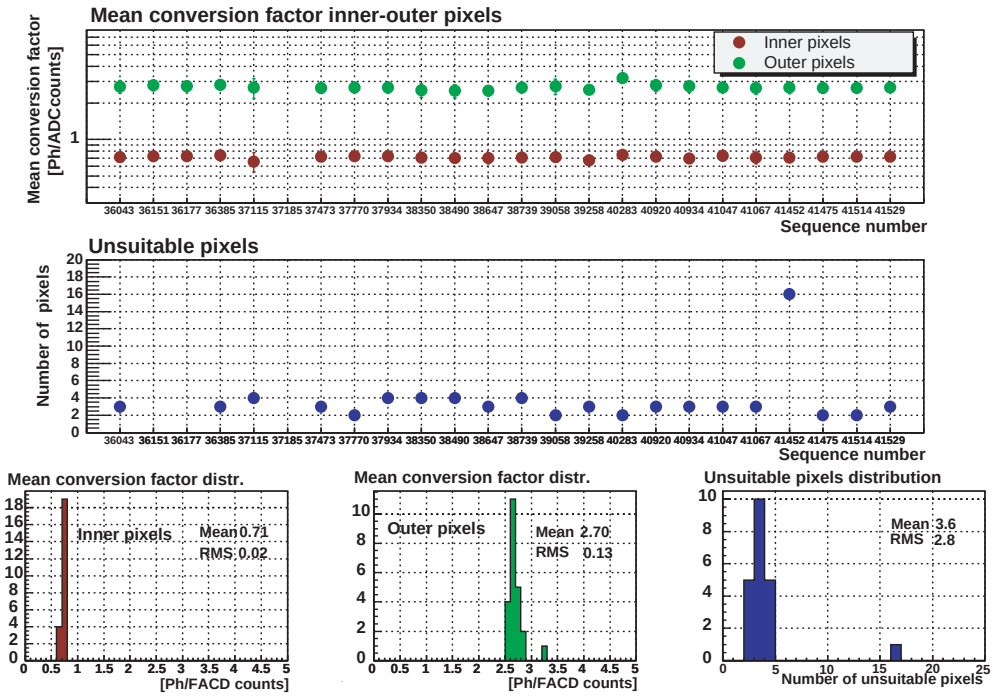

Figure 8.2: *Mean calibration constants, both for the inner and outer pixels of the MAGIC camera, in order of time when they were recorded (independent from the source analyzed), plotted in order to provide a selection criterium for the calibration runs to reject. The data are grouped in sequences, in which one or more calibration files are analyzed to obtain calibration factors, in association with one or more pedestal files. The sequence is identified by a number corresponding to the lowest run number of the files in the sequence. The mean calibration factor was quite stable during the period September-October 2004. The variation of the mean value of the calibration factor is about 2.6% for inner pixels and 5% for the outer ones. The number of pixels that were not possible to calibrate, because of hardware problems, are also displayed in blue. The calibration runs with too many uncalibrated pixels (corresponding to 5% of the total number of pixels available) have been rejected. In this case, there are 3 runs out of 24, that did not pass our selection. One calibration run gave no calibration factors (sequence number 37185): the scan of the file showed that no calibration pulses had been recorded. This shows that the performed test, even though not accurate, is able to point out the presence of major problems.*

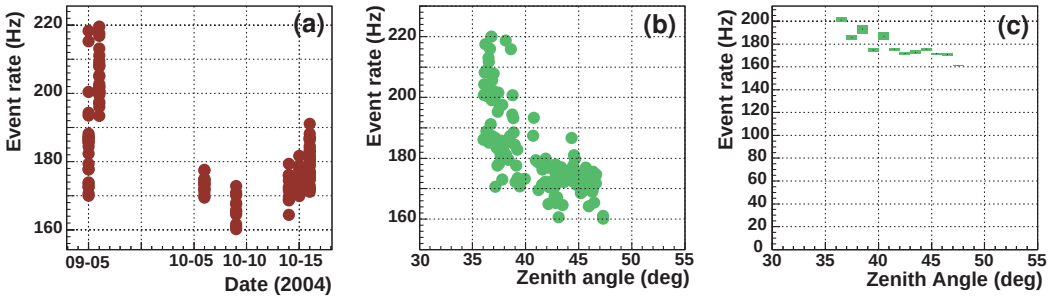

Figure 8.3: *Events rate in the raw data during the observation of 1ES1959 in 2004. The quality of the data runs was tested analyzing the number of events recorded in the files. The rate is expected to depend on the z.a. of the observation. This is confirmed by the plots (b) and (c).*

- Pedestals for the calculation of the calibration constants were taken from pedestal runs, while the pedestals for the data were extracted directly from data runs.

- The adopted image cleaning method is the so-called *absolute* one. The cleaning levels are: 40 photons for core pixels, 25 photons for the neighbors. Only one ring of pixels around the core pixels was accepted.

- Only images with a minimum SIZE of 800 photons (∼144 photo-electrons) were analyzed. Lower SIZE images were discarted. Sometimes stronger cuts in SIZE were applied during the different analysis steps. The image parameters distributions of the 3 data samples were compared (after normalization) for consistency and were found to have no systematic discrepancy. The image parameters plots before and after cuts can be found in Appendix B.2.

- The γ-hadron separation was optimized by training the Random Forest procedure using half of the available MC γ sample and the same number of random events extracted from the 1ES1959 data sample ($\sim$ 13 thousand events). Since the available statistics of OFF data was very limited, we decided to use the ON data itself as a source of background events for the RF training, with the advantage that there were no biases due to different FOV, or different operational conditions of the telescope with respect to the ON data itself. Another reason to use hadrons from the 1ES1959 data sample is a matter of statistics: using part of the OFF data for RF training means reducing the already limited statistics to about 50%, with big problems in evaluating the behaviour of the test OFF data sample after applying the cuts. The fraction of training events in the ON-data sample is less than 3% [4].

[4]Half of the MC γ data set and random events from OFF data were used to train the RF and check the method. For an appropriate analysis of 1ES1959 data, we decided to adopt as

The second half of the γ MC sample was used as test sample for the calculation of the cut efficiency and calculation of the differential spectrum. The splitting of the available MC γ events into two independent subsamples is necessary for testing the γ- acceptance after cuts and for calculating the effective area. We sacrificed part of the advantages of having high MC statistics in order to be able to check the quality of our cuts.

- The parameters used for the training of the Random Forest are (the index refers to the unit used to express the value of each parameter):

  - $\mathrm{SIZE}_{photons}$
  - DIST_{mm}
  - CONC2
  - CONC7
  - $\log(\mathrm{SIZE}_{photons})/(3.5 - 1.3 \cdot \log(\mathrm{LENGHT}_{mm}) + 0.6 \cdot [\log(\mathrm{LENGHT}_{mm})]^2)$
  - $\log(\mathrm{SIZE}_{photons})/(4.4 - 2.9 \cdot \log(\mathrm{WIDTH}_{mm}) + 1.43 \cdot [\log(\mathrm{WIDTH}_{mm})]^2)$
  - $\mathrm{M3Long} \cdot \mathrm{sign}(\cos(\mathrm{DeltaAlpha}))$

  The parameterization for the scaled WIDTH and LENGTH description were taken from the MC γ distributions.

  The cuts (hadronness< 0.1, ALPHA$<9°$) resulted in a background rejection power for events with SIZE larger than 1800 photons equal to $\sim 9 \cdot 10^{-4}$, with a $\sim 87\%$ of efficiency for γ. In figure B.8 of Appendix A, the efficiency of all the cuts applied for the spectrum analysis is plotted as a function of energy.

- We applied a cut in events with WIDTH/LENGTH > 0.7 ($\sim 3\%$ of γs rejected). This cut rejects roundish events. The events rejected by the cut did not have any preferred ALPHA value: they did not produce artificial peaks in the ALPHA plot. On the contrary, they showed up in the DISP map, accumulating in the same small region of the camera where they were produced. The cut in those events did not affect any other part of the analysis [5].

- The shape of the ALPHA plot resulted in a sort of shoulder at about 50° (see figure B.2), making difficult the description of the background with a second order polinomial function. The problem was solved by applying an additional cut in the DIST parameter, in order to get rid of events largely dominated by the signal in the outer part of the camera:

background sample the available hadronic images recorded while observing the source, since no significant difference in the resulted γ-ray signal was found.

[5] These roundish events could eventually be related to small discharges at some PMTs. The light of the discharge triggered the neighboring PMTs.

$$\begin{aligned} &\mathrm{DIST}_{deg} > 0.2^{\circ} \\ &\mathrm{DIST}_{deg} < 0.85 + (4 \cdot 10^{-4} \cdot \mathrm{SIZE}_{ph} \cdot 0.18) - (2.5 \cdot 10^{-8} \cdot (\mathrm{SIZE}_{ph} \cdot 0.18)^2) \\ &\mathrm{DIST}_{deg} < 1.3^{\circ} \end{aligned} \tag{8.1}$$

The distribution of DIST vs SIZE parameters are plotted in figure 8.4 for MC γ and for Crab ON data, together with the shape of the applied cut [6].

The efficiency for this particular cut is listed in table 8.2 for different SIZE intervals.

Table 8.2: *Efficiency of the DIST vs SIZE cut applied to the data.*

Size bin (photons)	Efficiency for MC γ
800 - 1300	60%
1300 -2050	77%
2050 - 3300	84%
3300 - 5300	87%
5300 - 8400	89%
8400 - 13500	89%
13500 - 21500	90%
above 21500	80%

- The background level was estimated from the ON data with a fit using a polinomial of second order function f(ALPHA) = $c_1 + c_2$ ALPHA^2 on the ALPHA plot region above 20°, far from the signal region. The same fit was applied to the OFF data sample for comparison. The extention of the fit to the small ALPHA region is in good agreement with the plot behaviour, as shown in Appendix, figure B.5.

8.2 Results of the Crab Nebula data analysis

8.2.1 The signal: ALPHA plot

Two hours of Crab Nebula data are expected to provide a strong signal. The use of Hillas parameters for the γ-hadron separation has been successfully tested

[6] Since the current way to calibrate MAGIC data is in terms of photo-electrons and not in photons, as it was at the time the present analysis started, the cut is such that SIZE is multiplied by 0.18, that is the conversion factor between the two units for the parameter.

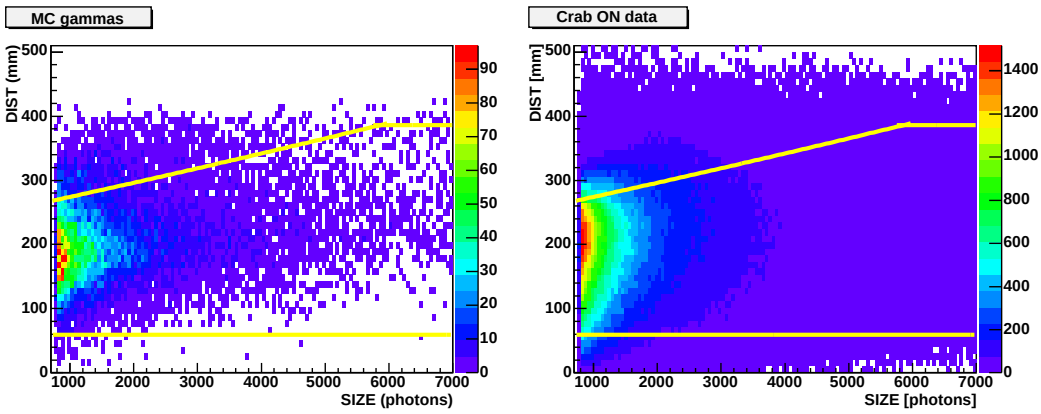

Figure 8.4: *The parameters DIST vs SIZE has been plotted for the MC γ-sample and the Crab Nebula ON data, together with the lines representing the applied cut. The efficiency of this cut on the MC γ-sample is shown in table 8.2.*

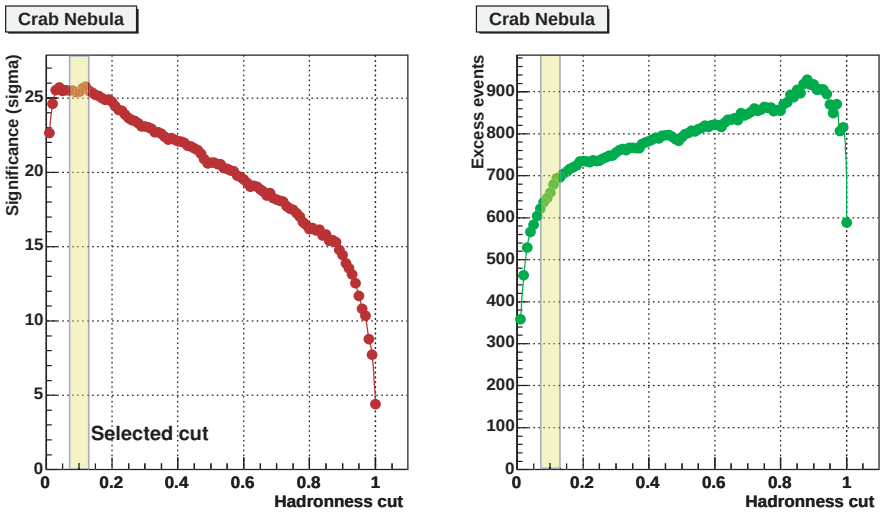

Figure 8.5: *Significance and number of excess events as a function of the hadronness cut applied to Crab data with SIZE >1800 photons. From this plot, the hadronness cut to apply to the 1ES1959 data was chosen. We selected the cut far from regions of big fluctuations (hadronness smaller than 0.1) and in case of a plateau, we decided to maximize the number of excess events (right).*

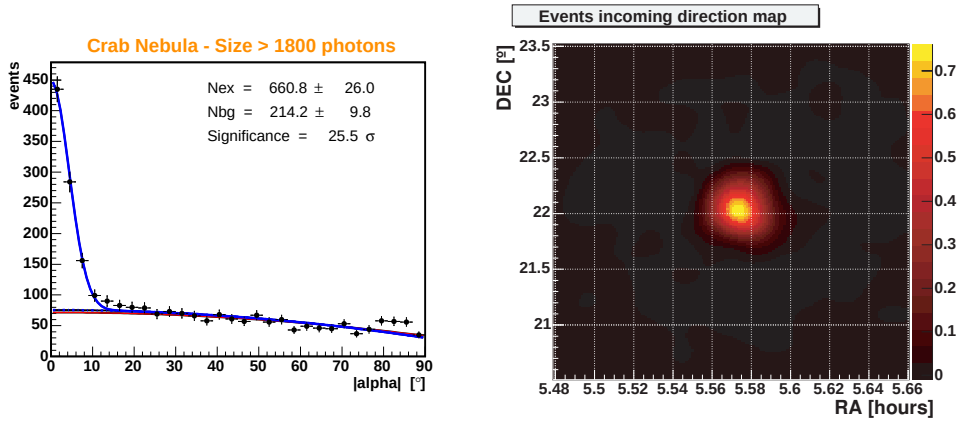

Figure 8.6: *ALPHA plot for the Crab Nebula data for a selection of data at relatively large SIZE (larger than 1800 photons), so as to apply one fixed cut in the parameter ALPHA. The data have been optimized so as to obtain the maximum significance on the same Crab data. Right: DISP map in sky coordinates, indicating the estimated incoming direction of the events. The peak corresponds to the Crab Nebula coordinates.*

in the past on energies higher than some hundreds of GeV. Most of the events recorded with MAGIC have lower energy: our strategy was to initially select events of relatively high energies, with a cut in the parameter SIZE of 1800 photons. Once a signal has been found in this sample, the lower SIZE events can be also analyzed with the same method. For lower energy events, the efficiency of the Hillas analysis is still not optimized and is under investigation: the events have different characteristics and the methods to distinguish γ and hadroninc showers with classical methods are less efficient.

The low SIZE (i.e. low energy) events are therefore not used in this first step and are treated separately: the peak in the ALPHA plot becomes significantly broader than the one we have for images with large SIZE, as can be seen in figures B.9 and B.10.

The cut in hadronness has been chosen so as to maximize the significance of the signal, calculated as described in the previous chapter, in the Crab data sample. The plots of figure 8.5 show how the significance and the number of excess events vary as a function of the cut in hadronness applied to the Crab data. The first region below hadronness $\sim$0.1 shows very strong varations. A low cut in hadronness causes, in fact, a strong reduction of the statistics. This hadronness cut region is therefore not taken into account for the selection. Above this region, the significance reaches a peak and starts decreasing smoothly. We selected the cut of 0.1 in hadronness. It is easy to see that the choice of the cut is not unique. We decided to take the hadronness value in the region of high significance and small fluctuations. In case of possible multiple cut choices, we used the looser hadronness cut in order to have the higher number of excess events with basically the same significance of the signal

above the background.

To better visualize the signal significance, we produced the ALPHA plot for selected events above 1800 photons in 3° wide bins and applied a fixed ALPHA cut. The cut value in this parameter has been calculated as ~ 1.8 times the sigma of the gaussian function describing the signal peak. The background level is determined with a fit on the background region above 21° and then extrapolated to 0°. As mentioned above, the cut of hadronness<0.1 was chosen for the Crab data set. The ALPHA plot is shown in the left part of figure 8.6. After a cut in ALPHA $< 9°$, we found 661 ± 26 excess events for a significance of 25.5 σ above the background.

In Figure B.5, I superimposed the shadowed histogram of the normalized OFF data sample, plotted for comparison. The cuts applied to the OFF data produce, as expected, a nearly flat ALPHA distribution, since there are no γ- showers expected in the FOV. The fit of the background region in the ALPHA plot of Crab is in good agreement with the behaviour of the OFF data histogram.

The right part of figure 8.6 shows a map, in sky coordinates, of the calculated events' origin, using the DISP method. A strong peak at the Crab sky coordinates is another confirmation of the measurement.

8.2.2 Flux and differential spectrum

For the determination of the spectrum we calculated for each event the most likely energy and sorted the events into a histogram as a function of their estimated energy. The cut efficiency and the energy estimation results are presented together with the ALPHA plots for every energy bin in Appendix B.5.

Figure 8.7 shows the differential spectrum for the Crab Nebula data (red hollow circles), together with the spectrum obtained with another analysis on another MAGIC Crab data set, recorded in the same period at smaller z.a. (green hollow circles, for details, see [136]).

The data points have been unfolded with a power law function, whose spectral index is in very good agreement with other MAGIC measurements. The flux level calculated for high z.a. measurements has a difference of about 30% compared to the low z.a. data. The difference is recovered (filled red squares) correcting the points obtained in this work for the camera inefficiency (see section 8.4.2).

The spectrum of the Crab Nebula data analyzed here can be well described by a power law:

$$\frac{dN}{dE} = (2.36 \pm 0.11_{stat.} \pm 0.74_{syst.}) \cdot 10^{-11} \left(\frac{\mathrm{E}}{1\mathrm{TeV}}\right)^{(-2.41 \pm 0.05_{stat.} \pm 0.03_{syst.})} \quad (8.2)$$
$$\mathrm{cm}^{-2}\mathrm{s}^{-1}\mathrm{TeV}^{-1}$$

where the systematic error quoted here is the sum of the error due only to the unfolding method applied and to the comparison with the measurements under better observational conditions (i.e. smaller z.a.). For an estimate of the systematic errors, see section 8.5.

Table 8.3: *Crab Nebula differential flux for events between 150 GeV and 2 TeV (before camera inefficiency correction). The mean energy bin is shifted to the left with respect to the bin center, taking into account the spectral slope. The data are plotted in Figure 8.7 (hollow red circles).*

Mean Energy GeV	**Flux ($\mathbf{TeV^{-1}\ cm^{-2}\ s^{-1}}$)**
115	$(2.27 \pm 1.52) \cdot 10^{-9}$
193	$(1.23 \pm 0.20) \cdot 10^{-9}$
324	$(3.49 \pm 0.31) \cdot 10^{-10}$
545	$(1.04 \pm 0.08) \cdot 10^{-10}$
914	$(2.79 \pm 0.25) \cdot 10^{-11}$
1535	$(7.46 \pm 0.62) \cdot 10^{-12}$
2577	$(1.24 \pm 0.22) \cdot 10^{-12}$

The spectrum obtained after correction for camera inefficiencies (see section 8.4.2) is:

$$\frac{dN}{dE} = (2.97 \pm 0.11_{stat.} \pm 1.16_{syst.}) \cdot 10^{-11} \left(\frac{\mathrm{E}}{1\mathrm{TeV}}\right)^{(-2.41 \pm 0.05_{stat.} \pm 0.23_{syst.})} \mathrm{cm}^{-2}\mathrm{s}^{-1}\mathrm{TeV}^{-1} \tag{8.3}$$

The spectral parameters of the Crab Nebula taken from published data are:

$$\frac{dN}{dE} = (2.83 \pm 0.04_{stat.} \pm 0.6_{syst.}) \cdot 10^{-11} \left(\frac{\mathrm{E}}{1\mathrm{TeV}}\right)^{-2.62 \pm 0.02_{stat.} \pm 0.05_{syst.}} \mathrm{cm}^{-2}\mathrm{s}^{-1}\mathrm{TeV}^{-1} \tag{8.4}$$

according to the measurements by the HEGRA System [47] between 500 GeV and 80 TeV, while:

$$\frac{dN}{dE} = (3.3 \pm 0.2_{stat.} \pm 0.7_{syst.}) \cdot 10^{-11} \left(\frac{\mathrm{E}}{1\mathrm{TeV}}\right)^{(-2.45 \pm 0.08_{stat.} \pm 0.05_{syst.})} \mathrm{cm}^{-2}\mathrm{s}^{-1}\mathrm{TeV}^{-1} \tag{8.5}$$

according to the measurements done with the Whipple telescope [137] from 300 GeV to 10 TeV.

The measured Crab spectrum (equation 8.3) was compared with equations 8.4 and 8.5. We first assumed that the shape of the spectrum of the Crab Nebula given by the equations above could be extended down to 200 GeV, without changing the curvature significantly. The measured Crab spectrum slope is in good agreement

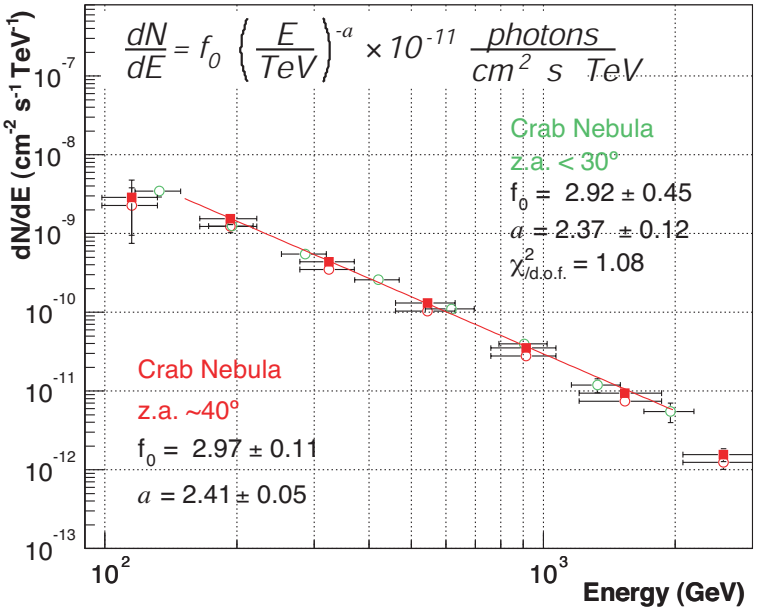

Figure 8.7: *Differential flux of the Crab Nebula above 150 GeV and below 2 TeV: comparison between measurements done in different z.a. regions with MAGIC and obtained with independent analysis. The red hollow circles are points obtained in this work, while the red filled squares are the points after applying the correction for the camera inefficiency. In green: the Crab Nebula spectrum taken from [136] and in the same energy range. The vertical error bars represent the statistical errors, the horizontal bars represent the energy resolution in each bin.*

with the value published by the Whipple collaboration. The spectral index of the HEGRA result is softer than the one measured with MAGIC.

One of the plausible reasons for the observed discrepancies is that the points obtained here are fitted only in a small region above the expected IC peak, where the spectrum should become flatter. Extending previous measurements to lower energies would not necessarily be a good solution. The large number of data points from past observations between 2 TeV and some tenths of TeV, where the spectrum is expected to be softer, influences the parameters of the fit. At lower energies the spectrum is supposed to change its slope and the fit with a simple power law formulation over a wide energy range is not optimal.

To conclude this section, I want to remark that the only reason for us to analyze Crab data at this z.a. is the analysis of 1ES1959 data and the comparison with the Crab Nebula results. Once we define the set of cuts, we want to apply our analysis on a data sample (i.e. 1ES1959 data) completely independent from the data sample used to optimize the cuts (i.e. Crab data). The good agreement of the results obtained for the Crab Nebula with previous measurements supports and

gives credit to the results obtained for 1ES1959.

8.3 Results of the 1ES1959+650 data analysis

8.3.1 The signal in the ALPHA plot

We applied the data checks and the cuts optimized to the Crab data to the 1ES1959 data sample, as described in the previous section.

In figure 8.8 the ALPHA plot is shown for events with SIZE>1800 photons. A peak below 10° is clear evidence for the presence of a γ-ray signal. The number of excess events is 282 ± 32 (statistical errors only), e.g. a flux significance of 8.8 σ above background.

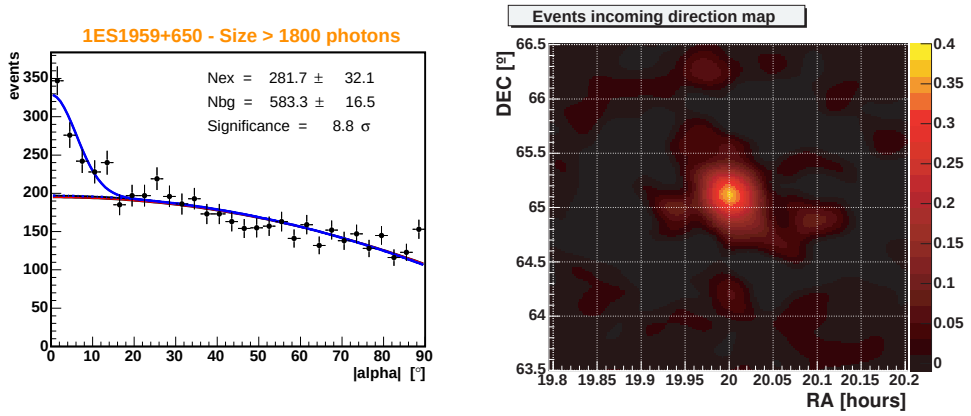

Figure 8.8: *Left: ALPHA plot for 1ES1959 for a selection of data at relatively high SIZE (SIZE>1800 photons, hadronness<0.1, DIST cut as in equations 8.1). The vertical bars represent the statistical errors only. The cuts for the γ-hadron separation were optimized on the Crab data set. Right: the calculated origin of the events from the 1ES1959 data sample, in sky coordinates, using the DISP method. The excess position coincides with the 1ES1959 sky location.*

The sigma of the Gaussian-like function describing the ALPHA peak in the 1ES1959 data (6.1 ± 1.2)° is quite compatible with the Crab value of (4.3 ± 0.2)° [7]. Under the assumption that the telescope's operating conditions were very similar, we expect to have compatible values. The similarities between the ALPHA plots allow us to apply the same cut in ALPHA at 9° to the 1ES1959 data as was used for the Crab data analysis.

[7]The slightly difference in the width of the ALPHA peaks can be explained: because of the steeper 1ES1959 spectrum, the ALPHA peak contains relatively more events of lower SIZE with respect to Crab data, which have a wider ALPHA distribution (see in App.B the plots of figures B.9 and B.10).

8.4 The light curve in September-October 2004

The presence of a signal in a sample of data from a variable source requires the study of possible variations of signal in the different nights of observation. The described analytical method was applied separately to the data of each of the seven nights of observation. The possible presence of a strong flare in one of them could, in principle, dominate the total signal. Figure B.6 (Appendix B) shows the ALPHA plots for each night, obtained with the same analysis used to produce the plot of figure 8.8.

In the table 8.4 the number of excess events per minute of effective observation time is listed. In figure 8.9, the measured γ-ray integral flux above 300 GeV is shown with the measured Crab flux, assumed to be constant.

We could not see significant variations of the γ-ray flux from 1ES1959 during the nights covered by observations with MAGIC. The mean flux above 300 GeV has been measured to be 14% the Crab flux. The highest recorded point was observed on October, 10th, with $\sim$ 25% the Crab flux. The nights of observations are few and spread over two months, but it can be concluded that in September-October 2004 the γ-ray activity of 1ES1959 was monitored with MAGIC during a period of low, i.e. quiescent (stable) state.

The mean 1ES1959 γ-ray flux above 300 GeV during the period of observations with MAGIC was determined to be $(1.98 \pm 0.21_{stat}) \cdot 10^{-11}$ photons cm^{-2} s^{-1} (corrected for the camera inefficiency, see section 8.4.2).

Table 8.4: *Summary of the flux analysis of 1ES1959 data above 300 GeV (before corrections for the camera inefficiency) divided into nights of observation. The corresponding ALPHA plots are displayed in figure B.6. The points corresponding to the light curve of the source (supposing that the condition of the telescope were comparable in the whole period) can be seen in figure 8.9.*

Date MJD	$\mathbf{T}_{eff}$ seconds	**Excess evts/min**	**Signif.** σ	**Flux (> 300 GeV)** 10^{-11} ph. cm^{-2} s^{-1}
1ES1959+650				
53254.0	3719 ± 15	0.82 ± 0.22	3.7	1.83 ± 0.47
53254.9	2537 ± 12	0.54 ± 0.24	2.2	0.74 ± 0.48
53285.0	2454 ± 18	0.95 ± 0.28	3.4	1.76 ± 0.67
53287.9	2187 ± 11	0.95 ± 0.30	3.2	1.34 ± 0.68
53292.9	1821 ± 10	0.53 ± 0.31	1.7	1.38 ± 0.75
53293.9	2842 ± 13	1.26 ± 0.27	4.7	2.69 ± 0.67
53294.9	5139 ± 17	0.69 ± 0.18	3.9	1.23 ± 0.40
Tot.	20958 ± 35	0.81 ± 0.09	8.8	1.57 ± 0.21
Crab Nebula				
Tot.	7427 ± 21	5.34 ± 0.21	25.5	11.11 ± 0.51

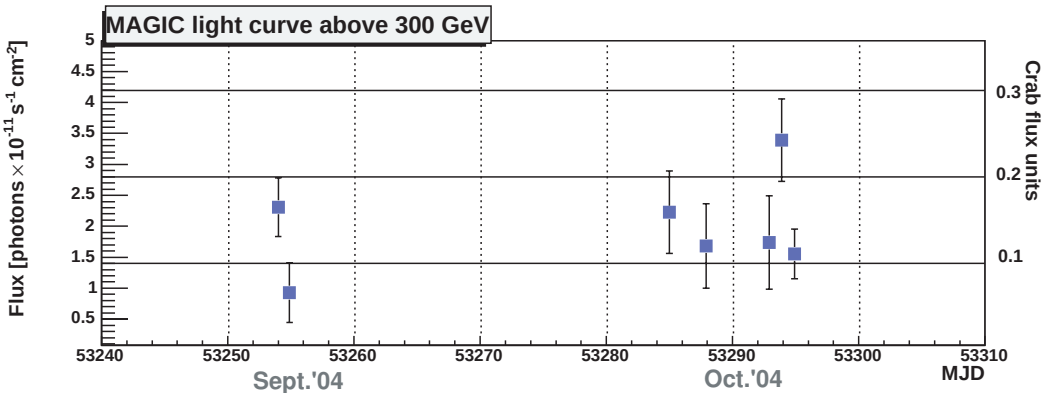

Figure 8.9: *Integral flux above 300 GeV of 1ES1959+650 (after corrections for the camera inefficiency), with an average 1ES1959 flux of ∼14% Crab. The Crab flux has been assumed to be constant.*

8.4.1 Differential energy spectrum

We applied the energy estimation to the 1ES1959 data sample and divided the data in five logarithmic bins of energy, between 150 GeV and 2 TeV. The ALPHA plots of figure B.10 show for each energy bin the resulting signal, summarized in table B.2.

The spectrum of 1ES1959 measured with MAGIC (figure 8.10, dashed line) is well described by an unbroken power law function:

$$\frac{dN}{dE} = (0.34 \pm 0.05_{stat.} \pm 0.02_{syst.}) \cdot 10^{-11} \left(\frac{\mathrm{E}}{1\mathrm{TeV}}\right)^{(-2.72 \pm 0.14_{stat.} \pm 0.05_{syst.})} \mathrm{cm}^{-2}\mathrm{s}^{-1}\mathrm{TeV}^{-1} \tag{8.6}$$

Here, the systematic error is due to the unfolding procedure only. Table 8.5 lists the differential flux values (in bins of estimated energy). In figure 8.10 the differential flux points of 1ES1959 (in blue) and Crab Nebula (in red) are plotted together with the result of the unfolding procedure. After correction for camera inefficiency (solid line) the energy spectrum of 1ES1959 can be described as in 8.7.

The discussion of this result is presented in chapter 9.

8.4.2 Correction for inefficiencies of the camera response

The distribution of events in the camera plane should be uniform under ideal camera conditions. The plots of figure B.3 (below, right) show the distribution of the centers of gravity of the images in the camera plane. The angular position of the events after γ-hadron separation cuts in the camera coordinates are plotted in Figures B.11 and B.12. The non-uniform distribution is evident especially in the Crab data

Table 8.5: *1ES1959 differential flux. The mean energy value is shifted to the left with respect to the bin center, in order to take into account the spectral slope (corresponding to the median of the bin content distribution). The points are plotted in figure 8.10, blue hollow circles.*

Mean energy GeV	Flux (TeV^{-1} cm^{-2} s^{-1})
192	$(3.09 \pm 0.83) \cdot 10^{-10}$
323	$(7.42 \pm 1.43) \cdot 10^{-11}$
542	$(1.98 \pm 0.39) \cdot 10^{-11}$
910	$(3.74 \pm 0.90) \cdot 10^{-12}$
1528	$(9.76 \pm 2.71) \cdot 10^{-13}$

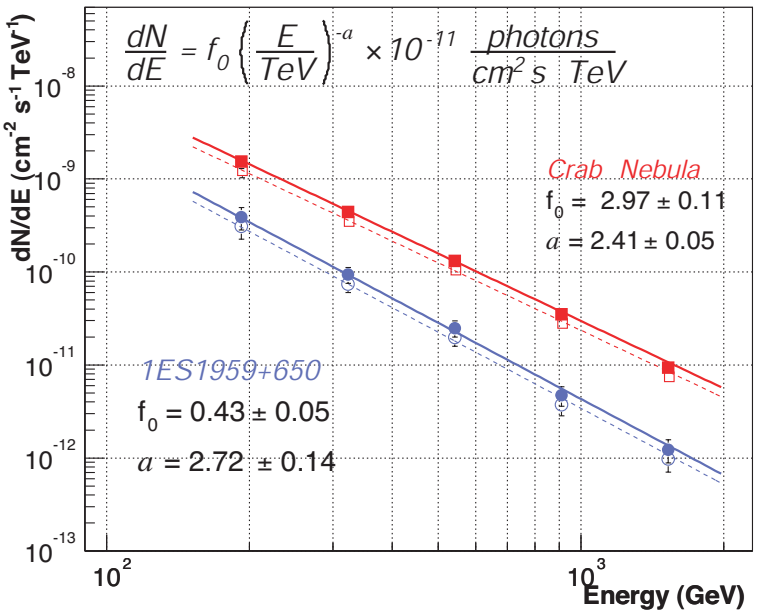

Figure 8.10: *Differential spectrum of the AGN 1ES1959 and the Crab Nebula, plotted here together for comparison. The blue hollow points of 1ES1959 correspond to those listed in table 8.5. The filled points are obtained after correction for the camera inefficiency (26% in flux, see section 8.4.2). The lines are the result of the unfolding procedure, assuming a power law function for the description of the spectrum. The vertical bars represent the statistical errors.*

at low energies, where a higher systematic error of ∼38% is expected, while in 1ES1959 data the underestimation of the flux would be stronger at high energies, reaching ∼72%. The measurements are such that a detailed study of the systematic

behavior of the different parts of the camera are difficult and not easy to quantify. We therefore apply an overall correction factor to the measured γ-ray flux of 26% (see appendix B.6 for the calculation).

After applying the correction, the Crab Nebula spectrum is described by equation 8.3. The mean Crab γ-ray flux has been measured to be $(14.0 \pm 0.5) \cdot 10^{-11}$ ph. cm^{-2} s^{-1}. The final differential spectrum for 1ES1959 results to be as in equation 8.7.

8.5 Possible sources of systematic errors

Besides the statistical errors, the results can also be affected by systematic errors. Sources of systematic errors are listed in the following. Most of them produce an effect that is difficult to evaluate with the present available instruments and only a coarse estimate can be done.

Atmospheric transmission. The conditions of the atmosphere was not monitored during the observations. In our MC simulations, a standard atmospheric model is used [111, 112], but real conditions of humidity, high clouds, and, in general, the non-ideal atmospheric conditions that possibly affect our data, lead to an underestimation of the measured flux.

The atmospheric information related to the days we observed 1ES1959 with MAGIC are provided by the NOT weather station, working in the same astronomical site and available at the NOT web-site:
`http://www.not.iac.es/weather/metdata.php`

The estimated uncertainty in the integral flux is 15%.

Calibration in absolute scale. The calibration system can introduce systematic errors that are still not understood at the moment. The hardware light pulser can have failed, or produced flashes of different intensities, due to temperature drift. The software procedure (based on the so-called F-factor method) can also introduce a systematic error, due to the poor knowledge of the PMTs signal-to-noise ratio. The uncertainties in the PMT quantum efficiency have been estimated to be 5%. The hardware flat-fielding procedure has a systematic error of 2%. The total uncertainty in the absolute calibration has been estimated to be 8-10% to be attributed to the conversion factors.

Causes of photon losses: Mirror's reflectivity. The mirror's reflectivity is on average 85% in our MC data. This number agree quite well with measurements, but an uncertainty of the reflectivity is possible because of dirt, dust, etc. Also the effective reflector focusing (in the MC simulation the PSF was fixed to 1.4 cm, corresponding to 0.047°) can be different from the simulated value and can fluctuate, depending on the AMC system working conditions. Failures to some AMC parts can also be responsible for defocussing of part of the mirror. The systematic uncertainty is estimated to be 5%.

Dust in the camera window. The plexiglas window which protects the PMTs from the dirt can also reduce the number of photons that reach the photocathode. The presence of dust or dirt in the camera window is not taken into account in the calculations and the error on the flux can be of 3%.

Light cone losses. The light cones in front of the PMTs can cause a small loss of photons, which is estimated to be about 5%.

The photon losses were evaluated with a dedicated study of the muon rings images [135]. As a result, an overall correction factor in the number of photons to convert to photo-electrons of 0.73 was applied to the MC data sample.

Difference between MC simulation and data The previous points can be partly summarized in the difference between the simulated detector and the real configuration during data taking. The flux estimate error can be due to the atmospheric profile included in the simulation; to the ideal conditions of the simulated detector; to the fluctuations of the response of the electronics with temperature, not realistically described in the simulation; to dust or dew deposited on the telescope reflector or camera window during data taking; to the eventual partial failure of the focussing procedure. We estimate that the listed causes can affect the reconstruction of low energy events more that high energy events. The difference of the simulated EM showers with respect to the recorded showers is not easily quantified, but (hopefully) negligible. The systematic error on the estimate of effective area for the calculation of the flux can be of 10% and on the energy reconstruction of 5%. An imprecise evaluation of the telescope pointing position (due to hardware reasons, as the bending of the structure for observations at high zenith angles, not properly corrected by the TPoint model) or of the tracking, reflects on the number of excess events and therefore on the flux evaluation. The error is anyhow partly included in the statistical errors.

Some hardware problems, such as the discriminator inefficiency (2%) or the record of spark-events (filtered in software: 2%) or uncertainties on the dead time corrections due to FADC instabilities (2%) can cause the loss of low energy events in the data sample. Also the software procedure (the signal extraction and the image cleaning) can cut out good low energy events from the analyzed data sample. To limit this problem, a cut in the lower SIZE events was applied to the analyzed data before γ-hadron separation and the systematic error is estimated to be 6%.

Effects of the earth's magnetic field The effects of the earth's magnetic field would show up on charged particles traveling perpendicular to the earth's magnetic field. Crab (both ON and OFF) data are taken observing at a mean azimuthal angle of 88-89°, while 1ES1959, at a mean azimuthal angle of -15°. The MC used for the analysis was generated with 0° azimuthal angle. This can affect the results on Crab data, but for 1ES1959 we do not expect a systematic error.

Analysis method The parameters adopted in the analysis can be a source of systematic errors. We have repeated the analysis under several conditions, in order to control the systematics. All the tests done reveal that the systematics due to the analysis methods are, in general, negligible.

The overall systematic error to the flux was evaluated from the above listed contributions to be ∼30%. The error is attributed to the flux value, since most of the effects described above are independent of the event SIZE.

The evaluation of the systematic error on the spectral index implies knowledge of the energy dependence of the errors listed above. The systematic uncertainty on the spectrum slope is typically at least ~ 0.2.

The Crab spectrum measured with MAGIC is reported in Equation 8.3 while the 1ES1959+650 spectrum is:

$$\frac{dN}{dE} = (0.43 \pm 0.05_{stat.} \pm 0.13_{syst.}) \cdot 10^{-11} \left(\frac{\mathrm{E}}{1\mathrm{TeV}}\right)^{(-2.72\pm0.14_{stat.}\pm0.25_{syst.})} \\ \mathrm{cm}^{-2}\mathrm{s}^{-1}\mathrm{TeV}^{-1} \tag{8.7}$$

The large systematic error that affects the measurements can be partly reduced with deep studies using MC simulations and with precise measurements and monitoring of the telescope subsystems. For the moment, this information is not available and the contribution of systematics have to be taken into account, even though most of them are only guessed values.

The parallel analysis of Crab data reduces the influence of the systematic errors on the relative comparison between the two data-sets. When the systematic uncertainty of the absolute Crab flux is reduced (and the magnetic field effects properly taken into account), the new values of flux for 1ES1959 can be directly derived.

Chapter 9

Discussion and conclusions

In this chapter, the results presented in the previous chapters are compared with published measurements at different wave-lengths by other collaborations and I will discuss their physics implications.

9.1 Comparison with published TeV γ-ray measurements

9.1.1 Comparison of the light curves

During the years 2000 and 2001, there were no campaigns of simultaneous observations with IACTs. With CT1, only a very short period of increased activity in those 2 years was recorded, at the end of June (MJD 51724.1-51725.1), in 2000. Very long periods of low activity seem to be a characteristics of the VHE γ-ray emissions of 1ES1959.

The HEGRA CT1 light curve of 2002 can be compared with other results from the multi-wavelength campaign, i.e. with Whipple and the HEGRA System data, as well as the RXTE X-ray data, optical and radio measurements. The light curves of the mentioned Cherenkov telescopes are shown in figure 9.1. The blue points are the CT1 measurements, added for a direct comparison to the light curves published in [78]. Is should be noted that some CT1 data were taken during partial moonshine. The threshold of the experiments are different (600 GeV for Whipple, 1 TeV for CT1 and 2 TeV for the HEGRA System) and the Whipple observations have a time difference of 6 hours delayed with respect to the HEGRA telescopes. Fluxes are scaled in units of the Crab flux: the bias on the flux between different experiments can be due to different energy thresholds of the instruments and to the fact that the spectral index of the source is different from the Crab one.

In general, the AGN 1ES1959 was in a high level of activity during 3 periods:

- During the second half of May: all three experiments confirm, at different levels, the high activity of the source. The flux was high all the days when measurements were possible before the full moon period. The peaks were

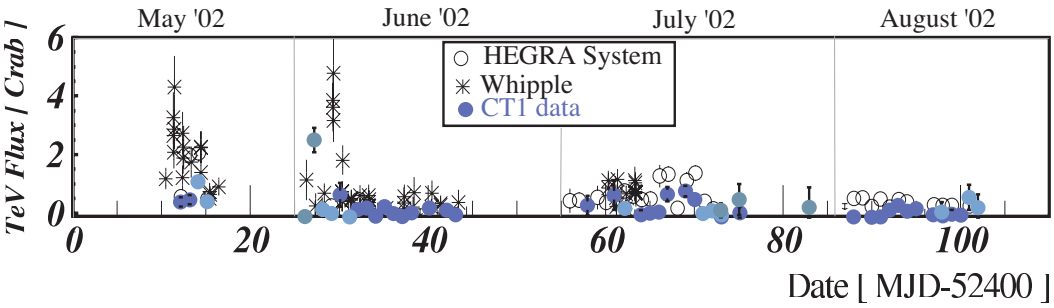

Figure 9.1: *The 1ES1959 light curves recorded during the 2002 multi-wavelength campaign. CT1 TeV flux above 1 TeV (in Crab units) are superimposed on the published data, for a direct comparison with the HEGRA System measured mean integral flux above 2 TeV and the Whipple measurements above 600 GeV (for details, see [78]).*

registered in different days for the different experiments, because of the time offset between the observations.

- Flare at the beginning of June: flaring events were recorded on two different days by CT1 and Whipple. On June, 2^{nd} (MJD 52427.1) a strong flare was recorded by CT1, but 6 hours later Whipple reported low activity. Two nights later, CT1 recorded low emissions, while during the observations with Whipple, 6 hours later, the emissions increased to 4 Crab level. One night later (MJD 52430) both experiments observed modest activity of the source, which remained in a quiescent state for the rest of the month.

- Flaring of mid July: a modest increase of the emissions was registered by HEGRA System and CT1 (MJD 52467 and 52469-70), while Whipple did not observe. As in June, the increased emission level lasted for some days.

The CAT experiment observed 1ES1959 in 2002 for 10.5 hours of observation. The detection had 13.5σ significance [93]. The CAT light curve is shown in figure 9.2, compared with CT1 measurements. The CAT instrument was located in Themis (France), thus the observations of the two detectors are almost simultaneous. Both experiments agree in showing a clear, strong increase of VHE γ-ray flux during the day 52427(June 2nd).

From the analysis of the light curves of the experiments with different thresholds, we can conclude that the variability of the source can be different in different energy regions of the spectrum, perhaps being higher at lower energies. Comparing the observations of HEGRA and Whipple, we can infer the fast variability of the source and the maximum duration of the flaring episodes being at most 6-8 hours, i.e. the time difference between their observations. The minimum flux time variation puts some constraints on the characteristics of the emitting region in the jet and it will be discussed in section 9.2. Longer periods of high emissions have been

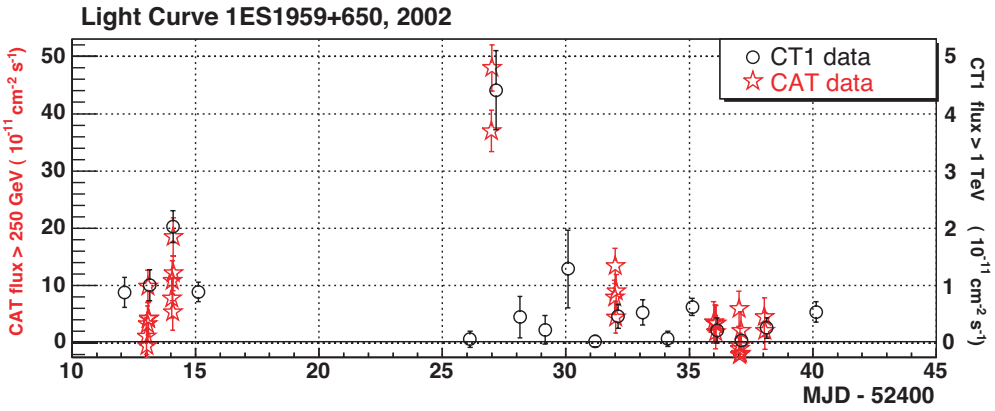

Figure 9.2: *The γ-ray light curve as measured by CAT (red stars) above 250 GeV [93], compared with CT1 light curve above 1 TeV, during the flaring periods of May-June 2002.*

observed, similarly as for other AGNs (Mkn421 and Mkn501), up to several weeks, as happened for example on May 2002.

During the observations with MAGIC in 2004, we have no reports of simultaneous measurements by other IACTs. The night-by-night activity of the source at energies above ∼200 GeV has never been published by other telescopes. The level of variability and the comparison of the spectra (see later), suggest that during the MAGIC observations the source was in a quiescent period. The observations with MAGIC open therefore new perspectives in the study of AGNs: the low emission periods can be monitored without the need for long observations before having collected a significant γ-ray signal, and the study of flaring patterns will be more accurate.

9.1.2 The 1ES1959 differential energy spectrum

The 1ES1959 spectrum at TeV energies

The study of the 1ES1959 spectrum during periods of weak γ-ray emissions can be carried out by analyzing the 2000-2001 observations using the measurements of CT1. The low statistics of the collected data do not allow us to obtain the differential energy spectrum of the source in that period. The HEGRA System measurements during periods when the emissions from the source did not exceed 0.5 Crab were defined as *low state* and used to compute the spectrum under these conditions in [91].

During the longest part of the observation time spent on 1ES1959 with CT1 in 2002 the source was in its *low state* according to the previous definition. Observations with nominal voltage, used to compute the spectrum, hardly reached the 0.5 Crab level.

The energy threshold of the HEGRA System measurements is 2 TeV, compar-

able to the CT1 energy threshold (1 TeV). As can be seen in the graph of figure 9.3, in the year 2002, CT1 spectrum recorded in 2002 is compatible with the low state spectrum measured with the HEGRA System and described by a simple power law function [91]:

$$\begin{aligned}\frac{dF}{dE} &= f_0 \left(\frac{E}{TeV}\right)^{-a} \\ &= (0.78 \pm 0.15 \pm 0.1) \left(\frac{E}{\mathrm{TeV}}\right)^{-(3.18\pm0.17\pm0.08)} \cdot 10^{-11} \quad \mathrm{cm}^{-2}\mathrm{s}^{-1}\mathrm{TeV}^{-1} \\ \text{with a } \frac{\chi^2}{d.o.f.} &= 0.22\end{aligned} \tag{9.1}$$

or with a power law with an exponential cutoff:

$$\begin{aligned}\frac{dF}{dE} &= f_0 \left(\frac{E}{\mathrm{TeV}}\right)^{-a} \exp\left(\frac{E}{E_0}\right) \\ &= (0.60 \pm 0.14 \pm 0.08) \left(\frac{E}{\mathrm{TeV}}\right)^{-1.8_{fix.}} \exp\left(\frac{E}{2.7^{+0.6}_{-0.4} \pm 0.6}\right) \cdot 10^{-11} \\ &\quad \mathrm{cm}^{-2}\mathrm{s}^{-1}\mathrm{TeV}^{-1} \\ \text{with a } \frac{\chi^2}{d.o.f.} &= 0.65\end{aligned} \tag{9.2}$$

The parameters of the fits used to describe the spectral shape (see equations 7.2 and 7.1 for the CT1 results) are marginally compatible within the errors.

The 1ES1959 spectrum above 200 GeV energy

MAGIC measurements extend downward to 200 GeV and are thus extended well below the threshold of previous measurements. Even around 200 GeV we still do not have indications of the position of the IC peak and the spectrum can be well described by a simple power law function.

The overlap of the HEGRA and MAGIC spectra is marginal. In the region of the overlap around ∼1.5 TeV, the spectrum measured by MAGIC is ∼66% of the one measured by the HEGRA System. The lower flux recorded by MAGIC at 1.5 TeV is another confirmation of the supposed low state of the source at the time of the observations with MAGIC.

The 1ES1959 spectrum was, at the time of the MAGIC observations, flatter than the published HEGRA result. The low state spectrum of the source measured with the HEGRA System had a spectral index of $\alpha = -3.18(\pm0.17)_{stat}\ (\pm0.08)_{sys}$

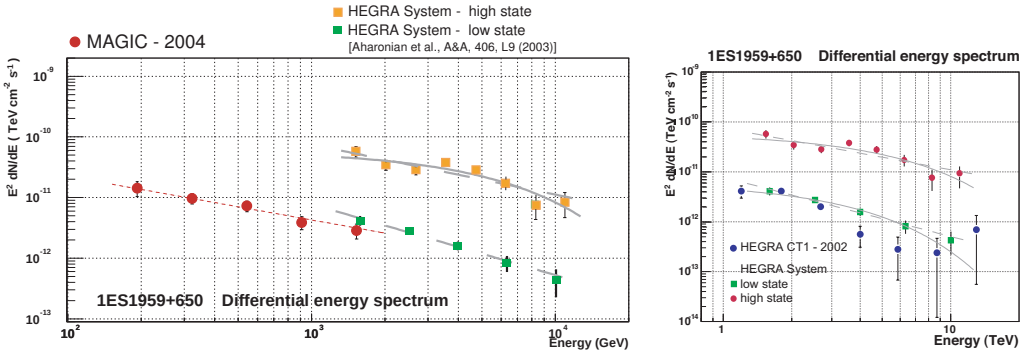

Figure 9.3: *Left: Spectral energy distribution (SED) of 1ES1959+650 (this work) and the published HEGRA System result for the low state nights (flux < 0.5 Crab) until 2002 [91]. Right: Spectrum of CT1 2002 (all data set recorded during moonless nights), compared with published results by the HEGRA System [91], divided in high state and low state of activity of the source. The spectrum measured by CT1 during moonless nights in 2002 is compatible with the low state measured by the System, until the statistics are high enough. Above 5 TeV the statistics of CT1 data are limited and therefore it is difficult to draw conclusions regarding the presence of a cutoff.*

[91]. This spectral index is valid for a higher energy range with respect to CT1 measurements. When approaching the IC peak, a flattening of the spectrum is naturally expected.

The mean integral flux registered by the HEGRA System is well compatible with that measured by CT1 during 2000 and 2001, considering that the measurement of the flux was carried out during many nights and the emissions of the source could be, in principle, different from one night to the other.

The MAGIC measurements cover a lower energy range with respect to previous data. The mean integral flux above 300 GeV measured during September and October 2004 is about 14% the Crab flux, measured in the same energy range. The flux given by HEGRA for the higher energy range of the low state is about 5% of the Crab flux , compatible with the fact that the spectrum of the source is steeper than the Crab spectrum. The Whipple collaboration could only set an upper limit to the low state flux [88], to 1.3×10^{-11} cm^{-2} s^{-1} above 350 GeV, comparable to the MAGIC result above 300 GeV of $1.96 \pm 0.21_{stat} \times 10^{-11}$ cm^{-2} s^{-1}.

The period of high VHE γ-ray emission permits the study of the changes of the source spectrum correlated to the state of the source. High state spectra were reported by the VERITAS collaboration and by the HEGRA System, whose measured spectra are compared in figure 9.4. Unfortunately, it is not possible to make a direct comparison with the CT1 spectrum of 2002 data, because of the low statistics.

The comparison of the spectra measured in different periods by a variable source is not an easy task. The compatibility of the measurements allows us only a coarse description. The CT1 measurements, and especially the MAGIC measurements,

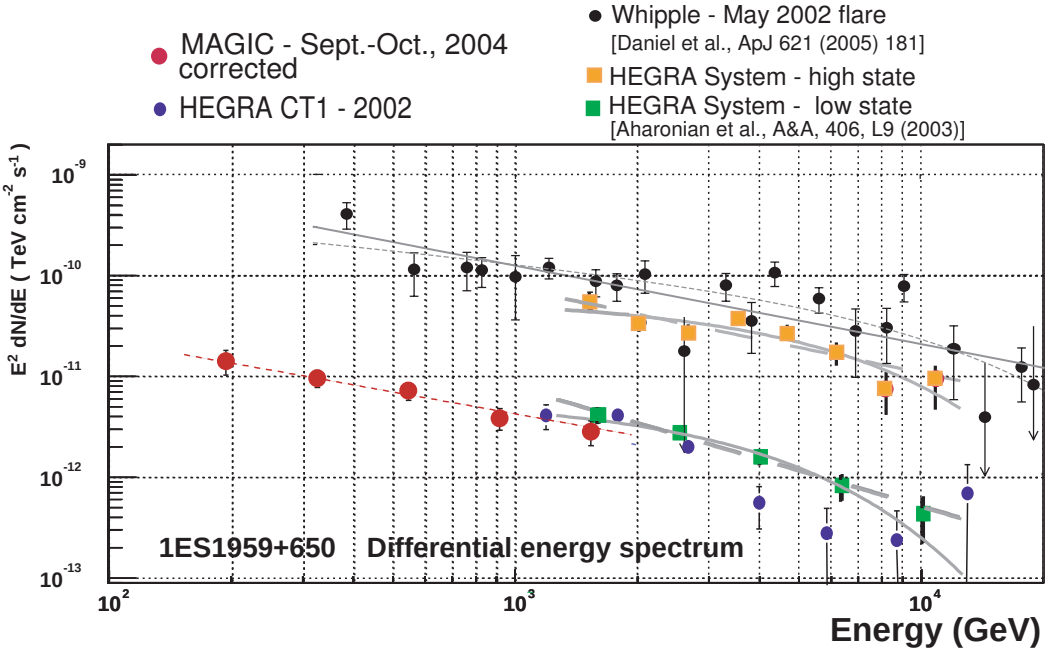

Figure 9.4: *Compilation of all published data related to the spectrum of 1ES1959, both in high and low state and comparison with the results obtained in this work from the HEGRA CT1 and MAGIC data analysis.*

certainly provide precious information for the future modeling of the source emission processes.

9.1.3 Multi-wavelength measurements

The correlation between X-rays and TeV emissions has been observed for several TeV blazars during flaring periods. No correlations between radio or optical activity with TeV emissions has been reported yet.

The study of correlations between activities at different wavelengths (in particular X-rays and γ-rays) are justified by the SSC leptonic models: electrons emitting X-rays by the synchrotron process are also responsible for the inverse Compton emissions, producing γ-rays. The correlations between X-ray and γ-ray emission can constrain parameters of the AGN jet, such as the Doppler factor and the magnetic field, once the effect of the EBL absorption is properly taken into account.

The multi-wavelength campaign for the simultaneous observation of 1ES1959 during the year 2002, when the highest variability of the source was observed, is of great interest in order to study possible correlations. The plots of figure 9.5 are the published data of the mentioned multi-wavelength campaign [78]. The light curve of CT1 has been added, after scaling the flux to Crab units. In this way a direct correlation study can be done.

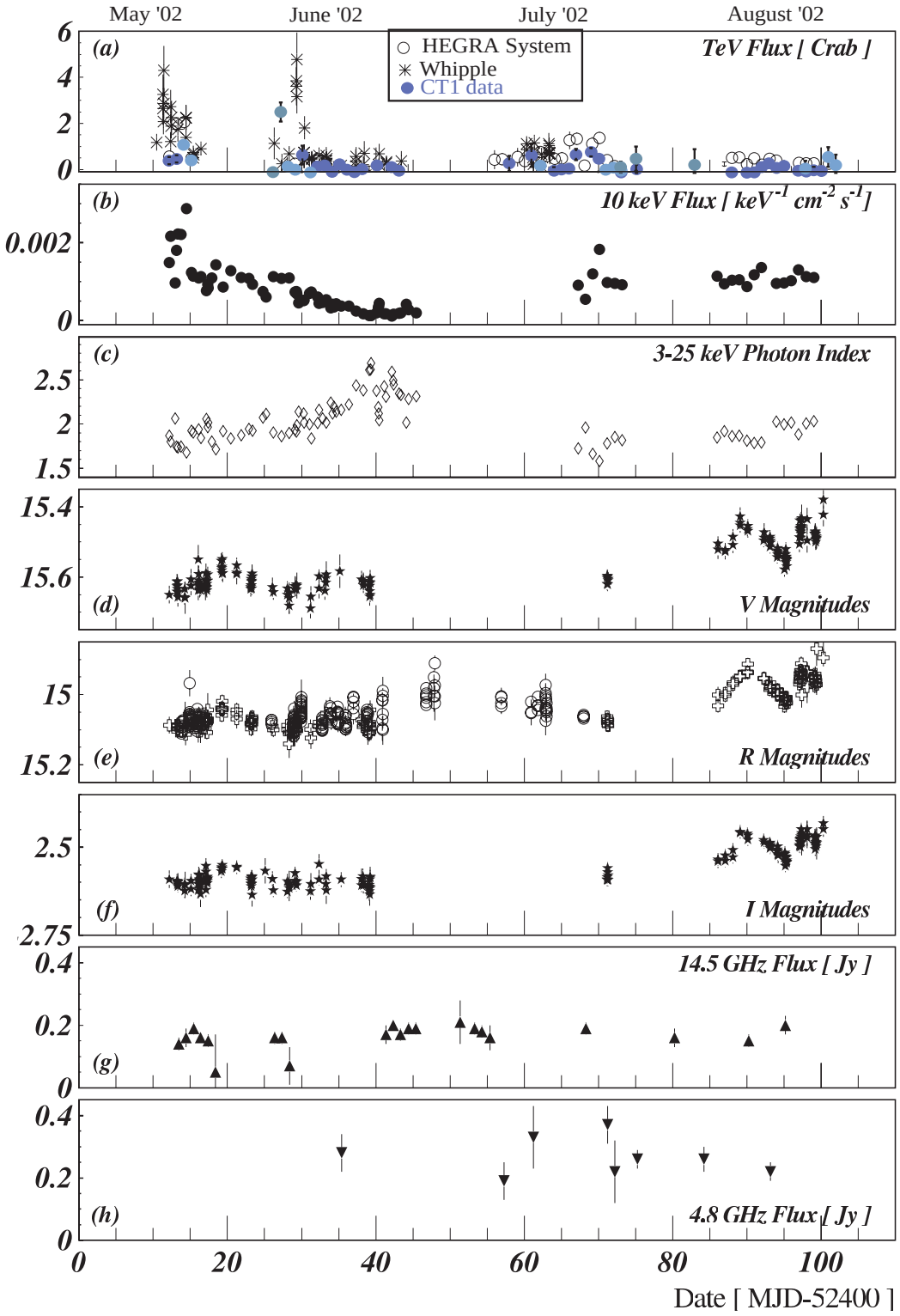

Figure 9.5: *The 1ES1959 light curves recorded during the 2002 multi-wavelength campaign. CT1 TeV flux above 1 TeV (in Crab units) are superimposed on the published data, for a direct comparison in panel (a): The HEGRA System measured mean integral flux above 2 TeV and the Whipple measurements above 600 GeV. (b) RXTE X-ray flux at 10 keV. (c) RXTE 3-25 keV X-ray photon index. (d) Absolute V magnitude. (e) Absolute R magnitude. (f) Relative I magnitude (wrt reference star 4 from [138]) (g) the 14.5 GHz flux density, in Jansky (h) 4.8 GHz flux density, in Jansky (for the definition, see p.xxiv). For details, see [78].*

Figure 9.8 shows the MAGIC light curve together with the X-ray and optical measurements of the same period.

Correlations with radio emissions

During the measurements of 2002, the radio emission stayed basically constant. The absence of substantial variation during periods of variability in other wavelengths is an indication of a possible independent process generating the observed emissions at GHz frequency. Also in other TeV blazars no correlation between radio and other wavelength emissions has been found.

Correlations with optical emissions

The light curves show no evident correlation between the optical, the X-ray and the TeV fluxes. The optical flux in the three available V-R-I bands did not show strong variations during 2002, except a small but significant variation in August.

A modest increase in the optical flux happened at the end of May, when the TeV and the X-ray activity strongly decreased. The optical flux remained constant during June, also when the TeV emissions increased, while in X rays the activity was still slowly decreasing. The following periods are not fully covered by optical observations, making correlation studies difficult in July, when another period of high γ-ray activity was reported.

In August the optical activity shows a clear variation. Starting from a mean flux value, the source reached a peak of emission in MJD 52490, then the flux smoothly decreased during the following 5 days. After this 10 days period, the optical flux rose again to the previous peak level and remained high for the last days of the campaign. Also in this last period of simultaneous observations, the increase of optical activity coincided with a period of (modest) decrease X-ray flux and a very modest increase of the TeV γ-ray flux.

The light curve of 1ES1959 in August 2002 measured by RXTE-ASM [139] (see figure 9.6) can help to find (even though qualitatively) correlations between X-rays and optical emissions, indicating also in this case a possible anti-correlation (see MJDs 52485.5-52488).

Even though this is only a naive hypothesis, we can try to give a plausible, qualitative description of the phenomenon. Assuming an SSC leptonic model for the description of the X-ray-TeV emissions, the decrease of the X-ray activity can be due to the decrease of the mean electron energy density.

The short observations of 2004 with the MAGIC telescope do exclude the possibility of studying any significant correlation between the optical and other wavelengths emission. The only evident characteristic of the optical measurements in 2004 is the very low state of the source during the optical observations, compared to the mean flux of the previous measurements started in 2002 (see comparison with the solid line of figure 9.8). Further measurements with MAGIC during a higher

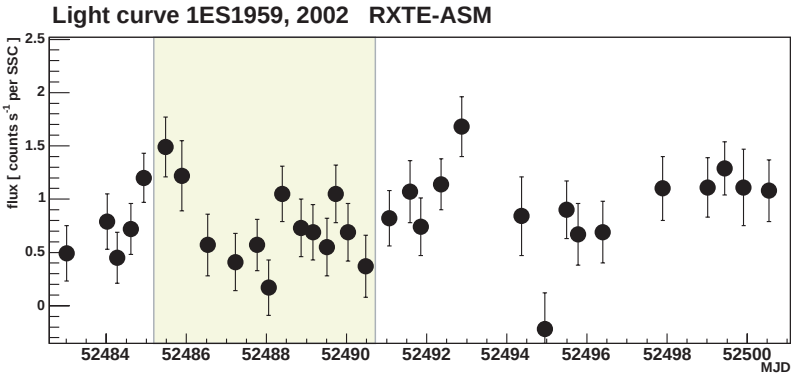

Figure 9.6: *The X-ray light curve from RXTE-ASM during August 2002. The MJDs 52485-90 are interesting because of a strong increase in the optical activity while the X-ray emission was decreasing.*

optical activity could help to study whether there is any correlation between optical and γ-ray fluxes during the low γ-ray emission level of the AGN.

The main difficulty in the interpretation of the optical flux measurements consists in the uncertainty on the origin of the optical emission. The light coming from the AGN accretion disc, also characterized by high variability, makes, in fact, a strong contribution to the measured flux, that can therefore be interpreted as an upper limit to the emission from the jet.

Correlation of the TeV emission with the X-ray emission

TeV and keV emissions are often correlated. The observed correlation has triggered the development of a popular model, the so-called SSC model, described in section 1.3.1, which can explain the emission from AGNs in a wide energy range.

The analysis of the multi-wavelength light curve in figure 9.5, panels (a) and (b), shows that in May the correlation between X-rays and γ-rays is quite strong. The high X-ray emission corresponds to strong TeV emission, even though it is difficult to see the connection between the X-ray flux and the flux measured by the IACTs. The peak of X-ray emissions on MJD 52414 agrees well with the observed TeV flare.

The June flares are the most interesting events and for this reason the expanded multi-wavelength light curve is reproduced in figure 9.7. Some of the strongest (and maybe fastest) TeV flares of 1ES1959 were observed in that period and they occur without any episode of variability at other wavelengths. The other interesting feature is that it happened twice, reported by two different experiments, CT1 and Whipple, within two days. In both cases, the X-ray emission stayed low and did not vary with the TeV flare, but followed the general trend of the period of slow and smooth decrease. The described TeV flares have therefore been called *orphan flares*.

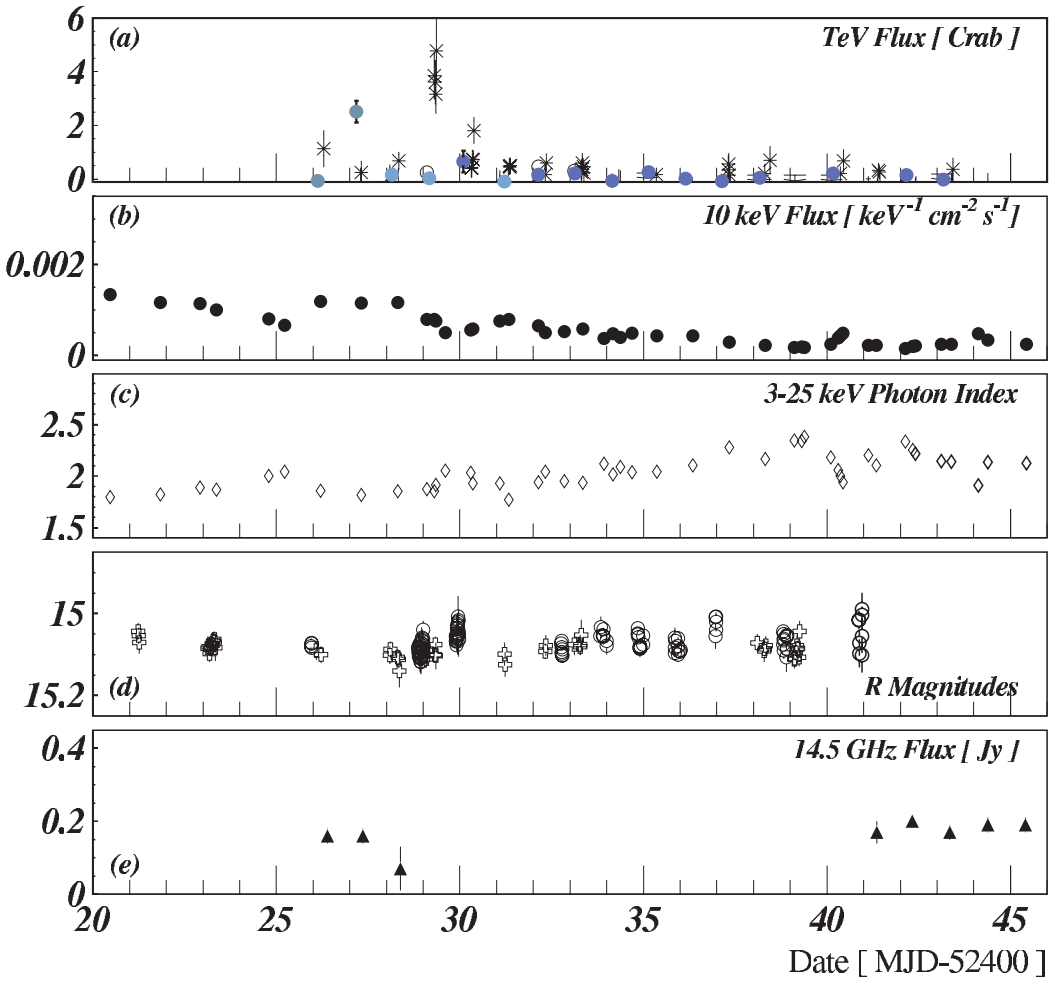

Figure 9.7: *Particulars of the 1ES1959 light curves recorded during the 2002 multi-wavelength campaign: zoom of figure 9.5 in the period when the orphan flare was detected. CT1 TeV flux above 1 TeV (in Crab units) are superimposed on the published data, for a direct comparison in panel (a): HEGRA System measured integral flux above 2TeV and Whipple measurements above 600 GeV, with the same symbols as in figure 9.5. (b) RXTE X-ray flux at 10 keV. (c) RXTE 3-25 keV X-ray photon index. (d) Absolute V magnitude. (e) Absolute R magnitude. For details, see [78].*

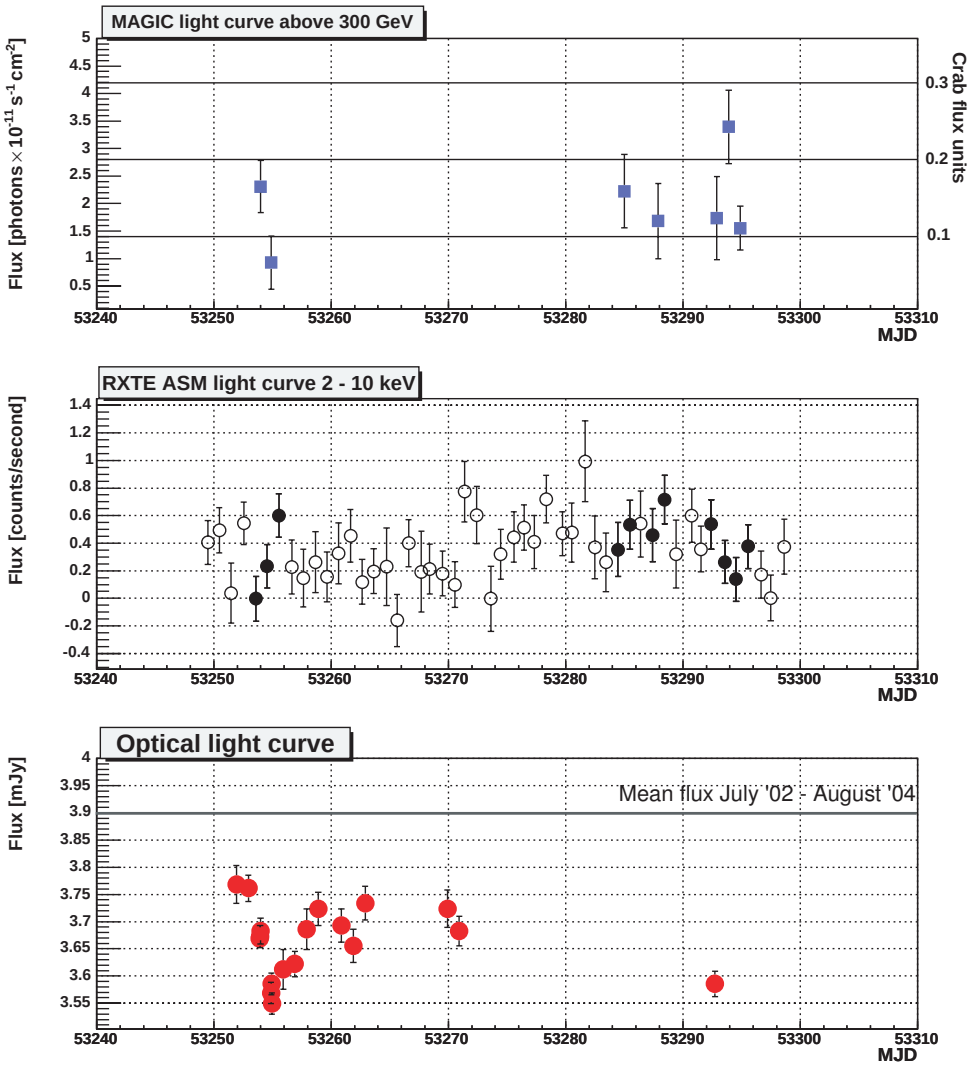

Figure 9.8: *Light curve of 1ES1959 during the observations with MAGIC in 2004. The γ-ray, X-ray and optical light curve are here plotted together for a direct comparison.*

This created a lot of interest in the TeV activity of the AGN, because the one zone SSC model is ruled out in this case. Other emission processes should coexist inside the 1ES1959 jet to be able to explain the *orphan flares*.

In July, the X-ray flux varied quite quickly, reaching a peak on MJD 52470. On the same day the TeV flux increased accordingly, confirming also in this case the correlation between increase of emission in the two wavelength bands.

A strong correlation between spectral index and flux in the X-ray energy range has been also confirmed during the 2002 observations [78].

In general, we noticed that during strong variations in the X-ray emissions, increased TeV fluxes are also observed, while strong X-ray variability does not always occur during TeV flares.

It is not easy to determine correlations between the absolute fluxes. On August 2002, for example, the X-ray flux was quite high, reaching a peak on MJD54493. The same day CT1 also recorded a small increase in the flux, but, in general, the TeV emissions followed the mean trend.

9.2 Comparison with the emission models

9.2.1 Synchrotron - Self Compton models

The multi-wavelength spectral features of 1ES1959 can be analyzed using the most popular models for the description of blazars. Particularly successful and simple is the model known as the *one zone (homogeneous) Synchrotron Self-Compton* (SSC) model [57, 59] (see section 1.3.1). The model attempts to describe the flaring TeV γ-ray emissions and the correlations with the X-ray activity of the source and I will briefly describe it here. In the blazar jet, a spherical region is moving with Lorentz factor Γ towards the observer (i.e. the angle θ between the jet axis and the observer's line of sight is small). The region (of radius R) is populated by relativistic electrons, which gain their energy by shock acceleration. They emit synchrotron radiation under effect of a randomly oriented magnetic field. The same electrons upscatter the synchrotron photons by inverse Compton process and accelerate them to TeV energies. The electron population spectrum is described using a broken power law, a minimum and maximum allowed energy. The parameters of the model are listed in table 9.1.

The model is constrained by some conditions (for a detailed description, see [140]):

- The source should be transparent to γ-rays: the seed photons in the jet could in fact absorb the higher energy photons and in this case no TeV radiation could be seen.
- The dimensions of the emitting region is constrained by the minimum observed variation time and the Doppler factor:

$$R \leq c\,\delta\,\mathrm{t}_{var} \tag{9.3}$$

Table 9.1: *Description of the parameters for the one zone SSC model.*

Emitting region parameters:	
Γ	bulk Lorentz factor: $E_e = \Gamma\, m_e\, c^2$
δ	Doppler factor: $\delta = [\Gamma(1 - \beta\cos\theta)^{-1}]$
R	radius of the emitting region
B	magnetic field inside the emitting region
Electrons population parameters:	
K	electron density in the emitting region
$n_{1,2}$	slopes of the electrons energy spectrum ($n_1 < 3$, $n_2 > 3$)
E_{min}	electrons minimum allowed energy
E_{max}	electrons maximum allowed energy
E_b	electrons break energy $E_b = \gamma_b mc^2$, $E_{min} < E_b < E_{max}$
Observable parameters:	
$\nu_{s,c}$	peak frequencies of the Synchrotron and the IC emissions
$L_{s,c}$	Synchrotron and IC peak luminosities
$\alpha_{1,2}$	power law spectral indices (left and right side of each peak)
t_{var}	minimum time-scale variation of the emissions

and the radius of the region cannot be too small, to limit increase of the Doppler factor.

- The model should also be able to explain the time lags between flares, observed in some AGNs. The time lags are interpreted as the time that is needed to cool the injected electrons. For 1ES1959 we do not have this information yet.

In addition, the IC peak is affected by the EBL absorption, which has to be taken into account when comparing the model with observations. The observed radio emissions are not described by the one zone SSC model: the emissions in the radio band are self-absorbed.

The relation between the parameters are such as to constrain as much as possible the magnetic field B and the Doppler factor δ:

- The dominant synchrotron power should be emitted by the electron with energy E_b (break energy). The emitted photons are then the target for the same electrons of energy E_b. Using the Thomson limit, we can find a relation between the synchrotron and IC peak frequencies.

- The peak luminosity of the synchrotron and IC emissions is directly proportional to the radiation energy density of the magnetic field and of the synchrotron photons, respectively. Using the upper limit for the R of the emission region (from the variability time scale) it is possible to find another constraint on the parameters of the model:

$$B\delta^3 \geq (1+z)\left[\frac{2(\nu_s L_s(\nu_s))^2 f(\alpha_1,\alpha_2)}{c^3 t_{var}^2 \nu_c L_c(\nu_C)}\right]^{1/2} \tag{9.4}$$

In many aspects 1ES1959 is very similar to Mkn501: long quiescent periods interrupted by strong isolated flaring episodes, sometimes lasting for weeks. The initial parameters for modeling 1ES1959 were therefore initially set to the ones describing Mkn501.

A first attempt to estimate the radius of the emitting region in the jet can be done, based on the duration time of the fastest observed flare, that is ∼7 hours, as explained in section 9.1.1. According to equation 9.3 and assuming a Doppler factor of δ=20, the radius of the emitting region responsible for the observed flares, results to be R $\lesssim 1.5 \cdot 10^{14}$ m ($\lesssim$ 6 light days).

The spectral energy distribution, published in [78], are shown in figure 9.9 together with the MAGIC measurements. The X-ray and γ-ray emissions described by the model are consistent with the observations, while the optical measurements are higher than predicted: this can be an indication of the fact that the electrons emitting the optical radiation belong to another population, with other parameters, maybe the same population responsible for the radio emissions, as claimed in [141]. Since the optical emission can also be generated in the accretion disc, the plotted value must be treated as an upper limit.

According to the parameterization found, the IC peak should occur at 100-400 GeV.

As mentioned in [87], the steady X-ray emissions from 1ES1959 can be due to bright knots inside the jet. In the SSC framework, the parameters of the emission region should also be able to provide GeV photons, as detected by MAGIC.

The comparison to the MAGIC measurements shows that the source was in a period of slightly lower emissions with respect to the HEGRA data sample, even though compatible within the errors. The new data seems to confirm the tendency of the IC peak to move to lower frequencies (well below 200 GeV) when the TeV source is fainter. On September-October 2002, the IC peak must have been at energies $\leq$ 100 GeV. The synchrotron peak behaved in the same way, as confirmed by the correlation of the spectral index and the flux intensity. Also, the hypothesis of anti-correlation between optical flux and X-ray flux was confirmed by the peaks shifts. The luminosity of the peak is surprisingly high for the expectations of the model, if the only change between HEGRA measurements is simply a lower electron energy density. This can be an indication of a larger emitting region R with a longer variation time or with increased Doppler factor. The simultaneous shift of the peaks would also be consistent with the assumption of the one zone electron break energy.

A first attempt to fit the observed MAGIC spectrum, considering the effect of the EBL absorption as in [146], was tried with a reasonable set of one zone SSC model parameters, compatible with the possible synchrotron and IC peak positions. The spectrum assumed for the X-ray range has been assumed to be the

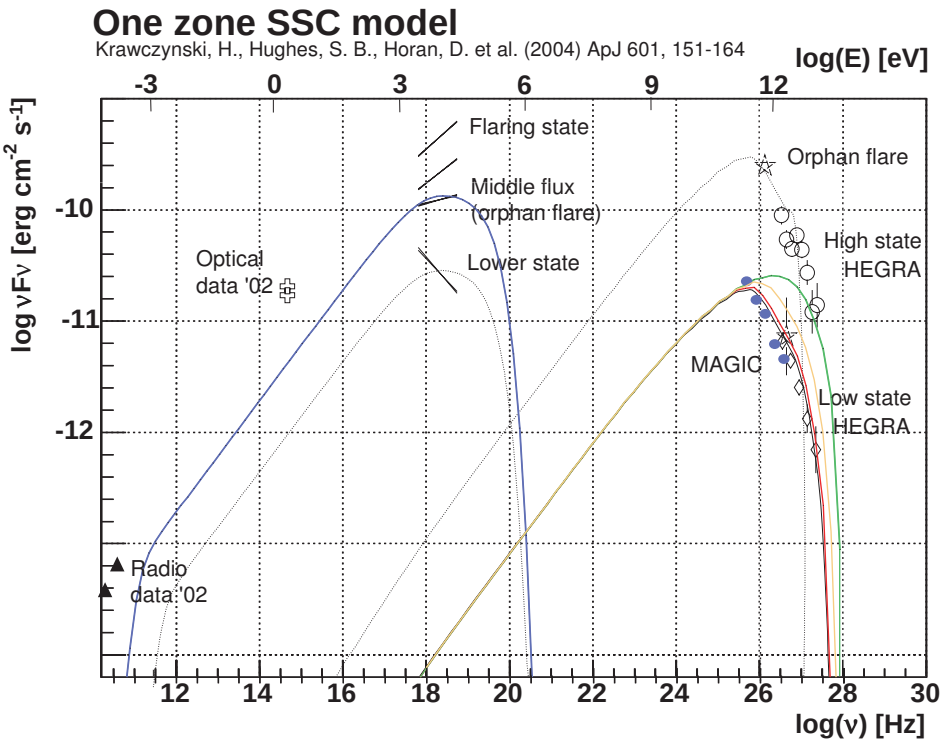

Figure 9.9: *Spectral energy distribution (SED) of 1ES1959+650 measured by MAGIC (blue dots) and the published result of the multi-wavelength campaign of 2002, from radio to γ-ray. The SSC model with parameters: δ=20, B= 0.04 G, R= 1.4×10^{14} m, electron E density = 0.014 erg/cm^3, log(E_{min}/eV)=3.5, log(E_{max}/eV)=12.2, log(E_b/eV)=11.45, was used to fit the low state data: the green solid line represents the IC peak without taking into account the EBL absorption, while the red line has been obtained with the EBL absorption model of Kneiske et al. [31] and the yellow line corresponds to the predictions of the EBL model by McMinn and Primack (1996) [146]. The synchrotron peak (blue line) fits the X-ray spectrum as measured during the orphan flare (average X-ray flux). The dotted line is an attempt to explain the additional γ-ray emission during the orphan flare (open stars) with a dense electron population (electron energy density: 17 erg/cm^3) confined in a small region (R=8×10^{12} m). Taken from [78].*

one measured during the low emissions period from the multi-wavelength campaign: on September-October 2004 the mean flux was (0.38±0.20) counts/s, compatible with the mean flux registered during the TeV observations during low state in 2000 with (0.35±0.24) counts/s and in 2001, with (0.41±0.34) counts/s. During the orphan flare on June 4^{th} the mean X-ray flux was $\sim$ (0.52±0.15) counts/s, while the lowest recorded spectral index was obtained when the mean flux was lower than (0.23±0.16) counts/s. The assumption takes into account the strong correlation found between the flux and the spectral index.

The result, shown in figure 9.10, gives an optical flux that is too high and X-ray

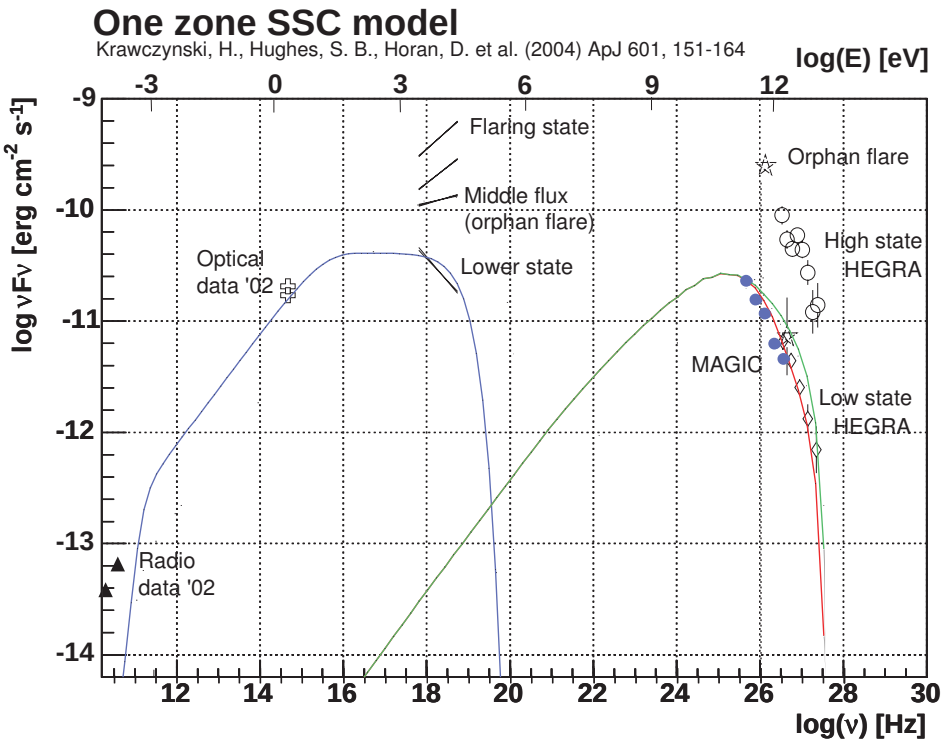

Figure 9.10: *SED of 1ES1959, fitted with the one zone SSC model using the following parameters: Doppler factor:21, B=0.04G, R=2.0×10^{14}m, electron E density = 0.014, erg/cm^3, log(E_{min}/eV) = 4.1, log(E_{max}/eV) = 11.8, log(E_b/eV) = 10.3. The red line shows the spectrum obtained taking into account the EBL absorption effect by McMinn and Primack (1996) [146]. With these conditions, the MAGIC data are well described, the X-ray flux results to be particularly low.*

flux which is a bit too low. The possible explanations are that either the effect of the EBL absorption is higher, or an absorption of the optical emissions masks the increasing of the flux in that energy region. The two possibilities can both influence the observations. Of course, we have to consider also the possibility that the observations of MAGIC are the results of processes of other physics origin (see later). The clear message arising from this picture is that a study of the source in quiescent state can be a complex mosaic of different emitting processes and therefore left for detailed studies by experts.

9.2.2 Leptonic models describing the orphan flare

The reported events of γ-ray flaring in absence of high X-ray activity gave rise to alternative hypothesis, outside the one zone SSC model, in order to explain the TeV emission from 1ES1959 without the expected X-ray activity. The possible scenarios listed below follow the interpretations published in [78] and references therein.

Multi-zone SSC model The introduction of a second electron population can provide a γ-ray flare without a X-ray counterpart (see figure 9.9, dashed line). The extra-emitting-zone can be characterized by electrons with an energy cutoff E_{max} low enough to produce only a γ-flare by IC process. On the other hand, the parameter conditions have to be fine tuned. Another possibility is that the spectrum of the electrons is so hard to produce synchrotron emissions at energies higher than the ones detected by RXTE.

External Compton models If seed photons are produced outside the jet and then injected within a short, limited time interval, the IC scattering by high energy electrons can produce the observed TeV flare without production of X-rays. The high anisotropy of the external photon field in the jet frame can strongly beam the emissions. The hypothesis of precession of the jet is then introduced to explain the fast and big change in the TeV emissions observed. Possible origin of external photon fields are the accretion disk (that can be intrinsically variable) or a region external to the jet and able to re-process photons (from the accretion disk or from the jet itself) sending them into the jet.

Alignment of magnetic field A possible explanation of the missing synchrotron observation can be the fact that the magnetic field of the emitting region is aligned with the jet axis (and therefore to the line of sight). Therefore only the IC photons can be seen from the earth, while the synchrotron radiation is emitted mostly in perpendicular direction.

9.2.3 Hadronic models

Protons can generate VHE γ-rays in an AGN jet via synchrotron process [68] in presence of a strong magnetic field ($\sim$ 100 G), or as products of cascades after hadronic interactions [66, 67], or via photomeson production, as mentioned in 1.3.1.

Reasonable hadronic model parameters are able to describe Mkn 421 and Mkn 501 flaring activities. The hadronic models, elaborated until now and attempting to explain the strong and fast TeV flares from AGNs, have a major problem in explaining fast variations in TeV γ-ray flux. The protons of a thin layer of the emitting region should be responsible of the short and strong flares, while synchrotron emissions can be produced in the entire region, with a slower X-ray emission. This flare pattern is not confirmed by observations, thus considered less probable. The correlation between X-ray and TeV γ-ray flares is a strong argument in favour of the leptonic one zone SSC model.

No steady γ-ray emissions have been reported before with sufficient precision (in time and flux) to give input for the setup of models. In principle, the fact that we observed 1ES1959 during a steady γ-ray emission period, without episodes of strong variations, gives more freedom to consider alternative sources of the low- quiescent γ-ray flux, for example protons. A nearly steady γ-ray emission, like the one reported here, implies production of photons, without strong variations. The steady

emission can be explained by protons without requiring extreme environmental conditions, like strong magnetic fields or extremely small emitting regions. Both proton acceleration and *cool down* are expected to be slow, i.e. stable in the time scale of months or years.

The steady low emission is not constrained by the cooling time problem: it is not unlikely that protons are responsible of the observations of MAGIC. Simultaneous multi-wavelength observations are necessary to monitor and give a picture of the source behaviour during the low, quiescent TeV state.

The observation of orphan flares can be explained in a framework of a specific hadronic model, that will be here briefly reported.

The hadronic model describing the orphan flares

The orphan flares are maybe the strongest argument in favour of a non negligible presence of accelerated protons in the plasma of the AGN jet. According to the model elaborated by Böttcher in [94], the orphan flare observed by Whipple can be attributed to the protonic component of the jet, as schematically explained in figure 9.11. The second *orphan* flare detected with CT1 can be compared with the predictions of the model.

The mirror model is, in my opinion, plausible, but unlikely to generate two such big flares in a short time: a natural mirror is unlikely efficient enough to provide such a concentration of soft photons in a limited time and space. The most improbable thing is that it happened twice within a few days. If, as claimed in [94], the radiation field came from the May flare, it would be natural to expect a flaring pattern similar to the previous one, but much more smeared out, with weaker flares. Unfortunately, the moon period just after the May flares and before the observation of the orphan flares prevented a detailed study over extended times. Another problem of this model is the high probability of hadronic interactions when the emitting region, filled with high energy protons, reaches the mirror cloud. To limit the hadronic interactions, the cloud should be located off-axis with respect to the jet.

Neutrino emission

Neutrino emission is naturally associated to the protonic activity in the jet. The observation of neutrinos is considered a key point for the confirmation of the presence of protonic processes, but the neutrino flux is considered too low to be detected in present detectors, even if the observations of neutrino events from 1ES1959 have been reported.

According to [143], 5 neutrinos have been detected from 1ES1959 with AMANDAII, one of them recorded in MJD 52429, just few hours after the reported time of the orphan flare seen by the VERITAS collaboration. The significance of this coincidence cannot be evaluated, because the atmospheric neutrino background is consistent with the observed neutrino rate. The fact that during the CT1 orphan

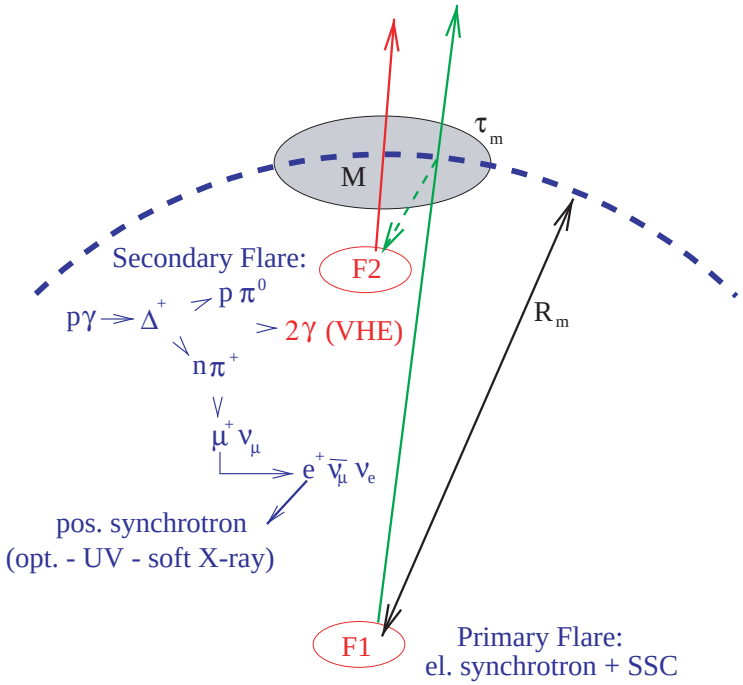

Figure 9.11: *Geometry of the hadronic synchrotron mirror model, taken from [94]. The emitting region F1, responsible of the the flare of May 2002, is moving towards the mirror M, consisting in a gas cloud which reflects the radiation. The electrons in the region are rapidly cooling down, but the protons cooling process is much slower. About 15 days later, the region F2, filled with high energy protons and with high* Γ *factor, approaches the mirror M. The mirror M is responsible for the re-entry into the jet of the primary synchrotron flare, produced in F1.*

flare no neutrinos were seen, does not rule out the possibility of hadronic acceleration in the 1ES1959 jet.

The estimate of a possible neutrino flare, according to the hadronic synchrotron mirror model applied to the observations of the Whipple telescope are presented in [142]. The authors claim that the TeV orphan flare should produce a neutrino flare, temporally coincident to the γ-ray flare (i.e. $\sim$15 days after the primary flare) and of the duration of $\sim$ 1/3 hours. The expected rate for the AMANDA detector was estimated to be 10^{-4} ν_μ events per hour. The event recorded by the neutrino telescope cannot be explained by the assumed model.

The orphan flare seen two days before the neutrino event can help, in a certain way, to enlarge the time window when possible neutrino events could be produced. The need for time coincidence between γ-rays and neutrino events is a more stringent parameter for the determination of the neutrino flux. As already mentioned, the non-detection by AMANDA does not rule out the hypothesis of a hadronic origin of the flares.

9.3 BH parameters and jet parameters

The 1ES1959 jet properties have been studied in relation to the BH properties, especially with its mass, and compared with properties of other blazars (Mkn421, Mkn501, 1ES2344+514, H1426+428) [78].

The comparison with 1ES1959 with other AGNs is interesting, because the 1ES1959 BH is the less massive of the list 9.2. The difference in the mass of the Mkn501 BH is nearly one order of magnitude.

Table 9.2: *Estimated mass of the super-massive BH (SMBH) of the TeV AGNs, from the stellar velocity dispersion (σ) and from bulge luminosity (blg).*

Source	$\mathbf{log(M_\bullet/M_\odot)_\sigma}$	Ref.	$\mathbf{log(M_\bullet/M_\odot)_{blg}}$	Ref.
Mkn 421	8.28±0.11	[144]	8.69	[70]
	8.50±0.18	[70]		
Mkn 501	9.21±0.13	[144]	9.07	[70]
	8.93±0.21	[70]		
1ES2344+510	8.80±0.16	[144]		
1ES1959+650	8.12±0.13	[70]	8.64	[70]
H1426+428			8.77	[70]

The attempt to connect the observations of the synchrotron and IC emissions, the spectral indices and flares duty-cycles with the BH mass is still far from giving a picture of the situation: the number of data available for the known AGNs is not sufficient to see any clear correlation.

9.3.1 Measurement of the IR background light

The effect of the EBL absorption appears in the AGN spectrum like a cutoff in the differential energy spectrum visible by a strong attenuation of the flux above a certain energy. The effect increases with the EBL level and with the distance of the source. In this sense, 1ES1959 is an interesting candidate for the study of the EBL, because of its distance, comparable, but a bit larger than the well studied AGNs Mkn 501 and Mkn 421.

The cutoff in the spectrum, according to the present measurements of the EBL, should show up at some TeV. The measurements collected up to now do not give strong hints of the presence of a cutoff in the 1ES1959 spectrum, even though the fits are compatible with a cutoff in energy of $4.2^{+0.8}_{-0.6 stat} \pm 0.9_{sys}$ TeV for the HEGRA high state spectrum. Deeper exposure for the collection of high energy events would be necessary to determine with more precision the shape of the last part of the 1ES1959 EM spectrum.

The intrinsic features of the energy spectra of the AGNs are considered to be the same for the observed AGNs. Of course, this is not necessarily the case, but

only a general assumption in order to derive general informations.

A recent discovery of the H.E.S.S. collaboration of two far distant AGNs with unexpected flat spectra [145] lowered considerably the previous EBL limit. The EBL would then have a weaker effect on the spectrum of 1ES1959. In figure 9.9 the comparison between the SED obtained with the model parameters given in caption with (red line) and without (green line) the effect of the EBL is shown.

If the EBL is indeed very low and can be neglected (extreme case), the parameters of the fit model should change considerably to be able to explain the observations at the higher energies, as shown in figures 9.9 and 9.10.

Further studies on this and other AGNs (especially at higher red-shift) should hopefully allow a good measurement of the IR background light above 1 TeV.

9.4 Concluding remarks

The MAGIC and CT1 measurements presented in this work considerably increased the information on the AGN 1ES1959 during periods of high TeV γ-ray activity and also during the low state.

- The most remarkable outcome of the CT1 data recorded in 2002 is the clear detection of an additional episode that can be classified as an *orphan flare*, occurring two nights before the flare reported by the Whipple collaboration. As an indication of the possible hadronic component of the jet, the episodes of orphan flare, make 1ES1959 a particularly interesting target for neutrino observations. The higher sensitivity of next generation neutrino telescopes to be installed in the southern hemisphere (IceCube [16]) will give interesting results in the next few years.

- The CT1 spectrum obtained for the 2002 low state is the first confirmation of the low state spectrum published by the HEGRA System.

- The MAGIC measurements of 1ES1959 are the first results obtained with this new generation instrument. The high sensitivity at hundred GeV energies allowed us, for the first time, to monitor the low state of 1ES1959, a faint TeV source outside flaring periods, with only few hours of observation. This possibility opens a new perspective on the study of AGNs in quiescent state. The hypothesis that 1ES1959 could be a hadronic accelerator makes further studies extremely valuable.

- The low state spectrum of 1ES1959 was for the first time obtained with MAGIC down to 200 GeV. The shape of the spectrum did not reveal any break. It can be well described with a power law function. The results obtained with MAGIC can be improved and refined. The telescope conditions were in fact not stable during the 2004 observation of 1ES1959. New data and longer monitoring will allow the study of the low γ-ray emission state. The joint observation of 1ES1959 with MAGIC and with the new γ-ray satellite GLAST, expected to measure up to energies of 300 GeV [44], will complete the drawing of the IC peak of 1ES1959 SED and its evolution during flaring periods.

Detailed models with quantitative implications are left to dedicated work by experts. We address here the possibility that in 1ES1959 both leptonic and hadronic regions emitting X-rays and γ-rays may coexist, the different episodes being determined by the jet conditions, the nature of the material injected and the cooling time of the processes involved. In particular, while correlated X-ray and γ-flaring episodes can be due to electron-positron plasma, the steady component can be due to long-term released energy by hadronic plasma regions. Even though the proposed view can be, on some occasions, used to explain *ad-hoc* the observations, we

consider that a complex jet composition, with different environmental conditions is perhaps a more realistic view than a simple uniformly populated region responsible for every possible change in the spectrum or flux level.

Appendix A

Data taken with HEGRA CT1: light curve

In the following the data of the 1ES1959 observations with the HEGRA CT1 telescope are summarized. The graphs relative to those data are presented and discussed in chapter 7 (figures 7.4, 7.5).

Table A.1: Light curve data of 1ES1959+650, calculated with the program *jacuzzi* by Daniel Kranich [96]. Data taken with HEGRA CT1 in 2000.

CT1 2000 data, nom hv (no moonlight, no hv reduction)									
MJD	flux		rate:		rate-off:		obs.time:
	(1e-11 $cm^{-2}s^{-1}$)		(h-1)		(h-1)		(h)
51723.1095	0.15	± 0.23	1.93	± 2.92	13.46	± 2.13	1.332
51724.1169	0.74	± 0.21	9.40	± 2.57	10.63	± 2.46	1.998
51725.1301	0.91	± 0.21	10.99	± 2.37	14.10	± 2.30	2.997
51726.1302	-0.16	± 0.20	-1.97	± 2.42	18.13	± 1.57	2.997
51727.1549	0.27	± 0.26	3.12	± 2.95	11.96	± 1.82	1.665
51728.1573	-0.10	± 0.20	-1.11	± 2.21	10.67	± 1.75	1.665
51729.1604	0.29	± 0.29	3.03	± 2.97	11.37	± 2.27	1.915
51730.1563	0.20	± 0.21	2.08	± 2.24	9.94	± 1.60	1.999
51731.1526	0.36	± 0.26	3.86	± 2.76	10.64	± 2.07	1.999
51732.1508	0.08	± 0.17	0.80	± 1.76	9.56	± 1.31	2.332
51733.1478	-0.08	± 0.16	-0.92	± 1.81	2.78	± 1.21	2.568
51734.1415	0.07	± 0.09	0.70	± 0.94	6.47	± 1.46	2.913
51735.1554	0.11	± 0.18	0.96	± 1.49	6.60	± 1.19	2.330
51736.1639	-0.02	± 0.07	-0.11	± 0.50	9.38	± 2.34	1.998
51784.9656	0.09	± 0.12	0.95	± 1.36	10.45	± 1.57	4.330
51785.9435	-0.04	± 0.11	-0.44	± 1.39	10.04	± 1.13	2.997
51786.9336	-0.08	± 0.14	-0.94	± 1.67	10.05	± 1.17	2.997
51787.9593	-0.14	± 0.10	-1.63	± 1.11	10.05	± 1.02	3.663
51807.8969	0.02	± 0.12	0.23	± 1.50	13.48	± 4.14	0.666

MJD	flux (1e-11 $cm^{-2}s^{-1}$)		rate: (h-1)		rate-off: (h-1)		obs.time: (h)
51808.8680	-0.10	± 0.23	-1.25	± 2.95	5.66	± 3.35	0.987
51809.8745	0.12	± 0.18	1.54	± 2.30	23.49	± 3.86	1.665
51810.8796	-0.17	± 0.43	-2.24	± 5.53	13.77	± 5.35	0.629
51811.8722	-0.01	± 0.06	-0.18	± 0.75	10.02	± 3.29	1.331
51812.8687	0.62	± 0.40	7.98	± 5.08	23.34	± 4.00	1.609
51813.8839	-0.32	± 0.68	-4.11	± 8.71	10.25	± 4.79	1.021

Table A.2: Light curve data of 1ES1959+650, calculated with the program *jacuzzi* by Daniel Kranich [96]. Data taken with HEGRA CT1 in 2001.

CT1 2001 data, nom hv (no moonlight, no hv reduction)							
MJD	flux (1e-11 $cm^{-2}s^{-1}$)		rate: (h-1)		rate-off: (h-1)		obs.time: (h)
52088.1232	0.28	± 0.24	3.52	± 2.95	8.15	± 2.10	2.331
52092.1826	0.29	± 0.29	2.81	± 2.84	9.06	± 1.99	1.332
52100.9486	1.25	± 0.80	4.47	± 2.58	8.44	± 1.52	1.998
52101.9576	0.14	± 0.35	0.68	± 1.75	8.92	± 1.25	2.331
52103.0226	0.06	± 0.25	0.74	± 3.01	16.72	± 10.28	0.333
52104.0356	-0.39	± 0.80	-4.87	± 9.85	11.27	± 4.76	0.999
52105.0419	-0.07	± 0.27	-0.84	± 3.45	7.93	± 1.98	1.332
52106.0524	0.34	± 0.22	4.33	± 2.70	10.50	± 2.00	1.998
52107.0665	-0.03	± 0.08	-0.44	± 0.98	10.06	± 1.29	2.664
52108.0378	-0.47	± 0.63	-5.89	± 7.96	7.20	± 2.90	1.664
52109.0631	-0.27	± 0.20	-3.39	± 2.44	8.83	± 1.16	3.329
52110.0815	0.07	± 0.12	0.90	± 1.40	9.37	± 1.49	3.331
52111.0736	-0.03	± 0.07	-0.35	± 0.80	11.63	± 1.21	3.663
52112.0725	-0.00	± 0.03	-0.03	± 0.35	12.71	± 1.40	2.853
52113.0760	-0.02	± 0.05	-0.30	± 0.59	10.60	± 1.11	3.663
52114.0762	-0.04	± 0.08	-0.46	± 1.00	7.81	± 0.92	3.826
52115.0634	0.17	± 0.11	2.02	± 1.33	3.93	± 1.04	4.327
52116.0777	0.04	± 0.07	0.51	± 0.87	3.23	± 0.76	3.657
52117.0896	0.13	± 0.17	1.45	± 1.96	5.11	± 1.47	2.997
52118.1007	-0.06	± 0.19	-0.59	± 2.00	5.68	± 1.15	2.329
52120.1235	-0.58	± 1.24	-4.57	± 9.77	10.64	± 5.53	0.999
52131.9831	-0.25	± 0.51	-3.15	± 6.49	10.13	± 5.11	0.666
52132.9928	0.56	± 0.27	7.10	± 3.43	9.28	± 2.22	1.332
52134.0176	0.35	± 0.20	4.32	± 2.37	8.07	± 1.85	2.665
52135.0181	0.04	± 0.09	0.50	± 1.09	9.56	± 1.19	2.997
52136.0131	-0.07	± 0.13	-0.83	± 1.53	8.06	± 1.09	2.997
52137.0125	0.07	± 0.10	0.83	± 1.17	8.39	± 1.58	2.664
52138.0103	0.06	± 0.11	0.74	± 1.39	11.22	± 1.20	2.997
52139.0167	0.35	± 0.18	4.19	± 2.13	8.37	± 1.30	2.998

MJD	flux (1e-11 $cm^{-2}s^{-1}$)	rate: (h-1)	rate-off: (h-1)	obs.time: (h)
52140.0148	0.28 ± 0.15	3.27 ± 1.80	5.14 ± 1.04	2.637
52141.0038	0.05 ± 0.09	0.61 ± 1.14	8.13 ± 1.23	2.597
52142.0151	0.06 ± 0.11	0.72 ± 1.31	7.33 ± 1.16	2.664
52143.0141	-0.15 ± 0.24	-1.73 ± 2.83	9.67 ± 1.64	2.169
52145.0107	0.23 ± 0.23	2.72 ± 2.75	5.55 ± 2.02	1.998
52146.0386	0.43 ± 0.71	4.10 ± 6.72	4.46 ± 5.63	0.665
52147.0319	0.37 ± 0.65	3.71 ± 6.44	4.90 ± 5.53	0.666

Table A.3: Light curve data of 1ES1959+650, calculated with the program *jacuzzi* by Daniel Kranich [96]. Data taken with HEGRA CT1 in 2002.

CT1 2002 data, nom hv (no moonlight, no hv reduction)				
MJD	flux (1e-11 $cm^{-2}s^{-1}$)	rate: (h-1)	rate-off: (h-1)	obs.time: (h)
52412.1232	1.31 ± 0.44	6.45 ± 1.55	6.48 ± 1.47	3.663
52413.1419	1.15 ± 0.39	8.44 ± 2.54	10.15 ± 1.33	3.012
52414.1450	1.98 ± 0.74	13.74 ± 4.66	12.90 ± 3.22	1.019
52415.1671	0.96 ± 0.23	11.48 ± 2.48	6.96 ± 1.98	1.998
52428.0700	0.81 ± 0.98	3.45 ± 4.03	14.94 ± 2.84	0.999
52429.0782	0.71 ± 0.92	3.86 ± 4.92	12.50 ± 3.75	1.332
52430.0818	2.02 ± 1.13	8.68 ± 4.28	9.67 ± 3.47	1.142
52431.1135	0.21 ± 0.20	2.18 ± 1.98	11.04 ± 1.27	2.997
52432.1187	0.53 ± 0.24	5.70 ± 2.52	15.22 ± 1.82	3.330
52433.1096	0.63 ± 0.26	6.08 ± 2.39	13.17 ± 2.12	3.663
52434.1264	0.08 ± 0.14	0.92 ± 1.65	16.40 ± 1.32	3.663
52435.1204	0.70 ± 0.17	8.04 ± 1.80	10.79 ± 1.77	3.664
52436.1228	0.24 ± 0.24	2.87 ± 2.85	17.82 ± 2.09	3.663
52437.1147	0.06 ± 0.08	0.64 ± 0.97	12.44 ± 1.94	3.663
52438.1388	0.27 ± 0.19	3.51 ± 2.41	15.18 ± 1.44	2.997
52439.1344	-0.33 ± 0.46	-4.17 ± 5.81	15.91 ± 2.30	2.997
52440.1360	0.57 ± 0.19	7.45 ± 2.34	9.31 ± 1.54	2.664
52441.1227	-0.14 ± 0.27	-1.72 ± 3.39	10.66 ± 1.69	3.331
52442.1306	0.45 ± 0.17	5.72 ± 2.10	9.86 ± 1.82	3.329
52443.1313	0.16 ± 0.15	2.07 ± 1.90	11.73 ± 1.33	3.203
52456.0103	-0.35 ± 0.76	-2.19 ± 4.69	13.15 ± 10.27	0.333
52456.9880	-1.12 ± 1.00	-4.23 ± 3.56	14.24 ± 2.46	1.228
52457.9885	1.07 ± 0.88	4.53 ± 3.55	9.79 ± 2.55	1.168
52459.0201	-0.05 ± 0.44	-0.47 ± 3.89	14.11 ± 20.84	0.257
52459.9805	2.51 ± 1.98	10.09 ± 7.42	11.35 ± 6.18	0.570
52460.9738	2.13 ± 1.49	7.42 ± 4.62	12.55 ± 3.12	0.999
52462.0810	0.75 ± 0.20	8.96 ± 2.26	8.99 ± 2.11	2.169
52462.9976	-0.15 ± 0.29	-0.99 ± 1.91	13.33 ± 1.56	2.203

MJD	flux (1e-11 $cm^{-2}s^{-1}$)	rate: (h-1)	rate-off: (h-1)	obs.time: (h)
52464.0115	0.19 ± 0.31	1.79 ± 2.88	14.76 ± 2.19	1.331
52465.0211	0.27 ± 0.22	2.95 ± 2.43	8.45 ± 1.69	1.998
52466.0176	0.34 ± 0.26	3.69 ± 2.78	10.61 ± 1.73	1.665
52466.9973	0.75 ± 0.55	6.36 ± 4.57	15.19 ± 2.88	1.009
52467.9930	-0.08 ± 0.18	-0.67 ± 1.45	12.74 ± 2.28	1.331
52469.0182	1.49 ± 0.71	18.49 ± 8.66	6.56 ± 7.93	0.693
52470.0974	1.07 ± 0.19	12.26 ± 1.80	10.39 ± 1.31	4.203
52471.1027	0.25 ± 0.14	2.90 ± 1.66	8.45 ± 0.97	4.232
52472.0865	0.28 ± 0.20	3.70 ± 2.66	8.73 ± 1.39	1.999
52473.0928	0.03 ± 0.11	0.44 ± 1.50	11.26 ± 7.78	0.666
52475.1581	0.37 ± 0.54	2.05 ± 2.90	5.64 ± 2.48	1.896
52476.1759	-0.17 ± 1.42	-0.48 ± 3.89	4.03 ± 2.85	0.998
52477.1922	-4.76 ± 7.93	-5.58 ± 8.74	6.51 ± 13.69	0.333
52482.9159	2.47 ± 2.64	9.42 ± 9.68	8.35 ± 7.96	0.666
52487.9765	0.04 ± 0.06	0.49 ± 0.69	12.40 ± 2.33	1.997
52488.9793	-0.02 ± 0.04	-0.24 ± 0.50	14.34 ± 1.98	1.998
52490.0064	0.03 ± 0.17	0.29 ± 1.84	14.23 ± 1.47	2.664
52491.0123	0.04 ± 0.10	0.42 ± 0.95	16.90 ± 1.58	2.997
52492.0225	0.51 ± 0.21	4.77 ± 1.89	5.89 ± 0.99	2.997
52493.0094	0.78 ± 0.20	8.25 ± 1.92	12.01 ± 1.25	4.995
52494.0155	0.43 ± 0.25	3.72 ± 2.14	10.35 ± 1.76	3.663
52495.0291	0.56 ± 0.23	6.43 ± 2.50	8.93 ± 1.41	2.331
52496.9742	0.18 ± 0.22	2.21 ± 2.72	8.26 ± 1.62	1.665
52498.0216	0.10 ± 0.13	1.11 ± 1.54	8.97 ± 1.98	2.331
52499.0405	0.21 ± 0.30	2.05 ± 2.96	11.66 ± 2.34	2.330
52500.0662	0.17 ± 0.25	1.49 ± 2.19	9.60 ± 1.57	1.665
52501.0859	-0.32 ± 0.90	-1.87 ± 5.33	9.82 ± 3.59	0.894
52502.0809	-0.30 ± 0.68	-1.71 ± 3.91	6.58 ± 2.97	0.999
52504.1048	1.76 ± 3.83	4.23 ± 9.04	2.74 ± 10.28	0.333
52513.9121	0.26 ± 0.27	3.36 ± 3.42	14.13 ± 2.22	1.332
52514.9424	0.58 ± 0.36	7.99 ± 4.86	15.46 ± 2.82	0.999
52515.9773	0.08 ± 0.46	1.01 ± 5.98	2.08 ± 4.74	0.659
52517.9974	0.19 ± 0.27	2.18 ± 3.09	8.03 ± 2.33	1.331
52518.9984	-0.01 ± 0.03	-0.10 ± 0.33	4.68 ± 0.91	2.994
52519.8988	-0.04 ± 0.23	-0.53 ± 3.01	17.77 ± 9.82	0.332
52520.9631	0.63 ± 0.22	7.06 ± 2.40	8.98 ± 1.93	2.664
52521.9636	0.28 ± 0.11	3.26 ± 1.29	4.01 ± 0.71	4.325
52522.9658	0.26 ± 0.13	3.06 ± 1.52	5.18 ± 1.04	3.624
52524.9784	0.03 ± 0.08	0.26 ± 0.62	5.05 ± 0.64	4.993
52525.9902	-0.05 ± 0.07	-0.44 ± 0.62	9.62 ± 1.93	2.331
52526.9634	0.35 ± 0.20	4.08 ± 2.33	12.24 ± 1.39	2.997
52527.9557	0.40 ± 0.21	4.79 ± 2.51	10.59 ± 1.41	2.996

MJD	flux (1e-11 $cm^{-2}s^{-1}$)	rate: (h-1)	rate-off: (h-1)	obs.time: (h)
52528.9666	-0.01 ± 0.04	-0.13 ± 0.43	6.81 ± 1.33	2.330
52530.0054	-0.16 ± 0.34	-0.91 ± 2.00	10.03 ± 2.07	1.332
52576.9287	0.17 ± 1.59	0.11 ± 1.00	1.05 ± 3.46	0.999
52577.9008	-0.83 ± 1.03	-2.22 ± 2.64	7.78 ± 1.59	1.662
52578.8882	1.14 ± 0.67	4.42 ± 2.26	6.46 ± 1.33	2.168
52579.9162	-0.42 ± 1.04	-0.32 ± 0.75	5.95 ± 2.65	1.331
52580.8739	0.25 ± 0.60	1.29 ± 3.05	9.51 ± 2.89	0.999
52581.8621	0.96 ± 0.63	5.79 ± 3.65	4.43 ± 3.17	1.517
52582.8897	-1.86 ± 2.54	-4.28 ± 5.61	7.92 ± 2.52	1.458
52583.8727	-0.65 ± 1.20	-2.86 ± 5.19	6.89 ± 4.68	0.788
52584.8652	-0.60 ± 0.81	-2.98 ± 3.93	8.22 ± 2.78	0.983
CT1 2002 data, hv00 (weak moonlight, no hv reduction)				
52414.0871	2.76 ± 4.47	3.32 ± 5.04	23.17 ± 7.07	0.666
52415.1162	3.21 ± 2.79	14.61 ± 12.23	34.60 ± 8.56	0.333
52426.0662	5.63 ± 4.58	10.65 ± 7.27	30.81 ± 4.47	0.762
52427.1000	5.82 ± 1.47	35.39 ± 6.45	36.27 ± 5.32	1.001
52428.1397	0.54 ± 0.51	6.05 ± 5.67	38.89 ± 4.31	1.982
52429.1562	0.20 ± 0.28	2.40 ± 3.36	33.36 ± 2.55	2.262
52431.1929	-0.05 ± 0.12	-0.68 ± 1.50	15.01 ± 7.23	0.666
52455.0196	-3.49 ±6.82	-21.43 ± 41.65	47.83 ± 25.90	0.175
52462.1727	-0.21 ± 0.47	-1.62 ± 3.56	10.69 ± 10.54	0.333
52470.9975	0.46 ± 0.62	4.29 ± 5.81	24.34 ± 6.35	0.666
52472.0286	1.54 ± 0.61	18.44 ± 7.15	19.34 ± 5.80	0.666
52473.0632	0.15 ± 0.31	1.87 ± 3.87	19.02 ± 4.51	0.666
52483.9636	-0.07 ± 1.58	-0.72 ± 15.58	1.36 ± 12.32	0.253
52484.9776	-0.06 ± 1.04	-0.64 ± 11.84	1.25 ± 9.37	0.333
52488.0043	-0.30 ± 0.66	-1.43 ± 3.16	27.39 ± 3.78	0.922
52489.0005	-0.20 ± 0.31	-1.07 ± 1.60	29.00 ± 5.74	0.999
52490.0198	5.74 ± 6.08	8.35 ± 7.74	29.07 ± 5.46	0.666
52491.8905	0.75 ± 4.95	2.19 ± 14.37	18.09 ± 9.97	0.333
52494.8951	-0.76 ± 1.59	-3.25 ± 6.77	20.47 ± 9.09	0.333
52496.8859	4.44 ± 4.05	17.00 ± 14.77	18.95 ± 12.78	0.333
52497.9032	0.42 ± 0.75	2.58 ± 4.61	18.71 ± 4.17	0.666
52498.9384	-0.86 ± 1.15	-9.74 ± 12.91	39.03 ± 8.08	0.333
52499.9561	-1.34 ± 1.72	-16.13 ± 20.61	34.58 ± 7.25	0.666
52501.0005	1.16 ± 0.71	14.47 ± 8.77	37.96 ± 5.04	0.666
52502.0144	0.58 ± 0.79	7.07 ± 9.53	30.68 ± 7.67	0.591
52513.9123	0.35 ± 0.55	3.96 ± 6.24	21.40 ± 4.01	0.634
52514.9714	1.45 ± 1.18	17.95 ± 14.50	16.01 ± 9.65	0.333
52522.8692	0.86 ± 1.04	9.54 ± 11.53	7.47 ± 10.56	0.333
52524.8664	0.87 ± 1.07	9.76 ± 11.99	10.32 ± 10.89	0.333

MJD	flux (1e-11 $cm^{-2}s^{-1}$)		rate: (h-1)		rate-off: (h-1)		obs.time: (h)
52526.8898	0.85	± 1.65	10.47	± 20.42	10.49	± 20.86	0.167
52529.9432	0.93	± 0.45	10.93	± 5.16	22.78	± 3.18	1.272
52531.0010	-1.04	± 1.62	-5.51	± 8.47	29.49	± 13.83	0.333
52577.8339	0.19	± 0.76	2.08	± 8.36	26.23	± 8.60	0.333
CT1 2002 data, hv04 (partial moonlight, 4% hv reduction)							
52415.0844	-5.07	± 6.92	-4.30	± 5.06	27.45	± 3.46	0.998
52426.1196	0.05	± 0.15	0.25	± 0.75	44.98	± 3.97	1.331
52427.1702	4.62	± 0.99	29.70	± 4.90	37.06	± 3.70	1.998
52428.2006	-1.74	± 2.57	-11.42	±16.86	31.94	± 9.51	0.333
52470.9431	3.28	± 3.29	4.56	± 3.86	17.45	± 2.46	1.332
52471.9737	6.89	± 2.02	23.69	± 3.79	16.17	± 3.10	1.664
52473.0167	1.02	± 0.89	6.24	± 5.37	27.66	± 2.94	1.331
52474.0281	2.71	± 1.51	17.37	± 9.35	40.85	± 5.32	0.666
52475.0986	-0.43	± 1.00	-2.68	± 6.24	24.98	± 4.46	0.666
52476.1357	0.59	± 1.13	2.47	± 4.68	20.09	± 4.03	0.665
52477.1742	3.39	± 6.00	5.30	± 9.00	27.64	± 9.59	0.333
52482.9672	-0.52	± 1.22	-2.83	± 6.55	36.63	± 9.17	0.333
52484.0169	-0.08	± 1.53	-0.51	± 10.06	14.17	± 6.61	0.433
52485.0261	0.63	± 0.87	4.11	± 5.70	4.96	± 5.81	0.999
52513.9646	-0.47	± 1.28	-3.10	± 8.43	16.57	± 10.50	0.333
52515.0030	-0.66	± 0.82	-3.90	± 4.87	24.97	± 3.32	0.998

Appendix B

MAGIC data and plots

B.1 Preliminary analysis of MAGIC data

The first analysis of the data was done using a preliminary test analysis version and selecting the following options:

- Calibration: as signal extractor, the Sliding Window method was chosen. Figure B.1 shows the distribution of mean conversion factors, the number of pixels which were not calibrated and the pedestal measured values.
- Pedestals for the calculation of the calibration constants have been taken from the mean value of FADC slices obtained from pedestal runs.
- The image cleaning method chosen is the so-called *scaled* [1], with cleaning levels: $4\sigma_p$ (pedestal RMS) for core pixels and $2\sigma_p$ for the neighbors. The boundary analysis includes rings up to the fifth one around the core pixels.
- The minimum number of photons in each image (SIZE) must be bigger than 2000: only higher energy events, for which stable and tested analysis was available, were selected.
- For the preliminary analysis, only a signal from the ALPHA plot was investigated and for this reason the entire available MC γ sample and an equivalent number of randomly selected events from 1ES1959 as hadronic background sample ($\sim$ 25 thousand events) have been used for the Random Forest training.

The first result obtained from this analysis are shown in the ALPHA plots of figure B.2.

[1] The *scaled* image cleaning method corresponds to the *absolute* method, explained in 6.5. The only difference corresponds to the scaling factor of the cleaning levels between inner and outer pixels: in the scaled option, the σ_p(outer)/σ_p(inner) factor is directly measured and corresponds to $\sim$3.2, while in the standard method the pedestal RMS of outer pixels is scaled with the pixel area, i.e. a factor 4.

Since the situation of the analysis improved very quickly, a confirmation of the detection was done by changing the parameters of the analysis, the signal extractor used in the calibration and the image cleaning methods. The preliminary results obtained are in good agreement with the final results, confirming that the signal from 1ES1959 is genuine.

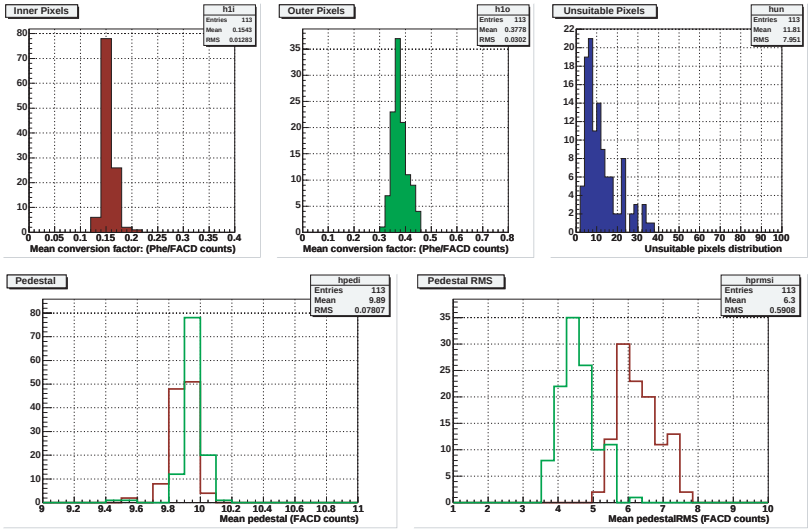

Figure B.1: Histograms of the calibration checks done for the preliminary calibration of the MAGIC data, using the sliding window algorithm as signal extractor.

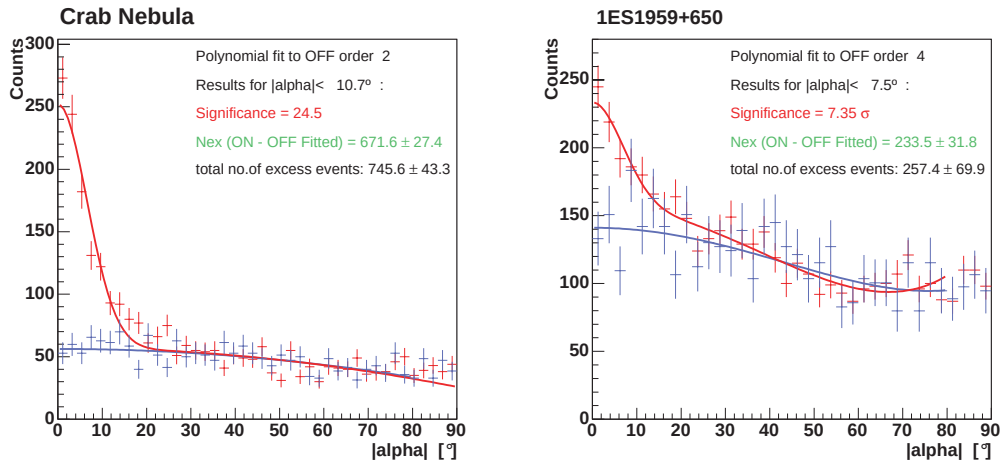

Figure B.2: Results obtained after the preliminary analysis of data with SIZE $>$ 2000 photons, using the options described in the text. In blue: OFF data. The fit to the background region is a polynomial function of order 2 ($c_1 + c_2$ ALPHA^2).

B.2 Analysis of the image parameters

After the calibration and image cleaning, the image parameters of the three analyzed samples of Crab, 1ES1959 and Off data were compared. Before selection cuts, the hadronic showers strongly dominate the γ-ray showers. Therefore we expect that the image parameters show the same distribution.

In figure B.3, the main parameters used for the γ-hadron separation are plotted, with different colors indicating the source of the events. The distributions match very well. In the lower right panel, the distribution in the camera plane of the center of gravities of the images is plotted. We expect to have a smooth and uniform distribution of hits, describing the geometry of the camera. The plots indicate that the camera had some inefficiencies, whose effect will show up in the flux estimate.

Figure B.4 shows the distributions obtained after the selection cuts applied for the γ-hadron separation, except for the ALPHA cut.

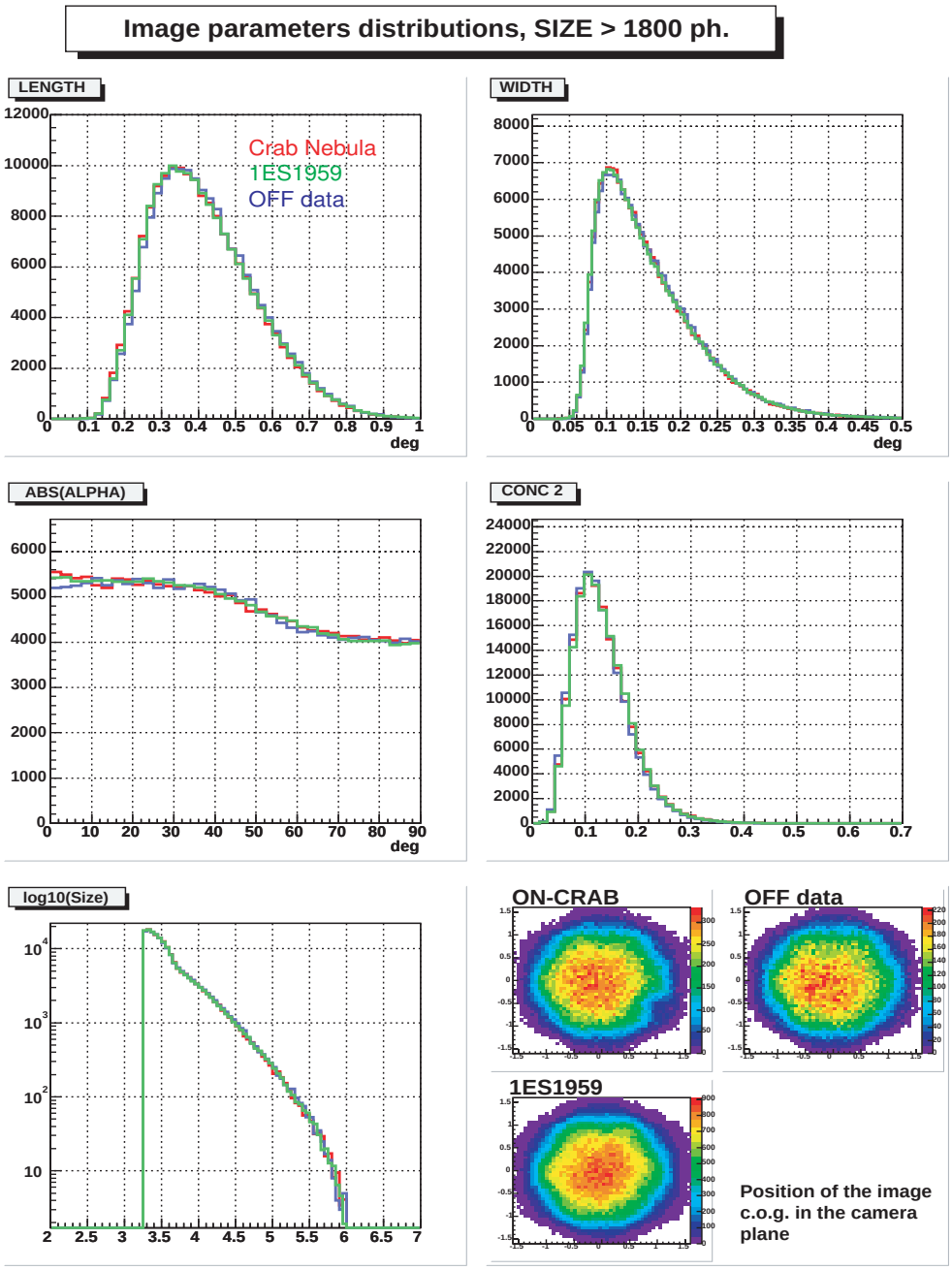

Figure B.3: Distributions of some parameters used for the γ-hadron separation, before cuts. Only a cut in SIZE>1800 photons was applied. The normalized distributions for Crab, OFF data and 1ES1959 data are plotted for a direct comparison. As the telescope observational conditions were the same when taking the data, we expect to have no difference between the 3 data samples distributions, except at small ALPHA angles. The ALPHA parameter distribution matches well in the background region above 20°.

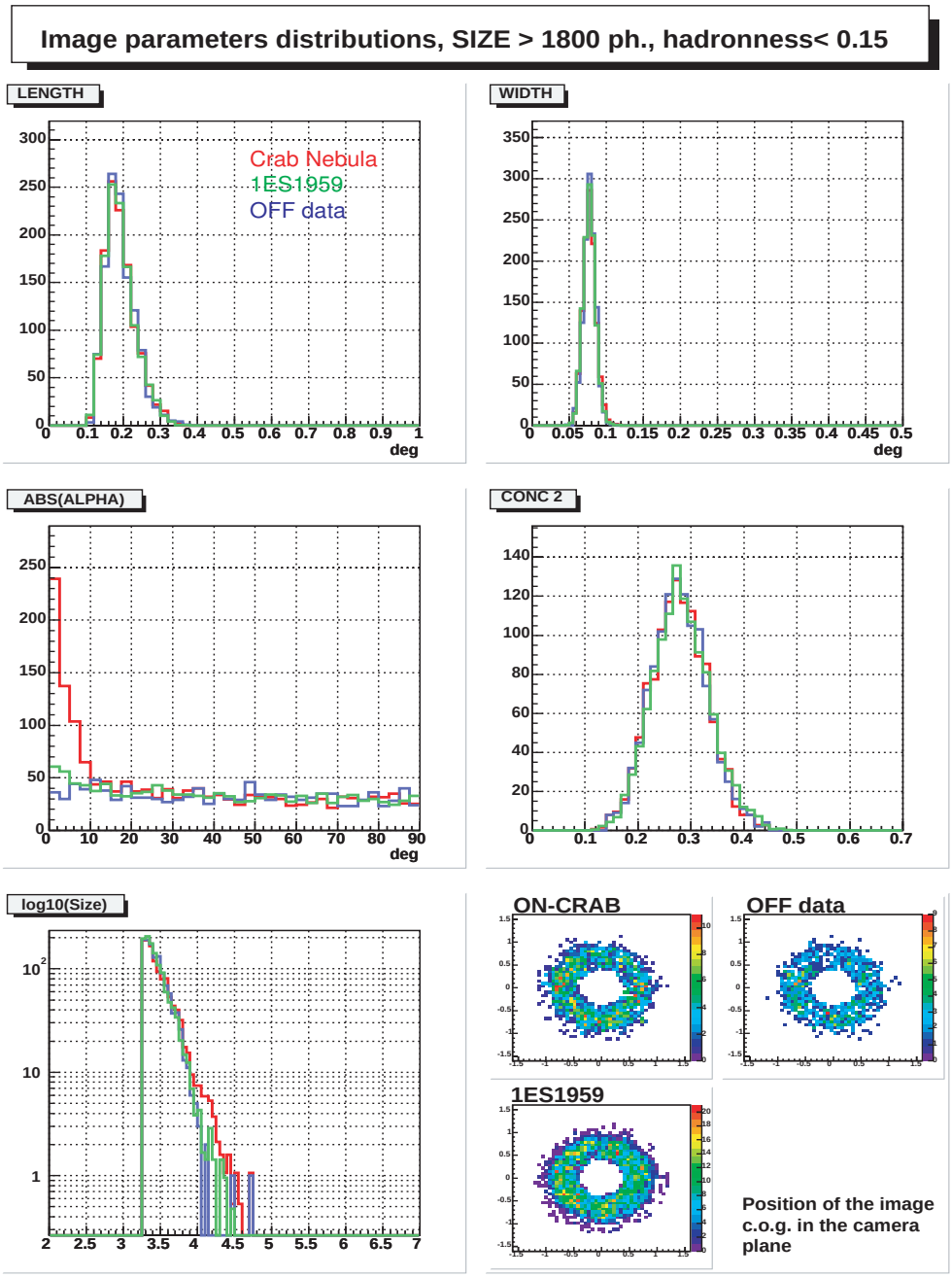

Figure B.4: The image parameter distributions for the 3 data samples, after analysis. SIZE above 1800 photons, hadronness cut below 0.15, DIST cut as in formula 8.1 and cut in roundish events: WIDTH/LENGTH< 0.7. The ALPHA parameter was not included in the cut optimization. The difference at small ALPHA angles between the 3 data samples is used to calculate the significance of the signal.

B.3 ALPHA plots: comparison with OFF - data

The ALPHA plots showed in chapter 8 are compared in figure B.5 with the ALPHA plots of the OFF data sample, after analysis and normalization. The fit on the background region (between 21° ans 81°) of the ON data histograms is in good agreement with the OFF data histogram. Here the calculation of the number of excess events, background events and the significance is calculated using the scaled OFF data.

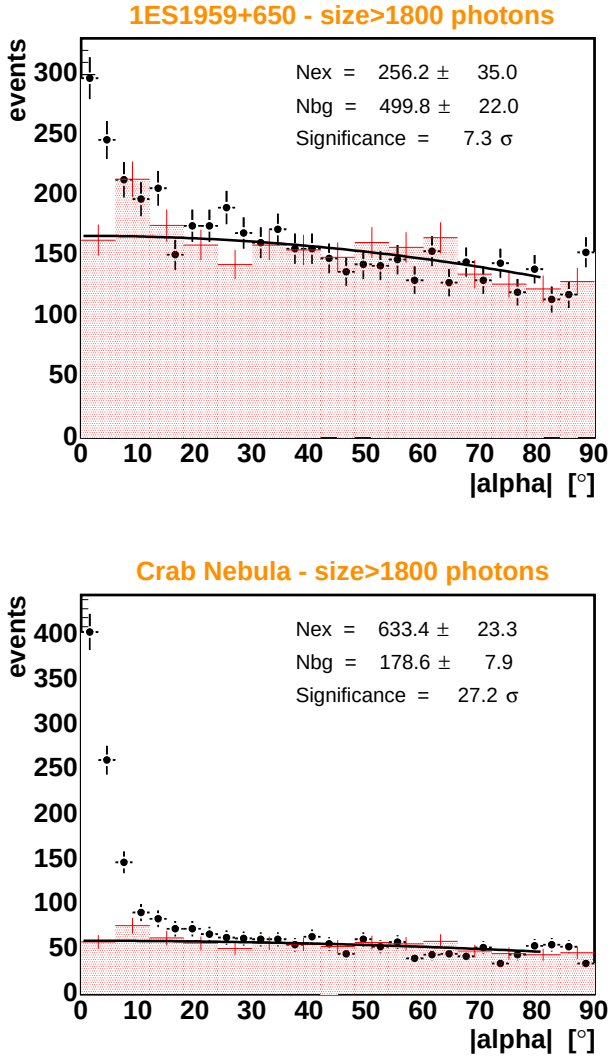

Figure B.5: The ALPHA plots for 1ES1959 and Crab, together with the OFF data sample, normalized to match the same number of entries in the background region, between 21 and 81°. The normalization factors are 1.44 for Crab and 4.02 for 1ES1959.

B.4 Light curve

Figure B.6 shows the plots of the ALPHA parameter for the 1ES1959 data set, divided into night of observation.

The ALPHA plots are produced by applying to data the same cuts used for figure 8.8: SIZE>1800 photons, hadronness<0.1. The fit to the bg region is done using the log-likelihood method, between 21° and 81°. The polynomial function used to fit the background region is plotted in red, the polinomial-plus-Gaussian function used to describe the background-plus-signal (i.e. the measured points for the entire ALPHA range) is plotted in blue. The excess in the ALPHA distribution was parameterized by a Gaussian function with a fixed sigma of 4.4°, identical to that of the Crab signal. In black, the prolongation of the polynomial function in the background region is drawn. The cut in ALPHA is 9°.

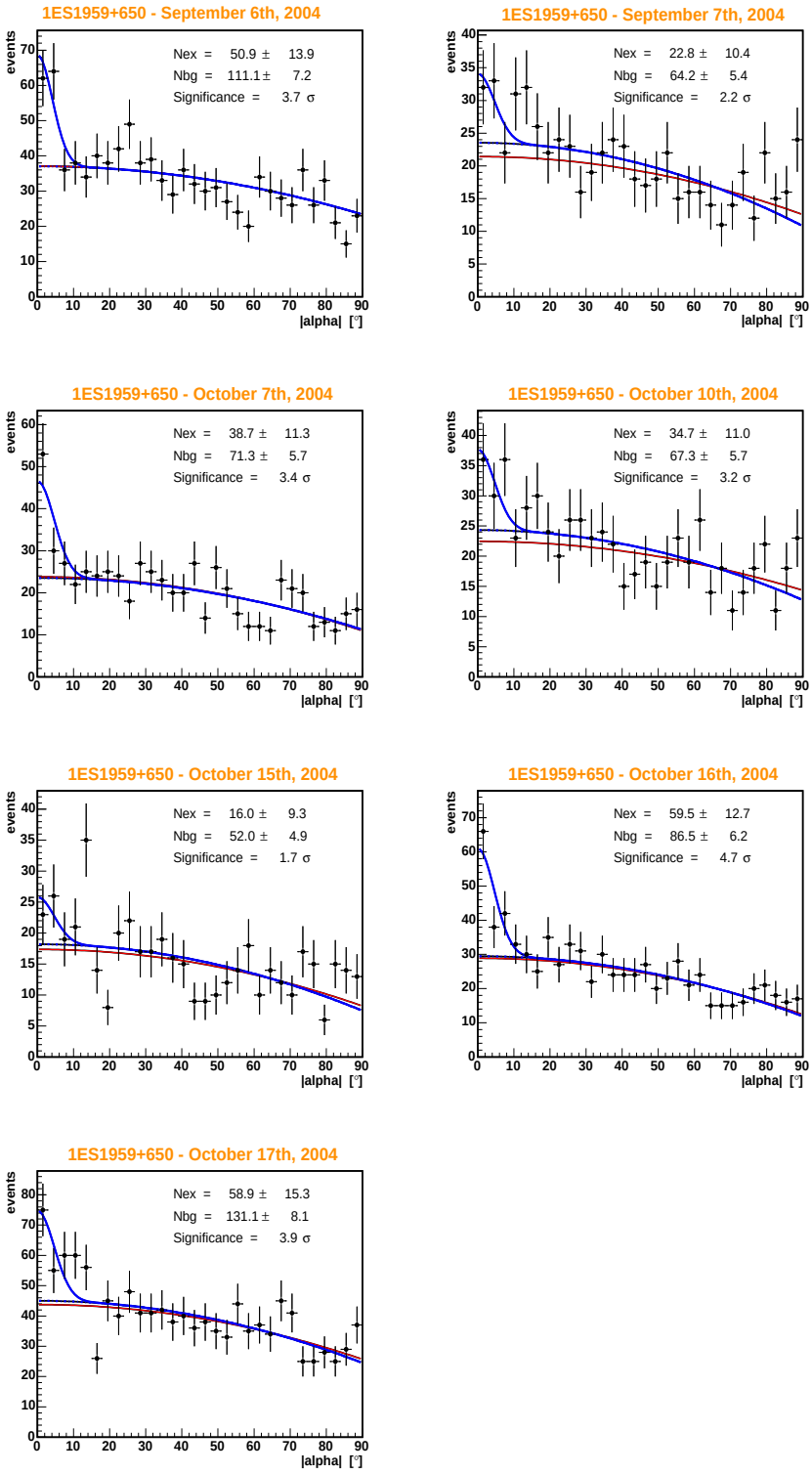

Figure B.6: ALPHA plots for 1ES1959 for each of the 7 days of observation. For the color code, see text on p.193.

B.5 Analysis in Energy bins

Figure B.7 shows the distribution of true (MC simulated) and estimated energy of a test MC γ-sample. The energy estimation procedure has a resolution of $\sim$26%.

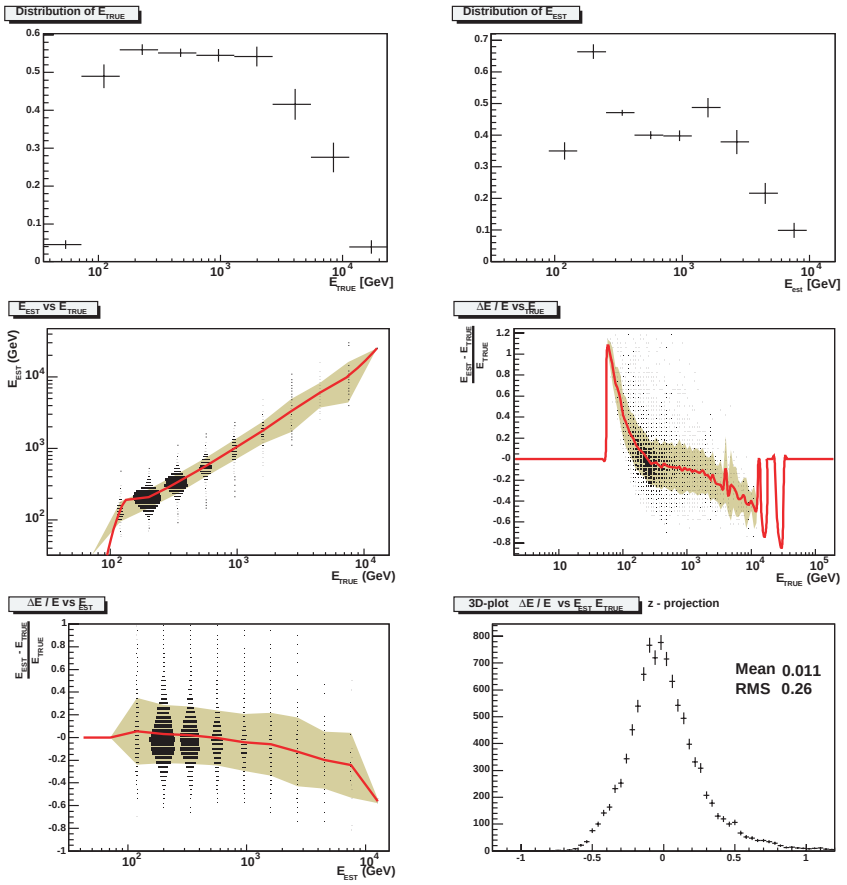

Figure B.7: Distribution of true energy and estimated energy for the test MC γ-sample used for the analysis.

In figure B.8 the effective collection area and the cut efficiency as a function of energy are shown. They have been used for the calculation of the differential flux.

The ALPHA plots, corresponding to the different energy bins into which we had divided the Crab and 1ES1959 samples, in order to compute the differential spectrum, are shown in figures B.9 and B.10. Tables B.1 and B.2 give a summary of the results

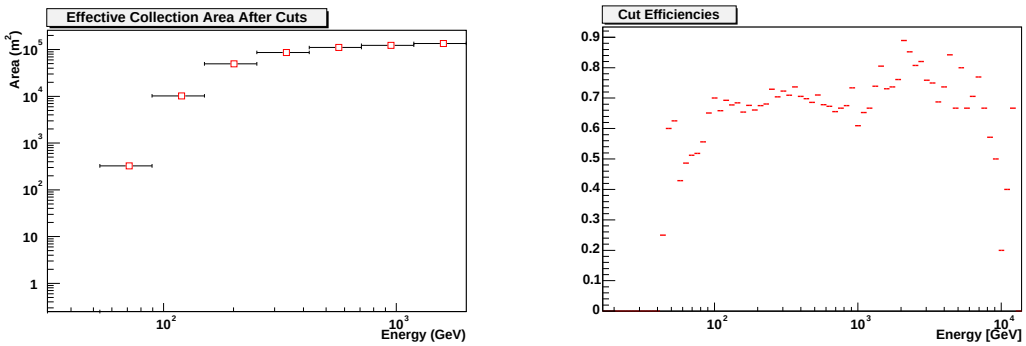

Figure B.8: Left: Effective collection area as a function of estimated energy obtained from MC γ used to compute the differential flux. Right: The γ-efficiency of the cuts listed in table B.1 and applied to the Crab data, as a function of energy.

Table B.1: Crab data analysis in bins of energy: summary. The corresponding ALPHA plots are shown in figure B.9. The background region for the normalization was set between 21° and 81°.

Crab Nebula				
Energy (GeV)	Had. cut	ALPHA cut	Excess evts	Signif.
150 - 252	0.30	18°	459.1± 74.9	6.1
252 - 423	0.30	12°	386.3± 33.4	11.6
423 - 710	0.30	9°	245.9± 18.1	13.6
710 - 1191	0.30	9°	123.6± 10.8	11.5
1191 - 2000	0.20	6°	60.7± 4.6	13.2

Table B.2: 1ES1959 data analysis in bins of energy (before unfolding): summary. The corresponding ALPHA plots are shown in figure B.10.

1ES1959+650				
Energy	Had. cut	ALPHA cut	Excess evts	Significance
150 - 252	0.20	12°	246.2 ± 66.5	3.7
252 - 423	0.20	12°	207.6 ± 39.7	5.2
423 - 710	0.20	12°	127.5 ± 25.8	4.9
710 - 1191	0.35	6°	46.4 ± 11.0	4.2
1191 - 2000	0.20	6°	22.2 ± 6.1	3.6

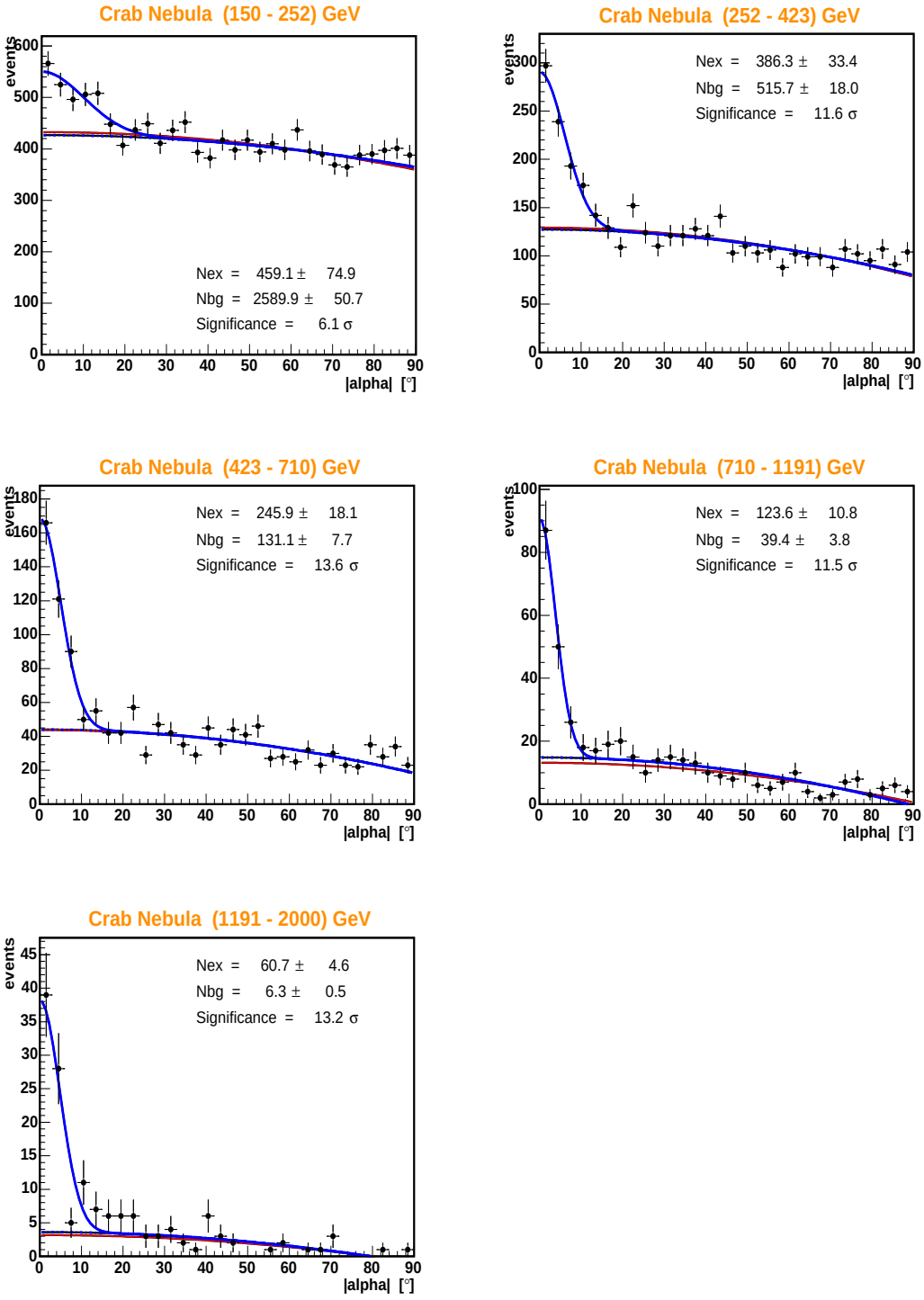

Figure B.9: ALPHA plots for the Crab data, one for each of the 5 energy bins used for the spectrum comparison. The fit to the bg region is done using the log-likelihood method. For the color code, see text on p.193. The parameters for the plots are given in table B.1. The quadratical sum of the signal significance found in each energy bin is 25.7σ, slightly improved (but compatible within 1σ) with the result found applying the standard method (SIZE>1800 photons, fixed ALPHA cut).

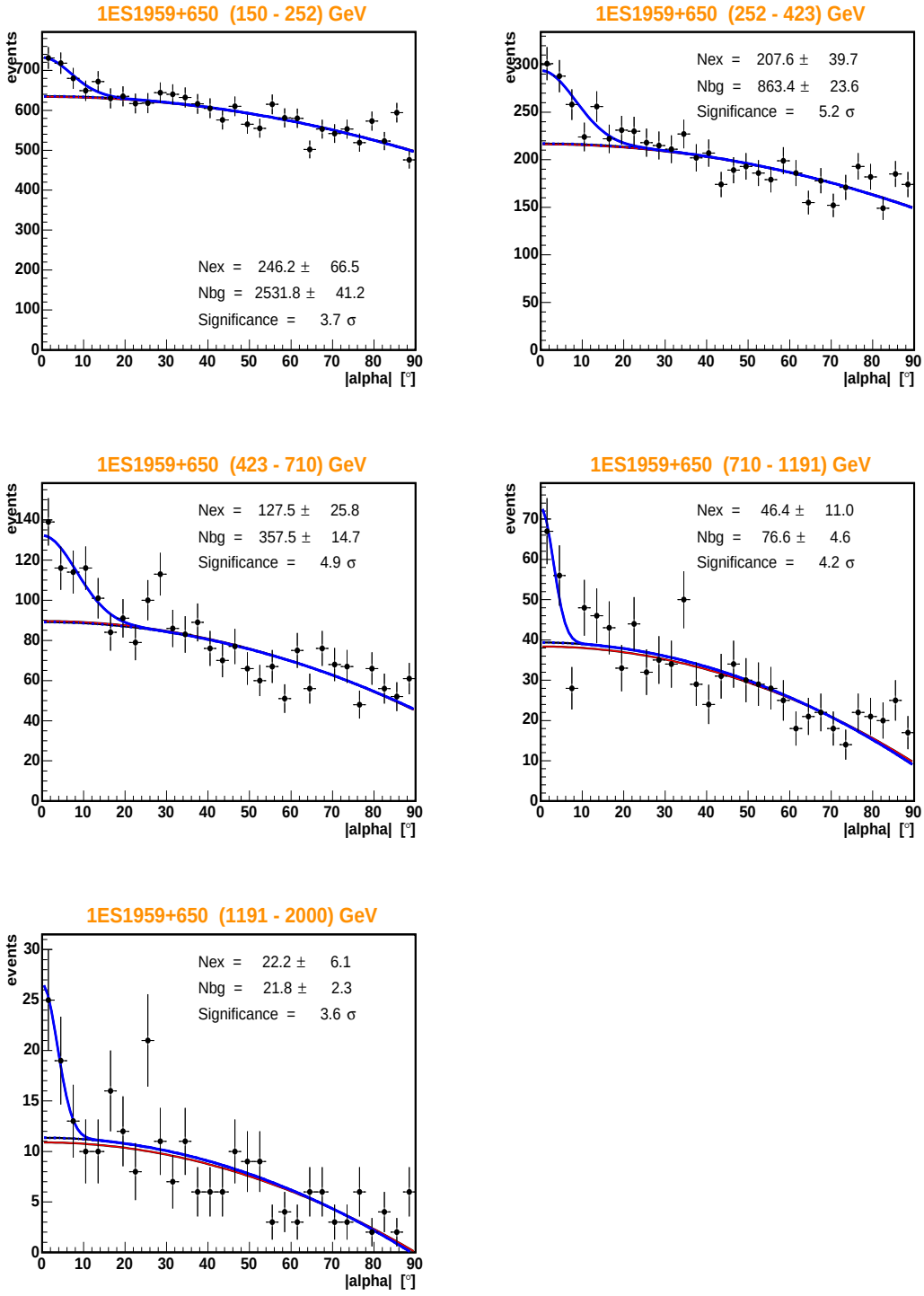

Figure B.10: ALPHA plots for 1ES1959 for each of the 5 energy bins used for the spectrum. The fit to the bg region is done using the log-likelihood method, with the parameters given in table B.2. For the color code, see text on p.193. The sigma of the Gaussian function approximating the ALPHA excess was fixed according to the Crab signal for the corresponding energy bin. The quadratical sum of the signal significance found in each energy bin is 9.8σ, slightly improved (but compatible within 1σ) with the result found by applying the standard method (SIZE>1800 photons, fixed ALPHA cut).

B.6 Estimate of the camera inefficiency

The camera inefficiencies are evaluated by means of the events distribution in the camera plane. The ideal case would foresee a flat distribution in ϕ angle in the number of events in the camera, while an inefficiency in an area of the detector would appear as a lower number of events coming from that region.

The reasons for the inefficiencies can be related to the trigger, the PMTs or shadows in front of the camera, but they are, at the moment, not fully understood.

We divided the Crab and 1ES1959 data samples into 2 bins of energy, the lower one between 150 GeV to 420 GeV and the higher one between 420 GeV to 2 TeV. A soft cut in hadronness<0.3 was applied, while the ALPHA cut was set to 12° for low energies, 9° for high energies. For every bin, we plotted the image center of gravity of the events surviving all the cuts, is shown in figures B.11 and B.12, above. The vertical line on those plots divides the data into 2 parts: regions above the line determine the high efficiency region; below, the low efficiency region. The line that defines the high and low efficiency region has been determined to be around 3:4 of the highest point and at the same time to have enough points in the two regions. In the absence of dedicated efficiency measurement I assumed that the camera is fully efficient in the 'high efficiency' region.

We calculated for each energy bin, each region and each source the number of excess events and background events and we determined how many events we lost due to the inefficiency.

The results are listed in table B.3.

From the distributions of events in the camera, it is possible to identify a common 'low efficiency' region, between 80° and 140°, and a 'high efficiency' region, between 160° and 180°. However, there is no clear systematic behavior of the different parts of the camera. The ALPHA plots also do not show the same effect of the camera inefficiency in the number of background and excess events, either. Therefore, I decided to calculate a mean global correction factor of 26% to apply to the calculated flux. This correction factor does not affect the spectral indices.

Further studies will be helpful to reveal the nature of the inefficiency and possibly will give a better indication of its effects on the spectrum calculation.

Table B.3: Calculation of the effect of the camera inefficiency for Crab and 1ES1959, on the number of excess events (that directly affects the flux calculation) and on the number of background events, as a check.

Crab Nebula					
Energy bin	High eff. area	Expected excess	Difference	Expected bg	Difference
150-420 GeV	44.4%	455.8 + 570.8	280.5 (37.6%)	1164.8 + 1457.9	380.2 (17%)
420-2000 GeV	50%	252.9 + 252.9	79.6 (18.7%)	122.1 + 122.1	41.4 (20%)
1ES1959+650					
Energy bin	High eff. area	Expected excess	Difference	Expected bg	Difference
150-420 GeV	38.9%	317.2 + 498.2	194.9 (31.4%)	2665.8 + 4187.2	568.5 (9%)
420-2000 GeV	38.9%	127.2 + 199.8	136.6 (71.7%)	201.8 + 317.0	9.2 (2%)

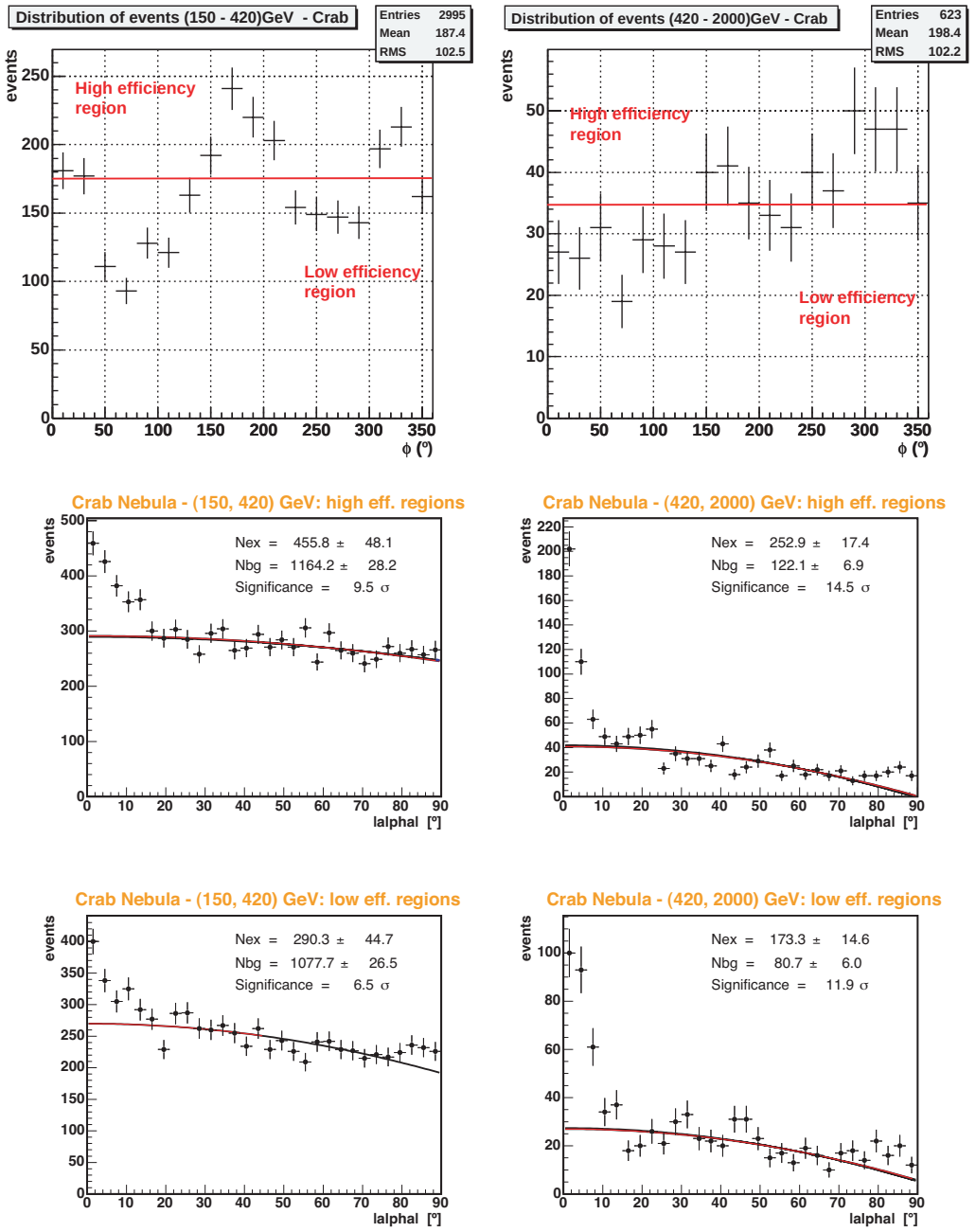

Figure B.11: Upper plots: distribution of events after cuts (in Hadronness, DIST e ALPHA), for 2 energy bins, around the camera. The inhomogeneity of the camera is especially strong for low energy for the Crab sample. Low: the ALPHA plots corresponding to the *low efficiency region* (left) and the *high efficiency region* (right) of the camera, as defined in the upper plots.

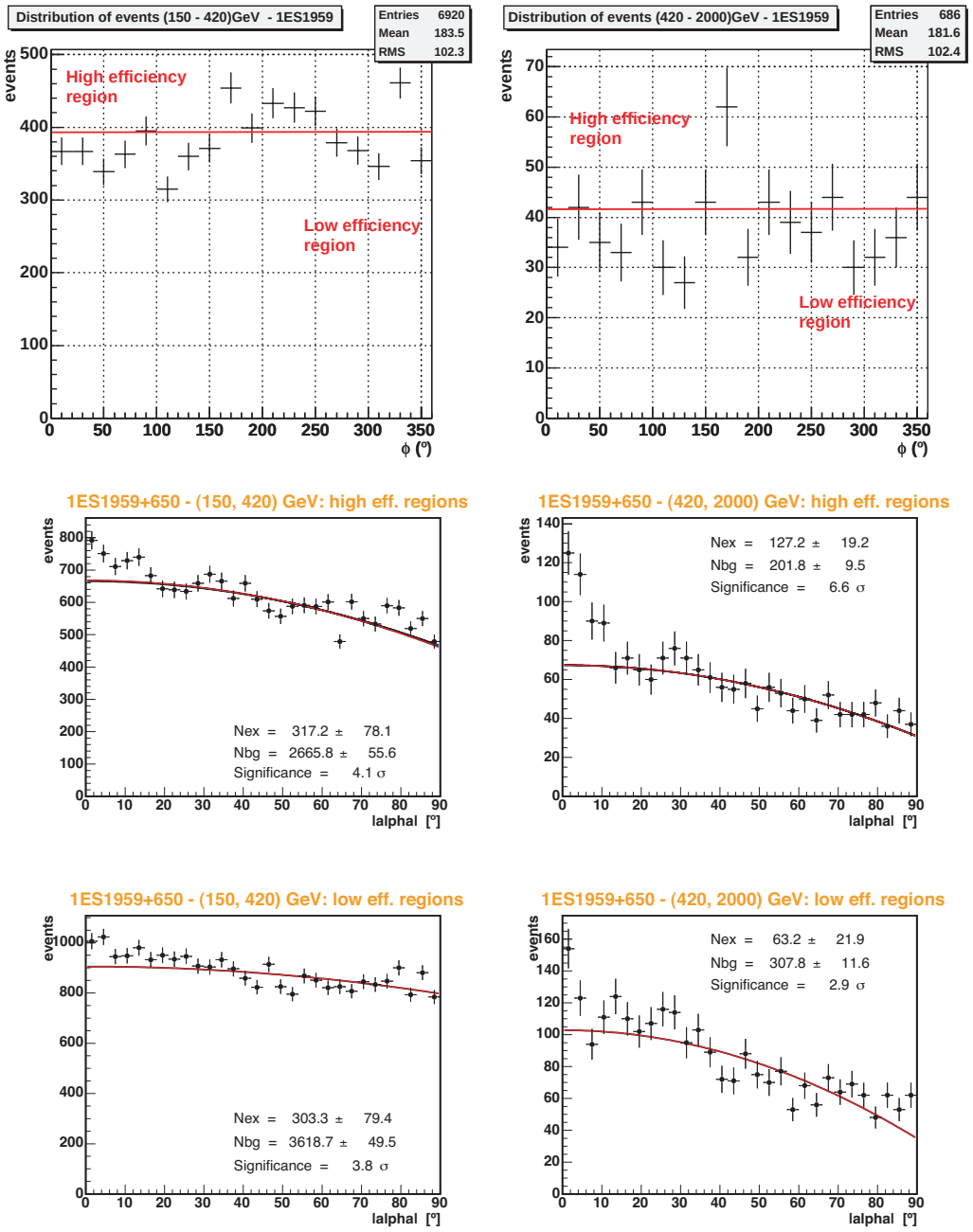

Figure B.12: Upper plots: distribution of 1ES1959 events after cuts (in Hadronness, DIST e ALPHA), for 2 energy bins, around the camera. Low: the ALPHA plots corresponding to the *low efficiency region* (left) and the *high efficiency region* (right) of the camera, as defined in the upper plots.

Bibliography

[1] Galbraith W. and Jelley V., Nature **171**, 349 (1953)

[2] Weekes T.C. et al., ApJ **342**, 379 (1989)

[3] Hartman R.C. et al., ApJ Suppl. **123**, 79 (1999)

[4] Weekes T.C., Proc. of the International Symposium on High Energy Gamma-Ray Astronomy, Heidelberg, 10431+ (2000)

[5] Torres D.F. and Anchordoqui L.A., Solicited review article prepared for Reports on Progress in Physics (2004) *astro-ph/0402371*

[6] Greisen K., Phys. Rev. Lett. **16**, 748 (1966)

[7] Zatzepin G.T. and Kuzmin V.A., JETP Lett. **4**, 78 (1966)

[8] Chiba N. et al., Nucl. Instr. Meth. **A 311**, 388 (1992)

[9] Ohoka H. et al. [AGASA Collaboration], Nucl. Instr. Meth. **A 385**, 268 (1997)

[10] Olinto A., Proc. of 28th International Cosmic Ray Conference **8**, 299 (2003)

[11] Corbato S.C. et al., Nucl. Phys. Proc. Suppl. **28B**, 36 (1992)

[12] Abu-Zayyad T. et al., Nucl. Instrum. Meth. **A 450**, 253 (2000)

[13] Abraham J. et al. [AUGER Collaboration], Nucl. Instr. Meth. **A 523**, 50 (2004)

[14] Farrar G.R. and Biermann P.L., Phys. Rev.Lett. **81**, 3579 (1998) *astro-ph/9806242*

[15] Andres E. et al. [AMANDA Collaboration], Astropart. Phys. **13**, 1 (2000)

[16] Alvarez-Muniz J. and Halzen F., AIP Conf Proc. **579**, 305 (2001) *astro-ph/9906203*

[17] Balkanov V.A. et al., Proc. of TAUP 99, Paris, Nucl.Phys.Proc.Suppl. **87**, 405-407 (2000) *astro-ph/0001145*

[18] Aslanides E. et al. [ANTARES Collaboration], *astro-ph/9907432*

[19] Grieder P.K. [NESTOR Collaboration], Nuovo Cim. **24C**, 771 (2001)

[20] Longair M.S., *High Energy Astrophysics*, Cambridge University Press (1992)

[21] Aharonian F.A. and Atoyan A.M., Phys.Lett. **99B**, 301 (1981)

[22] Primack J.R. et al., AIP Conf. Proc. **558**, 463 (2001)

[23] Aharonian F.A., Proc. of 27th ICRC, Hamburg (2001)

[24] Krennrich F. et al., ApJ **511**, 149 (1999)

[25] Vassiliev V.V., Astropart. Phys. **12**, 217-238 (2000)

[26] Primack J.R., Astropart. Phys **11**, 93-102 (1999)

[27] Scalo J.M., Fund. Cosmic Phys. **11**, 1 (1986)

[28] Punch, M. et al., Nature **358**, 477 (1992)

[29] Quinn J. et al., ApJ **456**, L83 (1996)

[30] Krennrich F. et al., ApJ **560**, L45-L48 (2001)

[31] Kneiske T.M. et al., A&A **386**, 1 (2002)

[32] Ong R., Proc. of 29th ICRC, Pune (2005)

[33] Urry C.M., Padovani P., Publ. Astr. Soc. Pacific **107**, 803 (1995)

[34] Aharonian F. et al., Science Express (2005)

[35] Beilicke M., Presentation at 3rd Conf. on Frontier Science: Physics and Astrophysics in Space, Villa Mondragone (2004)

[36] Kawachi A., Naito T., Patterson J.R., Edwards P.G. [CANGAROO-II Collaboration], Astrophys.J. **607**, 949-958 (2004)

[37] Kirk J. G., Ball L., Skjaeraasen O., Astropart.Phys. **10**, 31-45 (1999)

[38] Briggs M.S. et al., ApJ **459**, 40 (1996) *astro-ph/9509078*

[39] Catelli J.R., Dingus B.L. and Schneid E.J., AIP Conf.Proc. **428**, 309 (1997)

[40] Waxman E., in *Supernovae and Gamma Ray Bursters*, ed. K. Weiler (Springer), Lecture Notes in Physics **598** 393-418 (2003) *astro-ph/0303517*

[41] Barraud C. et al., A&A **400**, 1021-1030 (2003)

[42] Gehrels N. et al., Astrophys.J. **611**, 1005-1020 (2004)

[43] Gehrels N. [GLAST Collaboration], AIP Conf. Proc. **558**, 3 (2001)

[44] Gehrels N. and Michelson P., Astropart. Phys. **11**, 277 (1999)

[45] Trimble V., PASP **85**, n.507, p. 579 (1973)

[46] Horns D. and Aharonian F. A., Proc. of the 5th Integral Workshop (2004) *astro-ph/0407119*

[47] Aharonian F.A. et al., Astrophys. J. **614**, 897-913 (2004)

[48] Daugherty J.K. and Harding A.K., ApJ **252**, 337 (1982)

[49] Cheng K.S. et al., ApJ **300**, 500 (1986)

[50] Romani R.W., ApJ **470**, 469 (1996)

[51] Aharonian F.A. and Bulgovalov S.V., New Astronomy **8**, 85 (2003) *astro-ph/0208036*

[52] Weekes T.C. et al., ApJ **342**, 379-395 (1989)

[53] Kennel C.F. and Coroniti F.V, ApJ **283**, 694-710 (1984)

[54] Hillas A.M. et al., ApJ **503**, 744 (1998)

[55] De Jager O.C. and Harding A.K., ApJ **396**, 161 (1992)

[56] Biermann P.L. et al., Invited Lecture, Proc. of the 7eme Colloquium Cosmologie: 'High Energy Astrophysics from and for Space', Paris, eds. N. Sanchez and H. de Vega, in press (2002)

[57] Costamante L. and Ghisellini G., A&A **384**, 56 (2001)

[58] Gaidos J.A. et al., Nature **383**, 319 (1996)

[59] Kellermann K.I. and Pauliny-Toth I.I.K., ApJ **155**, L71 (1969)

[60] Maraschi L. et al., ApJL **527**, 81(1999)

[61] Takahashi T. et al., ApJL **542**, 105 (2000)

[62] Krawczynski H. et al., ApJ **559**, 187 (2001)

[63] Krawczynski H., `http://jelley.wustl.edu/multiwave/spectrum/` (2003)

[64] Inoue S. and Takahara F., ApJ **463**, 555 (1996)

[65] Mücke A. et al., Astropart. Phys. **18**, 593 (2003)

[66] Mannheim K., A&A **269**, 67 (1993)

[67] Mannheim K., Science **279**, 684 (1998)

[68] Aharonian F. A., New Astron. **5**, 377 (2000)

[69] Catanese M. and Weekes T.C., PASP **111**, 1193 (1999)

[70] Falomo R. et al., ApJ **569**, L35 (2002)

[71] Perlman E.S. et al., ApJS **104**, 251(1996)

[72] Stecker F.W., de Jager O.C. and Salamon M.H., ApJ **473**, L75-L78 (1996)

[73] Fossati G. et al., MNRAS **299**, 433 (1998)

[74] Horns D. et al., Contr. to International Symposium, Tokyo (2002)

[75] Nishiyama T. et al. [Utah Seven Telescope Array Coll.], Proc. 26th ICRC, Salt Lake City, **3**, 370 (1999).

[76] Weekes T. et al., in Central Bureau for Astronomical Telegrams, INTERNATIONAL ASTRONOMICAL UNION, Circular No. 7903 (17 May 2002)

[77] Daniel M. K. [VERITAS Collaboration], Astrophys.J. **621** 181 (2005)

[78] Krawczynski H. et al., Astrophys.J. **601** 151-164 (2004) *astro-ph/0310158*

[79] Tagliaferri G. et al., A&A **412**, 711 (2003) *astro-ph/0309568*

[80] Gregory P.C. and Condon J.J., ApJS **75**, 1011 (1991)

[81] Becker R.H., White R.L. and Edwards A.L., ApJS **75**, 1 (1991)

[82] Piner B.G. and Edwards P.G., Astrophys.J. **600**,115-126 (2004) *astro-ph/0309547*

[83] Heidt J. et al., A&A **341**, 683 (1999)

[84] Schroedter M. et al., Contr. to International Symposium Tokyo (2002)

[85] Elvis M. et al., ApJS **80**, 257 (1992)

[86] Kranich D. et al., Proc. of the 26th ICRC, Salt Lake City (1999)

[87] Giebels B. et al., ApJ **571**, 763 (2002)

[88] Holder J. et al., ApJ **583**, L9 (2003)

[89] Horan D. et al., ApJ **603**, 51 (2004)

[90] Robrade, J., *HEGRA observations of the Blazar 1ES1959+650*, Diplomarbeit, Inst. f. Exp. Physik, Hamburg (2001)

[91] Aharonian F. et al., A&A **406**, L9 (2003)

[92] Djannati-Ataï A. et al., in Active Galactic Nuclei: from Central Engine to Host galaxy, ed. S. Collin, F. Combes, I. Shlosman, San Francisco, ASP, 291 (2003)

[93] Khelifi B., *Recherche de sources gamma par une méthode de Maximum de Vraisemblance*, Ph.D Thesis, Laboratoire de Physique Corpusculaire et Cosmologie - College de France (IN2P3/CNRS), Universite De Caen (2002)

[94] Boettcher M., Astroph. Journal **621**, 176 (2005) *astro-ph/0411248*

[95] Halzen F. and Hooper D., Astropart. Phys. **23**, 537 (2005) *astro-ph/0502449*

[96] Kranich D., *Temporal and spectral characteristics of the active galactic nucleus MkN 501 during a phase of high activiity in the TeV range*, Dissertation an der Fakultät für Physik der TU München (2001)

[97] Mirzoyan R., Kankanian R., Sawallisch P. et al., NIM **A 351**, 513+ (1994)

[98] Barrio J.A. et al. [MAGIC collaboration], *MAGIC Design Report*, MPI-PhE/98-5 (1998)

[99] Brun R., Rademakers F., *ROOT - An Object-Oriented Data Analysis framework*, `http://root.cern.ch/`

[100] Tonello N., *Misure ottiche e strategie di trigger per il telescopio MAGIC*, Tesi di Laurea, Università di Padova (2002)

[101] Rossi B., *High energy particles*, Prentince-Hall Incorporated (1952)

[102] Greisen K., Prog. Cosmic Ray Phys. **3**, 1 (1956)

[103] Rossi B. and Greisen K., Rev.Mod.Phys. **13**, 240 (1941)

[104] Rodriguez-Frias M.D., del Peral L. and Medina J., Nucl. Part. Phys. **21**, 1121-1136 (1995)

[105] Gaisser T.K., *Cosmic Rays and Particle Physics*, Cambridge University Press (1990)

[106] Frank I.M. and Tamm I., Dokl. Akad. Nauk. **14**, 109 (1937)

[107] Jelley J.V., *Cherenkov radiation and its application*, Pergamon Press (1958)

[108] Benn C. and Ellison S., New Astronomy Review **42**, 503-507 (1998)

[109] Paneque D., *The MAGIC Telescope: development of new technologies and first observations*, PhD thesis, Fakultät für Physik der Technischen Universität, München (2004)

[110] Heck D. et al., Report FZKA 6019 (1998)
`http://www-ik.fzk.de/~heck/corsika/physics_description/corsika_phys.html`

[111] Elterman L., Applied Optics **3**, 6 (1964)

[112] Elterman L. et al., *Handbook of geophysics and space environments*, Mc Graw-Hill, N.Y. (1965)

[113] Muller D. and Tang K.K., Astrophys. J. **312**, 183 (1987)

[114] Wiebel B., *Chemical composition in high energy Cosmic Rays*, Technical Report, Universität Wuppertal, WUB 94-08 (1994)

[115] Alcaraz J. et al. [AMS Collaboration], Phys. Lett. **B 484** 10-22 (2000)

[116] Schmelling M., NIM **A 340** 400 (1994)

[117] Tikhonov A.N. and Arsenin V.Ja., *Methods of Solution of Ill-Posed Problems*, Nakura (1979)

[118] Bertero M., Advances in Electronics and Electron Physics **75** (1989)

[119] Bartko D. et al., Proc. of "Towards a Network of Atmospheric Cherenkov Detectors VII", Ecole Polytechnique, Palaiseau, France (2005) *astro-ph/0506459*

[120] Hillas A., Proc. 19th International Cosmic Ray Conference, La Jolla, **3** 445-448 (1985)

[121] Wallace P., "TPoint" `www.tpsoft.demon.co.uk/`

[122] Petry D., PhD thesis, TU München (1997), MPI-PhE/97-27

[123] Lessard R.W. et al., Astroparticle Physics **15**, 1 (2001)

[124] Kranich D. and Stark L.S., Proc. of the 28th ICRC, Tsukuba, Japan (2003)

[125] Schweizer T., PhD Thesis, IFAE- Universitad Autonoma Barcelona (2002)

[126] Domingo-Santamaria E. et al. [MAGIC collaboration], Proc. 29th ICRC, Pune (2005)

[127] Reynolds P.T. et al., ApJ **404**, 206-218 (1993)

[128] Reynolds P.T., Akerlof C.W., Cawley M.F. et al., Astrophysical Journal **404**, 206-218 (1993)

[129] Aharonian F.A. et al., ApJ *539* 317 (2000)

[130] Breiman L., FORTRAN program Random Forests Version 3.1, available at `http://oz.berkeley.edu/users/breiman`
Breimann L., Friedmann J.H., Olshen R.A., Stone C.J., *Classification and Regression Trees*, Wadsworth (1983)

[131] Zimmermann J., *Statistical Learning in High Energy and Astrophysics*, PhD thesis, Ludwig-Maximilians-Universität, München (2005)

[132] Li T.P. and Ma Y.Q., Astroph. Journ. **272**, 314-324 (1983)

[133] Aharonian F. et al., A&A **410**, 813-821 (2003)

[134] Tonello N. [HEGRA Collaboration], Proc. of 28th ICRC, Tsukuba (2003)

[135] Goebel F. et al. [MAGIC Collaboration], Proc. 29th ICRC, Pune (2005)

[136] Wagner R.M. et al. [MAGIC Collaboration], Proc. 29th ICRC, Pune (2005)

[137] Carter-Lewis D.A. et al., Proc. of the 25th ICRC, Durban (1997)

[138] Villata M., Raiteri C.M., Lanteri L., Sobrito G., Cavallone M., A&AS **130**, 305 (1998)

[139] Quick-look results provided by the ASM/RXTE team `http://heasarc.gsfc.nasa.gov/xte_weather/`

[140] Tavecchio F., Maraschi L. and Ghisellini G., ApJ **509**, 608 (1998)

[141] Dai B.Z., Xie G.Z. and Jiang Z.J., Chin. J. Astrophys. **2**, n.1, 8-16 (2002)

[142] Reimer A., Böttcher M. and Postnikov S., Astroph. Journal **630**, 186 (2005)

[143] Bernardini E., Proc. 29th ICRC, Pune (2005)

[144] Barth A.J., Ho L.C., Sargent W.L.W., ApJ **583**, 134 (2003)

[145] Aharonian F. et al. [H.E.S.S. Collaboration], submitted to Nature(2005) *astro-ph/0508073*

[146] MacMinn D. and Primack J.R., Space Sci. Rev. **75**, 413 (1996)

Acknowledgments

My work at MPI has been a memorable experience. I would like to thank who made it possible: Prof. Dr. Siegfried Bethke and Prof. Dr. Masahiro Teshima.

Thanks to whom so kindly and friendly helped me in the difficult German paper work: Sybille Rodriguez, Ina Wacker and Ursula Grenzemann.

I worked for the first months at MPI as a 'mirror expert': many thanks to Mosè Mariotti, who introduced me to Eckart Lorenz.

To Eckart I want to express all my gratitude for leading me and encouraging me in my work, with his scientific experience and human wisdom. He suggested me such an interesting argument for my thesis. It was really a successful and happy choice, I must say!

Working at the MAGIC mirrors allowed me to enjoy and appreciate the collaboration of Razmik Mirzoyan, Juergen Gebauer, Juergen Hose, Mustapha Laatiaoui, Peter Sawallish and Adriano Pepato. Thanks to all of you. A special thanks to Markus Garczarczyk, who organized with me the task forces for the mounting of the panels in Eching and the expeditions to La Palma. Many thanks to Denis Bastieri, who shared with me the times of mirror measurements at LT-Ultra, also for the good chats at the Felsenkeller in Pfullendorf.

My analysis of CT1 data would have not been possible without the help of Daniel Kranich. He also cross-checked most of my results and it gave me self-confidence. Thanks to Dorota Sobczynska for providing me with the MC data for CT1.

All the people of the MAGIC group I met in Munich are wonderful collaborators and very good friends. Many thanks to Wolfgang Wittek, Rudy Bock, Vincenzo Vitale, Keiichi Mase, J. Antonio Coarasa, Florian Goebel, Pratik Majumdar, Kenji Shinozaki, Patricia Liebing, David Paneque, Robert Wagner, Hendrik Bartko, Daniel Mazin, Nepomuk Otte and Masaaki Hayashida. Their collaboration was very important for my work. A special thank to Satoko Mizobuchi for her friendship and for the nice discussions, and to all the friends who helped me.

I am particularly grateful to Abelardo Moralejo for his especially critical view of my work, for his precious suggestions and for supporting me so patiently.

This thesis work is dedicated with gratitude to Valentino and Edda, my parents, that constantly encouraged and supported me, and to the memory of my dearly beloved grandmothers Gemma and Giulia, who taught me the value of each instant of a life time.